Investigations of helium transport in ASDEX Upgrade plasmas with charge exchange recombination spectroscopy

PROEFSCHRIFT

ter verkrijging van de graad van doctor aan de Technische Universiteit Eindhoven, op gezag van de rector magnificus prof.dr.ir. C.J. van Duijn, voor een commissie aangewezen door het College voor Promoties, in het openbaar te verdedigen op donderdag 23 oktober 2014 om 16:00 uur

door

Athina Kappatou

geboren te Thessaloniki, Griekenland

Dit proefschrift is goedgekeurd door de promotoren en de samenstelling van de promotiecommissie is als volgt:

voorzitter:	prof.dr.ir. G.M.W. Kroesen
promotor:	prof.dr. A.J.H. Donné
copromotoren:	dr. R.J.E. Jaspers
	dr. R.M. McDermott (Max-Planck-Institut für Plasmaphysik)
leden:	dr. W. Biel (Forschungszentrum Jülich)
	prof.dr. R.J. Fonck (University of Wisconsin-Madison)
	prof.dr. W.W. Heidbrink (University of California)
	prof.dr.ir. O.J. Luiten

Investigations of helium transport in ASDEX Upgrade plasmas with charge exchange recombination spectroscopy

by
Athina Kappatou

to my parents

Is it fiction, is it confession?
Is it passion or just a profession?
Is it performance, is it expression?
Is it passion or just an obsession?
Fates Warning - Monument

A catalogue record is available from the Eindhoven University of Technology Library
Kappatou, Athina
Investigations of helium transport in ASDEX Upgrade plasmas with charge exchange recombination spectroscopy
ISBN: 978-90-386-3704-4
NUR: 926

This work is part of the research programme of the Foundation for Fundamental Research on Matter (FOM), which is part of the Netherlands Organisation for Scientific Research (NWO).

This work has been carried out within the framework of the EUROfusion Consortium and has received funding from the European Unions Horizon 2020 research and innovation programme under grant agreement number 633053. The views and opinions expressed herein do not necessarily reflect those of the European Commission.

Cover design: “Purple and Teal”, by Matthias Bernert, with contributions from Athina Kappatou and Andreas Burckhart

Contents

Summary

Investigations of helium transport in ASDEX Upgrade plasmas with charge exchange recombination spectroscopy

Nuclear fusion is the merging of two light nuclei to form a heavier one; a process that can release significant amounts of energy. One does not have to look very hard to find fusion reactions. The sun, for example, is powered by fusion processes. Harnessing fusion reactions on earth for commercial energy production is the subject of fusion energy research. However, for the two nuclei to fuse, they must first be brought sufficiently close together so that the nuclear Strong force overcomes the Coulomb repulsion. This requires very high temperatures (hundreds of millions of degrees Celsius), meaning that the fusion "fuel" is ionised, forming a plasma. One of the most extensively explored ways to confine such a plasma on earth is the tokamak, which is a torus shaped device with a helical magnetic field that is employed to keep the plasma particles confined and prevent them from impinging on the tokamak wall. ITER, the international experimental fusion reactor, will be a tokamak.

The most promising fusion reaction for fusion energy production on earth, the deuterium-tritium reaction, leads to the production of helium, which carries 3.5MeV of kinetic energy (one fifth of the total produced energy). Understanding the behaviour of the helium in a future fusion reactor is critical for its performance. The fusion produced helium is needed to heat the plasma through collisions with the plasma particles. However, it is thermalised in this process, leaving (without a loss mechanism) a continuously increasing thermalised helium content in the plasma as the fusion reactions continue to take place. This increasing helium population causes dilution of the fusion fuel and stifles the fusion reactions. This so-called helium "ash" has to be removed

from the plasma core. It is, therefore, of great importance to understand and control the helium in a fusion plasma.

The helium in the plasma can be studied with charge exchange recombination spectroscopy, a diagnostic method which is based on the exchange of an electron between a neutral particle and a plasma impurity ion (e.g. helium). The impurity ion, after obtaining the electron, emits characteristic line radiation that contains key information on the impurity species. Charge exchange recombination spectroscopy provides spatially and temporally resolved measurements of impurity temperature, rotation and density in the plasma. This thesis attempts to shed light on the transport properties of helium in fusion plasmas, using charge exchange spectroscopy. A high étendue charge exchange spectrometer was installed and utilised for the helium measurements at the ASDEX Upgrade tokamak.

Helium charge exchange measurements are, however, hindered by the so-called "plume" effect, an additional emission which is comparable to the charge exchange signal. Accurate helium density profiles can be derived from the measurements only if the plume emission is modelled and subtracted from the measured spectra. For this reason, a model that takes into account the diagnostic observation geometry, the reconstructed magnetic equilibrium, appropriate atomic data, and involves a Monte Carlo approach to describe the velocity distribution of the plume ions was implemented at ASDEX Upgrade and benchmarked against experimental measurements. The model is shown to describe the underlying physics mechanisms accurately, as it can reproduce the experimental helium spectra, enabling accurate ion temperatures and rotations to be extracted from the data. Not only the plume to prompt emission intensity ratio is provided, but also the plume spectral emission line and its non-Maxwellian features are reconstructed.

With the confidence that accurate helium density profiles can now be derived from charge exchange measurements, investigations of helium transport have been undertaken at ASDEX Upgrade. To this end, a database of experimental measurements of helium and boron density profiles was assembled via specially designed experiments. The helium density profiles were found to follow closely the electron density profiles, while clear differences are observed between the helium and boron density profiles. To try and understand the experimental observations, these measurements were compared to the available theoretical predictions of both neoclassical and turbulent transport.

The neoclassical contributions were found to be small or negligible in the investigated region of the plasma. Rather, turbulent transport, as calculated via linear gyrokinetic modelling, was found to be the dominant mechanism. Qualitative agreement between the experiment and the turbulent transport predictions was found under certain conditions. However, cases were also found in which strong disagreements are observed. Further work on the theoretical side is motivated by these results, as knowing how the helium density profile will behave in future fusion reactors will be critical for their successful operation. Understanding of the helium transport in fusion plasmas and experimental validation of the theoretical understanding are required.

Charge exchange recombination spectroscopy is expected to provide ion temperature, rotation and helium "ash" measurements on ITER and can also provide some information on the fusion-produced, slowing-down helium. A study on the feasibility of such measurements using the reference design of ITER CXRS diagnostic shows that the signal-to-noise ratio of the slowing-down helium measurements will be very low. Nevertheless, by combining measurements on both the diagnostic and heating neutral beams on ITER, α particles with energies of up to 1MeV can be diagnosed, though with limited time and energy resolution. Higher optical throughput instrumentation will help in this regard, but the optics on the torus side pose a limit on the signal-to-noise ratio that can be achieved.

In conclusion, at ASDEX Upgrade a helium plume model has been implemented that for the first time is shown to be able to accurately reproduce the experimental spectra and enables helium transport studies to be performed via CXRS measurements. Experimental investigations have been undertaken at ASDEX Upgrade, which present the first steps towards a better understanding of helium transport in fusion plasmas.

Samenvatting

Onderzoek naar heliumtransport op ASDEX Upgrade met CXRS

Kernfusie is het samenvoegen van twee lichte atoomkernen tot een zwaardere; een proces dat een significante hoeveelheid energie vrijzet. Het is niet moeilijk in de natuur fusiereacties te vinden. Zo wordt bijvoorbeeld de energie van de zon opgewekt in fusieprocessen. Het onder controle krijgen van fusiereacties op aarde voor commerciële energieopwekking is het onderwerp van fusieonderzoek. Om twee atoomkernen te laten fuseren moeten ze echter eerst voldoende dicht bij elkaar gebracht worden, zodat de sterke kernkracht de afstotende Coulombkracht overwint. Hiervoor zijn zeer hoge temperaturen nodig (honderden miljoenen graden Celsius), waardoor de "fusiebrandstof" geïoniseerd raakt en een plasma vormt. Een van de meest onderzochte manieren om een dergelijk plasma op aarde op te sluiten is de tokamak; een torusvormige machine met een helisch magnetisch veld dat de plasmadeeltjes opsluit en voorkomt dat deze de wand raken. ITER, de internationale experimentele fusiereactor, zal een tokamak zijn.

De meest veelbelovende fusiereactie voor energieproductie op aarde, de deuterium-tritium reactie, resulteert in de productie van helium met 3.5MeV kinetische energie (een vijfde van de totale geproduceerde energie). Het begrijpen van het gedrag van dit helium in toekomstige fusiereactoren is cruciaal. Het door fusie geproduceerde helium is nodig om het plasma te verhitten, door botsingen met de plasma-elektrons en plasma-ionen. Het helium koelt af in dit proces, waardoor de hoeveelheid afgekoeld helium continu toeneemt naarmate er meer fusiereacties plaatsvinden, als de verliesmechanismes buiten beschouwing worden gelaten. Deze zogenaamde "helium-as" moet uit het plasmacentrum verwijderd worden. Het is daarom zeer belangrijk helium transport in een fusiereactor te begrijpen en te controleren.

Het helium in het plasma kan onderzocht worden met CXRS ('Charge eXchange Recombination Spectroscopy'), een diagnostische methode die gebaseerd is op de uitwisseling van een elektron tussen een neutraal deeltje en een verontreinigings-ion (bijv. helium). De lijnstraling die het verontreinigings-ion uitzendt na het ontvangen van het elektron bevat belangrijke informatie over de eigenschappen van de verontreinigingen. CXRS geeft in ruimte en tijd opgeloste metingen van de temperatuur, rotatie en dichtheid van de verontreinigingen. Dit proefschrift probeert licht te werpen op de transporteigenschappen van helium in fusieplasmas. Hiervoor is een CXRS spectrometer voor helium metingen en met een hoge "étendue" geinstalleerd op de ASDEX Upgrade tokamak.

Helium CXRS-metingen worden echter bemoeilijkt door het zogenaamde plume-effect, een additionele stralingsproces die vergelijkbaar in amplitude is met het CXRS-signaal. Nauwkeurige profielen van de heliumdichtheid kunnen enkel uit de metingen worden afgeleid als het plume-effect wordt gemodelleerd en van de metingen wordt afgetrokken. Om deze reden is op ASDEX Upgrade een model ontwikkeld dat rekening houdt met de observatiegeometrie, het gereconstrueerde magnetische evenwicht, de benodigde atomaire data en een Monte-Carlo simulatie om de snelheidsverdeling van de plume-ionen te beschrijven. Dit model is vergeleken met experimentele metingen. Het is aangetoond dat dit model de onderliggende fysische mechanismen nauwkeurig beschrijft, aangezien het de experimentele heliumspectra reproduceert. Dit maakt het mogelijk de ionentemperatuur en rotatie nauwkeurig uit de data af te leiden. Naast de verhouding tussen het plume-effect en de directe stralingsintensiteit wordt ook de spectrale emissielijn van het plume-effect met zijn niet-Maxwellse eigenschappen gereconstrueerd.

Met het vertrouwen dat de helium-dichtheidsprofielen nauwkeurig uit de CXRS-data kunnen worden afgeleid is onderzoek naar het heliumtransport op ASDEX Upgrade uitgevoerd. Hiervoor is aan de hand van speciaal ontworpen experimenten een database van experimenteel gemeten helium- een boor-dichtheidsprofielen aangelegd. Het is gebleken dat de helium-dichtheidsprofielen de elektronen-dichtheidsprofielen nauwkeurig volgen, terwijl er grote verschillen met de boor-dichtheidsprofielen waargenomen worden. Om deze experimentele observaties te verklaren zijn de metingen vergeleken met de beschikbare theoretische voorspellingen van zowel het neoklassieke en turbulente

transport. De neoklassieke bijdrages bleken klein of verwaarloosbaar te zijn in het onderzochte plasmagebied. Turbulent transport daarentegen, zoals berekend met lineaire gyrokinetische modellen, bleek het dominante transportmechanisme. Onder bepaalde voorwaarden werd een kwalitatieve overeenstemming tussen het experiment en de modelvoorspellingen voor turbulent transport gevonden. In andere gevallen werden echter ook grote afwijkingen waargenomen. Deze resultaten moedigen aan meer theoretisch werk te verrichten, aangezien het kennen van het gedrag van helium-dichtheidsprofielen cruciaal is voor het succesvol bedrijven van toekomstige fusiereactoren. Begrip van het heliumtransport in fusieplasmas en een experimentele bevestiging van de theoretische modellen is noodzakelijk.

CXRS zal op ITER metingen van de ionentemperatuur, rotatie en "helium-as" leveren, en kan ook informatie leveren over het door fusie geproduceerde snelle "slowing-down" helium. Uit onderzoek naar de haalbaarheid van zulke metingen, gebruikmakend van het referentieontwerp van ITER-CXRS, is gebleken dat de signaal-ruisverhouding van metingen van het snelle helium zeer laag zal zijn. Desalniettemin kunnen door het combineren van metingen aan de verschillende neutrale bundels op ITER (voor verhitting en als diagnostiekbundel) α-deeltjes met een energie tot 1MeV gemeten worden, weliswaar met beperkte tijds- en energieresolutie. Instrumentatie met een hogere lichtopbrengst zal in dit opzicht helpen, maar de optica aan de toruszijde begrenst de te bereiken signaal-ruisverhouding.

Conclusie: op ASDEX Upgrade is een plume-model voor helium geïmplementeerd dat voor het eerst in staat is de experimentele spectra nauwkeurig te reproduceren, en zo de studie van heliumtransport met CXRS-metingen mogelijk maakt. Het verrichte experimenteel onderzoek op ASDEX Upgrade is de eerste stap in de richting van een beter begrip van heliumtransport in fusieplasmas.

Zusammenfassung

Untersuchungen des Helium-Transports mit CXRS an ASDEX Upgrade Plasmen

Die Kernfusion ist das Verschmelzen von zwei leichten Atomkernen zu einem schwereren Kern: ein Prozess bei dem erhebliche Energiemengen freigesetzt werden können. Solche Fusionsreaktionen finden auch in der Natur statt. So produziert z.B. die Sonne ihre Energie durch die Fusion von Wasserstoff. Fusionsforschung versucht Fusionreaktionen auf der Erde für kommerzielle Energieproduktion nutzbar zu machen. Um die zwei Kerne zu verschmelzen müssen sie jedoch sehr nahe zusammengebracht werden, damit die starke Wechselwirkung die abstoßende Coulomb-Kraft übersteigt. Dazu sind sehr hohe Temperaturen notwendig (mehrere Millionen Grad Celsius), was bedeutet, dass der Fusionskraftstoff ionisiert ist und ein Plasma bildet. Der besterforschteste Weg ein Fusionsplasma einzuschließen ist der Tokamak, ein torusförmiges Gerät mit einem helikalen Magnetfeld, welches die Plasmateilchen einschließt und verhindert, dass diese an die Wand des Tokamaks stoßen. ITER, der internationale experimentelle Fusionsreaktor, wird ein Tokamak sein.

Die vielversprechendste Fusionsreaktion für die Energieproduktion auf der Erde, die Fusion von Deuterium und Tritium, führt zu der Produktion eines Heliumkerns, der eine kinetische Energie von 3.5MeV trägt (ein Fünftel der gesamten produzierten Energie einer Fusionsreaktion). Das Verständnis des Verhaltens von Helium in einem zukünftigen Fusionsreaktor ist für dessen Erfolg entscheidend. Das Helium, welches durch die Fusionsreaktion produziert wird, soll das Plasma durch Stöße mit den Plasmateilchen heizen. Hierdurch nimmt das Helium die Plasmatemperatur an, was ohne einen Verlustmechanismus zu einem stetig ansteigenden Gehalt von thermalisiertem Helium im Plasma führen würde, während die Fusionsreaktionen stattfinden. Diese

stetig ansteigende Helium-Konzentration würde den Fusionskraftstoff verdünnen und die Fusionsreaktion unterdrücken. Die sogenannte Helium-Asche muss aus dem Plasmakern entfernt werden. Deswegen sind das Verständnis und die Kontrolle von Helium in einem Fusionsplasma von großer Bedeutung.

Das Helium in dem Plasma kann mit Hilfe von Ladungsaustauschrekombinationsspektroskopie (CXRS) untersucht werden, eine diagnostische Methode, die auf der Austauschreaktion von einem Elektron zwischen einem Verunreinigungsion (z.B. Helium) und einem Neutralteilchen basiert. Nach Austausch des Elektrons emittiert das Verunreinigungsion charakteristische Linienstrahlung, die Schlüsselinformationen über die Verunreiningungsspezies enthält. CXRS bietet räumlich und zeitlich aufgelöste Messungen der Ionentemperatur, der Rotation und der Verunreinigungsdichte im Plasma. Die vorliegende Arbeit untersucht anhand der CXRS die Transporteigenschaften des Heliums in Fusionsplasmen. Ein Spektrometer mit hoher Etendue ist an dem ASDEX Upgrade Tokamak installiert und wird für Helium-Messungen benutzt.

Helium-CXRS-Messungen werden allerdings durch den sogenannten Plume-Effekt, der zu einer zusätzlichen Strahlung in der Größenordnung des CXRS-Signals führt, gestört. Genaue Profile der Heliumdichte können aus den Messungen nur errechnet werden, wenn die Plume-Strahlung modelliert und von den gemessenen Spektren abgezogen wird. Dafür wurde bei ASDEX Upgrade ein Modell entwickelt, welches die Diagnostik-Geometrie, das rekonstruierte magnetische Gleichgewicht und die dazugehörigen Atomdaten verwendet und zusätzlich ein Monte-Carlo-Verfahren zur Beschreibung der Geschwindigkeitsverteilung der Plume-Ionen beinhaltet. Dieses Modell wurde mit experimentellen Messungen verglichen. Es wurde gezeigt, dass das Modell die zugrundeliegenden physikalischen Mechanismen genau beschreiben kann, da es die experimentellen Helium-Spektren reproduziert. Dadurch können genaue Ionentemperaturen und Rotationen aus den Messungen bestimmt werden. Nicht nur das Verhältnis der Plume-Intensität zum direkten CXRS-Signal, sondern auch die Plume-Spektrallinie und ihre nicht-Maxwell'sche Eigenschaften werden berechnet.

Nachdem gezeigt wurde, dass genaue Profile der Heliumdichte aus den CXRS-Messungen abgeleitet werden können, wurden bei ASDEX Upgrade Untersuchungen des Helium-Transports durchgeführt. Dafür wurde anhand dedizierter Experimente eine Datenbank von Profilen der Helium- und der Bordichte zusammengestellt. Die Profile der Heliumdichte erwiesen sich denen der Elektronendichte sehr ähnlich, jedoch gibt es

deutliche Unterschiede zwischen den Profilen der Helium- und der Bordichte. Um die experimentellen Beobachtungen zu verstehen, werden diese Messungen mit den existierenden theoretischen Vorhersagen des neoklassischen und des turbulenten Transports verglichen. Es zeigt sich, dass die neoklassischen Beiträge in dem erforschten Plasmabereich gering oder gar vernachlässigbar sind. Der dominierende Mechanismus ist der turbulente Transport, wie er anhand der gyrokinetischen Modellierung berechnet wird. Unter bestimmten Bedingungen gibt es eine gute qualitative Übereinstimmung zwischen dem Experiment und der Vorhersage der turbulenten Transportvorgänge. Es gibt jedoch auch Fälle, bei denen man deutliche Unterschiede erkennen kann. Weiterführende Arbeiten auf der theoretischen Seite wurden durch diese Ergebnisse motiviert, da das Wissen über das Profil der Heliumdichte in zukünftige Fusionsreaktoren kritisch für den erfolgreichen Betrieb ist. Dafür ist das Verständnis des Heliumtransports in Fusionplasmen und die experimentelle Validierung des theoretischen Verständnisses erforderlich.

CXRS soll Messungen der Ionentemperatur, der Rotation und der Helium-"Aschen-Dichte an ITER zur Verfügung stellen und kann auch bestimmte Informationen über das fusionsproduzierte, heruntergebremste Helium geben. Eine Studie über die Machbarkeit solcher Messungen unter Verwendung des Referenzentwurfs der CXRS-Diagnostik von ITER zeigt, dass das Signal-zu-Rausch-Verhältnis der Messungen des heruntergebremsten Heliums sehr niedrig sein wird. Jedoch können durch die Kombination von Messungen an dem Diagnostik- und dem Heiz-Neutralteilchenstrahl Heliumteilchen mit Energien bis zu 1MeV diagnostiziert werden, allerdings nur mit eingeschränkter Zeit- und Energieauflösung. Trotz einer möglichen Verbesserung durch ein Spektrometer mit höherer Lichtstärke ist das erreichbare Signal-zu-Rausch-Verhältnis durch die Optiken am Vakuumgefäß limitiert.

Zusammenfassend gesagt: Ein Helium-Plume-Modell, das erstmalig die experimentellen Spektren reproduzieren kann, wurde bei ASDEX Upgrade implementiert. Erst dadurch sind Helium-Transport-Untersuchungen durch CXRS-Messungen möglich. Bei ASDEX Upgrade wurden experimentelle Untersuchungen durchgeführt, die die ersten Schritte zu einem besseren Verständnis des Helium-Transports in Fusionplasmen darstellen.

1

Introduction

1.1 Nuclear fusion

When two light nuclei fuse, a large amount of energy is released, as the binding energy of the fusing nuclei is larger than the binding energy of the fusion products. The energy source of the stars is based on fusion processes such as proton-proton fusion, the carbon cycle and the triple-α process. Since fusion reactions can yield large amounts of energy, they are considered to be an option to solve the global energy problem, considering the constantly increasing world energy demands combined with a limited supply of fossil fuels, which additionally are the main cause of the climate problem [1]. Moreover, nuclear fusion is proposed as a relatively clean, safe energy production alternative, with abundantly available fusion fuel [2].

Nevertheless, harnessing fusion reactions for controlled and cost effective power production is not very easy to achieve due to the difficulties associated with confining fusion-grade plasmas. While in stars gravity plays the role of keeping the plasma together and supplying the required pressure, fusion on earth has to follow a different approach. The two main methods of plasma confinement on earth can be categorised as follows: magnetic confinement, where a magnetic field configuration is used to contain the plasma, and inertial confinement concepts, where a fuel target is heated and compressed faster than the fuel expansion.

Magnetic confinement schemes with a toroidal configuration include among others stellarators, reversed field pinches, tokamaks and spherical tokamaks. The tokamak is perhaps the most extensively explored magnetic fusion configuration and ITER,

the international project with the goal to demonstrate the feasibility of producing commercial energy, will be a tokamak. The tokamak has a toroidal geometry and offers plasma confinement via the combination of a toroidal and a poloidal magnetic field. The plasma particles gyrate around the helical field lines created by these two magnetic field components and travel many times around the torus before impinging on the wall. Further details on the tokamak configuration are given in the next chapter.

The most promising reaction for fusion energy production on earth is the fusion between tritium and deuterium nuclei:

$$D + T \rightarrow^4 He + n + 17.6MeV \tag{1.1}$$

The cross section for this reaction is maximum at a temperature of approximately 100keV. Such high temperatures are needed to overcome the Coulomb barrier. Nevertheless, due to the quantum tunneling effect, fusion can occur at lower temperatures, approximately 15keV. As already mentioned, at these high temperatures the deuterium-tritium mixture is in a plasma state, in other words, it is a fully ionized gas. In current laboratory experiments, the power produced is less than the input power. For fusion to be a viable energy source, the fusion reactions in the plasma must be self-sustained, without additional input power to heat the plasma. This condition is called ignition and such a plasma is then called a burning plasma. Defining the ratio of fusion power to input heating power, $Q = P_{fusion}/P_{input}$, breakeven is achieved when Q=1 and a self-sustained plasma can be achieved above Q=5, when the alpha particles, carrying one fifth of the energy of the fusion reaction, have enough energy to heat the plasma. The condition for a D-T plasma to become self-sustained is:

$$n\tau_E T > 3 \cdot 10^{21} m^{-3} skeV, \tag{1.2}$$

where n and T are the density and temperature of the plasma and τ_E the energy confinement time. JET in the United Kingdom holds, so far, the record for the largest fusion power produced, with a Q of 0.6 [3]. ITER is expected to produce 500MW of power, or equivalently Q>10. Even so, fusion research, with the goal of producing commercially available fusion power, is still an ongoing struggle both from a physics and an engineering point of view [4].

1.2 The role of helium in a fusion plasma

Alpha particles, helium nuclei consisting of two protons and two neutrons, are a product of the D-T fusion reaction and they carry one fifth of the output fusion power, namely 3.5MeV. Understanding the behavior and processes affecting the helium alpha particles in a future fusion reactor is indispensable for determining the feasibility of sustaining a burning plasma [5].

Most importantly, the fusion produced alpha particles are needed to heat the plasma through collisions with the plasma ions. Considering a simplified power balance, the sum of the fusion heating power density P_{fusion} and externally applied heating power $P_{heating}$ should balance the radiation losses due to bremsstrahlung P_{Brems} and the thermal conduction losses P_{cond}:

$$P_{fusion} + P_{heating} = P_{Brems} + P_{cond}. \tag{1.3}$$

As the produced neutrons are not confined, the fusion heating power is actually the alpha heating ($P_{fusion} = P_{alphas}$) and for an ignited plasma the externally applied heating should ideally be zero, $P_{heating} = 0$ (in reality, external power will always be needed to enable control of the burning plasma, for example for profile tailoring, stabilisation of instabilities etc). The alpha heating power should balance the losses and it is, therefore, desired that the alpha particles transfer as much of their energy as possible to the plasma bulk. In other words, the confinement time of the fast α particles should be on the order of or greater than the collision time.

The fusion produced alphas are thermalised as they heat the core plasma through collisions, leaving a constantly increasing thermalised helium content in the plasma. This causes dilution of the fusion fuel, deuterium and tritium. This so called helium "ash" has to be removed from the core of the plasma to avoid stifling the fusion reactions [6]. The problem, therefore, arises when the confinement time of the thermalised helium is greater than its transport time.

Before being thermalised, however, alpha particles of sufficiently high energy might be expelled from the plasma due to magnetohydrodynamic phenomena such as sawteeth or toroidal Alfvén eigenmodes. The impact of high energy particles on the plasma facing components of the fusion reactor can cause severe damage and should be avoided.

Nevertheless, due to their large energy, energetic alpha particles can help stabilise the sawteeth themselves [7].

For a successful reactor operation, a burning plasma should be controlled. As described above, helium plays a significant role in the fusion process. Controlling the content of the thermalised helium in the plasma as well as the efficiency and exhaust of the alpha heating, is crucial for the fusion reactor performance and steady state operation [8].

It is, therefore, of great importance to understand the behavior of both thermal (helium "ash") and energetic (not yet thermalised) helium in a fusion plasma, both for prediction of plasma behavior and active control. In machines without D-T operation, the behavior of thermal helium in burning plasma conditions can be, to a certain extent, simulated with the injection of helium gas puffs, while that of energetic helium can be studied by helium beams or by accelerating the helium with minority heating schemes. These methods allow the investigation of the transport properties of thermal and slowing down helium under different plasma conditions. The interaction of helium with plasma instabilities, in particular the effect of sawtooth crashes on helium, can be studied and the theory describing these interactions can be benchmarked.

Alpha particles in the plasma can be diagnosed by means of active charge exchange recombination spectroscopy on a neutral beam, a powerful diagnostic technique that provides spatially and temporally resolved measurements of ion temperature, plasma rotation and impurity density in the plasma. This technique is used extensively in this thesis for the study of helium in ASDEX Upgrade tokamak plasmas.

1.3 This thesis

Impurity transport has been a main subject of tokamak research for the past decades, leading to increasingly better understanding of the processes determining the transport of impurities and their profiles. Special interest lies in the investigation of helium, since it is the product of the D-T fusion reaction and a serious concern for the success of a fusion reactor, as discussed in the previous section.

The work described in this thesis was conducted at the tokamak experiment ASDEX Upgrade, using charge exchange spectroscopy to measure the helium density profiles. A high etendue charge exchange spectrometer measuring simultaneously helium, carbon

and deuterium was installed and added to the charge exchange diagnostic suite at ASDEX Upgrade and was used to perform the helium measurements presented in this thesis. This goal of this work is twofold: to confirm our understanding of the helium charge exchange spectrum, and especially the helium plume effect and to shed light on the transport properties of helium in a fusion plasma.

Before embarking on the analysis of these research subjects, the ASDEX Upgrade experiment, where this work was performed, will be presented in Chapter 2, giving an overview of the auxiliary heating methods and diagnostics used in this thesis. In Chapter 3 the charge exchange diagnostic method will be described, with emphasis on helium charge exchange measurements. The theoretical understanding of impurity transport and its comparison to previous experimental studies will be given in Chapter 4.

In Chapter 5, the helium plume effect [9], an additional emission that has a strong impact on the interpretation of the helium charge exchange measurements, will be investigated. A detailed model for the helium plume emission contributing to the helium charge exchange spectra will be presented. Answers to the following questions will be given:

- Is the plume emission a significant contribution to the helium charge exchange spectra at ASDEX Upgrade?
- Can a detailed model for the helium plume emission be implemented that not only provides accurate helium density profiles, but also accurately reconstructs the shape of the helium plume emission line in the charge exchange spectra?
- Can such a model be benchmarked against experimental measurements?
- Employing a correction for the helium plume emission, can accurate ion temperature and rotation profiles be derived from the helium charge exchange spectra?

Subsequently, the transport properties of helium in ASDEX Upgrade plasmas are investigated in Chapter 6. The following questions will be addressed:

- What plasma parameters determine the gradient of the helium density profile?
- Does the helium density profile correlate with that of the electron density?
- How does helium compare with other low-Z impurities in terms of profile shape and transport properties?

- How do the experimental measurements of helium compare with the theoretical predictions? In particular, how do the measured helium density profiles compare with the predictions of gyrokinetic modelling of the electrostatic turbulence induced transport, which is expected to be dominant at the plasma mid-radius?

Charge exchange recombination spectroscopy will be expected to measure the helium "ash" in ITER. It can, however, also provide measurements on fast helium ions. The following questions will be answered in Chapter 7:

- Can charge exchange spectroscopy, with the currently planned requirements on the diagnostic and neutral beam design, provide measurements on the fusion produced α particles on ITER?
- What will limit the performance of these measurements in ITER?

Finally, the answers to all of these questions will be revisited and an outlook will be given in Chapter 8.

2

The ASDEX Upgrade tokamak

The main volume of this work has been carried out at ASDEX Upgrade, which is a medium size divertor tokamak. In this chapter, the tokamak concept for magnetic confinement fusion is introduced, giving basic details on tokamak operation, in Section 2.1. Then, more details on the ASDEX Upgrade experiment are presented. The heating systems available on ASDEX Upgrade are described, giving emphasis to the neutral beam injection system as it is vital for the charge exchange spectroscopy diagnostic. The main plasma diagnostics used in the course of this thesis are introduced. The discussion on charge exchange spectroscopy is deferred to Chapter 3, where the method is described in detail.

2.1 Tokamak operation

A tokamak is a torus shaped device that confines plasma through the application of a helical magnetic field [10]. This field is created by combining a toroidal and a poloidal magnetic field. The toroidal magnetic field is created by external toroidal field coils, while the poloidal magnetic field is created by driving a toroidal current in the plasma itself. This current is induced by a transformer coil, usually with an iron core, as the primary winding, and the plasma itself acting as the secondary winding of the transformer. In addition, a vertical magnetic field is applied to produce an inward $j \times b$ force. This force prevents the plasma from expanding due to the outward hoop force by providing an inward force.

2.1.1 Plasma equilibrium and shape

The plasma is considered to be in "equilibrium" when the plasma pressure and the magnetic forces are balanced. Ideal magnetohydrodynamics (MHD) provides the description for this plasma state, treating the plasma as an ideally conducting fluid subject to Maxwell's equations, without a displacement current in Ampere's law. In the plasma the force balance is satisfied:

$$\nabla p = \overrightarrow{j} \times \overrightarrow{B}. \tag{2.1}$$

Together with $\nabla \cdot \overrightarrow{B} = 0$ and $\nabla \cdot \overrightarrow{j} = 0$, it follows that in a volume where $\nabla p \neq 0$, the surfaces of constant pressure are tori and, according to the above equation, field lines lie in these surfaces. Therefore, closed flux surfaces are required to support a pressure gradient $\nabla p \neq 0$ and to confine a plasma. In the meantime, the constraint $\nabla \cdot \overrightarrow{B} = 0$ implies that on a given magnetic surface field lines cannot cross.

Assuming a circular, large aspect ratio tokamak, the safety factor q can be introduced to characterise the plasma stability:

$$q = \frac{r}{R}\frac{B_\phi}{B_\theta}, \tag{2.2}$$

where r and R are the minor and major radii, and B_ϕ and B_θ are the toroidal and poloidal magnetic fields, respectively.

Knowing the equilibrium configuration of the plasma, in other words knowing the current profile, pressure profile and the positions and shapes of the flux surfaces is required for several reasons. Reconstructing a solution to the ideal MHD plasma equilibrium equation (Grad-Shafranov equation) in a fast way is critical, as knowledge of the plasma position is required for control purposes during a plasma discharge. Moreover, knowledge of the current density and pressure gradients is necessary for stability analysis. Interpretation of measured plasma profiles requires knowledge of the flux surface configuration and diagnostic geometry, as well as knowledge of the relationship between positions in real space and plasma coordinates. Transport studies require equilibrium information in order to evaluate and design heating schemes, but also to bring together experimental measurements performed at different poloidal and toroidal angles, major radii and vertical positions. Furthermore, the modelling of the impurity turbulent transport is sensitive to the q-profile and magnetic shear used as input to the code [11].

The reconstructed 2D magnetic equilibrium entails the definition of the nested flux surfaces in the plasma. The magnetic flux is constant on these surfaces, as are to first order a number of other plasma parameters such as electron and ion temperature and electron density. As such, spatial profiles are conveniently mapped onto ρ_{tor}, a label for the magnetic flux surfaces. It is defined as:

$$\rho_{tor} = \sqrt{\frac{\Psi - \Psi_{axis}}{\Psi_{LCFS} - \Psi_{axis}}}, \tag{2.3}$$

where Ψ is the toroidal flux. Ψ_{axis} and Ψ_{LCFS} denote the toroidal flux at the magnetic axis and at the last closed flux surface (separatrix). The magnetic coordinate ρ_{tor} is 0 in the plasma center (magnetic axis) and 1 at the separatrix. Other coordinates used for the mapping of plasma profiles, depending on the task, include ρ_{pol}, where Ψ in the above equation is defined as the poloidal flux, the major radius R, and the normalised coordinate $\rho = r/a$, where a is the minor radius and r the distance from the magnetic axis.

At ASDEX Upgrade, a function parametrisation algorithm is used for real-time control of the plasma parameters and position, with a time resolution down to 100μs. After the discharge, CLISTE is used for the magnetic equilibrium reconstruction, with a time resolution of 1ms (possible down to 100μs) [12]. CLISTE is an interpretative code that solves the Grad-Shafranov equation assuming no knowledge of the magnetic axis location or the shape of the source profiles (pressure and poloidal current), but using diagnostics such as current measurements from magnetic probes, flux loops and edge current measurements to constrain the equilibrium reconstruction. Additionally, pressure constrained equilibria are available upon request, which use the sawteeth inversion radius as a constrain for the $q = 1$ surface [13, 14].

2.1.2 Magnetohydrodynamic (in)stability

Magnetohydrodynamics is the description of the plasma as a single magnetised fluid. The stability of the plasma is defined by its response to perturbations, or by the possibility to find a time independent solution to the MHD equations. The plasma can be destabilised by current gradients and pressure gradients, which, combined with the magnetic field curvature, lead to instabilities. The instabilities are characterised by the mode numbers n and m, where n is the toroidal and m the poloidal mode number. The

instabilities can be ideal or resistive, depending on whether they depend on the finite plasma resistivity.

The sawtooth instability is but one example encountered in tokamak plasmas [15]. It occurs when q in the plasma center drops below 1, creating a surface with $q = m/n = 1$ in the plasma. The exact nature of the sawtooth crash is not completely understood, but it is associated with a 1/1 precursor mode followed by a sharp crash of the core profiles, which is well modelled as a magnetic reconnection event [16]. As a result of the sawtooth crashes, a periodic increase and sudden decrease of the temperature is observed. As such, the sawtooth instability limits the peaking of electron temperature and density. Most importantly, sawteeth redistribute particles, which is an important issue for the confinement of fast particles and the expulsion of the helium "ash" from the plasma.

2.1.3 Tokamak wall

The interface between the plasma and the tokamak wall is of critical importance and may play a decisive role in the realisation of future fusion power plants. The harsh high temperature, high particle flux plasma environment poses challenges to the wall materials, such as material erosion and migration (redeposition), sputtering and melting.

Plasma facing components have to withstand the high heat and particle loads with a long lifetime, as well as transient loads such as plasma disruptions and Edge Localised Modes (ELMs). Moreover, they are part of the overall heat and particle exhaust system of the tokamak.

Graphite (carbon) is a favored choice for plasma facing component at many tokamak devices. However, carbon is problematic due to high yields for physical sputtering, chemical erosion and redeposition, but most importantly high tritium retention. Tungsten also has a high melting point (as does carbon), but additionally has low sputtering yield and features low tritium retention. Beryllium is the lightest metal with which wall components can be manufactured and does not have the disadvantage that heavier elements have, namely the increased radiation due to trace amounts in the main chamber plasma.

JET has recently switched from a full carbon wall to a beryllium-coated tungsten wall (ITER-like wall), similar to the one that is now envisioned for ITER. ASDEX Upgrade, on the contrary, is a full tungsten machine [17].

2.1.4 The ASDEX Upgrade tokamak

ASDEX Upgrade is a medium size tokamak, situated in Garching bei München in Germany. It has a major radius of 1.65m and a minor radius of 0.5m. It can be operated with a toroidal magnetic field on axis as high as 3T, created by sixteen toroidal field coils, while a plasma current of 0.4-1.4MA, driven by the transformer, creates the poloidal magnetic field. Other field coils allow for vertical and horizontal positioning of the plasma and an array of coils can be utilised to define the plasma shape. ASDEX Upgrade is a divertor tokamak with plasma facing components of tungsten coated graphite tiles, with a solid tungsten divertor since 2014.

Typical plasmas in ASDEX Upgrade utilise deuterium as the main ion and operate with densities up to $10^{20}m^{-3}$ and temperatures of a few keV. The additional heating systems available, described later on, allow for operation in the high-confinement mode (H-mode [18]). Plasma discharges last for up to 10 seconds, with a current flat-top of up to 8 seconds.

For reference, an overview of the most recent ASDEX Upgrade results can be found in [19].

2.2 Plasma heating systems on ASDEX Upgrade

The toroidal current heats the plasma through ohmic heating, however, the plasma resistivity decreases with increasing plasma temperature, making the ohmic heating less effective. For breakeven to be achieved, the plasma has to be heated to sufficiently high temperatures. This is typically done purely via ohmic heating. Heating of the plasma can be achieved either by coupling electromagnetic waves to the plasma or by injecting energetic particles. Waves launched into the plasma can heat primarily the plasma electrons (ECRH) or minority ions (ICRH), depending on the wave frequency. High energy injected neutral beams (NBI) also transfer energy to the plasma.

The additional heating systems of ASDEX Upgrade are described in this section. The locations of the available systems can be seen in Fig. 2.1.

2.2.1 Neutral beam injection (NBI)

One method of heating tokamak plasmas is the injection of neutral atoms into the plasma. These neutral atoms are not affected by the magnetic field and thus maintain

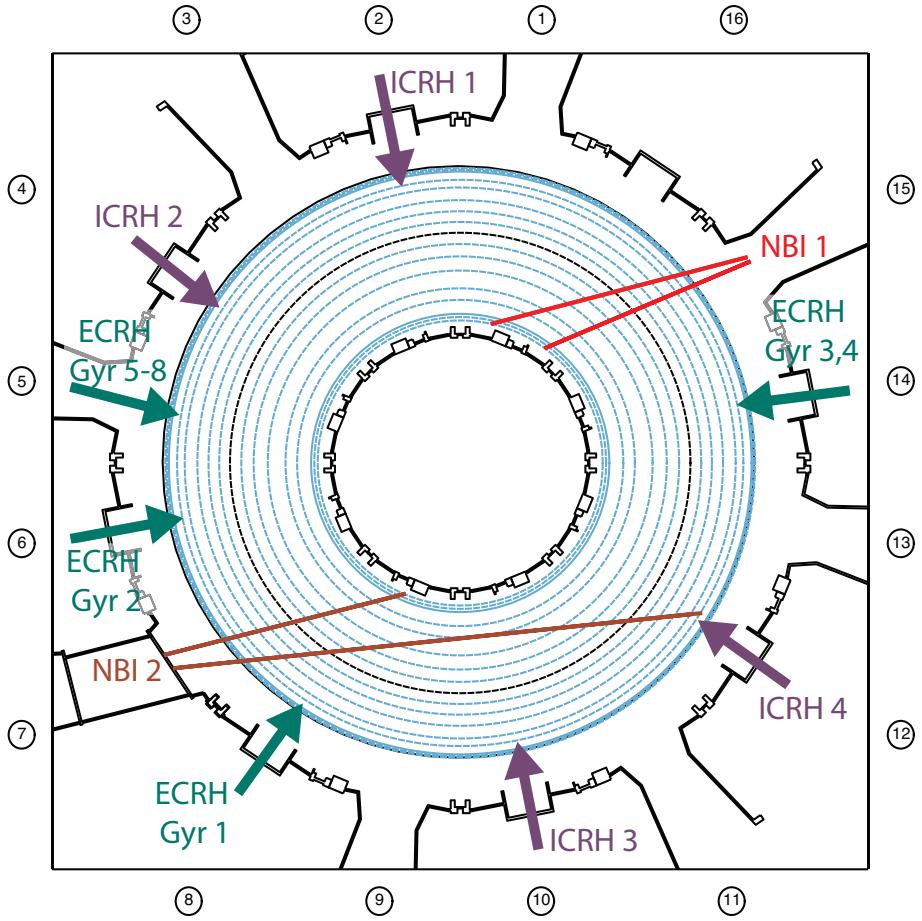

Figure 2.1: Schematic of the heating systems on ASDEX Upgrade (top-down view).

their injection trajectories. The neutral beam is attenuated mainly through charge exchange and ionisation with plasma ions and electrons. Both energy and toroidal angular momentum is transferred to the plasma [20].

To produce a neutral beam, a source of ions is produced and accelerated. Then, it is neutralised through charge exchange processes by passing through a neutraliser gas cell. The ions that are not successfully neutralised or those produced by reionisation in the neutraliser gas are deflected by a magnet to a dump.

Assuming a deuterium beam, the ion source produces D^+ ions but also molecular ions D_2^+ and D_3^+. These ions still acquire the same energy as they pass through the same accelerator voltage, but due to their higher mass, their velocities are lower. The molecules are dissociated in the neutraliser gas. Therefore, the D atoms produced

from the molecular ions have energies equal to one half (E/2) and one third (E/3) of the acceleration voltage (E). The fraction of atoms with E/2 and E/3 depends on the initial fraction of molecular D produced in the source system. The E/2 and E/3 energy components of the beam are more strongly attenuated than the first component and do not penetrate the plasma as well.

The ratio of neutral atoms produced due to charge exchange at the neutraliser gas to the ions produced due to reionisation depends on the beam energy, with higher beam energies leading to lower ratios. As a result, higher beam energies, such as those required for ITER, are difficult to achieve. This can be avoided by using negative ion sources for beam production, which have a much higher ratio of produced neutral atoms to ions. The neutral beams on ITER, which are planned to be operated at voltages of 100keV (for the diagnostic beam) and 1MeV (for the heating beam) will be created with negative ion sources.

The beam injected neutrals undergo charge exchange with thermal plasma deuterium ions. The produced neutrals spread through the beam volume and beyond before being reionised, forming a cloud of thermal deuterium neutrals around the neutral beam. This cloud is called the beam "halo" and plays an important role in the interpretation of charge exchange diagnostic measurements, as will be discussed in Section 3.2.

On ASDEX Upgrade, the NBI system consists of two injectors, each consisting of four ion sources, shown in Fig. 2.1 [21]. The first injector (quoted here as NBI 1), is located in sector 15 of ASDEX Upgrade (south-east injector) and is routinely operated at a voltage of 60keV for deuterium. Two of the sources (Q1 and Q4) are radial, while the other two (Q2 and Q3) are tangential. The second injector (NBI 2), consisting of sources Q5-Q8, is located in sector 7 (north-west injector) and is routinely operated at 93keV for deuterium. Sources Q5 and Q8 of this injector are tangential, while sources Q6 and Q7 are off-axis beams, utilized for current drive. All eight sources, when operated with deuterium and at maximum extraction voltage, can deliver 2.5MW of power, leading to a maximum injected power of 20MW by NBI. The energy fractions for the full, half and third energy components are approximately $0.47 : 0.36 : 0.17$ for NBI 1 and $0.43 : 0.39 : 0.18$ for NBI 2, calculated on a shot-to-shot basis, based on measured I-V curves [22]. Sources Q3 and Q8 are used for charge

exchange spectroscopy measurements. The diameter of the neutral beams (FWHM) in the plasma core are on the order of $\approx 20 - 25$cm.

2.2.2 Electron Cyclotron Resonance Heating (ECRH)

The electric field of electromagnetic waves propagating through the plasma can accelerate the electrons and ions therein. The plasma is heated as the accelerated particles collide with the rest of the particles. However, this collisional absorption is inefficient as it is proportional to $T_e^{1.5}$. More effective heating, on the other hand, is obtained with resonant absorption. The cold plasma dispersion relation can be used to identify the resonances. A wave propagates in the plasma only when $n_\perp^2 > 0$, where $n_\perp$ is the refractive index perpendicular to the magnetic field, while a resonance occurs when $n_\perp^2 \to \infty$. The electrons can be heated with waves at the electron cyclotron resonance frequency, propagating in the plasma in ordinary (O-mode) or extraordinary mode (X-mode). The accessibility of plasma regions with the injected waves depends on the density of the plasma and the magnetic field. Gyrotrons are used to provide the required millimeter waves (on the order of 100 of GHz). In [23] and references therein, a review of the application of ECRH for heating (and current drive) is given.

On ASDEX Upgrade, there are two ECRH systems injecting up to 4 MW of power into the plasma [24]. The first system, ECRH I, consists of 4 gyrotrons that can apply up to 400kW each for a maximum of 2 seconds. The second system, ECRH II, consists of another 4 gyrotrons that can each deliver up to 800kW for 10 seconds. Two frequency options exist, namely 105 GHz and 140 GHz, corresponding to the second harmonic of the electron cyclotron frequency at -2.0T and -2.5T, respectively. Typically the X2 mode is used. The radial deposition location depends on the value of the magnetic field (which is proportional to 1/R), and on the ECRH resonance frequency. The absorption location can be shifted vertically and toroidally with the use of movable mirrors.

Central ECRH is routinely applied in ASDEX Upgrade discharges to suppress the accumulation of impurities (tungsten) in the plasma core [25]. Moreover, a clear effect of the application of central ECRH on the electron density profile has been observed, leading to the flattening or peaking of the electron density profile depending on the plasma conditions [26, 27] (see also Section 4.3.3).

2.2.3 Ion Cyclotron Resonance Heating (ICRH)

The ion cyclotron resonance heating functions under the same physics principles as ECRH, only this time waves at the ion cyclotron frequency (tens of MHz) are coupled to the plasma. As ion cyclotron waves, also called shear Alfvèn waves, can propagate in the plasma only if injected from the high field side, the compressional Alfvèn wave is used for ion cyclotron heating [28].

On ASDEX Upgrade, there are four ICRH systems, each with its own antenna, delivering up to 2MW each, with a total achievable power of up to 7.2MW [29]. The minority heating scheme is typically used, taking advantage of the hydrogen minority present in the deuterium plasmas.

2.3 Plasma diagnostics on ASDEX Upgrade

Knowledge of the parameters of a tokamak plasma is of utmost importance: firstly, to facilitate understanding of the physical processes and secondly, to enable control of the plasma discharges in present day experiments and future devices. Unfortunately, direct access to the plasma is ruled out, apart from the extreme outer plasma regions. Consequently, a variety of methods have been developed over the years in order to diagnose the plasma, in the most efficient and least obtrusive ways possible.

Parameters on which diagnostic measurements are required include the electron temperature and density, ion temperature and plasma rotation, fast particles, radial electric field, impurity content, particle and energy fluxes, radiation and many more. Passive diagnostics rely on measuring naturally occurring emissions (e.g. passive spectroscopic methods, bolometry etc.) or particles coming from the plasma (e.g. fast ion loss detectors, neutral particle analysers), while active diagnostics require an actuator such as a neutral beam (active charge exchange spectroscopy, beam emission spectroscopy), electromagnetic waves (electron cyclotron emission), or lasers (Thomson scattering, interferometry).

Here, some of the main diagnostics used in tokamak plasma research are briefly described. The discussion is focused on the diagnostic suite of the ASDEX Upgrade tokamak (Fig. 2.3) and specifically the diagnostics used in this work, while a comprehensive overview of plasma diagnostic methods is given in [30].

2.3.1 Electron cyclotron emission

The electrons in the plasma gyrate around the magnetic field lines, emitting electromagnetic radiation at harmonics of the electron cyclotron frequency $\omega = n\omega_{ce} = \frac{eB}{m_e}$. The intensity of the emission for a specific harmonic is given by

$$I(\omega) = \frac{\omega^2 T_e(R)}{8\pi^3 c^2} \left[1 - \exp^{-\tau}\right], \tag{2.4}$$

where τ is the optical depth, which depends on the electron temperature T_e and density n_e. For optically thick plasmas ($\tau \gg 1$), the Rayleigh-Jeans law for blackbody emission applies at the electron cyclotron emission wavelengths, and the electron temperature can be directly extracted from the intensity of the emission [23].

The electron cyclotron emission diagnostic in tokamaks is benefited by the radial variation of the magnetic field (B(R) $\propto$ 1/R). Assuming a perpendicular view to the magnetic field lines and neglecting relativistic effects, the measurement of the emission at a certain frequency gives straightforwardly the temperature of the resonant region, in the low temperature regime (less than 10keV). As such, a spatial profile of the electron temperature can be obtained.

On ASDEX Upgrade, a multichannel heterodyne radiometer is used for Electron Cyclotron Emission (ECE) measurements at frequencies between 89 GHz and 187 GHz (magnetic field of 1.6-3.4 T), with a radial resolution down to 1 cm and a repetition rate of 32kHz. A 2D imaging system (ECE-I) is also in operation [31], providing 2D measurements of the electron temperature with high spatial and temporal resolution, at the plasma center (for toroidal magnetic field of 1.8-2.25T) or the low field side edge (for toroidal magnetic field of 2.35-2.9T), with a measurement area of $12 \times 40 cm^2$.

2.3.2 Thomson scattering

The Thomson scattering technique relies on the scattering of a laser beam and can provide information on the electron temperature and density. In the dipole approximation, the scattered spectrum is directly proportional to the velocity distribution [30]. Nevertheless, in practice, the spectral noise does not allow for direct reconstruction of the velocity distribution. Instead, a Maxwellian velocity distribution is fitted to the Thomson scattering spectra.

High energy and high power pulsed lasers have to be used for Thomson scattering measurements. The energy of the incident laser pulse defines the amount of scattered radiation and, as such, higher energy lasers provide better signal. Short pulsed powerful lasers are required as the collected plasma background light increases with the pulse length.

On ASDEX Upgrade, two Thomson scattering systems based on Nd-YAG lasers are used for electron temperature and density measurements, one in the core and one at the plasma edge, with 16 and 10 spatial channels, respectively, each with 4 spectral channels [32]. The Nd-YAG lasers are fired at regular intervals providing a measurement every 8.3ms for the edge system and 12.5ms for the core.

2.3.3 Lithium beam impact excitation spectroscopy

Information on the plasma edge density can be obtained by injecting a lithium beam into the plasma and observing the LiI(2s-2p) emission at 670.8 nm, induced by the collisions of the lithium atoms and the plasma particles. This emission depends strongly on the plasma electron density. A recursive algorithm based on a collisional radiative model is used to reconstruct the plasma electron density [33]. Improvements on the analysis of lithium beam data using probabilistic methods are presented in [34]. Lithium beams are very strongly attenuated and for this reason can provide information on the plasma density only in the outermost regions of the plasma.

On ASDEX Upgrade, a lithium beam of 30 to 60keV is injected radially almost at the midplane. One optical head is installed to measure the LiI(2s-2p) emission line with a time resolution of 50μs, using photomultiplier tubes and interference filters, providing measurements of the electron density at the plasma edge. A second optical head is used for lithium induced charge exchange spectroscopy measurements of C^{+} and He^{2+} at the edge [35]. The lithium beam is chopped to allow for background subtraction [36], with the beam on for 60ms followed by 20ms beam off.

2.3.4 Interferometry

Interferometry can be used to provide information on the plasma electron density. A laser beam that traverses a plasma experiences a phase shift that depends only on the electron density. Choosing the ordinary direction of polarisation, this holds also for magnetized plasma. The line-integrated electron density is calculated by comparing the

phase of the detector for a certain line-of-sight to that of the reference detector of the interferometer. The line-integrated signals are deconvoluted using an Abel inversion in order to provide radial density profiles.

On ASDEX Upgrade, two interferometers are installed. An interferometer using a deuterium cyanide laser (DCN, $\lambda = 195\mu$m) views the plasma horizontaly with 5 lines-of-sight at a sampling frequency of 10kHz [37]. Additionally, a two-color interferometer using a CO_2 and a HeNe laser (10.6μm and 633nm, respectively) views the plasma vertically with 2 lines-of-sight and at a sampling frequency of up to 500kHz.

2.3.5 Integrated data analysis

At ASDEX Upgrade, the profiles obtained from DCN interferometry, electron cyclotron emission and lithium beam impact excitation spectroscopy are combined in an Integrated Data Analysis (IDA) scheme, which utilises Bayesian probability theory [38]. Thomson scattering spectroscopy and reflectometry measurements can also be included, but this is done less routinely. With this method, electron temperature and density profiles are obtained with high temporal and spatial resolution. An example of the profiles measured via each diagnostic method and the profile obtained with IDA are shown in Fig. 2.2. All profiles are mapped on the same magnetic coordinates.

2.3.6 Fast ion loss detectors

Fast ion loss detectors provide time-resolved energy and pitch-angle measurements of escaping ions. On ASDEX Upgrade, three scintillator based fast ion loss detectors are installed, one of them as a head on the midplane manipulator probe, measuring escaping ions of energies up to 1.5MeV, to enable the investigation of the 3D spatial distribution of fast ion losses due to magnetohydrodynamics fluctuations [39]. The strike points of the fast ions on the detectors depend on their gyroradius, energy and pitch angle.

2.3.7 Neutral particle analysers

The fast ion velocity space can be probed with neutral particle analysers (NPAs) at defined pitch angles. Neutral particle analysers measure the energy and flux of charge

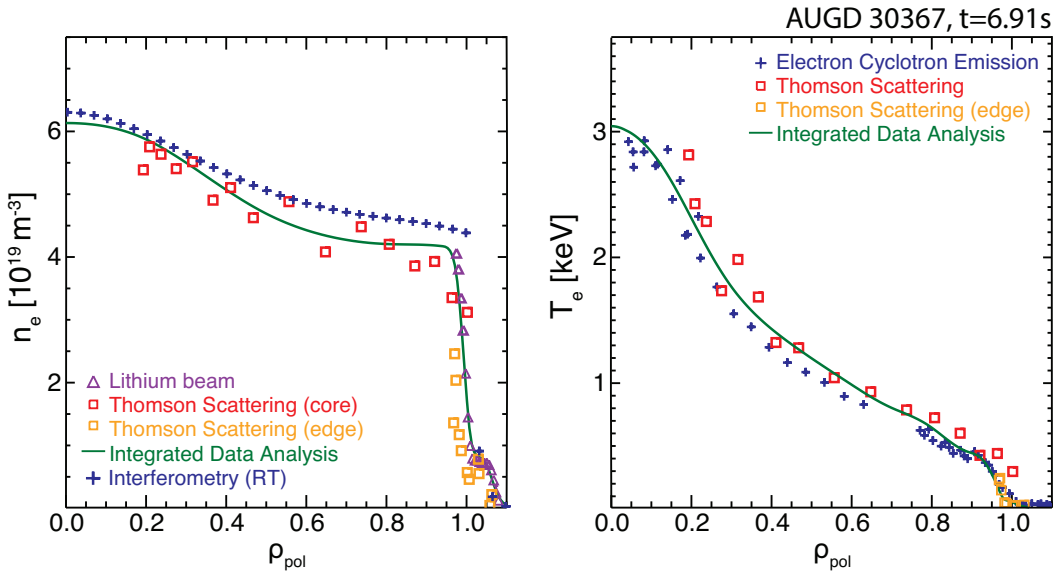

Figure 2.2: Electron temperature and density profiles measured with the Li-beam, Thomson Scattering, ECE and interferometry (here shown is the real time reconstructed profile) together with the integrated data analysis profiles.

exchange neutrals. Furthermore, they can provide information on the isotope ratio in the plasma, as well as an estimate of the ion temperature [40, 41].

On ASDEX Upgrade, the installed NPAs can measure D^+ and H^+ fast ions with energy ranges of 10-100keV and 20-200keV, respectively. Bulk ions of 0.5-7.5keV can also be measured.

2.3.8 Collective Thomson scattering

In the diagnosis of the confined fast ions in the plasma, the collective Thomson scattering diagnostic (CTS) can offer valuable information. The motion of ions in the plasma generate fluctuations in the electron velocity distribution which scatter high power probe radiation from gyrotrons. CTS detects this scattered radiation and provides spatially and temporally resolved measurements of the distribution function of the fast ions in one-dimensional velocity space [42]. On ASDEX Upgrade, the collective Thomson scattering system uses one of the transmission lines of the electron cyclotron resonance heating system, employing as a probing beam the gyrotron at a frequency of 105GHz [43, 44]. Unfortunately, as CTS employs two ECRH waveguides when it is in operation, the available ECRH power and flexibility is limited.

2.3.9 Effective charge

From the bremsstrahlung radiation level, the effective charge (Z_{eff}) profiles can be inferred. The bremsstrahlung background in charge exchange spectra can be used for this purpose, assuming knowledge of the electron temperature and density profiles. Effective charge calculations are unfortunately not accurate enough, since the uncertainties in the electron temperature, density and charge exchange measurements are propagated into the analysis, but also as the bremsstrahlung radiation measured by charge exchange spectroscopy is a line integrated measurement that requires deconvolution.

At ASDEX Upgrade, the evaluation of effective charge profiles is performed in the integrated data analysis framework described above, based on data from the ASDEX Upgrade charge exchange diagnostic suite [45].

2.3.10 Soft X-ray detectors

Soft X-ray radiation from a fusion plasma consists of the free-free bremsstrahlung continuum, free-bound recombination radiation and bound-bound line radiation. The intensity of the soft X-ray radiation depends on the electron density and temperature, as well as the impurity content in the plasma. It consists of a bremsstrahlung continuum, free-bound recombination radiation and bound-bound line radiation. The detection of soft X-ray radiation provides information on magnetohydrodynamic instabilities, medium to high Z impurity transport and magnetic equilibrium data such as the magnetic axis location.

A large number of soft X-ray pinhole cameras with many viewing lines are placed at different poloidal positions around the plasma, allowing for tomographic reconstruction of the signal in the plasma cross section. By looking at the signals of individual detectors, MHD phenomena such as the sawtooth instability can be identified and localised.

At ASDEX Upgrade, the soft X-ray diagnostic consists of 8 cameras, with one to three heads each [46]. Each head has one diode array and its own pinhole and beryllium filter foil, to block photons of energies up to 1keV. As such, the detected line radiation from light impurities is negligible. However, light impurities still contribute to the soft X-ray radiation in terms of Z_{eff}. The time resolution of the diagnostic is 2MHz, with a spatial resolution of 1cm.

2.3.11 Beam emission spectroscopy

The injection of fast neutral atoms into the plasma leads to intense Balmer-α emission due to interactions with the main plasma ions (charge exchange and excitation), the plasma impurities (excitation) and plasma electrons (electron impact excitation). For deuterium beams injected into deuterium plasma, important are:

$$D_b^0 + D_p^+ \rightarrow D_b^+ + D^{0*} \tag{2.5}$$

$$D_b^0 + D_p^+ \rightarrow D_b^{0*} + D_p^+ \tag{2.6}$$

$$D_b^0 + X_p^{+z} \rightarrow D_b^{0*} + X_p^{+z} \tag{2.7}$$

$$D_b^0 + e \rightarrow D_b^{0*} + e \tag{2.8}$$

where the subscript b denotes beam atoms, p denotes plasma ions, $*$ the excited state and X^{+z} represents the plasma impurity ions.

The last three processes contribute to the beam emission spectrum. For positive ion source neutral beam injectors, the beam consists of three energy fractions (see section 2.2.1), leading to three separate components in the beam emission spectrum, shifted by three different Doppler shifts, corresponding to the velocity of each energy fraction component. Due to the Lorentz electric field each of these lines is split into 15 Stark components.

Simplified, the beam emission intensity can be written as:

$$I_{BES} = \frac{1}{4\pi} \sum_{i=1}^{4} n_e Q_{BES}^i \int_{los} n_b^i dl, \tag{2.9}$$

where n_e is the electron density, i corresponds to the three energy fractions in the beam plus the beam halo, n_b the local beam density, while the integration is along the line-of-sight. Q_{BES}^i is the effective photon emission coefficient for the beam energy fraction i, which depends on the beam energy, the local Z_{eff}, the ion temperature and the electron density and temperature.

Beam emission spectroscopy (BES) can be used to diagnose the neutral beam attenuation in the plasma. The beam attenuation can be calculated using the appropriate effective beam stopping cross sections $\sigma^{\text{eff}}_{stopping}$, which include electron and ion impact ionisation and charge exchange processes. Then the beam density at a location x in the plasma relative to the density at the origin of the beam path, $n_b(0)$, is:

$$n_b(x) = n_b(0) \exp\left(- \int_0^x n_e \sigma^{\text{eff}}_{stopping} \right) \tag{2.10}$$

Calculation of the beam attenuation leads, however, to increasing errors along the beam path [47], which can be avoided by inferring the local beam density from the measured beam emission intensity. In the latter case, the error corresponds to the uncertainties in the measurements and the beam emission rates, but the error is then local and does not accumulate as in the previous case.

Further applications of beam emission spectroscopy include the derivation of absolute impurity density profiles by combining beam emission and charge exchange data [48, 49], as will be described in Sections 3.2.2 and Appendix A. Furthermore, as the Stark multiplet shape and intensity depends on the electric and magnetic field present, beam emission can be used for magnetic field measurements, as the Stark splitting is proportional to the Lorentz electric field [47]. Finally, beam emission spectroscopy can contribute to the integrated data analysis described in 2.3.5, for the determination of the electron density profile [50].

As a final note, negative ion source neutral deuterium beam injectors have only one energy fraction and, therefore, only one beam emission component instead of three. The same holds in the case of helium neutral beams.

On ASDEX Upgrade, beam emission spectroscopy shares the lines-of-sights of the CER optical head (see 3.1.5) and has a time resolution of 11ms. A new system has been installed during the 2014 experimental campaign, looking at beam source Q8, which has a time resolution of 2ms for 15 lines-of-sight.

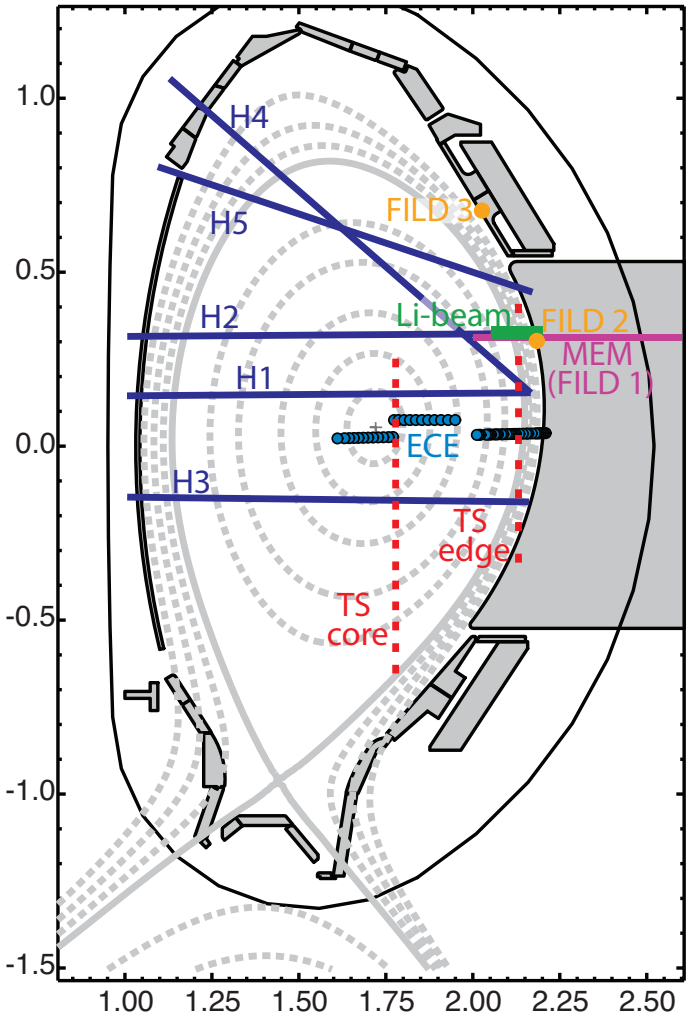

Figure 2.3: Poloidal cross-sections of ASDEX Upgrade showing the measurement locations of some of the main ASDEX Upgrade diagnostics used in the course of this work: Electron cyclotron emission (ECE) in cyan, DCN interferometer in blue, Thomson scattering (TS) in red, lithium beam in green, midplane manipulator (MEM) in magenta and fast ion loss detectors in orange and magenta.

3

Charge exchange recombination spectroscopy

Diagnosing low-Z impurity ions with spectroscopic methods encounters the difficulty that impurities in the core of the fusion plasma are fully stripped and do not emit any light. The injection of a neutral beam, typically hydrogen or deuterium, provides a solution to this issue, as the ionised impurities X^{Z+} gain an electron via charge exchange. The hydrogen-like ion produced is in an excited state (n_2) and prompt light emission follows as the ion decays to state n_1:

$$X^{Z+} + H^0 \rightarrow X^{(Z-1)+}(n_2) + H^+ \tag{3.1}$$

$$X^{(Z-1)+}(n_2) \rightarrow X^{(Z-1)+}(n_1) + hv. \tag{3.2}$$

This diagnostic method that utilises this emission is called active Charge Exchange Recombination Spectroscopy (CXRS) and is routinely used for the measurement of ion temperature, plasma rotation and impurity densities in tokamak plasmas. The emitted line radiation is broadened due to the temperature of the impurity ions (Doppler broadening), while the line is shifted due to the bulk rotation of the plasma (Doppler shift). The integrated intensity of the measured line is proportional to the impurity density. The charge exchange diagnostic method and its applications have been the subject of many publications in the last decades, among others [9, 51–54]. In this chapter, the charge exchange spectrum and how it can be used to acquire information on the plasma

are explained.

The description concentrates on the peculiarities of the helium charge exchange spectrum. Charge exchange measurements of helium impurity ions with a deuterium neutral beam based on the HeII line at 468.6nm can be performed with standard optical instruments that operate in the visible:

$$He^{2+} + D^0 \rightarrow He^+(n = 4) + D^+ \tag{3.3}$$

$$He^+(n = 4) \rightarrow He^+(n = 3) + hv(\lambda = 468.6nm). \tag{3.4}$$

Other helium lines that have been used for charge exchange diagnostics in the past include the n=3-2 and n=2-1 transitions in the UV (wavelengths 164nm and 30.4nm, respectively) [9] and double charge exchange emission lines [55], but these either demand special instrumentation as in the first case, or have much lower intensity, as in the second case. At ASDEX Upgrade the HeII line at 468.6nm is used for helium charge exchange measurements. Helium charge exchange measurements can provide spatially and temporally resolved density profiles of the He^{2+} ions in the plasma, as well as T_i and v_ϕ profiles, assuming that the helium plume emission, described separately in Chapter 5, is properly taken into account. As such, charge exchange spectroscopy is a crucial diagnostic in the investigation of transport properties of the He^{2+} in the plasma. Both thermal and energetic helium can be studied. Furthermore, the interaction of helium impurity ions with magnetohydrodynamic instabilities can be analysed, for example the effect of sawteeth crashes on thermal and fast helium.

Consequently, the fully ionized helium in the plasma has been the subject of many past studies. Both thermal and energetic helium, either injected with neutral beams (^{3}He or ^{4}He) or produced by fusion reactions in machines that had D-T operation, have been studied with charge exchange spectroscopy, under a multitude of diagnostic names such as CER, CXRS, CXS, CHERS and α-CHERS.

3.1 Components of a charge exchange spectrum

Several processes and emissions contribute to a typical charge exchange spectrum, making the interpretation of the measurements a complicated task [56]. In this section, the

components that are present in a charge exchange spectrum are described.

3.1.1 Active charge exchange emission

The photon flux Φ_{CX} due to the charge exchange reactions can be written as:

$$\Phi_{CX} = \frac{1}{4\pi} \int_{los} Q_{CX}^{\text{eff}} n_b(l) n_X(l) dl, \tag{3.5}$$

where l is the coordinate along the line-of-sight, $n_b(l)$ is the local neutral beam density, $n_X(l)$ the local impurity density, and the integration is over the intersection of the line-of-sight through the neutral beam. The effective rate coefficient Q_{CX}^{eff} for emission due to charge exchange is defined as:

$$Q_{CX}^{\text{eff}} = \langle \sigma_{CX}(\upsilon_{col}) \cdot \upsilon_{col} \rangle, \tag{3.6}$$

where υ_{col} is the collision velocity between the impurity ions and the beam neutrals. In reality, injected hydrogen or deuterium neutral beams produced with positive ion sources have three fractions with different velocities $\upsilon_b^i = \upsilon_b/\sqrt{i}$, for the i-th beam component (see Section 2.2.1). Consequently, Eq. (3.5) should properly be written as:

$$\Phi_{CX} = \frac{1}{4\pi} \sum_{i=1}^{4} \sum_{n=1}^{2} \int_{los} \langle \sigma_{CX}(\upsilon_{col}) \cdot \upsilon_{col} \rangle^{i,n} n_b^{i,n}(l) n_X(l) dl, \tag{3.7}$$

where $i = 4$ corresponds to the charge exchange with the thermal neutrals of the beam halo that should also be considered. Charge exchange with neutrals both in the ground (n=1) and in excited states (n=2 and higher) take place [57, 58], hence the summation on n.

Assuming that the impurity ions have a Maxwellian velocity distribution and that the ion temperature at a certain location in the plasma is T_i, the impurity ion velocity is $\overrightarrow{\upsilon} = \overrightarrow{\upsilon_m} + \overrightarrow{\upsilon_\phi}$, where $\overrightarrow{\upsilon_m}$ is the Maxwellian velocity and $\overrightarrow{\upsilon_\phi}$ the solid body rotation, and the local impurity density is n_{imp}, then the velocity distribution of the impurity ions is:

$$f(\overrightarrow{\upsilon}) = n_{imp} \left(\frac{m_{imp}}{2\pi k T_i} \right)^{\frac{3}{2}} \exp\left(- \frac{m_{imp} |\overrightarrow{\upsilon} - \overrightarrow{\upsilon_\phi}|^2}{2 k T_i} \right). \tag{3.8}$$

Therefore, the local impurity density in an infinitesimally small part of the velocity

space can be expressed as:

$$d^3 n_{imp} = f(\overrightarrow{v}) d\upsilon_x d\upsilon_y d\upsilon_z. \tag{3.9}$$

The impurities undergo charge exchange with the beam neutrals, which have a density of n_b at this location, leading to a photon flux which can be written as:

$$d^3 \Phi_{CX} = \frac{1}{4\pi} Q_{CX}^{\text{eff}} n_b d^3 n_{imp} dl \tag{3.10}$$

Defining a Cartesian coordinate system x,y,z with the z-axis along the line-of-sight of the diagnostic, the velocity along the z-axis corresponds to the velocity component of the ion along the line-of-sight, υ_λ. This causes a shift in wavelength in the observed spectrum equal to $\lambda - \lambda_0$, where λ_0 is the nominal wavelength of the line. The observed spectrum, expressed in terms of velocities along the line-of-sight is then obtained by integrating Eq. (3.10):

$$I(\upsilon_\lambda) = \frac{1}{4\pi} dl \int_{\upsilon_x} \int_{\upsilon_y} \int_{\upsilon_z} Q_{CX}^{\text{eff}}(\upsilon_{col}) n_b f(\upsilon_x, \upsilon_y, \upsilon_z) \delta(\upsilon_\lambda - \overrightarrow{v} \cdot \cos\theta) d\upsilon_x d\upsilon_y d\upsilon_z, \tag{3.11}$$

where $\overrightarrow{v}$ is the ion velocity and θ the angle between the ion velocity and the line-of-sight (z-axis). The effective emission coefficient stays within the triple integral as it depends on the velocity, while the line-of-sight segment dl has been moved out of the integral to denote that the integration is in the velocity space and not in real space. As such, $I(\upsilon_\lambda)$ is the intensity from the line-of-sight segment dl. The above expression can be rewritten in a more familiar way to give the observed intensity in wavelength [photons/$(m^2 \cdot sr \cdot s \cdot nm)$]:

$$I(\lambda) = \frac{1}{4\pi} \frac{c}{\lambda_0} dl \int_{\upsilon_x} \int_{\upsilon_y} \int_{\upsilon_z} Q_{CX}^{\text{eff}}(\upsilon_{col}) n_b f(\upsilon_x, \upsilon_y, \upsilon_z) \delta(\upsilon_\lambda - \overrightarrow{v} \cdot \cos\theta) d\upsilon_x d\upsilon_y d\upsilon_z. \tag{3.12}$$

Finally, assuming that $\upsilon_{th} \ll \upsilon_b$, it is safe to say that $Q_{CX}^{\text{eff}}(\upsilon_{col}) \approx Q_{CX}^{\text{eff}}(\upsilon_b)$. Also, for small enough dl, the neutral density and impurity density are constant. Inserting now the Maxwellian velocity distribution function, displaced by the plasma rotation velocity, the observed spectral intensity is:

$$I(\lambda) = \frac{1}{4\pi} n_{imp} n_b Q_{CX}^{\text{eff}}(\upsilon_b) dl \frac{c}{\lambda_0} \sqrt{\frac{m_{imp}}{2kT_i}} \exp\left(- \frac{c(\lambda - \lambda_0 - \Delta\lambda_{rot})^2 m_{imp}}{2kT_i \lambda_0^2} \right), \tag{3.13}$$

where $\Delta\lambda_{rot}$ corresponds to the wavelength shift due to the plasma rotation. If the impurity measured is He^{2+}, then an analytical form for the observed helium spectra is given by the equation above.

3.1.2 Passive charge exchange and edge emissions

Passive charge exchange (PCX) emission is the prompt emission following charge exchange reactions between neutralized ions in the plasma originating from the walls or recombined neutrals and ionized impurities. The passive emission gives a background to the active signal that needs to be corrected for, so that one may extract physical information from the active emission. The passive emission layer for low-Z impurities is in the outer plasma region and the passive charge exchange emission at a certain location in the plasma depends on the local impurity and neutral densities, as well as on the effective emission rates for the charge exchange reaction:

$$\Phi_{pcx}(r) = \frac{1}{4\pi} n_0(r) n_{imp}(r) Q^{\text{eff}}_{PCX} \tag{3.14}$$

It should be noted that the passive charge exchange with neutrals at the $n = 2$ excited state is the dominant contribution [57, 58].

Even further outside at the edge of the plasma, impurities are excited by electron impact, which is followed by additional emission:

$$X^{Z+} + e \rightarrow X^{Z+,*} + e \tag{3.15}$$

$$X^{Z+,*} \rightarrow X^{Z+} + hv \tag{3.16}$$

In plasmas of temperature less than a few keV, electron radiative recombination can also contribute to the emission [59]. This emission depends on the local impurity and electron density and the relevant effective emission rates for electron recombination:

$$\Phi_{rec}(r) = \frac{1}{4\pi} n_e(r) n_{imp}(r) Q^{\text{eff}}_{rec} \tag{3.17}$$

It has been observed at JET that two Gaussian components were required to fit the passive charge exchange spectra, one cold for the edge and one "luke-warm" originating from further inside the plasma [60]. This "luke-warm" feature is stated to exist for the

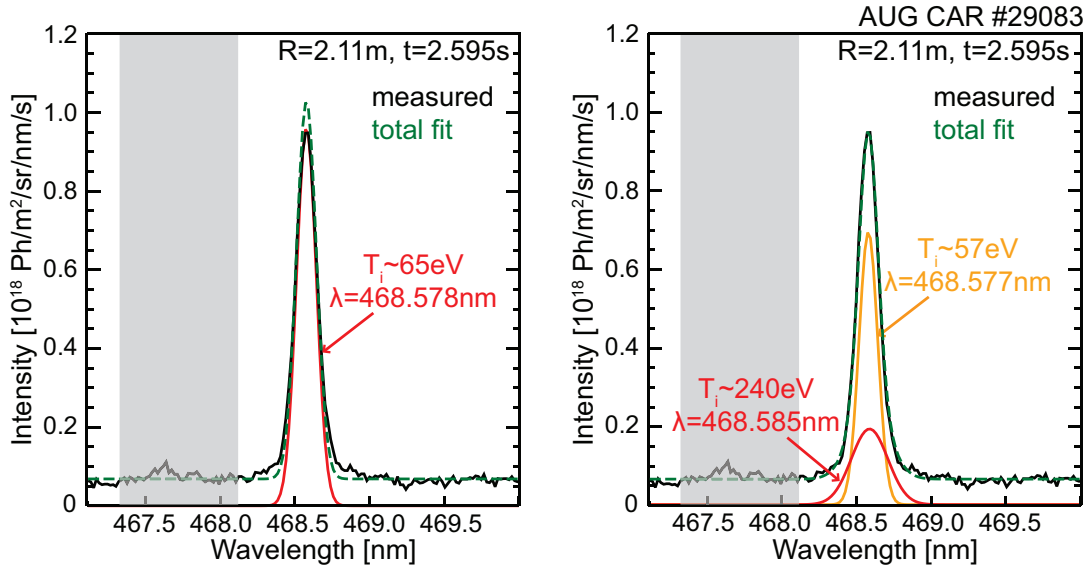

Figure 3.1: A helium spectrum measured when the neutral beam is switched off (passive spectrum), fitted with one (left) and two (right) Gaussians. One Gaussian shape does not fit the line satisfactorily, while a much better fit is obtained with the use of two Gaussians. The part of the spectrum highlighted in grey has not been included in the fitting process.

HeII, CVI and HI lines. However, it is stated that this phenomenon can be neglected for ion temperatures below 5keV. Neverthless, steep gradients in the temperature and rotation velocity at the edge, make the approximation of the passive emission with one single Gaussian inaccurate.

For helium, the emission that is present when the neutral beam is switched off arises from two processes: the electron impact excitation of He^+ at the edge and the thermal charge exchange, again at the edge but further inside the plasma. As can be seen from Fig. 3.1, the passive emission line at ASDEX Upgrade cannot be fitted well with a single Gaussian. As mentioned above, in literature, it has been suggested that the helium passive charge exchange line should be fitted with two Gaussians [61]: a narrow line representing the edge emission, and a broader, so-called "luke-warm" emission, due to charge exchange between the neutral hydrogen layer and the fully stripped helium near the plasma boundary [60]. In other references, only one Gaussian is used to fit the passive emisison line, for example in [62].

To isolate the active emission, the passive emission in these cases can be modelled [59, 63]. Alternatively, beam modulation schemes can be used in order to subtract all passive emission lines from the charge exchange spectra. The neutral beam injec-

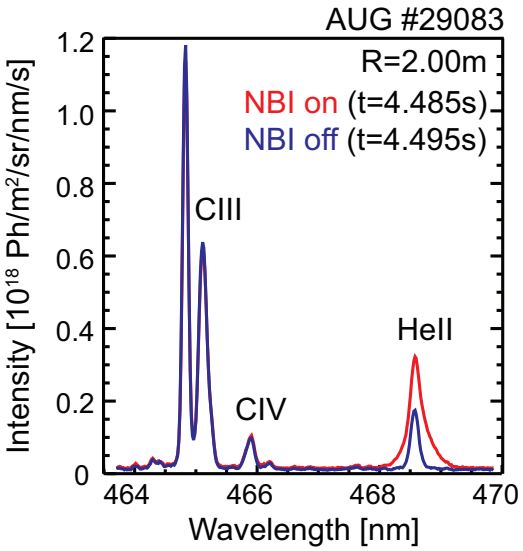

Figure 3.2: Example of a helium spectrum when the neutral beam is on (red), compared to the spectrum measured directly after the neutral beam is switched off (blue).

tion is modulated and a passive spectrum (neutral beam off) is subtracted from the time-adjacent active spectrum (neutral beam on). Although this method increases the error bars in the spectrum, the uncertainties associated with the passive emission and with the fact that it may or may not be approximated with a single Gaussian line are eliminated. An example of a passive and an active helium charge exchange spectrum measured at ASDEX Upgrade just before and just after the switching off of the neutral beam injection is shown in Fig. 3.2.

On ASDEX Upgrade, a forward model was developed to describe the edge emission and to deconvolute the line-integrated measurements [64]. The local emissions obtained by the deconvolution of the line-integrated measurements were compared with the radiation simulated by the 1D impurity transport code STRAHL. It was found that both thermal charge exchange and electron impact excitation contribute to the passive C^{5+} edge emission, with thermal charge exchange being the dominant effect [63]. Nevertheless, the measured passive spectra of C^{5+} can be fitted well with one single Gaussian, making it difficult to separate the two contributions. It should be noted that the measured passive line is a superposition of several Gaussians, corresponding to different rotation velocities and ion temperatures. Regarding the passive line component of He^{+}, on the other hand, it was shown that thermal CX is not the dominant process

and that electron impact excitation should be sufficient to describe the observed line shape. However, a quantitative evaluation was not possible, as the measured passive intensity is much smaller than the predicted one, because of the helium recycling in the scrape-off layer and the diagnostic location in-between two limiters [64].

For the core CXRS diagnostic used in this work the passive helium charge exchange spectra cannot be fitted satisfactorily with a single Gaussian. Nevertheless, it is not yet clear whether this is due to the line shape consisting of many Gaussians with different rotation velocities and ion temperatures, or two distinct emission components from two different plasma layers, as implied in the fit shown on the right hand side of Fig. 3.1. For this reason, the beam modulation technique has been used for the majority of the results presented in this work.

3.1.3 Bremsstrahlung background

Measured charge exchange spectra are superimposed on an emission background due to bremsstrahlung radiation $P_{bremsstrahlung}$:

$$\frac{dP_{\text{bremsstrahlung}}}{d\lambda} = \frac{32\pi}{3}\left(\frac{e^2}{4\pi\epsilon_0}\right)\sqrt{\frac{2\pi}{3m_eT_e}}\frac{1}{mc^2}g_{ff}n_e^2Z_{\text{eff}}\frac{1}{\lambda^2}\exp\left(-\frac{hc}{\lambda T_e}\right), \qquad (3.18)$$

where g_{ff} is the free-free Gaunt factor, which is a weak function of the electron temperature T_e and effective charge Z_{eff}. As such, the bremsstrahlung level in the charge exchange spectrum depends on the plasma electron temperature T_e and density n_e as well as on the effective charge (impurity content) of the plasma. The bremsstrahlung contribution to the spectrum is a line-integrated value. The bremsstrahlung level measured in charge exchange spectra can be used to evaluate Z_{eff}, using spectral regions without line emissions, if the electron temperature and density are known (measured with diagnostics other than charge exchange spectroscopy) [45].

3.1.4 Contribution from the beam halo

Neutral beam halo is a cloud of deuterium neutrals around the injected neutral beam, which are produced from charge exchange between the injected beam neutrals and the thermal plasma deuterium ions. As neutrals, they can spread out of the beam volume before being reionised. An additional emission from charge exchange between the impurity ion and the neutral beam halo is present in the spectra. The consequence of not including the halo in the extraction of He^{2+} densities from the charge exchange measurements can be significant. In Fig. 3.3, the predicted charge exchange emission with beam halo neutrals, contributing to the helium charge exchange measurements, is illustrated. Assuming a flat He^{2+} concentration profile of 0.2%, the corresponding charge exchange intensity with and without the contribution from halo neutrals is shown. The Monte Carlo based code FIDASIM [65] was been used for the calculation of beam injected neutrals and halo neutrals.

3.1.5 Plume emission

There are additional complications in the interpretation of the charge exchange data. In particular, helium charge exchange spectroscopy is hampered by the so-called “helium

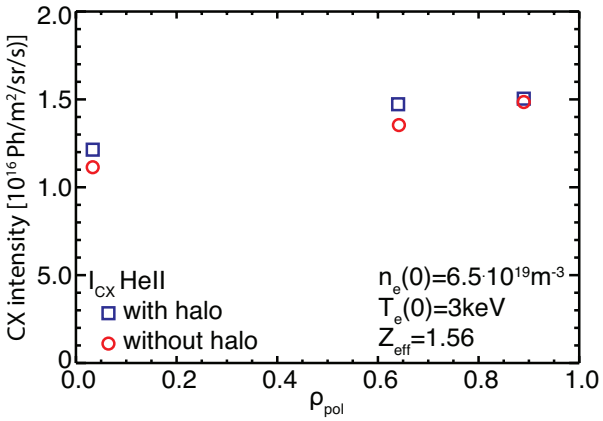

Figure 3.3: The charge exchange intensity that would be observed for three lines-of-sight of the high etendue spectrometer, assuming a 0.2% flat concentration of He^{2+} in the plasma, for discharge 29083 at t=2.555s. The beam injected and halo neutrals are calculated with FIDASIM.

plume effect". The plume emission component, described in detail in Chapter 5, is a non Gaussian spectral contribution whose intensity is the same order of magnitude as the active charge exchange emission. The He^+ ions produced after the charge exchange reactions in the neutral beam volume can travel a significant distance along the field lines, where they can be excited by electron impact excitation before being reionised. The light emitted as they are de-excited, the helium plume emission, exists in the same wavelength region and is of comparable magnitude to the active charge exchange signal in the case of helium, while it is negligible for elements such as carbon and boron. Not taking the helium plume emission into account leads to inaccurate ion temperature and rotation profiles and overestimated (by up to a factor of 2) helium density profiles. The helium plume effect has been studied and a model for its interpretation has been implemented at ASDEX Upgrade in the course of this thesis. The model is presented in Chapter 5 and the comparison of the model results with the experimental measurements is discussed.

3.1.6 Contributions from other impurities

A number of lines originating from charge exchange reactions involving impurities other than the ones intended to be measured may be present in the spectrum. In the case of HeII spectra, the carbon (CIII) impurity line triplet passive emission is also measured

at wavelengths of 464.742nm, 465.025nm and 465.147nm, with a relative intensity of 5:3:1 and the same ion temperature for all CIII lines [60]. An illustration of an ASDEX Upgrade measured spectrum can be seen in Fig. 3.2. Other carbon lines in this wavelength range include CII at 466.586nm, CIV at 465.830nm.

At ASDEX Upgrade, other impurity lines such as nitrogen and tungsten can appear in the helium spectra. In machines like JET, which operate with beryllium in the plasma facing components, beryllium lines are expected in the wavelength range of interest, namely BeIV n=6-5 at 465.85nm, BeIV n=8-6 at 468.525nm and BeII at 467.34nm, complicating further the fit of the helium charge exchange spectra [60]. No beryllium sources, however, exist at ASDEX Upgrade.

3.1.7 Fast ion tail

Not only thermal impurity ions can be diagnosed with charge exchange spectroscopy, but also impurities of higher energies. If, in addition to the thermal impurity population, there is also a population of fast impurity ions, then they will have a much more broadened emission line, due to their higher temperature. This will then appear as wings in the charge exchange spectra.

In this way, the fast ions from a neutral beam injected in the plasma can be diagnosed. Assuming a deuterium beam injected in a deuterium plasma, fast deuterium ions capture an electron from the neutral deuterium atoms from the beam and end up in an excited state. The Balmer-α light emitted from the deexcitation of these atoms can be observed:

$$D + D^+ \rightarrow D^+ + D^*. \tag{3.19}$$

The spectral shift due to the higher velocity of the ions allows for the separation of this component from the other D_α emissions.

Fast helium ions can also be measured with charge exchange spectroscopy, for example when helium neutral beams are injected in the plasma [60], or the helium ions are accelerated by ICRH (^{3}He ions). The fast helium ion wing in the charge exchange spectra is also present due to fusion produced α-particles. This has been seen in machines that had D-T operation [66].

3.2 Charge exchange recombination spectroscopy as a plasma diagnostic

3.2.1 Physical quantities from CX spectra

Active charge exchange recombination spectroscopy is a standard diagnostic in many fusion experiments, as it provides vital information on plasma parameters such as the ion temperature, plasma rotation and impurity content in the plasma core.

Assuming that the impurity has a Maxwellian velocity distribution, it has been shown that the observed charge exchange emission line has a Gaussian shape. The diagnostic capabilities of charge exchange spectroscopy are based on the interpretation of this line shape in order to provide information on the impurity ion temperature T_i, the plasma rotation v_ϕ and the impurity content n_i. These values are extracted from the measured spectrum as follows (see also Fig. 3.4):

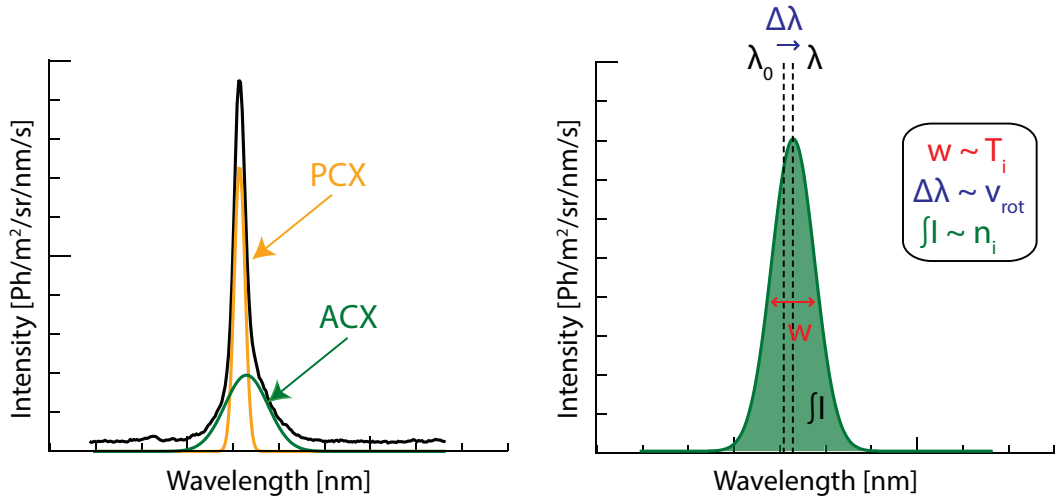

Figure 3.4: An illustration of the active (ACX) and passive (PCX) emissions contributing to a typical charge exchange spectrum (left). The information that can be extracted from the active charge exchange emission line is illustrated on the right.

a) The ion temperature T_i causes the Doppler broadening of the line and is as such related to the width of the measured Gaussian line:

$$kT_i = \frac{mc^2 \mathrm{FWHM}^2}{8 \ln 2 \lambda_0^2}, \tag{3.20}$$

where k is the Boltzmann constant and FWHM the full-width-half-maximum of the

line.

b) The component of the rotation velocity along the line-of-sight causes the wavelength shift of the Gaussian line. The rotation velocity v_{rot} can therefore be calculated as:

$$v_{rot} = \frac{\Delta\lambda_{rot} c}{\lambda_0 \cos\alpha}, \tag{3.21}$$

where α is the angle between the line-of-sight and the toroidal direction.

c) The integral over wavelength of the intensity of the emission line is related to the local impurity density n_{imp}:

$$n_{imp} = \frac{4\pi \int I(\lambda) d\lambda}{n_b Q_{CX}^{\text{eff}}(v_b) dl}. \tag{3.22}$$

In practice, charge exchange measurements are made using injected neutral beams or gas puffs. This work has utilised solely charge exchange spectroscopy on a neutral beam. Using a neutral beam for the neutral source, active charge exchange provides localised measurements (in contrast to line integrated measurements), as the light emitted after the charge transfer reaction between the neutral beam atoms and the impurity ion is coming from the intersection of the observation line-of-sight and the neutral beam. In Fig. 3.5, the areas from which the active and passive emissions originate are drawn for one line-of-sight, in a top-down view of ASDEX Upgrade. How accurately localised the measurement is depends on this path through the beam volume and defines the radial resolution of the measurement.

In general, charge exchange emission lines with wavelengths in the visible are preferred for diagnostic purposes, as this simplifies significantly the required optical equipment and instrumentation. Impurities that are routinely observed with charge exchange spectroscopy include helium, boron, carbon, nitrogen, oxygen and argon.

As already described, the charge exchange spectra are superpositions of active and passive emission lines on a bremsstrahlung background. Interpreting the spectra means fitting all the separate contributions in order to extract values with a physical meaning. Fitting the charge exchange spectra on ASDEX Upgrade is performed using a least square fitting code, called CXSfit [67], which can deal with the full complexity of the spectra. The active and passive components of the helium emission as well as the background level (considered flat within a narrow wavelength range) have to be identified in the fitting process.

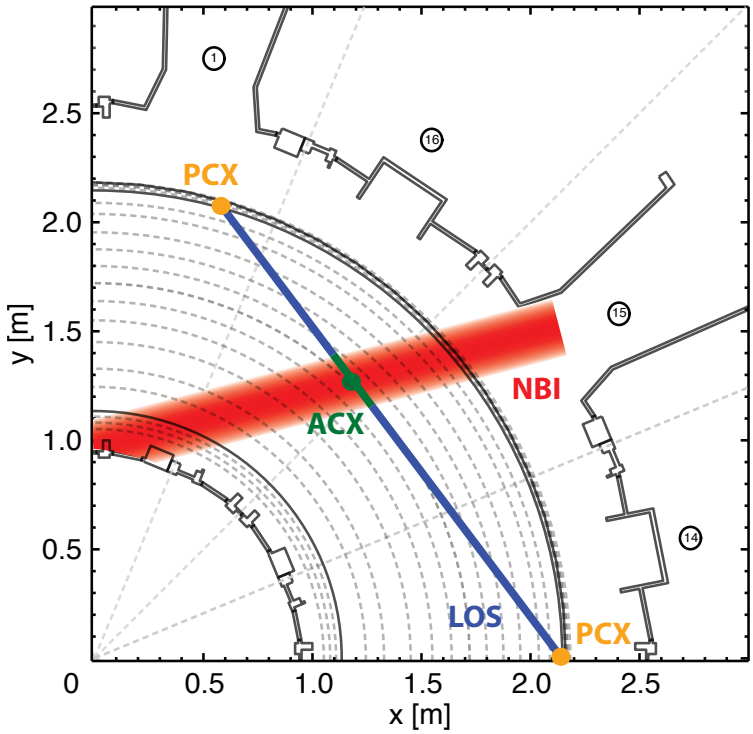

Figure 3.5: Top-down view of ASDEX Upgrade, where the locations of active and passive charge exchange emission are highlighted, for one line-of-sight. The red line represents the path of Q3, the main ASDEX Upgrade heating beam used for charge exchange measurements. The active charge exchange measurement is localised, as the emission comes only from the intersection of the line-of-sight with the neutral beam. The passive charge exchange emission originates from the two intersections of the line-of-sight through the cold plasma edge.

3.2.2 Derivation of impurity density profiles

The ability of charge exchange to provide absolute impurity density profiles relies on information on the neutral beam density in the plasma, see Eq. (3.22). This information can be obtained either from neutral beam attenuation codes, or from beam emission spectroscopy (BES), described in detail in section 2.3. Both options are associated with uncertainties. The errors in the determination of the neutral beam density in the plasma using BES involves the errors in the measurement and calibration of the instrument, as well as the atomic rates which determine the emission, while neutral beam attenuation codes also depend on the quality of the beam stopping rates used and the uncertainties in the density measurements. The importance of the atomic data in the interpretation of beam emission spectra is clearly described in [68]. The measurement uncertainties

in the electron density and temperature increase the uncertainties. Furthermore, the beam halo provides an additional complication.

At ASDEX Upgrade, the Monte Carlo forward modelling code FIDASIM [65, 69] provides the density of neutrals in the beam volume, as well as the beam halo. Also, beam emission spectroscopic measurements are available that can provide the neutral beam density.

Combining charge exchange and beam emission spectroscopy data provides a very useful method to obtain absolute impurity density profiles without the need for an absolute intensity calibration of the diagnostic. The measured charge exchange and beam emission intensities are:

$$I_{CX} \propto \int_{los} n_{imp} \sum_{i=E,E/2,E/3} Q_{CX}^{\mathrm{eff},i} n_b^i dl \tag{3.23}$$

$$I_{BES} \propto n_e Q_{BES} \int_{los} n_b^i dl, \tag{3.24}$$

where i represents the different energy components in the beam. If the same lines-of-sight are used for the two measurements, then determination of the intersection integral between the neutral beam and the line-of-sight is not needed. For neutral beam density equal to $n_b^i = f^i \frac{I_{BES}}{Q_{BES} n_e}$, where f^i are the beam energy fractions, then the impurity concentration is given by [47]:

$$c_{imp} = \frac{n_{imp}}{n_e} = I_{CX} \sum_{i=E,E/2,E/3} \frac{Q_{BES}}{Q_{CX} I_{BES}}. \tag{3.25}$$

Taking into account that the sensitivities of the detectors measuring the charge exchange and beam emission spectra are not equal, calibration factors should be included in Eq. (3.23) and Eq. (3.24), namely A_{CX} and A_{BES}. The ratio of these calibration factors can be derived by comparing the background bremsstrahlung levels in the two spectra at the corresponding wavelength, performing a cross-calibration of the two detectors [70]:

$$\frac{A_{CX}}{A_{BES}} = \frac{C_{CX}}{C_{BES}} \frac{\lambda_{CX}}{\lambda_{BES}}, \tag{3.26}$$

where C_{CX} and C_{BES} are the continuum levels of each of the spectra at wavelengths λ_{CX} and λ_{BES}, respectively. Using this method, no absolute calibration of the detectors is required; all the required information to obtain absolute impurity density profiles

can be found in the spectra themselves in order to relatively calibrate the spectra. An illustration of this technique for the calculation of absolute carbon density profiles in TEXTOR can be found in the Appendix A.

3.2.3 Charge exchange cross sections and cross section effects

The charge exchange cross-sections, required for the calculation of impurity densities from the observed charge exchange emissions, depend on the collision energy of the neutral and the ion. The total cross-sections for charge exchange between fully stripped helium impurities and hydrogen neutral beams as a function of collision energy are shown on the left of Fig. 3.6, while the effective charge exchange emission coefficients for the HeII n=4-3 transition are shown on the right, for the n=1 and n=2 excited state of deuterium. The effective cross-sections showcase a maximum at a specific collision energy ($\sim 30 keV/amu$ in the case of He (n=4-3)), dropping strongly at lower or higher energies.

The deuterium population in an excited state is much less than the deuterium in the ground state ($\sim 1\%$). Nevertheless, as can be seen from Fig. 3.6, the cross-sections between He^{2+} and D(n=2) are about two orders of magnitude larger than those for D(n=1), making their contribution to the charge exchange spectra significant. The deuterium population in the n=3 excited state is even less than that in the n=2. The effective emission rates between B^5+ and H(n=3) are shown to be of the same order of magnitude as those between B^5+ and H(n=2) and it can be important in high density conditions [57]. In ASDEX Upgrade plasmas, the contribution from the n=3 excited state of deuterium is negligible.

For the derivation of Eq. (3.11), it was assumed that $Q_{CX}^{\text{eff}}(\upsilon_{col}) \approx Q_{CX}^{\text{eff}}(\upsilon_b)$, which is valid as long as $\upsilon_{th} \ll \upsilon_b$. However, when the temperature and thus thermal velocity of the ions is large, then a wide range of υ_{col} comes into play for the calculation of the effective emission rate. When a broad Maxwellian distribution function is convolved with an effective emission rate that varies significantly, a distorted emission line is produced that deviates from the previously discussed Gaussian line shape. This distortion, termed cross section effects, depends on the ion temperature, the beam injection energy and the observation geometry in relation to the neutral beam. Analytical approximations of the cross section effects are presented in [72] and corrections to the apparent ion temperatures and velocities are given.

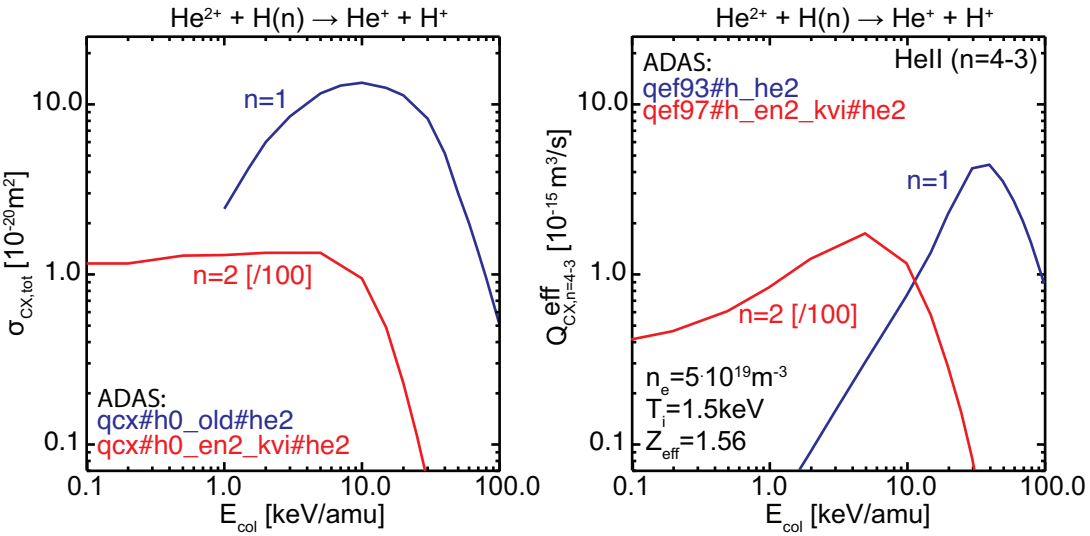

Figure 3.6: Atomic data for helium charge exchange spectroscopy, obtained from ADAS [71]. On the left, total cross-sections for charge exchange between fully stripped helium impurities and hydrogen neutral beams. On the right, effective charge exchange coefficients for the HeII n=4-3 transition, for typical plasma parameters. The ADAS datasets from which the atomic data come from are annotated.

As an illustration, we use the approximate function presented in [72] for the effective emission rate of helium, using the observation geometry of the main CXRS diagnostic on ASDEX Upgrade. We overplot a Maxwellian distribution with an ion temperature of 3keV, typical of ASDEX Upgrade plasmas, for a neutral beam injection energy of 30keV/amu. In addition, a Maxwellian distribution of 25keV for a neutral beam injection energy of 100keV/amu, which will be the energy of the diagnostic neutral beam on ITER, is plotted as well. As can be seen in Fig. 3.7, in the case of lower temperatures, a much smaller range of the emission rate is sampled, while in the case of high temperature, the variation of the emission rate is significant. In general, cross section effects are negligible for ion temperatures up to a few keV.

In Figure 3.8, the true and observed ion temperature and rotation velocity profiles are simulated using the approximations discussed in [72]. The simulation corresponds to the actual observation geometry of the charge exchange diagnostic used in this thesis, for a 60keV deuterium beam (source Q3 of NBI 1) and charge exchange measurements on the HeII line at 468.6nm, taking into account only the first energy component of the beam. The effect on the ion temperature profile is minimal, less than 1%,

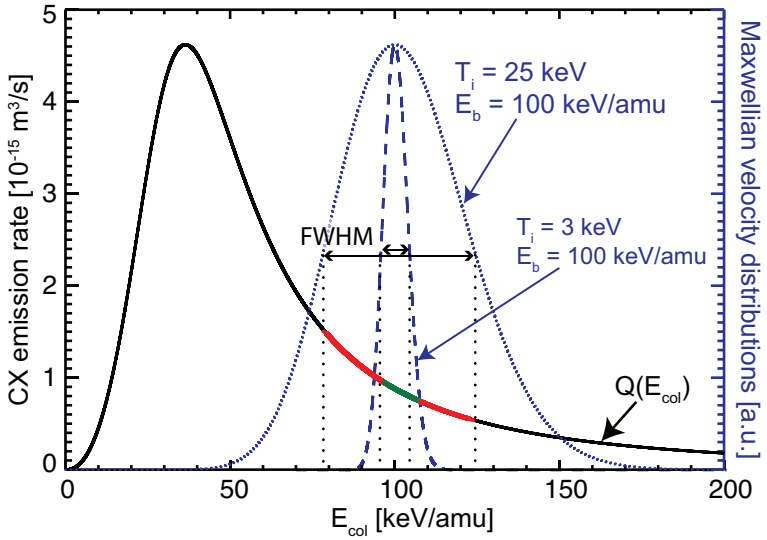

Figure 3.7: The charge exchange emission rate of helium, calculated using the approximation function found in [72], is plotted together with two illustrative Maxwellian distribution functions. The dashed line corresponds to a relatively low ion temperature (3keV) and a beam injection energy of 100keV/amu, as the diagnostic neutral beam will be on ITER. The dotted line corresponds to higher ion temperature (25keV). The range of the emission rate that is sampled by these two velocity distributions is highlighted in green and red, respectively.

while the effect on the rotation velocity profile is somewhat larger, between 2-3%. The measurement error bars on this diagnostic can be as low as 1.5%, assuming that there is sufficient signal. The cross-section effects have been, therefore, ignored in the analysis.

3.2.4 Charge exchange spectroscopy for fast ions

Not only thermal ions can be diagnosed with charge exchange spectroscopy, but also ions of higher energies. If, in addition to the thermal population, there is also a population of fast ions, then they will have a much more broadened emission line, due to their higher temperature. This will then appear as wings in the charge exchange spectra.

Fast ions in the plasma undergo charge exchange reactions with neutrals from the neutral beam. Assuming a deuterium beam injected in a deuterium plasma, fast deuterium ions capture an electron from the neutral deuterium atoms from the beam and end up in an excited state. The Balmer-α light emitted from the deexcitation of these atoms can be observed:

$$D + D^+ \rightarrow D^+ + D^*. \tag{3.27}$$

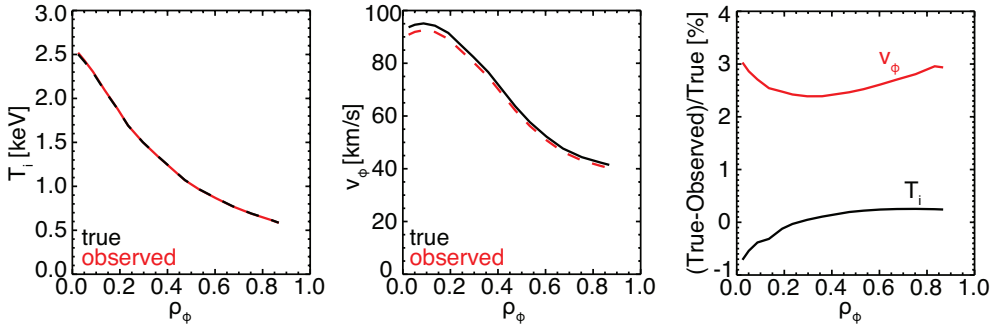

Figure 3.8: True and observed T_i and v_{rot} profiles for charge exchange measurements on the HeII line at 468.6nm. The simulation is based on the analysis performed in [72], for a 60keV deuterium beam, taking into account only the first energy component. The real geometry of the high etendue spectrometer used in this work, described in 3.3, focused on source Q3 of NBI 1 is used. On the right, the corrections in the measurement, expressed as the difference between the observed and true value, are shown.

The spectral shift due to the higher velocity of the ions allows for the separation of this component from the other D_α emissions.

The technique is usually called FIDA (fast ion D-alpha) spectroscopy, despite being, in principle, an application of charge exchange spectroscopy. FIDA spectroscopic diagnostics have been implemented among others at DIII-D [73] and ASDEX Upgrade [74]. An example of a deuterium spectrum, where the FIDA emission is highlighted, is found in Fig. 3.9.

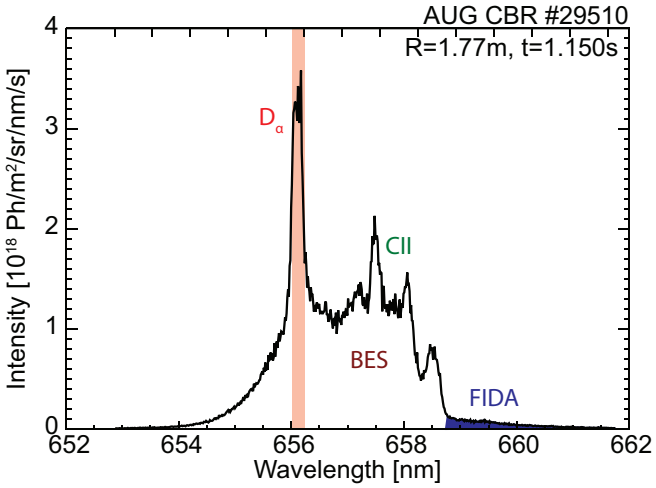

Figure 3.9: Example spectrum of deuterium, with the red shifted FIDA emission highlighted. The $D_\alpha$emission (saturated) as well as the beam emission are also shown.

At each wavelength of the FIDA spectrum, fast ions of different pitch angles and energies can contribute. The measurement is a one-dimensional projection of the fast ion distribution in velocity space. A FIDA diagnostic weights the fast ion distribution function in velocity space, with the weight function being a complicated function of energy and pitch angle [75]. It is possible, however, to reconstrunct the velocity-space distribution function, if sufficient data with different wavelength shifts and observation views are available [76]. A Monte Carlo forward model has been implemented on DIII-D [73] and also adjusted for ASDEX Upgrade [74]. The fast ion distribution function calculated with TRANSP [77, 78] and the computed neutral beam and halo densities are used to derive the spectral intensity and to compare with the measurements.

Using charge exchange spectroscopy for fast ion measurements is not limited to deuterium ions. Fast helium ions can also be measured. FIDA spectroscopy allows for the investigation of subjects such as the fast ion transport and the effect of MHD instabilities such as sawteeth on fast ions [74], as well as the effect of ion cyclotron resonance heating on the fast ions [75].

3.3 CXRS diagnostic instrumentation at ASDEX Upgrade

ASDEX Upgrade is equipped with an extensive suite of charge exchange diagnostics, covering both the core and the edge [63]. An overview of the charge exchange diagnostics can be seen in Fig. 3.10. In the course of this thesis work, a high étendue spectrometer suitable for core charge exchange spectroscopy on ITER has been installed and utilised on ASDEX Upgrade [79]. With this spectrometer, three separate wavelength ranges can be observed simultaneously, namely carbon (n=8-7, 529.1nm), helium (n=4-3, 468.6nm) and D_α(n=3-2, 656.1nm), the last including also the beam emission spectrum. Details on the spectrometer capabilities can be found in table 3.2, while an engineering design of the instrument can be seen in Fig. 3.11.

This instrument has been designed according to the ITER requirements for charge exchange spectroscopy measurements. The core charge exchange diagnostic on ITER is expected to provide measurements of T_i, υ_ϕ and helium "ash" concentration. The ITER charge exchange diagnostic requirements are listed in Table 3.1. However, charge exchange spectroscopy will face a number of challenges in ITER. The high electron density of ITER plasmas means high bremsstrahlung background in the charge exchange

spectra, and also strong attenuation of the neutral beams. The higher continuum level makes distinguishing the emission line more difficult, while the fact that fewer neutrals from the beam reach the plasma core means much fewer charge exchange reactions and, therefore, lower signal. Moreover, strong deterioration of the front optics is expected on ITER, lowering the amount of collected light even further: the first mirror reflectivity and characteristics are strongly affected by erosion and redeposition due to plasma ions [80], which will be more severe in ITER than in present devices.

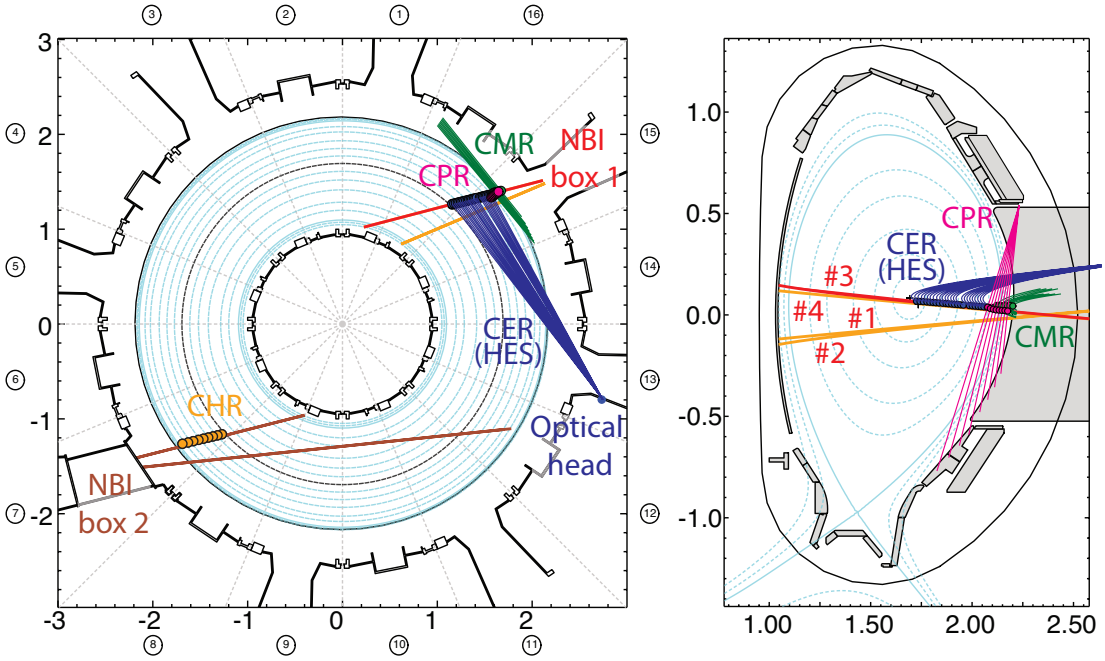

Figure 3.10: Top down (left) and poloidal cross-section view (right) of ASDEX Upgrade, showing the lines-of-sight and measurement locations of the core and edge charge exchange diagnostics available on ASDEX Upgrade. The high etendue spectrometer (HES) used in this work employs a subset of the CER lines-of-sight, looking at neutral beam source Q3 of NBI box 1, shown in red. The lines-of-sight intersect partially also the other three beam sources of this injector, shown in orange.

The high etendue spectrometer has, accordingly, been designed to deal with the unfavorable ITER environment. The signal-to-noise ratio of the measurement depends on the exposure time t_{exp}, the spectral resolution $\Delta\lambda/\lambda$ and the detector sensitivity R [82]:

$$\frac{S}{N} \propto \sqrt{t_{exp}\frac{\Delta\lambda}{\lambda}R}. \tag{3.28}$$

Table 3.1: Requirements for core charge exchange spectroscopy measurements per plasma parameter on ITER [81].

Parameter	Location	Time resolution	Spatial resolution	Accuracy
T_i	r/a<0.9	100ms	a/10	10%
v_{rot}		10ms	a/30	30%
Z_{eff}		10-100ms	a/10	10-20%
Impurity densities	r/a<0.9	100ms	a/10	20%
Core helium	r/a<0.9	100ms	a/10	10%
Confined α	Energy <3.5MeV	100ms	a/10	20%

The detector sensitivity is defined as:

$$R = QE \cdot T \cdot \Delta\Omega \cdot A, \tag{3.29}$$

where QE is the quantum efficiency, T the transmission and $\Delta\Omega \cdot A$ the étendue of the optical system. For this reason, an optical system with high optical efficiency, good spectral resolution and an étendue value of 1mm^{2}sr has been constructed. Measuring simultaneously impurity charge exchange spectra and the beam emission spectrum (found in the D_α spectrum) allows for determination of absolute impurity density profiles, without the need for absolute intensity calibration of the detectors (see Sections 3.2.2 and A).

The high light collection capability of the instrument allows for measurements even with quite low impurity content in the plasma in comparison to other charge exchange spectrometers. The noise level is also low, and subsequently the error bars on the spectrum and on the derived profiles are also smaller than in instruments with lower étendue. The high spectral resolution allows for identification of the different impurity lines in the spectra and identification of lower intensity emission lines that might interfere with the interpretation of the emission line of interest. However, on ITER the expected signal-to-noise ratio is so low (see Chapter 7) that one spectrometer like the one described here is foreseen for each radial channel in the plasma core, while at the plasma edge more than one radial location will be measured per spectrometer.

The detectors of the original spectrometer design were three Andor iKon charge-coupled devices (CCD detectors), one for each spectrometer channel. A chopper was used so that the camera chips could be kept dark during the readout period. Unfor-

Table 3.2: Design parameters of the high etendue spectrometer [79].

Etendue	$1mm^2sr$		
F/#	F/1		
Resolution	~ 0.2nm		
Dispersion	~ 0.02nm/px		
Efficiency	55%(0.92 transmission $\times$0.6 grating efficiency)		
Lines-of-sight	54 (400μm) / 27 imaged / 15 on CER periscope		
	HeII	CVI	D_α/ BES
Wavelength	460-474nm	520-534nm	648-667nm
Grating order	7^{th}	6^{th}	5^{th}

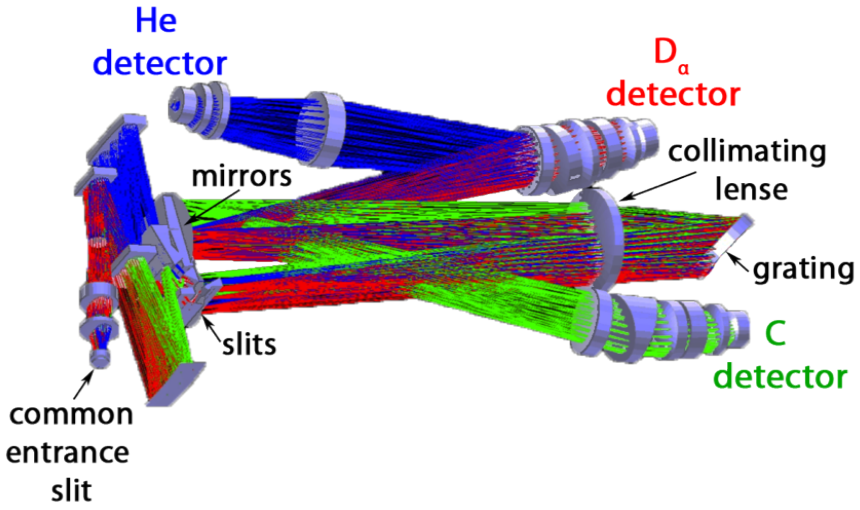

Figure 3.11: Engineering design of the high etendue spectrometer. The light enters the spectrometer from a single slit and is split with dichroic filters into three wavelength ranges. Each wavelength channel has its own slit. The different diffraction orders of a single grating are used for the different wavelengths [79].

tunately, the use of the chopper limited the exposure time to approximately 21msec, with a cycle time of approximately 68ms, meaning a dark time in between acquisitions of 47ms. For this reason, an upgrade of the detectors was implemented. The helium channel is now equipped with an Andor iXon EMCCD (Electron-Multiplying Charge-Coupled Device), while the carbon and D_α channels are equipped with Andor Neo sCMOS (scientific Complementary Metal Oxide Semiconductor) detectors. The sCMOS detectors were mainly selected because of their ability to deliver short exposure times, down to the millisecond range. An sCMOS detector is not employed for the helium channel, since the quantum efficiency of these detectors at the helium wavelength

is unacceptably low (46%).

The spectrometer has been operated regularly with an integration time of 10ms on all channels. However, the helium channel has been operated with shorter integration times, down to 4ms, and the other two channels with integration times down to 2ms, depending on the requirements of the experiment. For these short exposure times, the collected light has been sufficient for measurements, with the exception of carbon, for which longer integration times were usually required due to the low carbon content in ASDEX Upgrade plasmas.

The spectrometer detectors are triggered externally from the ASDEX Upgrade triggering system. One second before the discharge is initiated, a number of background frames are acquired, to be used for the subtraction of the detector background from the spectra (DVI1 trigger). The series of triggers for acquisition during the discharge is initiated with the TS06 trigger which signifies the beginning of the plasma discharge.

The acquired raw data are transferred from the detectors' buffers to local PCs and from there to the ASDEX Upgrade storage system, where they are stored in the form of shotfiles (ASDEX Upgrade shotfile system). The raw data shotfiles, called Level 0 shotfiles, contain the measured spectra as well as further information on the acquisition, for example, the names of the lines-of-sight used, exposure time, spectrometer details etc.. The Level 0 diagnostic names are CAR, CBR and CCR for the helium, D_α and carbon channels, respectively. The analysed data, obtained after fitting the measured spectra with CXSfit, namely the ion temperature, plasma rotation and intensity profiles, are stored in Level 1 shotfiles, with diagnostic names CAZ, CBZ and CCZ, respectively. The calculated impurity densities are stored in Level 2 shotfiles, named CAS, CBS and CCS, respectively. In this work these names will be used to refer to the data obtained from these diagnostics.

The spectrometer measures 15 radial locations in the plasma, between the magnetic axis and the plasma edge, enabling full radial low-field side profiles to be measured, with a possibility to measure up to 27 radial locations upon request. The lines-of-sight are focused on beam source Q3 of NBI 1, see Fig. 3.10, but also partially intersect the other three beam sources (for a more detailed description of the ASDEX Upgrade neutral beam injection system see section 2.2.1). Further details on the optical head properties can be found in [63]. The lines-of-sight geometry is obtained by the FARO 3D

measurement technology [83], which provides the coordinates of points along the lines-of-sight. The measurement locations in the plasma, in other words the intersections between the lines-of-sight and the neutral beams, are then calculated.

3.3.1 Calibration of CXRS measurements

The analysis of charge exchange spectra relies on the calibration of the instrumentation used. Determination of the measured wavelengths is required for the derivation of the ion temperature and toroidal rotation, while a conversion of detector counts to collected photons is required for the derivation of impurity densities.

In order to extract accurate information on the ion temperature and plasma rotation, wavelength calibrations of the spectrometer are required. The wavelength calibration is performed using laboratory pen lamps of elements that have well-known emission lines in the wavelength range of interest (for example neon or xenon). In addition, knowledge of the instrument function is required to allow for deconvolution of the measured line to extract ion temperature measurements.

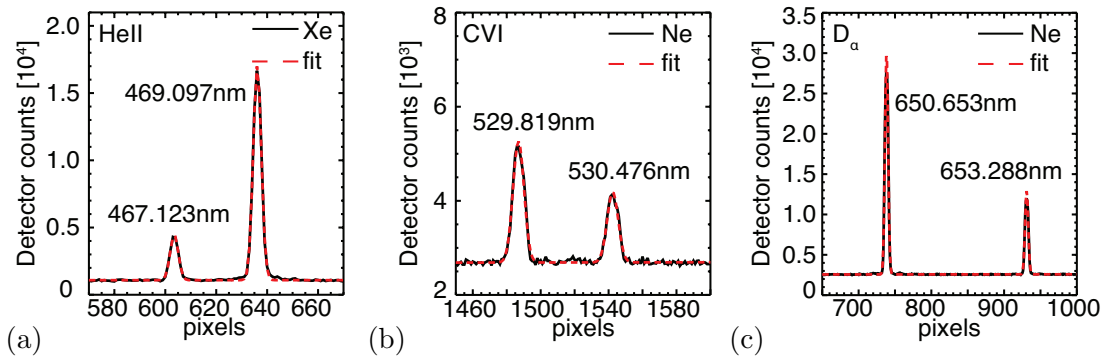

Figure 3.12: Neon and xenon spectra examples for each channel of the high etendue spectrometer, used for wavelength calibration of the instrument and determination of the dispersion and instrument response function. a) Xenon spectrum in the helium wavelength. The dispersion is 0.0186nm/px (pixel size 13μm) and the σ width of the fitted Gaussian line is 0.029nm. b) Neon spectrum in the carbon wavelength. The dispersion is 0.0118nm/px (pixel size 6μm) and the σ width of the fitted Gaussian line is 0.037nm. c) Neon spectrum in the D-alpha wavelength. The dispersion is 0.0135nm/px (pixel size 6μm) and the σ width of the fitted Gaussian line is 0.034nm.

The dispersion of each spectrometer channel is determined using two or more well known emission lines when the spectrometer fibers are illuminated with a neon (for the carbon and D_α channels) or a xenon (helium channel) pen lamp. For two emission lines

with known wavelengths $\lambda_1(nm)$ and $\lambda_2(nm) > \lambda_1$ and pixel locations px_1 and px_2, respectively, the dispersion d is then identified as follows:

$$d[nm/px] = \frac{\lambda_2 - \lambda_1}{\mathrm{px}_2 - \mathrm{px}_1}. \tag{3.30}$$

Example fitted neon spectra for the calibration of the carbon and D_α channels and an example fitted xenon spectrum for the calibration of the helium channel are shown in Fig. 3.12. A single Gaussian is used to fit the lines.

The shape of the observed spectrum is a convolution of the actual emission line shape with the instrument function. The entrance slit of the spectrometer has a finite width which causes the instrumental broadening. Assuming an infinitesimally narrow emission line, the instrument function is the observed, broadened line shape. The xenon or neon lines for all spectrometer channels can be fitted well with a single Gaussian. Finally, each spectrometer channel has its own entrance slit, shown in Fig. 3.11, and therefore has a different instrument response function.

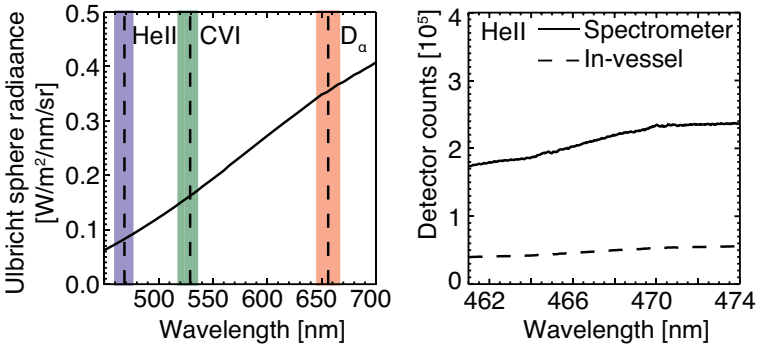

Figure 3.13: On the left, the spectral radiance curve of the Ulbricht sphere used for the intensity calibration of the instrument. The wavelength ranges for the three channels of the high etendue spectrometer are highlighted. On the right, a white light spectrum example for the helium channel of the high etendue spectrometer, obtained with the Ulbricht sphere. The solid line represents the measurement when the spectrometer fibers are illuminated with the integrating sphere, while the dashed line corresponds to the in-vessel measurements. The ratio of the two curves gives the transmission of the optical path from the torus to the spectrometer.

The intensity calibration of the diagnostic is performed by illuminating the spectrometer fibers with an integrating Ulbricht sphere whose spectral radiance is known, see Fig. 3.13. This allows for absolute measurements of the collected light intensity, as the counts recorded on the detectors can be converted into photons, but also the

sensitivity of the detectors across the pixels is identified. The calibration provides the conversion factor of the counts recorded on the detector to photons, which is calculated as:

$$A = \frac{R^{\lambda}_{ulb}[\frac{W}{m^2 \cdot sr \cdot nm}]}{counts^{\lambda}/t_{exp}}, \tag{3.31}$$

where R_{ulb} is the ulbricht sphere radiance at wavelength λ, *counts* is the number of counts recorded on the detector and t_{exp} the exposure time used for the acquisition.

Furthermore, the transmissions of the optics from the in vessel optical components to the spectrometer entrance slit have to be characterised. This is achieved by comparing the measured light when the spectrometer fibers are illuminated with the integrating sphere to the measurement when the integrating sphere is placed inside the torus (in-vessel intensity calibration), in front of the diagnostic optical head. Knowing the transmissions allows for flexibility in the operation, as the spectrometer settings can be changed independently.

An example white light spectrum for the helium channel is shown in Fig. 3.13. The solid line represents the measurement when the spectrometer fibers are illuminated with the integrating sphere, while the dashed line corresponds to the in-vessel measurements. The ratio of the two curves gives the transmission of the optical path from the torus to the spectrometer. The wavelength axis is determined using laboratory pen lamps as described above.

CXRS measurement uncertainties

Uncertainties in the interpretation of the charge exchange measurements arise from the instrument calibration, but also from the fitting procedure. The radial resolution of the measurement depends on the diagnostic observation geometry and the intersection of the lines-of-sight and the neutral beam. The wavelength calibration and characterisation of the instrument dispersion and instrument function are also characterised by uncertainties, which are, however, not taken into account in the calculation of the error bars of the temperature and rotation profiles.

The error bars on the charge exchange spectrum intensity are defined by the photon noise and the readout noise. Additional uncertainties come into play because of the detector background subtraction and the smear correction (found to be almost negligible in most cases for the instrument described here). When the beam modulation

technique is applied, the error on the spectrum is defined as $\sqrt{\delta I_{\text{on}}^2 + \delta I_{\text{off}}^2}$, where δI_{on} and δI_{off} correspond to the intensity errors of the time frame when the beam is on and the time frames when the beam is off, respectively.

The uncertainties on the impurity density profiles measured with charge exchange include the uncertainty on the measured intensity and the fitting of the spectra, as mentioned above. Furthermore, uncertainties in the calculation of the neutral beam attenuation and the effective charge exchange emission rates contribute to the error bars of the impurity density profiles. These contributions are estimated in the calculations of the uncertainties on the final impurity density profiles.

4

Impurity transport theory

Understanding the transport properties of impurities in fusion plasmas is vital for the operation of ITER and other future fusion devices. Low-Z impurities, such as the helium "ash", can cause dilution of the D-T fuel mixture, while high-Z impurities can cause radiative collapse of the plasma if they accumulate in the plasma core. The transport of seeding impurities, such as nitrogen, will also have a significant impact on the plasma operation. This work concentrates on the transport properties of low-Z impurities and specifically helium in the plasma core.

Neoclassical transport theory, which provides the necessary corrections to the classical collisional transport, taking into account the toroidal geometry of the plasma, cannot by itself describe the radial cross-field transport of impurities in a tokamak plasma and explain the experimentally observed transport. In a large part of the plasma, turbulence provides the major contribution to the radial transport of impurities. This is the case particularly for low-Z impurities.

In this chapter, the basic theoretical considerations of impurity transport are given, with the neoclassical and turbulent components described in Sections 4.2 and 4.3, respectively. Further studies on helium transport, relevant to the confinement, recycling and pumping of helium, are reported on in Section 4.4.

4.1 Radial impurity transport

Charged particles gyrating around magnetic field lines can undergo Coulomb collisions and thus be transferred to other magnetic flux surfaces. This provides a mechanism by which transport of charged particles can occur perpendicular to the magnetic flux surfaces.

Macroscopically, the time evolution of the distribution function f_α of a species α in a multi-species plasma is given by the Vlasov - Fokker-Planck equation (kinetic equation):

$$\frac{\partial f_\alpha}{\partial t} + \overrightarrow{v} \cdot \nabla f_\alpha + \frac{e_\alpha}{m_\alpha}(\overrightarrow{E} + \overrightarrow{v} \times \overrightarrow{B}) \cdot \frac{\partial f_\alpha}{\partial \overrightarrow{v}} = C_\alpha(f_\alpha) + S_\alpha, \tag{4.1}$$

where C_α is the Coulomb collision operator and S_α contains all source and sink terms. The kinetic equation can be solved perturbatively using an expansion of the distribution function [84–87].

The moments of the kinetic equation provide the conservation of particle density, momentum and energy [88]. The equation for particle conservation can be obtained by the zeroth moment of the kinetic equation for impurities (denoted by subscript I) and is given in Eq. (4.2):

$$\frac{\partial n_I}{\partial t} + \nabla \cdot \Gamma_I = S_I, \tag{4.2}$$

where Γ_I is the impurity flux density, defined as $\overrightarrow{\Gamma_I} = -D\nabla n_I + \overrightarrow{v_I} n_I$, with $n_I = \int f_I d^3v$ being the impurity density and $\overrightarrow{v_I} = (1/n_I) \int \overrightarrow{v} f_I d^3v$ being the flow velocity. S_I stands for the sources and losses (sinks) of the impurity due to processes such as ionisation, recombination, charge exchange, neutral beam injection and fusion in the case of helium "ash". D is a tensor that contains the diffusion coefficients along and perpendicular to the magnetic field.

The transport along the magnetic field is much larger than perpendicular to the field. Thus, the impurity density and temperature are to lowest order constant on a flux surface. We are mainly interested in the transport between flux surfaces, the so-called radial transport. When averaging the transport equation Eq. (4.2) over a flux surface, one obtains the radial impurity transport equation. For a flux surface label r, which has a simple relation to the volume enclosed by the flux surface $V = \pi r^2 2\pi R_{axis}$,

the radial transport equation has a simple analytical form:

$$\begin{aligned}\frac{\partial n_I}{\partial t} &= -\frac{1}{r}\frac{\partial}{\partial r}(r\Gamma_I) + S_I = \\ &= -\frac{1}{r}\frac{\partial}{\partial r} r(D\frac{\partial n_I}{\partial r} - \upsilon_d n_I) + S_I,\end{aligned} \tag{4.3}$$

where D here represents the flux surface averaged radial diffusion coefficient and υ_d the flux averaged drift velocity. Both neoclassical and anomalous transport contributes to D and υ_d and will be described in the following sections. For $S_I = 0$ and $\frac{\partial n_I}{\partial t} = 0$, the logarithmic impurity density gradients is obtained as υ_d/D.

4.2 Neoclassical impurity transport

Classical transport describes the collisional transport in a cylindrical plasma, in the presence of a homogeneous magnetic field. However, in tokamaks the magnetic field has a curvature, which introduces additional effects such as the trapping of particles due to the magnetic field curvature and the ∇B drift, that are not taken into account in the classical transport theory. The corrections to the classical transport theory for a plasma with toroidal geometry are given by the neoclassical transport theory, meaning that all fluxes in a tokamak plasma are comprised of a classical and a neoclassical part. The neoclassical part of the fluxes depends on the plasma collisionality ν^* defined as the ratio of the collision frequency ν and the particle bounce frequency $\nu_b = \epsilon^{3/2}\upsilon_{th}/qR$ of a trapped particle, where $q = (r/R)(B_\phi/B_\theta)$ is the safety factor, r is the minor radius of the flux surface, R is the major radius of the tokamak and $\epsilon = r/R$ is the inverse aspect ratio of the flux surface. The low collisionality regime ($\nu^* < 1$) is called the banana-plateau (BP) regime, while the high collisionality regime ($\nu^* > \epsilon^{-3/2}$) is called the Pfirsch-Schlüter (PS) regime. The neoclassical particle and heat fluxes are themselves comprised of three components, namely the classical (CL), banana plateau (BP) and Pfirsch-Schlüter (PS) fluxes:

$$\Gamma_I^{NC} = \Gamma_I^{CL} + \Gamma_I^{BP} + \Gamma_I^{PS} \tag{4.4}$$

$$Q_I^{NC} = Q_I^{CL} + Q_I^{BP} + Q_I^{PS}. \tag{4.5}$$

In these equations, I denotes the impurity (though similar equations hold for bulk ions and electrons) and the electrostatic flux contribution is neglected, as the electrostatic force is typically not strong enough to trap particles and can be neglected for low-Z impurities. The components of neoclassical transport will be briefly discussed below, following the derivations and discussions found in [84, 88].

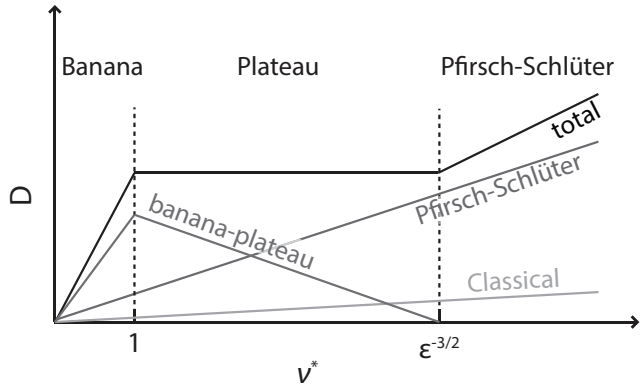

Figure 4.1: Illustration of the dependence of the diffusion coefficients on collisionality and the identification of the different regimes contributing to neoclassical transport (adapted from [89]).

Classical transport

In the particle picture, classical transport can be understood as a random walk process where every collision time τ_{col} the gyrating ions are radially displaced by a Larmor radius ρ_L. This leads to a diffusion coefficient $D_{CL} \approx \rho_L^2/\tau_{col}$. The collision time is given by $\tau_{col} = 1/\nu$, where ν is the collision frequency. The ion thermal diffusivity is given by $\chi_i \approx \nu_i \rho_{L,i}^2$, which exceeds significantly the electron thermal diffusivity $\chi_e \approx (m_e/m_i)^{1/2}\chi_i$.

In the fluid picture, the radial gradients of density and temperature lead to diamagnetic flows in the flux surface perpendicular to the magnetic field. These flows are different for the different species and the Coulomb collisions cause friction forces between the different species, which finally cause a radial flux.

The classical fluxes across magnetic flux surfaces can be calculated by evaluating the gyroangle dependent part of the distribution function (for a treatment see [88]).

Classical transport is very small, but there are additional contributions to the particle transport described by neoclassical theory.

Pfirsch-Schlüter contribution

The diamagnetic flows perpendicular to the magnetic field within the flux surface are not divergence free and parallel flows build up to ensure that the total flow has zero divergence. These parallel flows are calles the Pfirsch-Schlüter flows. Since the diamagnetic flows of the different ion species are different, also the Pfirsch-Schlüter flows differ. Here, the Coulomb collisions cause again friction forces between the different species, which lead again to a radial flux. This effect causes a diffusion which is roughly:

$$D_{PS} \approx 2q^2 D_{CL}, \tag{4.6}$$

where q is the safety factor. For q values of 3-4, this leads to coefficients $2q^2 = 18 - 32$ times larger than the classical diffusion coefficient.

Banana-plateau contribution

Plasma particles with $v_\parallel \lesssim \sqrt{\epsilon} v_\perp$ are trapped in magnetic mirrors formed at the outer side of the torus due to the $1/R$ dependence of the magnetic field. The particles bounce between two mirror reflection points and perform so-called banana orbits. Trapped ions travel along the banana orbit such that they move in the direction of the electric current, when they are on the outside and against the current on the inside of the banana orbit. Thus, a similar effect is obtained for the diamagnetic flow due to the gyromotion of the ions: radial density and temperature gradients lead to a parallel flow of the trapped particles. These flows cause again a radial flow due to the parallel friction forces. The resulting diffusion coefficient is roughly:

$$D_{BP} \approx \frac{q^2}{\epsilon^{3/2}} D_{CL}. \tag{4.7}$$

However, if the collisionality is above 1, the particles cannot finish their travel along the banana orbit without undergoing a collision. Thus, the above mentioned anisotropy of the velocity distribution vanishes for large collisionalities. The corresponding diffusion coefficient goes to zero for collisionalities much larger than 1. Typically, the

banana-plateau contribution is negligible when reaching the Pfirsch-Schlüter collisionality regime.

Low-Z impurities such as helium and boron in the core of a typical ASDEX Upgrade plasma are typically in the banana-plateau (or long mean free path) regime. The edge of the plasma is mostly in the Pfirsch-Schlüter regime. The transport in the region in between is characterised by both banana-plateau and Pfirsch-Schlüter contributions. The classical contribution is small in all plasma regions.

4.2.1 Neoclassical predictions of impurity transport

Despite the fact that neoclassical transport theory alone cannot fully describe the impurity transport in the plasma, there are plasma regions and plasma regimes in which neoclassical transport is sufficient to explain the observed transport.

The neoclassical diffusion coefficients and drift velocities are the sum of the diffusion coefficients and drift velocities in each of the regimes. The coefficients can either be calculated by numerical codes, such as NEOART [89, 90], or with simpler analytical expressions such as those given in [91]. Total diffusion and drift coefficients can also be derived from experimental measurements, but they would also contain turbulent contributions. The diffusion coefficients for a large aspect ratio circular plasma are given below [91]:

$$\begin{aligned} D^{NC} &= D^{CL} + D^{PS} + D^{BP} \\ D^{CL} &= \frac{1}{B_0^2}\frac{m_I k T \nu_{ID}}{e^2 Z^2} \\ D^{PS} &= \frac{2q^2}{B_0} K^{PS} \frac{m_I k T \nu_{ID}}{e^2 Z^2} \\ D^{BP} &= \frac{q^2}{\epsilon^{3/2} B_0^2}\frac{k T \mu^*_{ID}}{e^2 Z n_I} \end{aligned} \tag{4.8}$$

where k is the Boltzmann constant, q is the safety factor, ν_{ID} is the collision frequency between the impurity and the main ions, B_0 is the vacuum toroidal field, K^{PS} is a function of the impurity strength parameter $n_I Z I^2/n_D$ [91, 92] and the main ion collisionality, μ^*_I is the weighted viscosity coefficient of the impurity and main ions, dependent also on ν_{ID}, and ϵ the inverse aspect ratio. Here, we just consider the collisions between the impurity and the main ion deuterium. The collision frequency is $\nu_{ID} \propto Z^2/T^{3/2}$ and D_{CL} is nearly independent of Z. In the plasma core, the banana

plateau contribution dominates the diffusion, while the Pfirsch-Schlüter contribution dominates the plasma edge.

The convective part of the impurity transport is defined by the drift velocities. The total neoclassical drift velocity is the sum of the drift coefficients in each of the regimes. The drift velocity in each regime is driven by the gradients in deuterium density and ion temperature:

$$\begin{aligned} v^{NC} &= v^{CL} + v^{PS} + v^{BP} \\ v_X &= D_X Z \left(\frac{d \ln n_D}{dr} + \alpha_T \frac{d \ln T_i}{dr} \right) \end{aligned} \tag{4.9}$$

where X denotes each contribution (CL, PS, or BP) and α_T is a function of the impurity strength parameter and the main ion collisionality [91, 92]. The drift velocity is, therefore, comprised of an inward part, proportional to the main ion density gradient, and an outward part, proportional to the temperature gradient, as α_T is negative [93]. This outward contribution to the drift velocity plays a screening role and is described below.

Temperature screening

Neoclassical transport theory predicts the phenomenon of impurity "temperature screening", which leads to impurity transport in the outward direction. The drift velocity of an impurity can be analytically written as [94]:

$$v_I = D_I Z \left(\alpha_n \frac{d \ln n_D}{dr} + \alpha_{T_i} \frac{d \ln T_i}{dr} + \alpha_{T_e} \frac{d \ln T_e}{dr} \right), \tag{4.10}$$

where the dependence on the gradients is defined by the factors α_n,α_{T_i}, α_{T_e}, which are functions of the impurity strength parameter and the impurity and main ion collisionality. The factor α_n includes only collisions between the main ions and the impurity, as momentum transfer between electrons and impurities can be considered negligible, and for the same reason, α_{T_e} is very small. If $|\alpha_n| \gg |\alpha_{T_i}|$, impurities are predicted to have a peaked density profile when the electron density profile is peaked. If, however, the main ion density profile gradient becomes small then the ion temperature gradient term becomes important. In the banana-plateau regime the coefficient of the ion temperature gradient term is negative. This outward convective flux is called temperature

screening. The temperature screening factor is a complicated function of Z, m and n_I; no direct conclusions can be drawn for the dependencies of the temperature screening effect. It is noted in [93] that helium has a higher (but still negative) temperature screening factor than heavier, higher-Z impurities, and for this reason temperature screening is expected to be weaker for helium.

Ware pinch

The Ware-pinch [95] is a radial particle flux driven by the toroidal electric field. Due to the toroidal electric field, trapped particles in banana orbits are accelerated in one direction, which leads to reduction of their pitch angle, and decelerated in the other direction, which leads to an increase of their pitch angle. Therefore, the banana orbits are displaced and a net inward flux is observed. The banana orbits drift towards the magnetic axis with a velocity of cE_ϕ/B_θ, where E_ϕ and B_θ are the toroidal electric field and the poloidal magnetic field, respectively. This neoclassical inward flux leads to a peaking of the density profiles. This effect reduces with collisionality as the banana-plateau transport and is only important in the hotter central part of the plasma. For impurities, the Ware pinch is usually small compared to the gradient driven fluxes.

4.2.2 Neoclassical impurity transport observations

Neoclassical transport and the comparison of the neoclassical theory with experimentally derived transport coefficients has been the subject of research in many tokamaks over the last decades. In this section, experimental investigations in comparison to neoclassical theory are briefly reviewed.

In the plasma core ($\rho_{pol} < 0.3$), diffusion coefficients and drift velocities derived from neoclassical theory compare well with experimental measurements for low-Z impurities performed at ASDEX Upgrade, with significant discrepancies for higher Z [91]. The diffusion coefficient is stated to be either neoclassical or anomalous inside $r \sim \alpha/4$, with α being the minor radius, with the diffusion coefficient increasing strongly and becoming anomalous when central ECR heating is applied [25]. A strong inward drift is observed in this region when the diffusion coefficient is neoclassical, decreasing strongly in the anomalous cases. Neoclassical simulations of the diffusion and drift coefficients have shown agreement with the experimental observations in this region for lower-Z elements. However, they underpredict the coefficients for high-Z elements [91]. It should

be noted, however, that many past analyses of neoclassical transport were neglecting the enhancement of neoclassical transport produced by rotation effects, which could be more than one order of magnitude for heavy impurities.

In the confinement region, defined as $0.3 < r/a < 0.8$, the experimentally deduced diffusion coefficients are one order of magnitude larger than those predicted by neoclassical theory. ASDEX Upgrade and JET results show that the diffusion coefficients are much larger than the neoclassical predicted values, with v/D values smaller than the neoclassical ones [25, 96]. The impurity transport is anomalous in this plasma region [25, 27, 97]. Nevertheless, neoclassical transport can become important for higher-Z elements and at higher collisionalities. This is the region of concern for this work. In the edge transport barrier region, in H-mode plasmas, impurity transport is observed to be neoclassical and characterised mainly by the Pfirsch-Schlüter neoclassical term [90, 98].

The diffusion coefficients deduced from neoclassical theory are in the range of $10^{-3}m^2/s$ to $\leq 10^{-1}m^2/s$, while experimentally deduced coefficients, which include anomalous transport due to turbulence, diverge strongly from the neoclassical values [92]. Strong variations and different divergences from the neoclassical theory are found in different machines due to different operational regimes and experimental uncertainties. Nevertheless, the general observation in all tokamak experiments is that neoclassical transport alone cannot explain the observed impurity density profiles. Neoclassical transport predicts profiles that are much more peaked than those experimentally measured. As such, both neoclassical and anomalous effects must be considered.

Also in the case of helium, experimental evidence has supported the argument that there are contributions additional to the neoclassical transport. Helium diffusivities and heat conductivities in TFTR supershots were found to be radially hollow, increasing strongly from the sawtooth inversion radius to the plasma edge and larger by at least an order of magnitude than those predicted by neoclassical theory, even inside the sawtooth inversion radius, except for the region around the magnetic axis. Inward convection was observed to be larger than the neoclassical values for $r/a < 0.5$ [99, 100]. Furthermore, evidence for electrostatic turbulence as the dominant transport mechanism has been identified, as it was observed that $D_{He}(r) \sim \chi_i(r) \sim \chi_\phi(r) \sim \chi_e(r)$, as expected if helium is a trace impurity and the dominant transport mechanism is electrostatic turbulence.

In enhanced reversed magnetic shear plasmas in TFTR, the helium diffusivities compare well with neoclassical predictions derived with NCLASS [101], within the reverse shear region ($r/a < 0.35$) where plasma fluctuations are very small. However, strong enhancement of the diffusion coefficients is observed outside [102, 103], implying turbulent contributions.

At DIII-D, in plasmas with suppressed turbulent transport, small ion density gradient, and strong ion temperature gradient (very high confinement mode plasmas [104]), the so-called "temperature screening" of impurities, which leads to outward impurity transport, was experimentally documented [94]. In the early phases of these plasmas, while still in L-mode with strong turbulence, the low-Z impurity density profiles are observed to have similar shapes compared with the electron density, independent of the charge and mass of the impurity. In the very high confinement mode phase, the observed transport is found to be enhanced in comparison to the neoclassical predictions, which is attributed to anomalous transport.

Previous helium studies performed at ASDEX Upgrade also support the evidence of anomalous helium transport in the confinement region. Diffusion coefficients in the range of 0.4 - $3m^2/s$ and drift velocities of -15 - $0m/s$ increasing radially from the core to the edge, are reported for helium and neon, 5-10 times larger the collisional expectations [105].

As a general conclusion, experimental evidence for helium transport in the confinement region shows deviations from the neoclassical theory predictions. The contribution of anomalous electrostatic turbulence to the helium transport is significant, if not the dominant mechanism, and necessary to explain the observed impurity transport.

4.3 Turbulent transport

Neoclassical transport theory cannot explain all of the experimental observations of impurity transport, meaning turbulence can play an important role in determining the transport of electrons, impurities and main ions. Depending on the turbulent plasma state, typically either the Trapped Electron Mode (TEM) regime, in which trapped electron modes dominate, or the Ion Temperature Gradient (ITG) regime, in which ion temperature gradient modes dominate, different behaviours are predicted.

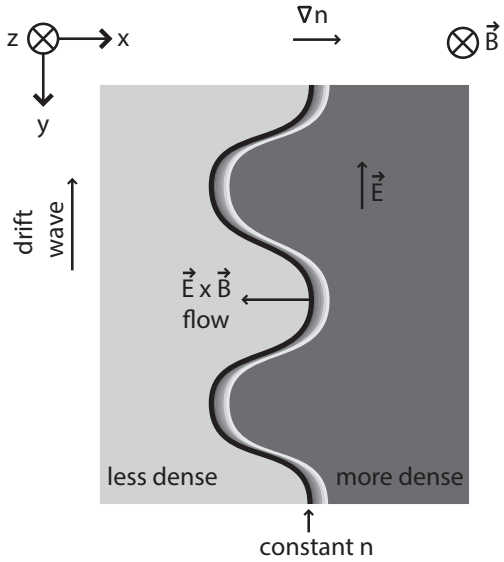

Figure 4.2: Illustration of the electron drift wave.

A complete understanding of impurity transport requires taking both the neoclassical and the turbulence-induced transport mechanisms into account.

4.3.1 Plasma turbulent states

Plasma turbulence is created by microinstabilities in the plasma, both mainly electrostatic and electromagnetic in nature. For impurities, instabilities of high k, in other words with short wavelengths comparable to the ion Larmor radius scale, and of mainly electrostatic nature are of interest. In particular, the TEM instability, driven by the electron drift wave, and the ITG instability, driven by the ion acoustic wave, are the dominant players under most conditions.

Electron drift wave

The electron drift wave is a plasma wave of electrostatic nature, responsible for the development of the trapped electron mode instability [10]. Assuming a slab of plasma in a shearless, uniform magnetic field in the z-direction, that exhibits a density gradient in the x-direction, the wave defines density isobars, as shown in Fig. 4.2. The density perturbation $\widetilde{n}$ in the y-direction is of the form $n_1 = \exp i(k_y y - \omega t)$.

If the perturbation n_1 is identical in phase and magnitude along the magnetic field (z-direction), then the density along this direction changes as a function of time ωt, but as there is no gradient along the magnetic field direction, there is no instability.

We now assume that n_1 has a gradient or phase change in the z-direction. The electrons are adiabatic and flow freely along the magnetic field line, keeping the Boltzmann relation. In this way, a potential fluctuation ϕ_1 is created in the y-direction, given by:

$$n = n_0 + n_1 = n_0 \exp\left(\frac{e\phi}{T_e}\right). \tag{4.11}$$

Linearising the above equation yields:

$$\frac{n_1}{n_0} = \frac{e\phi}{T_e}. \tag{4.12}$$

There is no phase difference between the density and potential perturbation. As now the high density regions become positively charged, due to the flow of the electrons, and the low density regions become negatively charged, an electric field is created by the potential perturbation in the y-direction:

$$\overrightarrow{E_1} = -\overrightarrow{\nabla}\phi. \tag{4.13}$$

The electric field is 90^o out of phase with the density perturbation n_1 and causes an $\overrightarrow{E} \times \overrightarrow{B}$ drift in the direction of the density gradient (x-direction):

$$v_{\overrightarrow{E}\times\overrightarrow{B}} = \frac{\overrightarrow{E_1} \times \overrightarrow{B}}{B^2}. \tag{4.14}$$

The radial transport caused by a density perturbation $\widetilde{n}$ and a $\widetilde{v}_{\overrightarrow{E}\times\overrightarrow{B}}$ drift velocity is given by $\Gamma_r = \langle \widetilde{n} \cdot \widetilde{v}_{\overrightarrow{E}\times\overrightarrow{B}} \rangle \sin(\delta)$. Since the density perturbation and the drift velocity are 90^o out of phase, $\sin(\delta) = 0$ and no radial transport is observed.

The continuity equation can now be written:

$$\left(\frac{\partial}{\partial t} + v_{\overrightarrow{E}\times\overrightarrow{B}} \cdot \nabla\right) n + n \nabla v_{\overrightarrow{E}\times\overrightarrow{B}} = 0. \tag{4.15}$$

The unperturbed part of the density n_0 is constant: $\frac{\partial n}{\partial t} = 0$. Moreover, as the $\overrightarrow{E} \times \overrightarrow{B}$

flow is along the x-direction, $n\nabla v_{\vec{E}\times\vec{B}} = n\frac{\partial}{\partial x}|v_{\vec{E}\times\vec{B}}|\hat{x} = 0$. Therefore:

$$\frac{\partial n_1}{\partial t} + v_{\vec{E}\times\vec{B}} \cdot \nabla n_0 + v_{\vec{E}\times\vec{B}} \cdot \nabla n_1 = 0. \tag{4.16}$$

The last term on the left hand side is zero and as such:

$$\frac{\partial n_1}{\partial t} = -v_{\vec{E}\times\vec{B}} \cdot \nabla n_0. \tag{4.17}$$

The time derivative of the density perturbation is:

$$n_1 = \exp i(k_y y - \omega t) \Rightarrow \frac{\mathrm{d}n_1}{\mathrm{d}t} = -i\omega n_1. \tag{4.18}$$

Taking into account that the potential perturbation is in phase with n_1 (Eq. (4.12)), the electric field created is $\overrightarrow{E} = -\nabla\phi_1 = -ik_y\phi_1$. Replacing now in the continuity equation, the wave frequency obtained:

$$\omega = -\frac{k_y T_e}{eB}\frac{\nabla n_0}{n_0}, \tag{4.19}$$

which is k_y times the electron diamagnetic velocity, assuming no or small temperature variation.

If a mechanism, such as collisions, Landau damping or a temperature gradient, make the density perturbation out of phase with the potential perturbation, then radial transport becomes possible. This can be expressed as a small correction to the Boltzmann relation ($i\delta$-model):

$$\frac{n_1}{n_0} = \frac{e\phi}{T_e}(1 - i\delta). \tag{4.20}$$

As such, the drift wave is destabilised and leads to turbulent microinstabilities. The result is turbulent transport due to the so-called electron drift mode microinstability [106, 107].

Trapped Electron Mode (TEM)

Trapped particle modes [108, 109] can be categorised into collisionless and dissipative. In collisionless modes, the trapped particles stay in the bad curvature region for most of the time, so that the curvature drift is always in the same direction. The $\overrightarrow{E} \times \overrightarrow{B}$ flows

can therefore enhance the perturbation. If the collisions, however, become frequent enough in comparison to the drift frequency, the trapped particles can become passing and vice versa.

Trapped electron collisions in combination with an electron temperature gradient provide a destabilising mechanism for the electron drift wave mode, with a growth rate that depends on the drift wave frequency and the trapped particle velocity dependent collision frequency, as well as on the η_e parameter:

$$\eta_e = \frac{1}{T_e}\frac{dT_e}{dr}\left(\frac{1}{n}\frac{dn}{dr}\right)^{-1}, \tag{4.21}$$

where r is the radial coordinate, and dT_e/dr is the electron temperature gradient, acting as the main drive for the instability.

Ion temperature gradient (ITG)

If the ion density perturbation is out of phase with the potential perturbation due to dynamics acting on the ions, such as the presence of an ion temperature gradient, then ion drift wave instabilities, such as the ion temperature gradient mode, can occur.

The ion temperature gradient mode can be separated into two structures depending on whether toroidal effects are responsible. The first one, the 'slab' mode structure [110], evolves from the coupling between a poloidally propagating drift wave arising due to an ion temperature gradient and a parallel ion acoustic (sound) wave. The parallel sound wave compression (z-direction in Fig. 4.2) affects the ion density response, causing an instability. The toroidal mode structure [111] evolves from the coupling between the magnetic curvature and the drift wave in the presence of an ion temperature gradient. In this case, the ion density response is changed by the toroidal drift. The growth rate of the ITG mode depends on the η_i parameter, defined as for the electrons in Eq. (4.21), making clear the dependence of the mode appearance on the ion temperature gradient.

4.3.2 Turbulent impurity fluxes

Impurity transport caused by electrostatic plasma turbulence, which is non-linear in nature, can be studied within a fluid or a gyrokinetic approach with a variety of non-

linear and quasi-linear models. The dependences of the turbulent impurity fluxes are analysed in detail in [112–115].

The impurity particle and heat fluxes due to turbulent transport processes can be decomposed into a diffusive, a thermodiffusive, a rotodiffusive and a convective term as follows:

$$\frac{R\Gamma_I}{n_I} = D_{d,I}\frac{R}{L_{n_I}} + D_{th,I}\frac{R}{L_{T_I}} + D_{u,I}u'_I + RV_{p,I} \tag{4.22}$$

$$\frac{RQ_I}{n_I T_I} = \chi_{d,I}\frac{R}{L_{n_I}} + \chi_{th,I}\frac{R}{L_{T_I}} + \chi_{u,I}u'_I + RH_{p,I}. \tag{4.23}$$

There, the local normalised logarithmic gradients R/L_X are defined as:

$$\frac{R}{L_X} = -\frac{R}{X}\frac{\mathrm{d}X}{\mathrm{d}r} \tag{4.24}$$

with r being the flux surface averaged plasma minor radius and R the plasma major radius, while the radial gradient of the toroidal plasma velocity is given by u'

$$u'_I = -\frac{\mathrm{d}\Omega_I}{\mathrm{d}r}\frac{R^2}{v_{th}}, \tag{4.25}$$

where Ω_I is the angular toroidal rotation velocity.

The decompositions of the turbulent fluxes are comprised of the following contributions:

- The diagonal diffusive flux is proportional to the local impurity density gradient and is characterised by the particle diffusion coefficient $D_{d,I}$ in the case of the particle flux and by the heat diffusivity coefficient $\chi_{d,I}$ in the case of the heat flux. Diffusion arises mainly from the $\overrightarrow{E} \times \overrightarrow{B}$ advection and is, therefore, charge independent.

- The thermodiffusion piece is proportional to R/L_{T_i}, characterised by the particle thermodiffusivity coefficient $D_{th,I}$ and the heat conductivity coefficient $\chi_{th,I}$. Thermodiffusion arises from the coupling between temperature and density fluctuations, due to the curvature and ∇B drifts. Due to the inverse charge dependence of these drifts, the thermodiffusive contribution to the fluxes is expected to be more important for lower-Z impurities. Thermodiffusion is directed inwards when a TEM is dominant, or outwards when ITG are dominant.

- The rotodiffusion part is proportional to the radial gradient of the plasma toroidal velocity and is characterised by the particle rotodiffusion coefficient $D_{u,I}$ and the corresponding heat coefficient $\chi_{u,I}$. This term arises from the $\overrightarrow{E} \times \overrightarrow{B}$ advection in the presence of a background rotation gradient [11]. Similar to the thermodiffusion term, the direction of the rotodiffusion is inward when a TEM is dominant and outward when an ITG is dominant. Rotodiffusion is connected with parallel dynamics and scales with A/Z [115].

- The pure convective part is characterised by the (heat) pure convective velocity. This pure convection is the result of many mechanisms: the compression of the $\overrightarrow{E} \times \overrightarrow{B}$ drift, which provides a charge-independent contribution, the curvature and ∇B drifts, which provide a decreasing contribution with increasing charge, as well as parallel dynamics which is dependent on Z/A. Pure convection is direct inwards for monotonic q profiles (for the toroidal part). However, the part due to the parallel dynamics can be directed either outward or inward, depending on the mode [113, 116].

The coefficients encountered in each turbulent flux term depend on the mass and charge of the impurity, as well as on the background main ion plasma properties. A formulation of the coefficients can be found in [115] and the references therein.

Both turbulent and neoclassical transport mechanisms should be taken into account to express the impurity density. Therefore, the local normalised logarithmic impurity density gradient is given by the ratio of the total convection to the total diffusion, taking into account both turbulent (turb) and neoclassical (NC) transport, assuming that the total impurity particle flux is zero:

$$\frac{R}{L_{n_I}} = -\frac{RV_I^{turb} + RV_I^{NC}}{D_{d,I}^{turb} + D_{d,I}^{NC}} \tag{4.26}$$

Despite their names, the last three terms of Eq. (4.22) together, namely the thermodiffusion, the rotodiffusion and the pure convection, give the total turbulent convection [27].

Assuming only turbulent transport contributions, as is expected in the confinement region of the plasma and especially around the mid-radius for low-Z impurities, the

impurity density logarithmic gradient can be derived from Eq. (4.22), setting $\Gamma_I = 0$:

$$\begin{aligned} \left.\frac{R}{L_{n_I}}\right|^{turb} &\simeq -\left(\frac{D_{th,I}}{D_{d,I}}\frac{R}{L_{T_I}} + \frac{D_{u,I}}{D_{d,I}}u'_I + \frac{RV_{p,I}}{D_{d,I}}\right) \\ &= -\left(C_T\frac{R}{L_{T_I}} + C_U u'_I + C_P\right) \end{aligned} \tag{4.27}$$

which can be compared to the one calculated assuming only a neoclassical contribution:

$$\left.\frac{R}{L_{n_Z}}\right|^{NC} = -\frac{RV_{p,I}^{NC}}{D_{d,I}^{NC}}. \tag{4.28}$$

4.3.3 Applications of turbulent transport theory

Though the description here is focussed on impurity transport, turbulent electron transport has provided very important insights on subjects such as the electron density peaking. The experimentally observed electron density peaking with the application of central electron cyclotron heating is associated with the transition between the different plasma turbulent states (ITG/TEM). An overview of this process is given here, as it is important for the understanding of the helium transport experimental investigations. Subsequently, previous work on the turbulent transport of low-Z impurities such as boron will be presented.

Effect of electron heating on the electron density profile

The application of central electron heating has been observed to have different effects on the electron density profiles under different conditions. A flattening of the electron density profile, also called "pump-out", has been observed in low density L-mode plasmas, but also in high densities, where it was partially attributed to the reduction of the Ware pinch [26, 95]. On the other hand, under certain conditions, the electron heating leads to peaking of the electron density profile [26, 27].

Through modelling of the turbulent transport, it has been shown that this behaviour can be explained by the turbulent plasma state. It was found that there is a clear non-monotonic relation between the peaking of the electron density with the real frequency of the most unstable mode ω_r [26, 27]. Looking at an illustration of the logarithmic normalised electron density gradient as a function of ω_r, and as a proxy with the effective collisionality, shown in Fig. 4.3, the observed behavior of the electron density

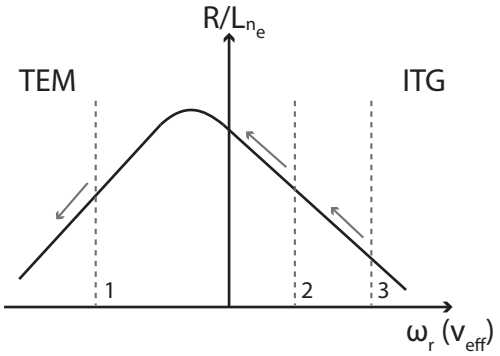

Figure 4.3: Illustration of the predicted dependence of the normalised logarithmic electron density gradient on the real frequency of the most unstable turbulent mode ω_r and collisionality v_{eff} in the ITG and TEM regimes.

profile under electron cyclotron heating can be explained. The description below is according to the present theoretical interpretation of the observations, which is in the process of being validated.

Starting from very low densities (case 1 in the figure), application of central ECRH increases the electron temperature and decreases the effective collisionality, leading to flattening of the electron density. Adding ECRH to an ITG dominated regime (case 2), decreases the effective collisionality leading to a transition from an ITG dominated towards a TEM dominated regime and peaking of the electron density profile. As this happens, the thermodiffusive term contributing to the electron turbulent flux reverses, from inward to outward and can lead to flattening of the density profile. Considering now cases with high effective collisionality (case 3), the application of central ECRH might not be sufficient to change the T_e/T_i ratio and hence no change in ω_r or to the density gradient is expected. The strongest peaking of the electron density profile is predicted near the transition from the ITG to the TEM regime, in the TEM regime.

In low density, low current H-mode ASDEX Upgrade plasmas, the electron density is observed to peak strongly with increasing central electron heating and this behaviour is again linked to the transition from an ITG to a TEM regime [27]. Good agreement has been found comparing the measured electron density profiles with the results of the gyrokinetic simulations.

Effect of electron heating on the density profile of light impurities

A similar effect of the electron heating via the change in turbulence regimes has been observed in ASDEX Upgrade also for light impurities, such as boron [11, 27]. Flat and even hollow boron profiles have been observed in NBI only heated discharges, while the boron density profiles peak as the dominant turbulent mode transitions from ITG to TEM. The boron profiles are always observed to be less peaked than the electron density. Neoclassical transport was found to be negligible in comparison to the turbulent transport at mid-radius of the plasma.

The gyrokinetic simulations of the logarithmic normalised boron density gradients compare well qualitatively with the measured profiles, if the rotodiffusive term is included in the simulations [11]. The effect of the background toroidal plasma rotation profile contributes to the explanation of the peaked boron profiles. Furthermore, the rotodiffusive term provides an outward contribution to the flux in the case of peaked rotation profiles. The rotodiffusion contribution is almost negligible during phases of strong electron heating, as the rotation profile flattens in this case. Nevertheless, the modelling of turbulent transport even including this term cannot fully reproduce the hollow boron profiles in NBI only phases, indicating that an additional contribution might be missing from the modelling.

Taking the ratio of electron to ion temperature T_e/T_i as a proxy for the collisionality, it was observed that the thermodiffusion contribution reverses from outward to inward in as T_e/T_i increases and the transition from ITG to TEM occurs [27]. The same is observed for the rotodiffusion term, while pure convection is always directed inwards. Via the modelling, clear correlations have been found between these off-diagonal contributions to the turbulent boron transport and the real frequency of the most unstable mode.

Since some of the terms contributing to the turbulent particle flux depend on the impurity charge, variations are expected in the profiles of different impurities. Comparing helium, which is of interest in this work, with the heavier boron, the main difference is expected to be the thermodiffusion, which is inversely proportional to Z. Gyrokinetic modelling of the helium "ash" transport in ITER, including neoclassical transport (important within $r/\alpha < 0.1$) predicts inward directed convection, but the

diffusion is expected to be large enough to avoid helium "ash" accumulation in the core of the ITER plasma [114].

Motivated by these results and the need to have experimental verification of the theoretical predictions, in Chapter 6, helium density profiles will be compared with the boron and electron density profiles as a function of theoretically relevant parameters, such as the normalized gradients of the electron density, the ion temperature and the toroidal rotation.

4.4 Experimental studies on helium confinement, exhaust and recycling

Over the years there has been great interest to identify the properties of the transport of thermal helium (helium "ash"), with the ultimate goal being to identify a mechanism that removes the thermalised helium from the plasma, preferably without simultaneous removal of the high energy α particles. Helium confinement and helium exhaust are important issues of helium transport that will play a significant role in the operation of future fusion devices such as ITER.

During the D-T operation of TFTR, helium "ash" was found to transport rapidly from the center, where it is produced, to the plasma edge, where it is pumped [62]. Using previously calculated values for the diffusivity and convective velocity [100], the helium global confinement time τ^*_{He} was calculated to be on the order of $6 - 10\ \tau_E$, where τ_E is the energy confinement time and, therefore, in the range of what is required for continuous reactor operation, namely $7 - 15\ \tau_E$ [5]. τ^*_{He} is the mean dwell time of helium in the vessel and includes the effect of helium recycling and pumping. On the other hand, τ_{He}, without taking recycling into account, was estimated to be on the order of only two times the energy confinement time. This shows that reflux from the edge will be the limiting factor determining the removal of helium "ash" and not core transport.

In TEXTOR, Hillis et al [117] studied the transport and exhaust of helium in L-mode and in an H-mode-like regime, induced by a polarising electrode. The ALT-II toroidal belt pump limiter could completely remove the helium from the plasma, and also provided measurements of He and D_α in the limiter duct, enabling exhaust studies to be performed. Helium was puffed into the plasma to simulate the helium "ash"

and observed with charge exchange spectroscopy at two radial locations. In L-mode discharges, the puffed helium appears quickly in the plasma core and is then transported radially to the plasma boundary, where it was seen to be removed by the ALT-II pump limiter system within 1s. In the enhanced confinement discharges, however, the helium ions stay in the plasma core for much longer, two or three times longer compared to the L-mode. The ratios of global particle confinement over energy confinement time, τ^*_{He}/τ_E, was between 9 and 20 in L-mode plasmas, while it increased to ∼70 in the H-mode-like plasmas. These high values would be detrimental in future reactor operation. In connected helium transport studies in DIII-D, the helium recycling coefficient was 1 in ELM-free phases of H-mode discharges, as the helium density was observed to be constant. Giant ELMs were observed to expel helium ions from the plasma edge, leaving the core ($\rho < 0.5$) unaffected.

Helium exhaust studies in improved core confinement or internal transport barriers scenarios at ASDEX Upgrade with the LYRA divertor, showed that helium exhaust is low and does not seem to be limited by the core plasma transport [118]. Short helium gas puffs cause a simultaneous and equal increase of the helium density both inside and outside the transport barrier, which decays rather slowly with the same rate for both locations.

Finally, helium recycling provides an additional source of helium in the plasma, increasing the effective helium particle confinement time, as the recycling coefficient R (typically close to 1), enhances the particle confinement time by a factor of $1/(1-R)$. Understanding helium recycling in current and future machines is also of fundamental importance, as it relates with the capability to remove the helium "ash" from the plasma [119].

In summary, the effective particle confinement time has been found both optimistic (TFTR) and detrimental (TEXTOR H-mode-like operation) for future reactor operation. In all cases, however, recycling and reflux from the plasma edge are recognised as the critical factor for the removal of helium "ash". Even if the transport in the core is satisfactorily manipulated, this remains a decisive parameter. However, it remains outside the scope of this work.

5

The helium plume effect

Helium charge exchange measurements are hindered by the so-called "plume" effect [9], a feature which has a strong impact on the measurement and cannot be distinguished from the prompt charge exchange signal. The intensity of the plume emission line is of comparable magnitude to the intensity of the prompt emission, leading to significant overestimation of the He^{2+} density profiles.

For this reason, a forward model of the helium plume emission is required to interpret the helium charge exchange spectra correctly. In this work, a detailed model for the helium plume emission, which takes into account the diagnostic observation geometry, the reconstructed magnetic equilibrium and the appropriate atomic data, has been developed for ASDEX Upgrade.

In this chapter, the helium plume emission is described in Section 5.1. Subsequently, the helium plume model developed is presented. In Section 5.3, the dependencies of the plume emission and the ratio of plume to prompt intensity are illustrated through the modelling. The model is benchmarked against the experiment in Section 5.4. The plume emission line shape is reconstructed and the modelled plume and prompt lines are compared to the measured spectra in Section 5.5. Finally, a few remarks on the plume effect are given in Section 5.6.

5.1 The helium plume emission

Following the charge exchange reactions between fully ionized helium ions and deuterium neutrals from a neutral source (see Eq. (3.1)), a population of He^{+} ions is produced. Considering charge exchange reactions with a neutral beam, this population is born in the neutral beam volume. These He^{+} ions are reionised to fully stripped helium due to electron impact:

$$He^{+} + e^{-} \rightarrow He^{2+} + 2e^{-} \tag{5.1}$$

However, there is a finite time before the reionisation takes place, equal to $\tau_{ion}^{-1} = n_e \cdot q_{ion}^{e}(T_e, n_e)$, during which the He^{+} ions can travel along the magnetic field lines away from their birth locations. During this time there is a high probability that they are excited by electron impact (and ion, for high ion temperatures). If they are excited

back up to the n=4 state, from where they can be de-excited again down to the n=3 state:

$$\begin{aligned} He^+(n=1) + e^- &\rightarrow He^+(n=4) + e^- \\ He^+(n=4) &\rightarrow He^+(n=3) + hv(468.571nm). \end{aligned} \tag{5.2}$$

then they emit additional photons at the same wavelength as the active charge exchange signal, causing an additional contribution to the measured signal. This is the so-called helium plume emission [9]. The helium plume signal is superimposed and of comparable magnitude to the active charge exchange (prompt) signal and, as such, it disturbs the measurements and leads to overestimation of the He^{2+} density.

The prompt charge exchange emission corresponding to each diagnostic line-of-sight depends on the local He^{2+} density, as well as the local neutral beam density, and the relevant charge exchange cross sections. On the other hand, the total helium plume emission observed by one diagnostic line-of-sight is given by:

$$\Phi_{Plume} = \frac{1}{4\pi} \int_{los} n_{He^+} n_e Q^e_{exc} dl, \tag{5.3}$$

where Q^e_{exc} is the electron impact excitation coefficient. For typical ASDEX Upgrade plasmas, only electron impact excitation is relevant. However, at higher temperatures, ion impact excitation becomes important. n_{He^+} depends on the source of He^+ ions, i.e. on all the charge exchange reactions that lead to the production of He^+ ions, as well as the ionisation time which defines the lifetime of these ions in the plasma before they are ionised.

Calculation of the helium emission, therefore, requires knowledge of the He^+ density along the lines-of-sight of the diagnostic. The He^+ born in the beam volume due to charge exchange reactions must be followed along the magnetic field lines and the density of the He^+ ions at the intersection points of the magnetic field lines and the lines-of-sight has to be determined.

He^+ ions in the plasma can be produced through:

1. charge exchange of fully stripped helium with deuterium:
   $He^{2+} + H^0 \rightarrow He^+(n=4) + H^+$

2. electron recombination of He^{2+}:
   $e + He^{2+} \rightarrow He^{+(*)} + hv$

The helium plume ions are produced through the first reaction, the second one is the main driving mechanism for the passive emission.

The modelling of the helium plume emission entails the solution of the continuity equation for the transport of He^+ ions along the field lines:

$$\frac{\partial n_{He^+}}{\partial t} + \nabla(n_{He^+} v_{\parallel}) = S_{He^+} - L_{He^+}, \tag{5.4}$$

where $v_{\parallel}$ is the velocity of the plume ions along the magnetic field lines and S_{He^+} is the source of the hydrogen-like plume ions, due to the charge exchange reactions of fully ionised helium with the beam neutrals from each of the three neutral beam energy fractions plus the neutral beam halo:

$$S_{He^+} = \sum_{i=1}^{n=4} \langle \sigma v \rangle_i^{tot} \int_l n_{He^{2+}} n_b^i dl \tag{5.5}$$

and the loss mechanism L_{He^+} is the ionisation process due to electron and ion impact:

$$L_{He^+} = \frac{n_{He^+}}{\tau_{ion}}, \tag{5.6}$$

where τ_{ion} is the ionisation time. The complete set of atomic processes that contributes to the loss of helium plume ions is the following:

1. Electron impact ionisation:
   $He^+ + e \rightarrow He^{2+} + e + e$.
   This is the most important process for ASDEX Upgrade relevant parameters and the only one that has been taken into account in this work.

2. Ion impact ionisation:
   $He^+ + H^+ \rightarrow He^{2+} + e + H^+$.
   It is relevant only at higher ion temperatures, when collisions with protons are more important.

3. Charge exchange with hydrogen-like ions:
   $He^+ + H^+ \rightarrow He^{2+} + H^0$.
   This process is significant only if one of the two populations is not thermal, as higher collision energies are required.

4. Charge exchange with fully stripped helium:
   $He^+ + He^{2+} \rightarrow He^{2+} + He^+$.
   In practice, with this process, no He^+ ions are lost.

Assuming steady state conditions, i.e. $\frac{\partial n_{He^+}}{\partial t} = 0$, and that the plume ions are only allowed to move along the magnetic field lines with velocity $\upsilon_\parallel$, then Eq. (5.4) can be written as:

$$\upsilon_\parallel \frac{\partial n_{He^+}(x)}{\partial x} = \sum_{i=1}^{n=4} \langle \sigma\upsilon \rangle_i^{tot}(x) n_{He^{2+}}(x) n_b^i(x) - \frac{n_{He^+}(x)}{\tau_i}, \tag{5.7}$$

where x is defined as the coordinate along the magnetic field line. Perpendicular transport is ignored as it is negligible in comparison to the transport along the field lines.

Once the density of the He^+, i.e. $n_{He^+}(x)$ along the magnetic field lines is known, the density of the He^+ along each diagnostic line-of-sight can be evaluated at the points of intersection between the line-of-sight and the field lines. Subsequently, the plume emission for each line-of-sight can be derived from Eq. (5.3).

The plume effect for impurities other than helium

The plume effect is significant for He^{2+}, but negligible for impurities such as B^{5+} and C^{6+}. The plume contribution to the charge exchange spectra of helium and carbon can be compared by looking at the ionisation and excitation rates of He^+ and C^{5+}, for typical plasma parameters. For example, for $n_e = 8 \cdot 10^{19} m^{-3}$, $T_e = 3keV$ and $T_i = 2.7keV$, the electron impact ionisation rates for helium are 27 times higher than those of carbon. Defining the ionisation length as $\lambda_{ion} = \upsilon_{th}(T_i) \cdot n_e^{-1} \cdot q_{ion,e}(T_e, n_e)^{-1}$, where $\upsilon_{th}(T_i) = \sqrt{(2 \cdot k \cdot T_i)/m}$ is the group thermal velocity of the ions, the distance that the helium plume ions travel before being ionised is $\sim$0.063 times the distance that the carbon plume ions travel. In other words, carbon plume ions have the chance to spread along the field line, while the helium plume ions tends to be centered near the source. This also means that for the same source rate there are more carbon than helium plume ions. However, the electron impact excitation rates for He^+ are $\sim$210 times higher.

On the left hand side of Fig. 5.1, the densities of helium and carbon plume ions along a magnetic field line are compared assuming the same source of He^+ and C^{5+} ions. There are more carbon than helium plume ions (note the normalisation factor),

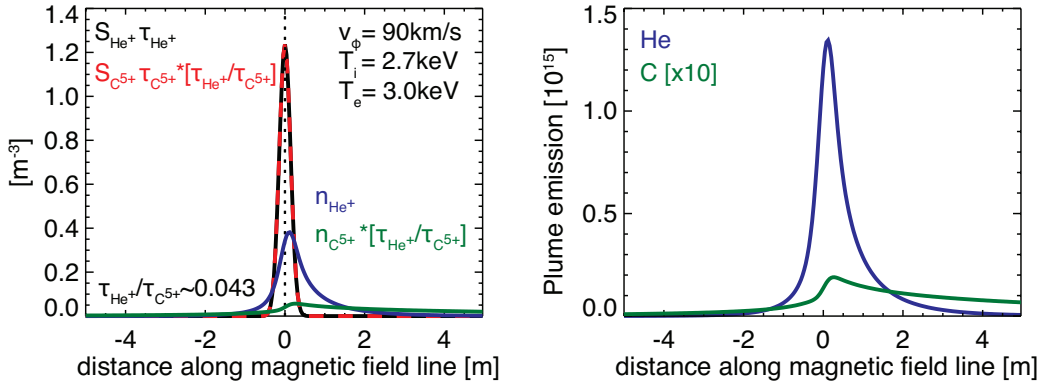

Figure 5.1: Comparison of the plume emission for helium and carbon. On the left, the distribution of helium and carbon plume ions along a magnetic field line is shown, assuming the same source of plume ions ($S_{He^+} = S_{C^{5+}}$), for typical plasma parameters. On the right, the carbon plume emission is a factor of 70 smaller than the helium plume emission.

but if one compares the plume emission along the field line shown on the right hand side, it is clear that the plume emission contribution to the carbon charge exchange spectra is negligible compared to the helium.

5.2 Modelling of the helium plume emission

As the helium plume emission is "in-phase" with the prompt, or direct active charge exchange signal, it always contributes to the helium charge exchange spectra when there is an active signal, in other words when the neutral beam is on. It cannot be subtracted using techniques such as beam modulation. For this reason, the helium plume emission has to be modelled in order to evaluate the He^{2+} charge exchange spectra correctly.

To deduce correct $n_{He^{2+}}$ profiles, it would be sufficient to know the ratio of plume to prompt emission for each line-of-sight. Assuming that one calculates the He^{2+} density at a certain location in the plasma without taking into account the helium plume effect, then this density can be corrected in the following way:

$$n_{He^{2+}}^{\text{plume}-\text{corrected}} = \frac{1}{1+R} n_{He^{2+}}^{\text{no correction}}, \tag{5.8}$$

where R is the ratio of plume to prompt emission intensities:

$$R = \frac{I_{Plume}}{I_{CX}} \tag{5.9}$$

An iterative scheme can be used to deduce the He^{2+} density, starting from an assumed input He^{2+} density profile and iterating the modelling until good agreement is found with the measured spectra (see Section 5.5).

To deduce correct T_i and v_ϕ profiles, however, more detailed information on the spatial distribution of the plume along the lines-of-sight is required, to account for the non-locality of the plume emission. Emissions originating from different locations in the plasma, with different local plasma parameters such as T_i and v_ϕ, will contribute to the charge exchange spectrum at different wavelengths. As a matter of fact, the plume ions can travel quite a distance away from the neutral beam volume before intersecting a line-of-sight, as illustrated in Fig. 5.2. Hence, a proper treatment of the plume is required to derive accurate profiles from helium spectra.

At ASDEX Upgrade, a model from the helium plume emission has been developed in the course of this work. It consists of the following steps:

First, to evaluate the prompt charge exchange and the plume emission, knowledge of a number of local plasma parameters are required. The electron temperature and density profiles are used as an input to the helium plume model and are obtained routinely from IDA (see Section 2.3.5). The ion temperature and rotation profiles are obtained from a charge exchange diagnostic that is measuring an impurity other than helium, for example boron or carbon. For these impurities the plume effect is negligible, as already discussed. The He^{2+} density is defined initially as $n_{He^{2+}} = c \cdot n_e$, where c is an initial assumption for the helium concentration in the plasma, or calculated from the measured charge exchange intensity, without taking into account the plume.

Second, the the diagnostic line-of-sight geometry and the neutral beam geometry are reconstructed. The plasma equilibrium is used to trace the magnetic field lines through the plasma, so that the distribution of the plume ions along the field lines can be determined. For each point along the line-of-sight a magnetic field line is traced around the torus.

Third, the distribution of the neutral particles in the beam volume is calculated. To this end, the forward-modelling code FIDASIM, a Monte Carlo code that models the density of the beam and beam halo neutrals [69], can be used to calculate the neutral beam attenuation, or information on the neutral beam density can be inferred from beam emission spectroscopy (see Section 2.3.11).

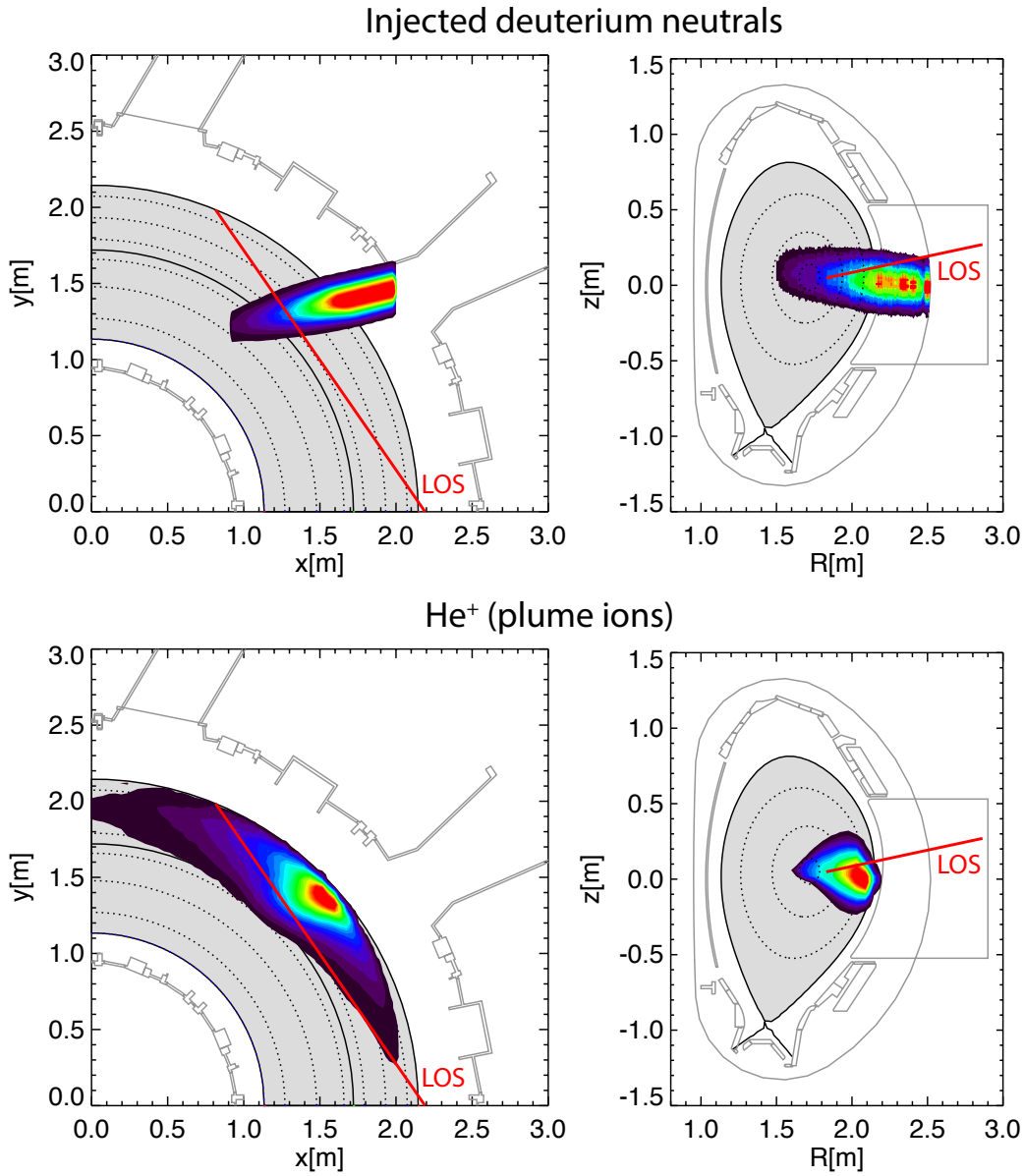

Figure 5.2: Top: The beam neutrals injected into the plasma are shown in a top-down and a poloidal view of ASDEX Upgrade together with a line-of-sight of the diagnostic. The intersection of the line-of-sight with the beam injected neutrals shows where the measured signal from the charge exchange reactions between neutral deuterium and He^{2+} ions come from. The He^{+} ions are born in the volume of the neutral beam. In the bottom, the spatial distribution of these plume ions as they spread along the field lines is depicted. Note that the line-of-sight intersects with this extended volume and, therefore, collects plume emission that originates in many different radial positions.

Fourth, the He^+ ions that are born after charge exchange of He^{2+} ions with beam atoms are calculated along the magnetic field lines that cross the beam volume.

Fifth, these He^+ ions are followed along the magnetic field lines and their loss through a number of atomic processes, electron impact ionization being the most important loss mechanism for ASDEX Upgrade relevant parameters, is evaluated. The modelling of the spread of the He^+ ions along the field lines is discussed in Section 5.2.1.

Finally, some of the He^+ ions undergo electron impact excitation in the viewing lines of the diagnostic, and the plume photon flux is derived using the appropriate photon emission coefficients, following Eq. (5.3). The emission along each line-of-sight is integrated, providing the total plume emission observed for each line-of-sight.

The atomic data needed are obtained from the ADAS database [71]. The electron impact ionisation rates and photon emission coefficients are plotted in Fig. 5.3 for typical plasma profiles. The ionisation time ${\tau_{ion}}^{-1} = n_e \cdot q^e_{ion}(T_e, n_e)$, where $q^e_{ion}(T_e, n_e)$ is the electron impact ionisation rate coefficient, and the ionisation length, defined as $\lambda_{ion} = \upsilon_{th}(T_i) \cdot n_e^{-1} \cdot q_{ion,e}(T_e, n_e)^{-1}$, where $\upsilon_{th}(T_i) = \sqrt{(2 \cdot k \cdot T_i)/m}$ is the group thermal velocity of the ions, are also shown.

5.2.1 Distribution of helium plume ions in the plasma

The transport of helium plume ions along the magnetic field lines is given by Eq. (5.4), assuming steady state conditions. The determination of the parallel velocity of the plume ions in Eq. (5.7) is non-trivial and has important repercussions for the determined plume emission. There are several approaches to determining $\upsilon_\parallel$. First, it can be assumed that all plume ions move with a single velocity equal to the thermal velocity of the He^{2+} ions. Second, the plume ions are assumed to be born with and maintain a Maxwellian distribution of velocities equal to that of the He^{2+} in that location. Lastly, a Monte Carlo approach can be used to determine the distribution of He^+ with different energies along the magnetic field line. These concepts and their merits or drawbacks with respect to the modelling of the helium plume emission are discussed here.

With the first assumption, the plume ions move in both directions along the magnetic field line from the birth location with a velocity $\upsilon_\parallel = \upsilon_{th}$ in both the positive

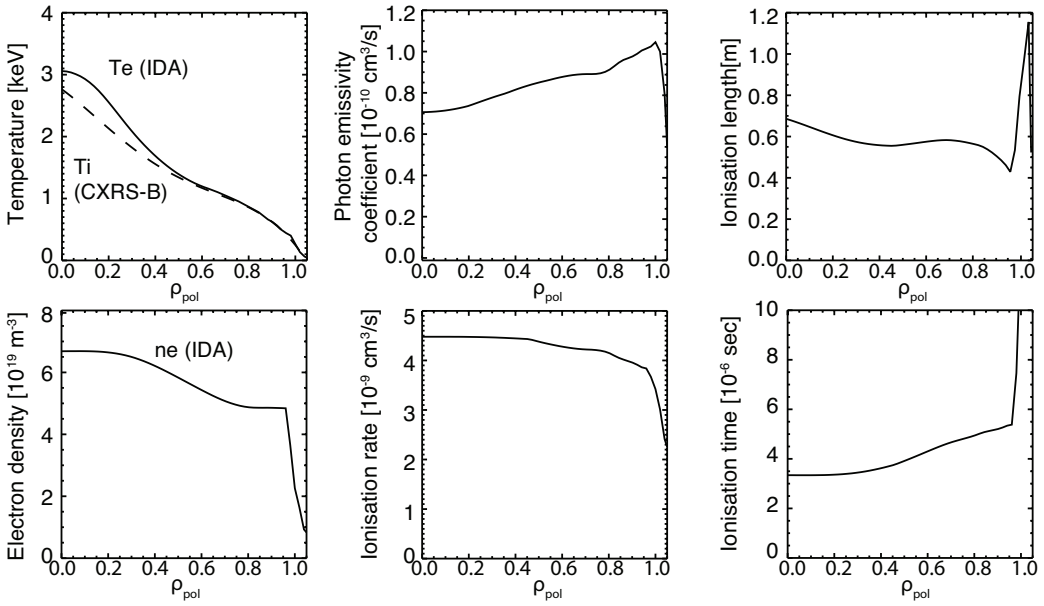

Figure 5.3: The photon emissivity coefficients and electron impact ionisation rates are shown for typical plasma parameters (AUG discharge 29083, t=2.555s). The ionisation time and ionisation length of the plume ions, assuming they have a group velocity equal to the thermal velocity, are also shown.

direction and negative direction. The transport continuity equation is then written as:

$$v_{\parallel}\frac{dn_{He^+}(x)}{dx} = S_{He^+}(x) - \frac{n_{He^+}(x)}{\tau_{ion}}, \tag{5.10}$$

for the particles moving in the positive direction and

$$-v_{\parallel}\frac{dn_{He^+}(x)}{dx} = S_{He^+}(x) - \frac{n_{He^+}(x)}{\tau_{ion}}, \tag{5.11}$$

for the particles moving in the negative direction.

Here, x is defined as the coordinate along the magnetic field line and $S_{He^+}(x)$ is the plume ion source term given by Eq. (5.5).

Due to ionisation losses, the plume ion density is assumed to attenuate exponentially along the magnetic field lines according to $n_{He^+} = c(x)\exp\left(-\frac{x}{v_{\parallel}\tau_{ion}}\right)$ where τ_{ion} is the ionisation time. Substituting this in Eq. (5.10) and solving for $c(x)$, we find that

$$c(x) = \frac{1}{v_{\parallel}}\int S_{He^+}(x')\exp\left(\frac{x'}{\tau_{ion}v_{\parallel}}\right)dx', \tag{5.12}$$

giving the following solution for the plume ions moving in the positive direction:

$$n^{pos}_{He^+}(x) = \frac{1}{\upsilon_\parallel} \exp\left(-\frac{x}{\tau_{ion}\upsilon_\parallel}\right) \int_{-\infty}^{x} S_{He^+}(x') \exp\left(\frac{x'}{\tau_{ion}\upsilon_\parallel}\right) dx', \tag{5.13}$$

where the integration extends from $-\infty$ to the point on the magnetic field line where the particles are born. Similarly, solving Eq. (5.11), the plume ions moving in the negative direction are given by:

$$n^{neg}_{He^+}(x) = \frac{1}{\upsilon_\parallel} \exp\left(\frac{x}{\tau_{ion}\upsilon_\parallel}\right) \int_{x}^{\infty} S_{He^+}(x') \exp\left(-\frac{x'}{\tau_{ion}\upsilon_\parallel}\right) dx' \tag{5.14}$$

Consequently, the density of plume ions along a magnetic field line is given by the sum of the particles moving in both directions:

$$\begin{aligned} n_{He^+}(x) =& n^{pos}_{He^+}(x) + n^{neg}_{He^+}(x) \\ n_{He^+}(x) =& \frac{1}{\upsilon_\parallel} \int_{-\infty}^{x} S_{He^+}(x') \exp\left(-\frac{x-x'}{\tau_{ion}\upsilon_\parallel}\right) dx' + \\ & \frac{1}{\upsilon_\parallel} \int_{x}^{\infty} S_{He^+}(x') \exp\left(-\frac{x'-x}{\tau_{ion}\upsilon_\parallel}\right) dx' \end{aligned} \tag{5.15}$$

However, the He^{2+} ions in the plasma have a Maxwellian velocity distribution, and it is far more realistic to assume that the He^+ ions born from the charge exchange reactions retain (at least at first) the same velocity distribution. The assumption that all plume ions have a single velocity inevitably introduces an error in the prediction of the helium plume emission, as particles with higher or lower velocities than the thermal velocity will be distributed differently along the field lines and, consequently, the probability that they are in the observation region when they are excited is different. It is, therefore, worthwhile to investigate this difference.

For the case with a Maxwellian velocity distribution, the solution to the continuity equation is again straightforward, but now an additional integration over velocities is required. The plume ion density is now $n_{He^+}(x, \overrightarrow{v})$ and the source of plume ions is given by

$$S_{He^+}(x, \overrightarrow{v}) = S_{He^+}(x) \frac{1}{\pi^{3/2}\upsilon_{th}^3} \exp\left(-\frac{(\overrightarrow{v} - \overrightarrow{\upsilon_\phi})^2}{\upsilon_{th}^2}\right), \tag{5.16}$$

where the impurity ions have a Maxwellian velocity distribution, shifted towards higher velocities due to the plasma bulk rotation υ_ϕ. As a consequence, more particles are

moving in the positive direction than in the negative direction, assuming co-current plasma rotation. Now Eq. 5.15 corresponds to:

$$\begin{aligned} n_{He^+}(x) =& n^{pos}_{He^+}(x) + n^{neg}_{He^+}(x) \\ n_{He^+}(x) =& \int_{-\infty}^{x}\int_{0}^{\infty} \frac{1}{\upsilon_\parallel}\frac{1}{\sqrt{\pi}\upsilon_{th}} S_{He^+}(x') \exp\left(-\frac{\upsilon_\parallel^2}{\upsilon_{th}^2}\right) \exp\left(-\frac{x-x'}{\tau_{ion}\upsilon_\parallel}\right) d\upsilon_\parallel dx' + \\ & \int_{x}^{\infty}\int_{-\infty}^{0} \frac{1}{\upsilon_\parallel}\frac{1}{\sqrt{\pi}\upsilon_{th}} S_{He^+}(x') \exp\left(-\frac{\upsilon_\parallel^2}{\upsilon_{th}^2}\right) \exp\left(-\frac{x'-x}{\tau_{ion}\upsilon_\parallel}\right) d\upsilon_\parallel dx' \end{aligned} \tag{5.17}$$

Examining Eq. 5.17, it can be concluded that the He^+ ions, despite being born with a Maxwellian distribution of velocities, can no longer be described by a Maxwellian distribution once they are spread along the magnetic field lines. The factor $\exp\left(-\frac{\Delta x}{\upsilon_\parallel \tau_{ion}}\right)$, where Δx is the displacement along the magnetic field line, "distorts" the Maxwellian distribution. This factor depends, not only on the location of the ion on the magnetic field line (Δx), but also on the local plasma parameters, as the ionisation time is a function of the electron temperature and density of the flux surface in which the field line lies.

This approach is a dramatic improvement over the single thermal velocity assumption. Nevertheless, this description is still not accurate enough. At ASDEX Upgrade, discrepancy in the ion temperature and rotation measurements between helium and boron or carbon is observed and is attributed to the plume emission line in the helium spectra (see also Section 5.4). The plume emission line reconstructed with this method is not "cold" or "slow" enough to explain the disagreement.

In order to get a good explanation of the spectra it is required to consider non-Maxwellian effects, similar to the approach in [120] for the halo. These effects arise because the plume particles are not quickly equilibrated with the background ions, as the momentum exchange time is much larger than the ionisation time (almost 3 to 4 orders of magnitude larger in the plasma core). As a consequence, the faster particles in the original Maxwellian velocity distribution leave the observation volume, while the slower remain and lead to apparently smaller ion temperature and rotation. An illustration of this phenomenon can be seen in Fig. 5.4, where the distribution of n_{He^+} along a magnetic field line is shown in the top plots, for a case with zero rotation and a case with a rotation of 150km/s. Assuming tangential view to the magnetic field lines, the plume ions over three different ranges in x are summed together and their

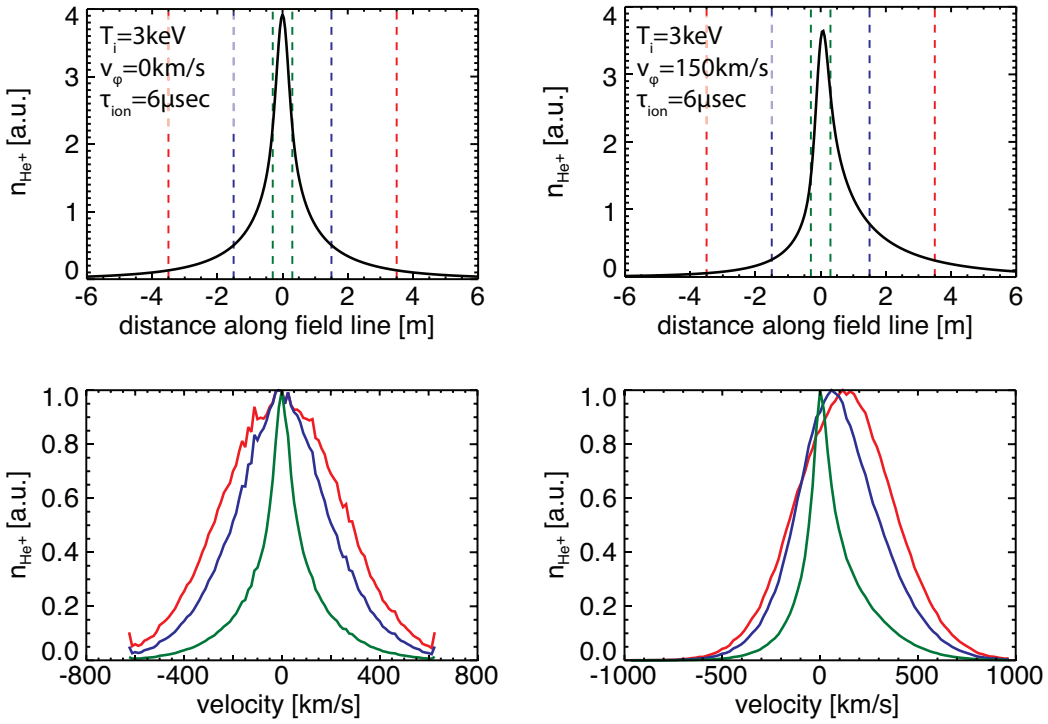

Figure 5.4: Distribution of plume ions along a magnetic field line (top plots) for zero rotation (left) or $v_\phi = 150 km/s$ (right). In the bottom, the corresponding velocity distributions of plume ions summed over the ranges indicated in the top plots.

velocity distribution is shown (normalised to one) in the bottom plots. If particles from far away are included (total distance 7m, red lines), the velocity distribution is almost gaussian. However, if the sum is over a much narrower range along the field line ($\sim 60cm$), as is the case in reality, a much narrower velocity distribution is obtained, meaning a "colder" and "slower" emission line.

To deal with this, a Monte Carlo approach can be used to describe the distribution of the plume ions along the magnetic field lines. In this case, a large number of particles is assumed to be born at a certain location on the field line. Then each of these particles is randomly assigned a velocity sampled from a Maxwellian velocity distribution. The particle is followed along the magnetic field line until its ionisation. The particle contributes to the final plume density at all positions passed by and additionally it is classified on a velocity grid. For this the original velocity is used, because the collision frequency of He^+ is much smaller than the ionisation frequency.

According to the time-of-flight of each particle, defined as the distance along the

field line from the birth location over the parallel velocity, the particle is assigned to a specific location along the magnetic field line grid and classified in a velocity grid. Again, transport perpendicular to the magnetic field lines is ignored. The Monte Carlo modelling provides not only the spread of the plume ions, but also their velocities. In other words, the kinetic effects of the plume and an accurate description of the plume ions in velocity space are obtained.

In Fig. 5.5, a source of plume ions with a Gaussian shape is plotted in comparison to the distribution of the He^+, calculated assuming that a) all the particles have a thermal velocity, b) the particles are born with a Maxwellian distribution and are transported along the field line following Eq. (5.17) and c) the particles are distributed along the field line with the Monte Carlo method. The Maxwellian velocity distribution and the Monte Carlo method give a better description of the plume ion distribution along the field line in comparison to the single thermal velocity assumption, as most of the plume emission comes from regions in or very close to the source volume. Nevertheless, the non-Maxwellian characteristics of the plume emission are not fully described with the Maxwellian distribution method. The main advantage of the Monte Carlo method lays in the more accurate description of the velocities of the plume ions, which will provide a more accurate reconstruction of the plume spectral emission and its non-Maxwellian features. This subject is discussed in Section 5.5.

All three options are implemented in the model of the helium plume described here. Since the Monte Carlo approach has been determined to be the best choice to reconstruct the helium plume emission line, this method was used for all the plume calculations in this work.

5.3 Dependence of the helium plume emission on plasma parameters and diagnostic characteristics

Both the prompt and plume emissions contributing to the charge exchange spectra depend on the local plasma parameters as well as on the neutral beam characteristics and the viewing geometry of the charge exchange diagnostic. In this section, the dependence of the helium plume emission on plasma and beam parameters is investigated through the modelling, in terms of the ratio of the plume emission integrated along each line-of-sight to the prompt emission.

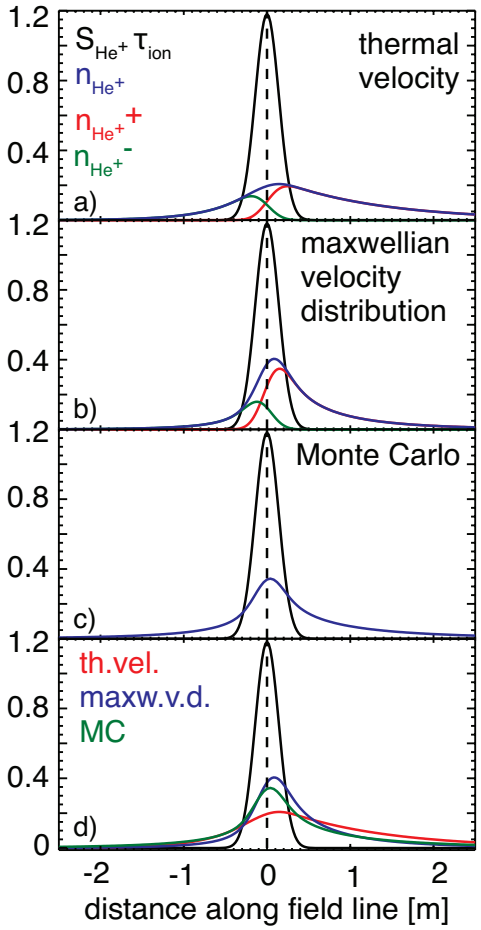

Figure 5.5: Comparison between the different methods that can be employed to model the helium plume effect: a) all plume ions are assumed to have the same thermal velocity, b) the plume ions have a Maxwellian distribution and c) the plume ions are distributed along the magnetic field line following a Monte Carlo approach. In d) the three methods are compared.

The ASDEX Upgrade discharge 29083 at 2.575s using the toroidal viewing geometry of the CER optical head is taken as the reference, unless stated otherwise. Then, different parameters are varied artificially to showcase their effect on the plume emission. While each parameter is varied the rest remain the same, as shown in Fig. 5.3, in an attempt to deconvolve the effect of the different parameters.

5.3.1 Dependence on the shape of the electron density profile

The penetration of the neutral beam in the plasma depends strongly on the plasma electron density. As the intensity of the charge exchange signal depends on the neutral beam density and the impurity density, the electron density plays a significant role in the prompt charge exchange emission. In simple words, higher plasma density means lower beam density and lower charge exchange signal (assuming all other parameters such as impurity density are the same).

The dependence of the plume emission on the electron density is not as straightforward. Starting from Eq. (5.3), the plume emission for a line-of-sight is proportional to the integral of the electron density along the line-of-sight. The electron impact excitation rates are lower with increasing electron density, but the dependence is weak. The source of He^+ plume ions depends on the charge exchange reactions taking place and therefore, the neutral beam density. If the neutral beam is more strongly attenuated, then fewer charge exchange reactions occur and fewer He^+ ions are produced. However, the ionisation time of the He^+ ions is inversely proportional to the electron density and to the electron impact ionisation rates, which in turn are weakly proportional to the electron density. Higher density in this case means shorter ionisation lengths and larger loss term of the plume ions.

Fig. 5.6 shows the effect of varying the electron density on the plume emission. A number of artificial electron density profiles, shown on the top left, are used as input to the model. All other parameters are kept constant including the He^{2+} density which is assumed to be flat ($n_{He^{2+}} = 4.e17m^{-3}$). The effect of the variations of the electron density on the prompt and plume emissions, integrated along the lines-of-sight, can be seen in the bottom left figure. For example, by comparing the cases with flat density profiles one can see that increasing electron density has a larger impact on the prompt emission than the plume. This translates into higher plume-to-prompt ratios with higher densities (see upper right figure). In addition, the gradient of the electron density profile plays a role in the comparison between the plume and prompt emission for certain lines-of-sight, as can be seen in the bottom left plot.

As the correlation of the He^{2+} density profile with the electron density gradient is an important part of the helium transport studies, it is interesting to investigate how big the mistake in the helium density and density gradient would be if the plume effect

is ignored. The He^{2+} density profile used as input is plotted with a dashed line in the bottom right figure. The solid lines correspond to the He^{2+} density profiles that would be extracted from the spectra if all of the signal was attributed to the prompt emission (in other words, ignoring the plume effect). It is observed that the gradient of the apparent helium density profile is almost the same as the gradient of the input profile within error bars (not shown). However, in terms of logarithmic normalised impurity density gradients, which will be used in the course of this work (Chapter 6), the difference in the magnitude (approximately a factor of 2) is the main player.

5.3.2 Dependence on the He^{2+} density profile and concentration

The concentration of He^{2+} in the plasma is not expected to alter the expected plume-to-prompt intensity ratio (see Fig. 5.7), as both the plume and prompt emissions will scale together in the same way. However, the shape of the He^{2+} density profile plays an important role in the plume emission that is observed at each radial location. As an example, the He^{2+} profile has been assumed to be flat, hollow and peaked, while the electron density has been assumed flat. These input He^{2+} density profiles are plotted with dashed lines on the left graph of Fig. 5.8. The calculated plume-to-prompt intensity ratios can be seen on the right graph. The apparent He^{2+} density profiles if the plume effect was ignored are shown with solid lines on the left figure.

To assess the error that would occur if the plume effect were not taken into account, the normalised logarithmic gradient of the input He^{2+} density profiles (dashed lines) are compared with the gradients of the apparent profiles (solid lines). The flat input profile appears to be slightly peaked (apparent gradient at $\rho_{tor} = 0.35$ $R/L^{app}_{n_{He^{2+}}} = 0.10$), while the hollow profile appears less hollow ($R/L^{app}_{n_{He^{2+}}} = -1.72$ instead of $R/L^{true}_{n_{He^{2+}}} = -2.05$). The peaked profile with $R/L^{true}_{n_{He^{2+}}} = 1.42$ appears less peaked ($R/L^{app}_{n_{He^{2+}}} = 1.24$), while the most peaked profile with $R/L^{true}_{n_{He^{2+}}} = 1.66$ appears even more peaked ($R/L^{app}_{n_{He^{2+}}} = 1.90$). It is, therefore, clear that the helium plume effect should be taken into account when evaluating helium density profiles and it is not simple to estimate the effect of the plume on the gradient without a proper calculation.

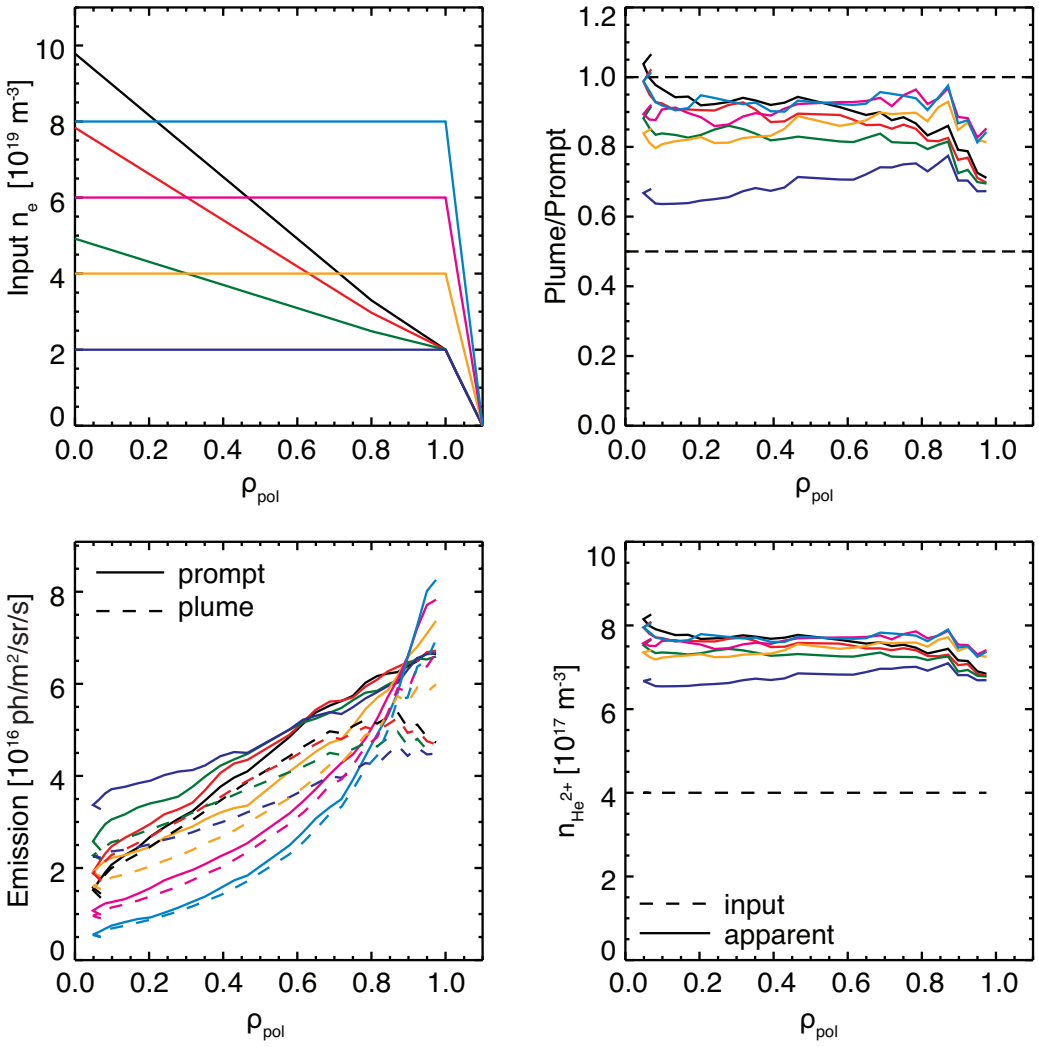

Figure 5.6: Dependence of the plume (and prompt) emission on variations in the electron density profile. On the top left, the electron density profiles used as input for the helium plume model are shown. All other parameters are constant and taken from discharge 29083 (t=2.575s). On the top right, the resultant plume-to-prompt ratio is given. The prompt and plume emissions integrated along the lines-of-sight can be compared in the bottom left figure. In the bottom right, the input He^{2+} density profile is compared to the He^{2+} that would be derived from the spectra if the plume contribution was ignored.

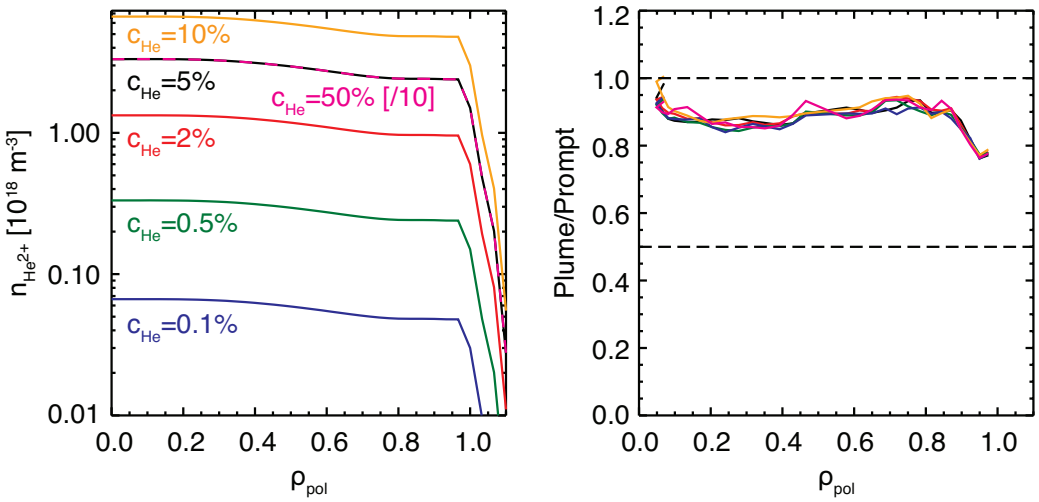

Figure 5.7: Almost no dependence on the He^{2+} concentration in the plasma (He^{2+} density profiles shown on the left) is found in terms of plume-to-prompt ratio, shown on the right. The calculations are performed for the plasma parameters of discharge 29083, t=2.575s.

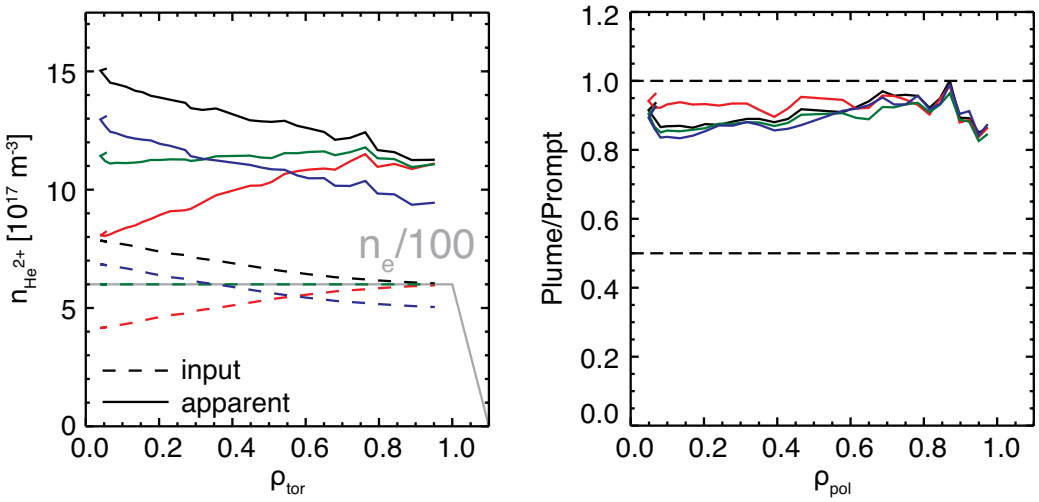

Figure 5.8: Dependence of the plume-to-prompt ratio, shown on the right, on the gradient of the He^{2+} density profile, assuming a flat electron density profile.

5.3.3 Dependence on the shape of the toroidal rotation profile

A similar approach was followed in order to investigate the dependence of the plume emission on the toroidal rotation. The plasma rotation influences the spread of the plume ion cloud away from the neutral beam volume. Therefore, it strongly influences, indirectly, the probability that they are excited to the n=4 state while still in the region of the lines-of-sight.

Artificial rotation profiles, shown in the top left figure in Fig. 5.9, are used as inputs to the model, keeping all other plasma parameters constant. A counter-current ("reverse") plasma rotation is also assumed (grey profile). The prompt and plume emission integrated for each line-of-sight are shown in the bottom left figure, while the plume-to-prompt ratios are shown in the top right figure. Small variations are observed in the prompt emission, which can be explained by the fact that the plasma rotation also affects the distribution of the beam neutrals in the plasma, albeit in a limited way.

The effect on the helium plume emission is also small, and the plume-to-prompt ratio is roughly the same for all cases. However, the plume emission along the line-of-sight is not necessarily the same. This becomes clear if one looks into the distribution of the helium plume ions along the magnetic field lines and along the lines-of-sight.

The distribution of the plume ions along a line-of-sight and along a magnetic field line is shown in Fig. 5.10. The colors corresponds to the profiles of Fig. 5.9. On the left figure, it can be seen that the distribution of He^+ is different for different rotation profiles. The location $x = 0$ along the field line corresponds to the intersection of the field line with the line-of-sight. On the right, the distribution of He^+ ions along the line-of-sight is plotted, while the dotted line identifies the point of the line-of-sight from which the magnetic field line has been traced. Despite the differences in the distribution of the plume ions, the integrated emission along a line-of-sight is very similar. This means that the toroidal rotation is not important for the derivation of accurate He^{2+} density profiles, but it is important for correctly reproducing the spectra and hence deriving correct ion temperature and rotation profiles from the helium spectra.

Note that the input helium profile in this case is not flat as in in the previous section and as a result a clearer difference in the gradient is observed. Here, the apparent helium profile has a factor of 2 larger gradient than the input profile.

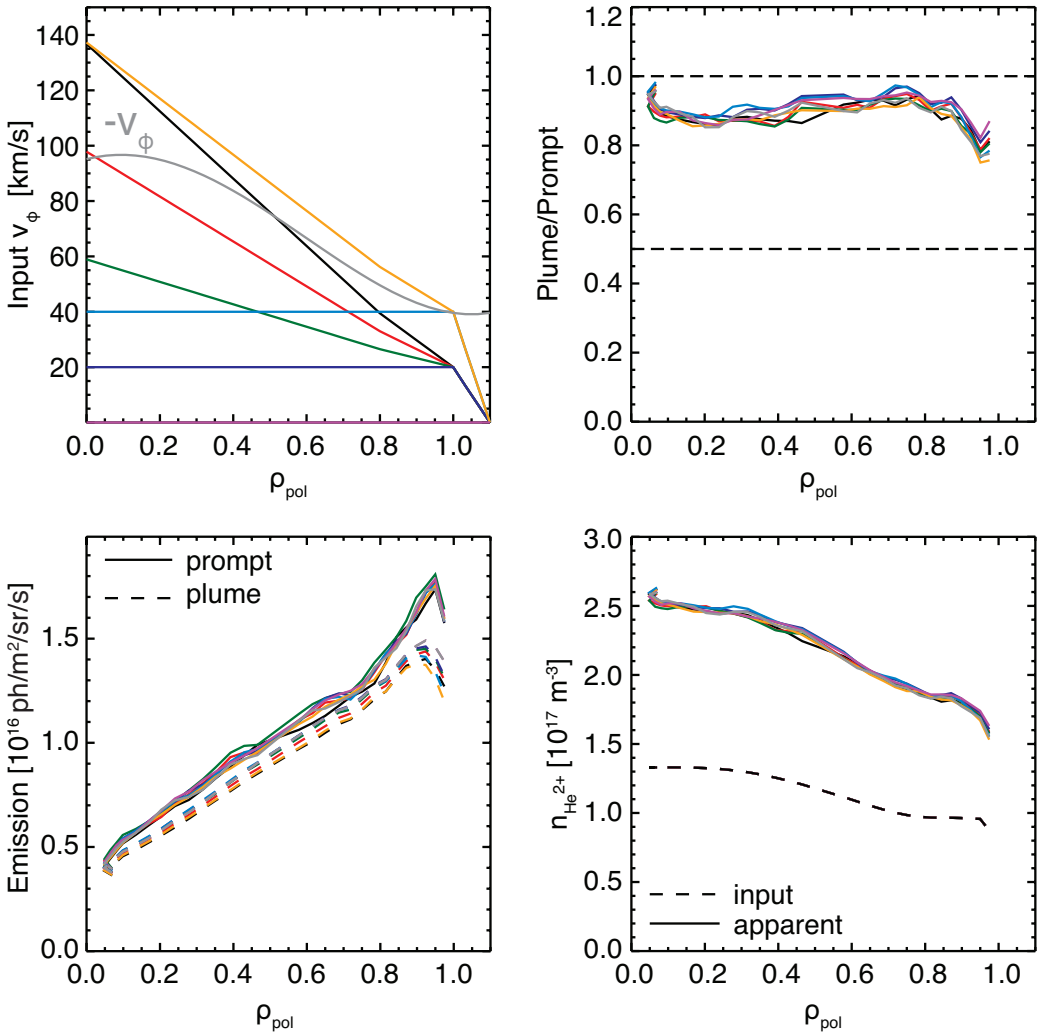

Figure 5.9: Dependence of the plume (and prompt) emission on variations in the toroidal rotation profile. On the top left, the rotation profiles used as input for the helium plume model, while keeping all other parameters the same, are shown. On the top right, the plume-to-prompt ratio is given. The prompt and plume emissions integrated along the lines-of-sight can be compared in the bottom left figure. In the bottom right, the input He^{2+} density profile (dashed line) is compared to the He^{2+} that would be derived from the sum of the plume and prompt emission, i.e. if the plume contribution to the spectra were ignored.

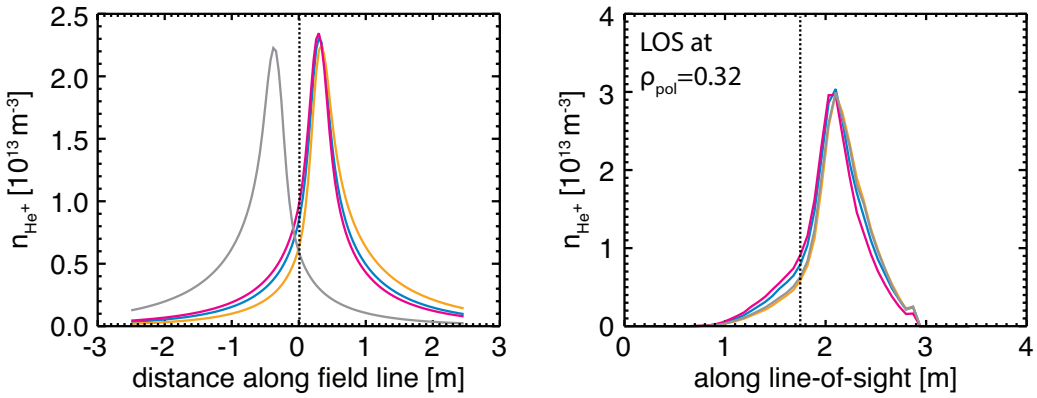

Figure 5.10: The effect of the toroidal rotation value on the distribution of the plume ions along the magnetic field line (left) and along a line-of-sight (right) is showcased for an example line-of-sight and an example field line traced from this line-of-sight. The vertical dotted lines correspond to the intersection between line-of-sight and field line.

5.3.4 Dependence on the neutral beam energy

The ASDEX Upgrade neutral beam injectors are routinely operated at full voltage (60kV for injector 1 and 93kV for injector 2), but lower voltages are possible. Operating the neutral beams at lower voltage means larger beam attenuation and also a lower particle flux. Furthermore, the charge exchange rates are lower for lower beam energy (for energies below the maximum in the rates). The partial charge exchange cross-sections for the HeII n=4-3 transition, however, fall more rapidly with the decrease in beam energy than the total charge exchange cross-sections do (see Fig. 3.6). Consequently, as mentioned also in [9], the plume-to-prompt intensity ratio will be higher for lower beam energies.

To illustrate this the voltage of the neutral beam was varied in the model, in order to observe the effect on the plume-to-prompt ratio and the results are shown in Fig. 5.11. Real parameters of the ASDEX Upgrade NBI source #3 were used, so that realistic particle fluxes and species mix could be used. The particle flux of NBI source 3 is $3.5 \cdot 10^{20}$ particles/s when the NBI voltage is 58kV and drops to $3.2 \cdot 10^{20}$ at 47kV. The species mix (E/1:E/2:E/3) is also different for different beam voltages, namely 0.39:0.35:0.26 at 47kV, instead of 0.46:0.37:0.17 at 58kV. As expected, the voltage reduction affects the intensity of the prompt emission more strongly than that of the plume emission.

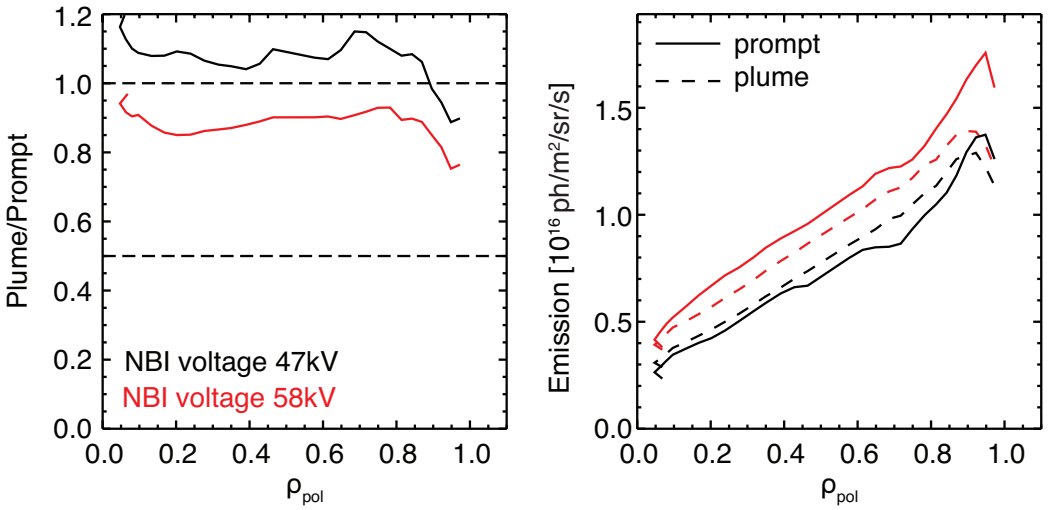

Figure 5.11: The plume-to-prompt emission ratio as well as the prompt and plume emissions are compared for two different neutral beam injection voltages, 58kV and 47kV, which are within the operational range of the ASDEX Upgrade neutral beam injection systems, including the full, half and third energy components and the beam halo.

5.3.5 Dependence on the neutral beam halo

Taking into consideration the beam halo neutrals for the evaluation of impurity density profiles from the charge exchange emission intensity is very important, as already discussed in Section 3.1. In Fig. 5.12, the expected intensity of the prompt emission for a helium concentration of 0.2% and for the plasma and beam parameters of discharge 29083 at 2.575s, taking into account the charge exchange of fully stripped helium with the beam halo neutrals (blue solid line) is shown. In comparison with the prompt emission intensity expected if the beam halo is ignored, it is found that the difference is significant ($\sim 15\%$ at the edge).

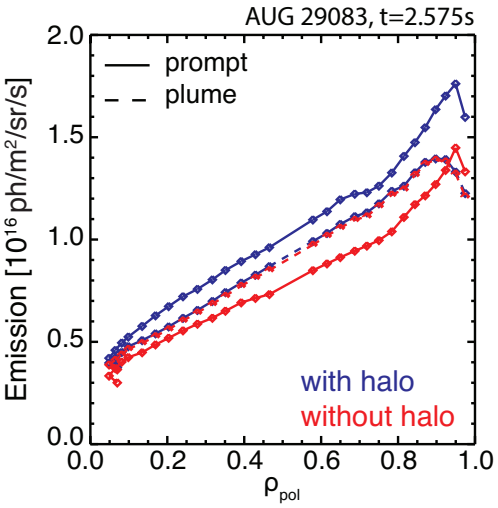

Figure 5.12: The effect of including the neutral beam halo in the modelling of the prompt and the plume emission.

The difference is not as large for the plume emission intensity as for the prompt

emission. The thermal charge exchange is not sensitively influencing the total charge exchange rates, but it does influence the charge exchange rates into $n = 4$ and thus the charge exchange photon emission.

Hence, the halo is very important for determining correct helium density profiles as it plays an important role in interpreting the prompt signal, but it is almost unimportant for the plume analysis. In this work, the beam halo is always taken into account.

5.3.6 Dependence on the diagnostic observation geometry

The observation geometry of the diagnostic defines how much the helium plume emission pollutes the spectra. Diagnostic lines-of-sight that are parallel or almost parallel to the magnetic field lines, i.e. with toroidal observation geometry, will observe higher levels of plume emission than lines-of-sight viewing the neutral beam perpendicularly to the magnetic field lines, i.e. with purely poloidal observation geometry. Nevertheless, as the plume emission is localised close to the actual measurement location (in and close to the neutral beam volume), even purely poloidal observation geometries have to deal with a significant amount of plume emission in the spectra.

To illustrate the significance of the observation geometry, the plume emission corresponding to a variety of geometries has been calculated. In addition to the existing optical heads CER and CFP, three artificial optical heads with different observation angles in relation to the magnetic field lines have been tested; an optical head that observes the neutral beam vertically from the top of the torus, an observation geometry with lines-of-sight with zero poloidal angle and an optical head located in between the existing optical heads CER and CFP. All of the lines-of-sight, both real and artificial, are shown in Fig. 5.13. Once again, the plasma parameters from discharge 29083, t=2.575s are used as input.

The intensity of the prompt emission observed by each diagnostic geometry depends on the path through the neutral beam, which has a finite width. The plume intensity depends on the path through the plume ion cloud. In Fig. 5.14, the plume-to-prompt intensity ratio is found to depend on the observation geometry as expected. The prompt and plume emissions are compared in the top right figure, while the path of an example line-of-sight (at $\rho_{pol} = 0.13$) from each optical head though the plume cloud is shown in the bottom right figure.

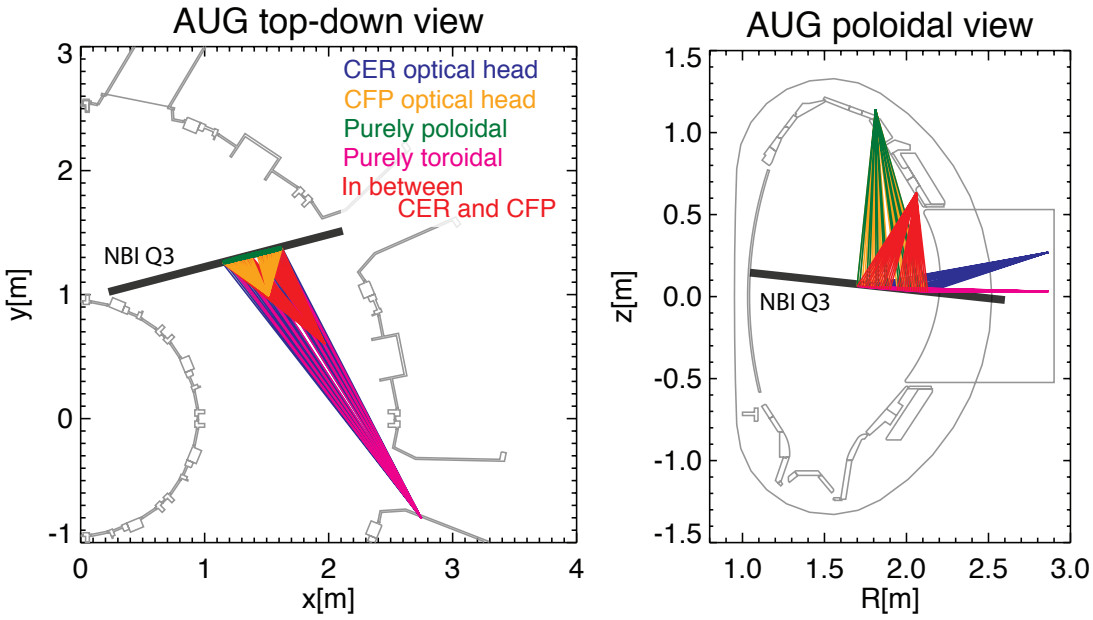

Figure 5.13: In addition to the existing optical heads CER and CFP, three artificial optical heads with different observation angles in relation to the magnetic field lines are tested; an optical head that observes the neutral beam vertically from the top of the torus, an observation geometry with lines-of-sight with zero poloidal angle and an optical head located in between the existing optical heads CER and CFP. The plume emission that is expected to be collected for these observation geometries can be seen in Fig. 5.14.

Note that a q scan is in principle equivalent to scanning the geometry of the lines-of-sight and for this reason the q scan is omitted here.

In summary, the poloidal observation geometries are much less hindered by the plume effect in comparison to predominantly toroidal views. Even so, the plume emission contributing to the spectra is not negligible and should be taken into account.

5.3.7 Dependence on the electron and ion temperature

Both the ion and electron temperature profiles play a role in the plume emission contributing to the helium charge exchange spectra. Again here, various artificial electron and ion temperature profiles are used as input to see the effect on the plume-to-prompt intensity ratio. Either the electron or the ion temperature is varied, keeping the other plasma parameters constant (discharge 29083, t=2.575s) and the results are shown in Fig. 5.15 and 5.17.

The ion temperature defines the width of the Maxwellian distribution of velocities

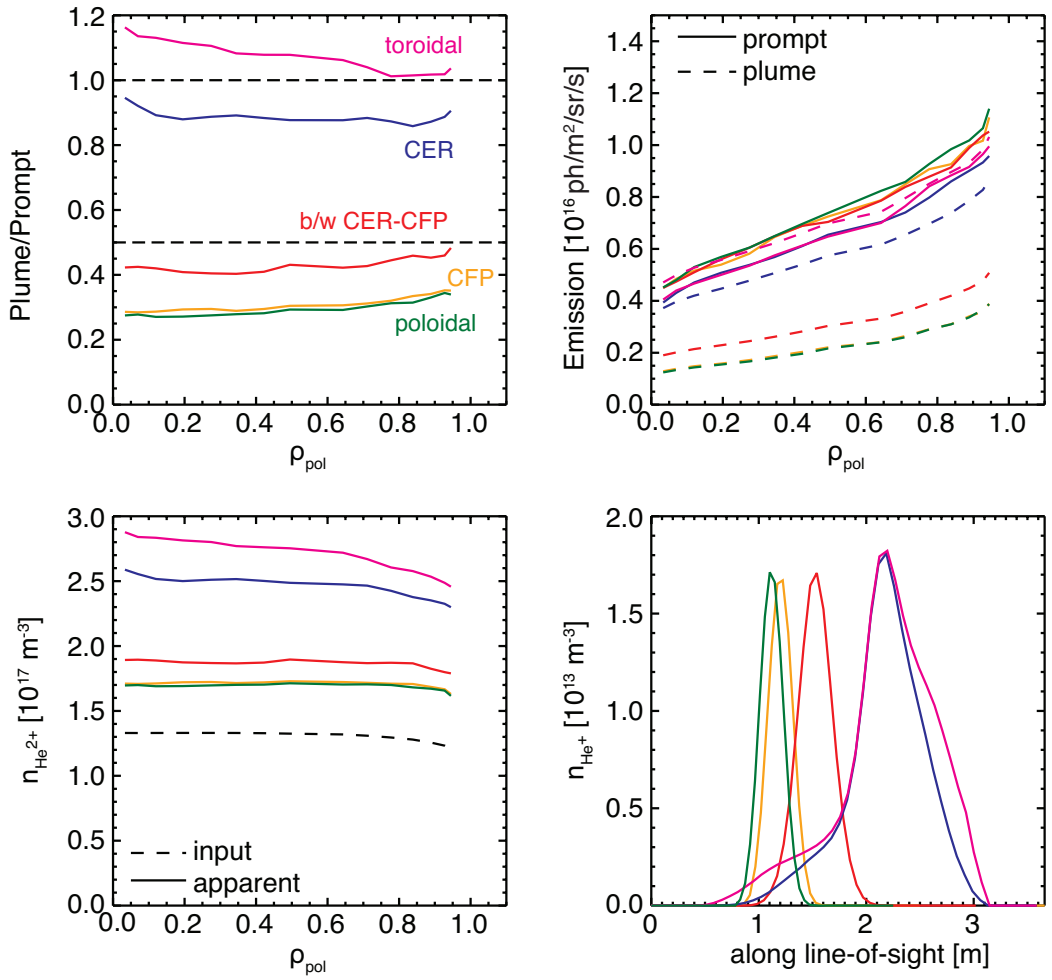

Figure 5.14: Dependence of the plume (and prompt) emission on the observation geometry. On the top left, the plume-to-prompt ratio for the specified optical heads and line-of-sight shown in Fig. 5.13 is given. The prompt and plume emissions integrated along the lines-of-sight can be compared in the top right figure. The input He^{2+} density profile used as input in the code is compared to the He^{2+} that would be derived from the sum of the plume and prompt emission, if the plume contribution to the spectra was ignored, is shown in the bottom left figure. The plume emission seen by the 5th line-of-sight for each of the observation setups is shown in the bottom right figure.

with which the plume ions are assumed to be born, and consequently defines their spread along the magnetic field lines. This can be seen in Fig. 5.16. Looking at Fig. 5.15, the trend is that the higher the ion temperature the lower the plume emission intensity.

In addition, both the ionisation rate and the photon emission coefficients depend on the local electron temperature. The ionisation rates show a maximum at approximately

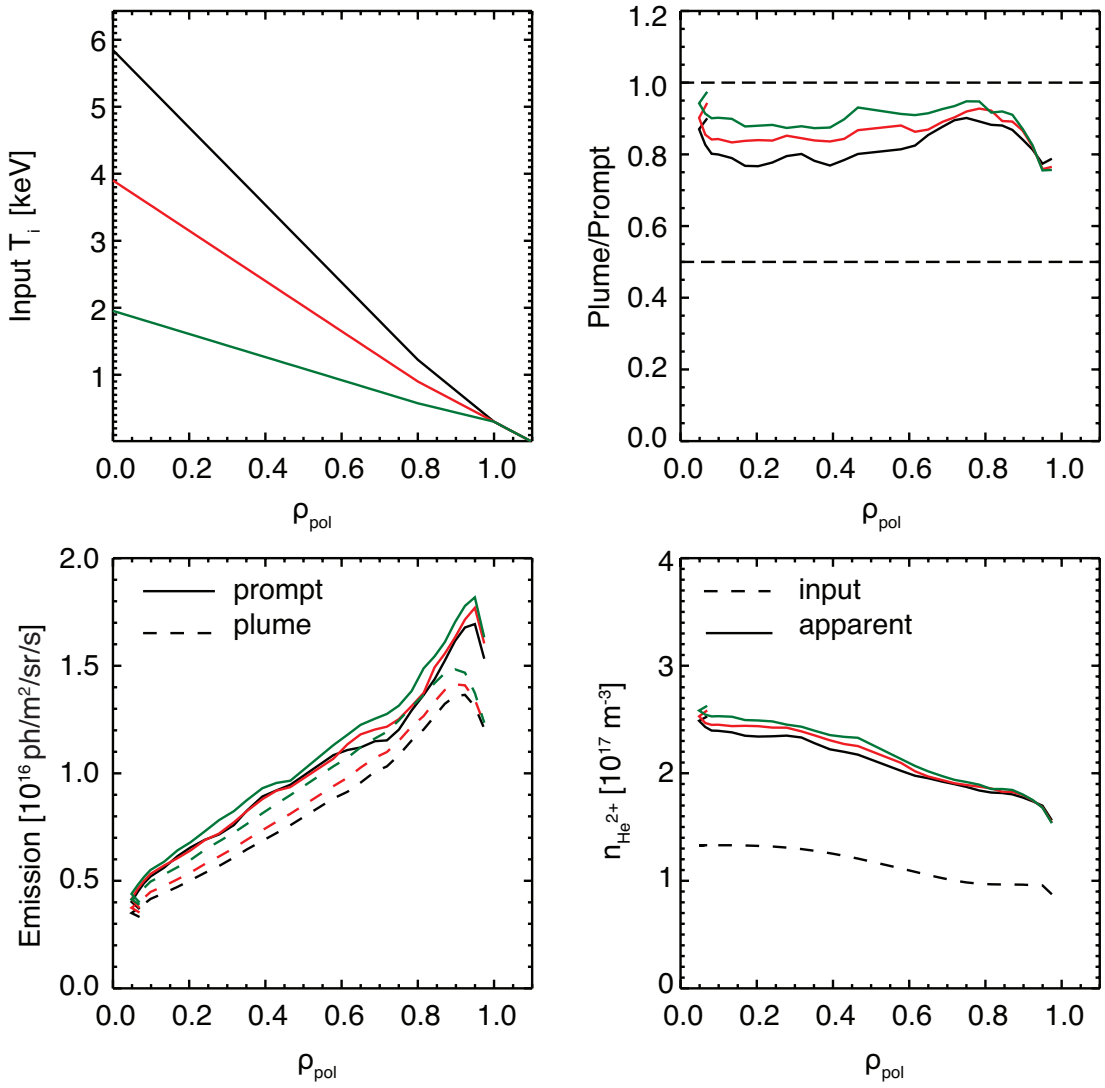

Figure 5.15: Dependence of the plume (and prompt) emission on variations in the ion temperature profile. On the top left, the ion temperature profiles used as input for the helium plume model, while keeping all other parameters the same, are shown. On the top right, the plume-to-prompt ratio for the specified lines-of-sight is given. The prompt and plume emissions integrated along the lines-of-sight can be compared in the bottom left figure. The input He^{2+} density profile used as input in the code (dashed line) is compared to the He^{2+} that would be derived from the sum of the plume and prompt emission, if the plume contribution to the spectra were ignored.

500eV and drop with higher electron temperatures. This means that the higher the electron temperature, the smaller the ionisation rate and, therefore, the ionisation time becomes larger. However, the electron impact excitation rates for the n=4-3 transition

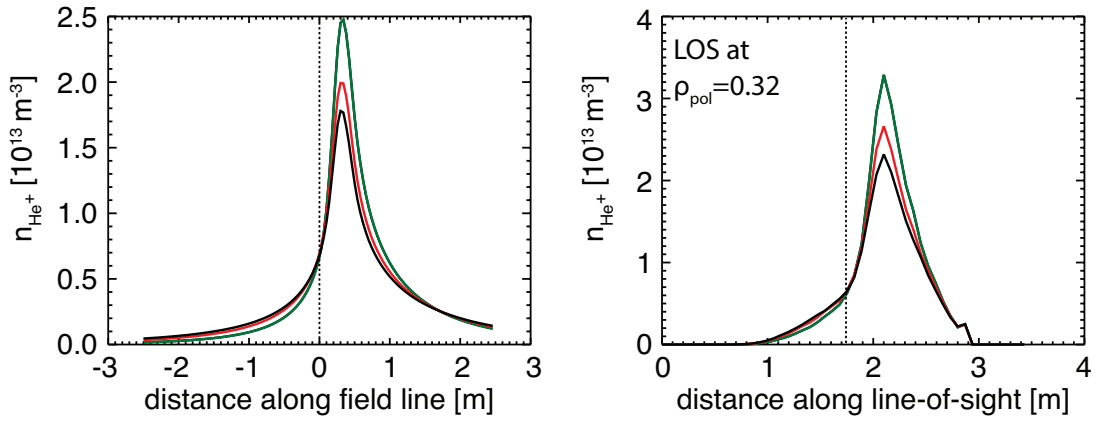

Figure 5.16: The effect of the ion temperature on the distribution of the plume ions along the magnetic field line (left) and along a line-of-sight (right) is showcased for an example line-of-sight and an example field line traced from this line-of-sight. The vertical dotted lines correspond to the intersection between line-of-sight and field line. Colors correspond to the profiles shown in Fig. 5.15.

show a maximum at approximately 200eV and drops for higher electron temperatures, which translates into a smaller probability that these plume ions are excited due to electron impact. The drop in the photon emission coefficients is stronger than the drop of the electron impact excitation rates for the n=4-3 with increasing electron temperature. It can generally be stated that higher electron temperature means lower plume emission intensity, which can be seen in the bottom left plot of Fig. 5.17.

5.3.8 Conclusions

The helium plume emission is determined by a complicated interplay between the plasma and beam parameters, the magnetic equilibrium and the diagnostic observation geometry. This sensitivity study sheds light on parameters that can affect the plume emission. The diagnostic geometry is a critical factor that can vary significantly the contribution of the plume emission to the spectra, though it can never be completely avoided. In addition, a strong variation of the plume-to-prompt ratio is observed with the neutral beam voltage [9]. The electron density profile affects the apparent He^{2+} density profile. However, a significant parameter that defines the plume emission contributing to the charge exchange spectra is the He^{2+} profile itself, especially its gradient, which is also the unknown in the modelling. Because of this, comparison with the measured spectra and iteration of the plume emission calculation is required.

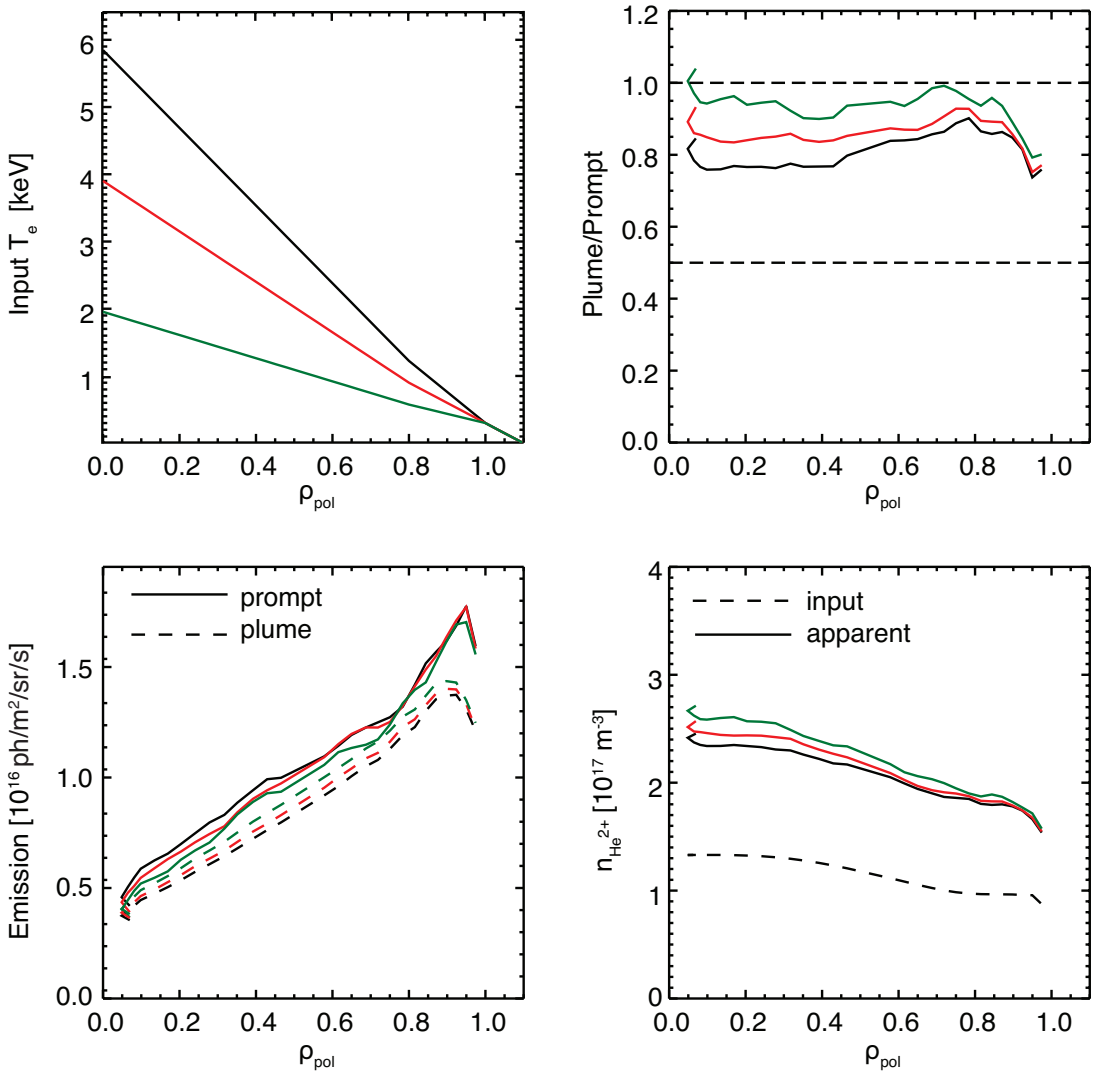

Figure 5.17: Dependence of the plume (and prompt) emission on variations in the electron temperature profile. On the top left, the electron temperature profiles used as input for the helium plume model, while keeping all other parameters the same, are shown. On the top right, the plume-to-prompt ratio for the specified lines-of-sight is given. The prompt and plume emissions integrated along the lines-of-sight can be compared in the bottom left figure. The input He^{2+} density profile used as input in the code (dashed line) is compared to the He^{2+} that would be derived from the sum of the plume and prompt emission, if the plume contribution to the spectra were ignored.

5.4 Experimental investigation of the helium plume effect

The existence of the helium plume emission in ASDEX Upgrade plasmas can be identified experimentally in two ways. First, via a comparison of the T_i and v_ϕ profiles derived from the helium charge exchange measurements and those derived from measurements on boron or carbon. Due to the plume emission, disagreement is expected, since the helium plume emission originates from colder and slower plume ions belonging to a different part of the velocity space (see Fig. 5.4). Second, by a comparison of apparent helium density profiles from different geometries. The He^{2+} density profiles derived from the charge exchange measurements without any treatment of the plume effect are expected to vary between different observation geometries, as the plume-to-prompt intensity ratio depends on the diagnostic observation geometry (see Section 5.3.6). Both of these indications for the plume are observed at ASDEX Upgrade. For example, in Fig. 5.18, the ion temperature and rotation profiles from helium and boron are compared for ASDEX Upgrade discharge 29083 at 3.8s.

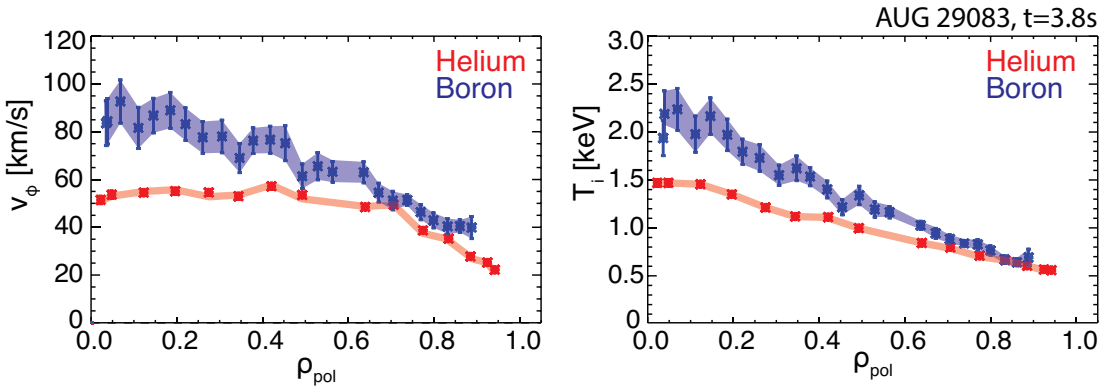

Figure 5.18: Comparison of rotation and ion temperature profiles obtained from measurements on helium and on boron. Strong discrepancies are observed, especially in the plasma core. The passive emission has been subtracted from the spectra.

The discrepancies in the ion temperature and rotation profiles are due to the non Gaussian shape of the plume emission line that is part of the measured helium spectra. The shape of this line depends strongly on the velocity, ion temperature and ionisation time of the plume ion population that contributes emission to the measurement. The plume emission line in the core will be wider, due to the higher temperature of the plume ions, and shifted more to higher wavelengths than the plume emission line at

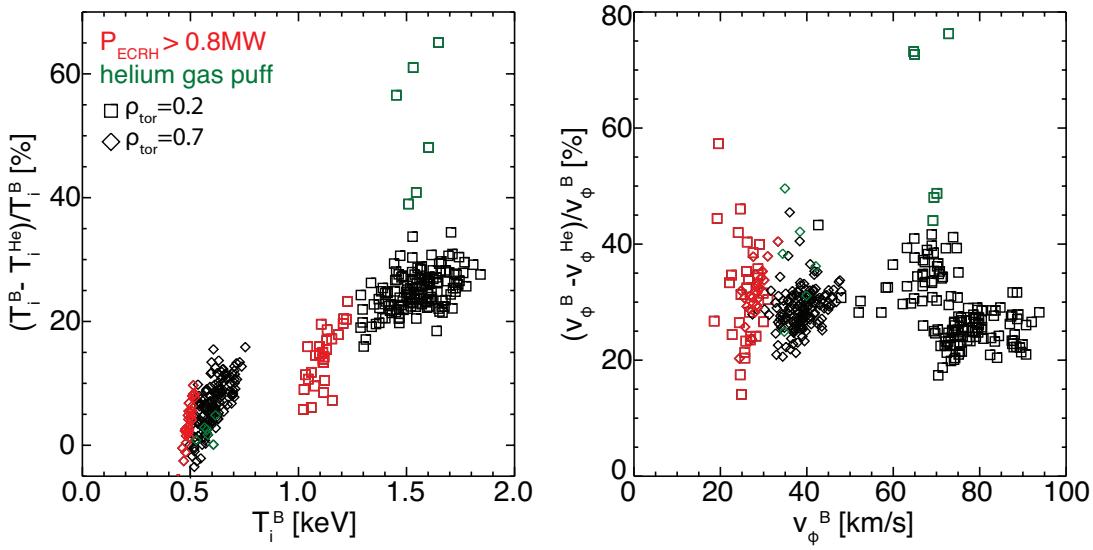

Figure 5.19: Comparison of toroidal rotation and ion temperatures at $\rho_{tor} = 0.2$ and $\rho_{tor} = 0.7$ derived from helium and boron charge exchange measurements for all measurement time points in discharge 29083. Time points with additional ECRH power or close to a helium puff are indicated.

the edge. Due to the fact that an additional passive contribution from the plasma edge complicates the analysis, all investigations have been performed with beam modulation in order to unambiguously remove the passive emission line.

An overview of how strong this discrepancy due to the plume can be is obtained by plotting the difference of the T_i and v_ϕ values obtained from the percentage of the T_i and v_ϕ values obtained from boron. In Fig. 5.19, all the time points from discharge 29083 are plotted. The time points during which additional ECRH power is applied and the time points close to a helium puff are identified. This discrepancy arises from the plume emission line in the spectra which results from a complicated interplay of plasma parameters. A larger discrepancy between the two ion temperature measurements is observed in time points close to a helium puff, which can be attributed to the change in the shape of the He^{2+} density profile. Smaller discrepancies in the ion temperature are observed in the phases with additional ECRH, which shows that as plasma parameters change, the spectral emission line changes as well by the interplay of lower v_ϕ, lower T_i and higher T_e. At outer regions of the plasma, the discrepancies are still significant, especially for the rotation measurements.

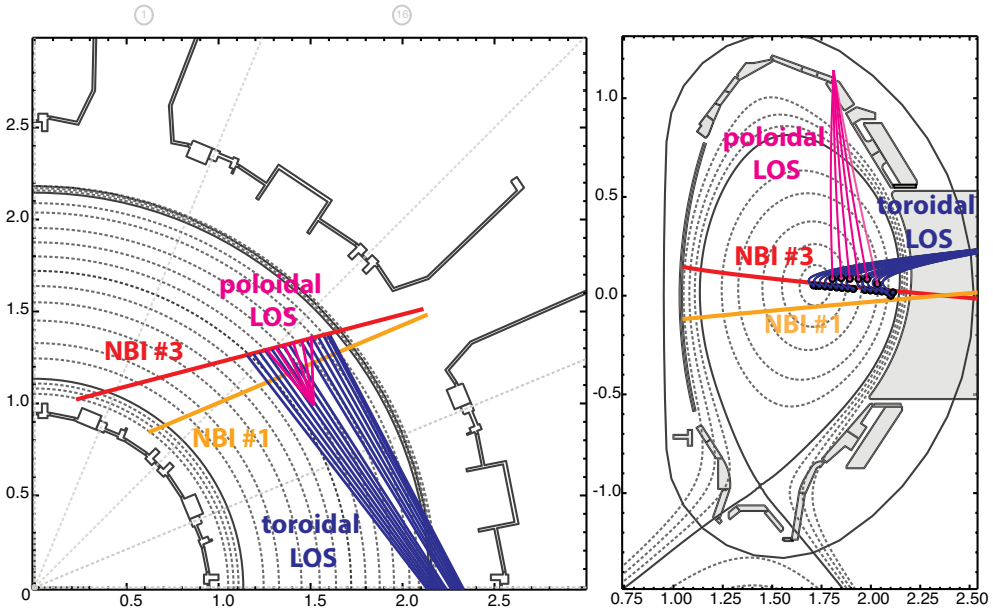

Figure 5.20: Top down and poloidal view of ASDEX Upgrade, with the geometry of the two sets of LOS and the two beam sources used in the experiment.

Plasma discharge 29083 was specifically designed to benchmark the helium plume model presented here. In this discharge, the helium spectra were measured using the high etendue spectrometer described in Chapter 3 [79]. The spectrometer was connected to two optical heads: one with predominantly toroidal LOS and one with more poloidal LOS, all focussed on neutral beam source Q3 (see Fig. 5.20). The plume-to-prompt intensity ratio is expected to be different for these two observation geometries, as the path through the plume ion cloud is different.

The time traces of the most relevant plasma parameters during the discharge are shown in Fig. 5.22. The experimental discharge was planned to have as stable plasma conditions as possible. In addition, a specific scheme was implemented for the injection of neutral beams. The neutral beam source (Q3) on which the helium and boron charge exchange measurements were performed was modulated so that the passive emission could be subtracted using the off-beam frames. The input power was kept constant by supplementing Q3 with a source (Q5) on the other side of the torus. It should be noted here that no plume ions originating at sources injected at the other side of the torus (namely sources Q5-Q8) are expected to reach the spectrometer lines-of-sight.

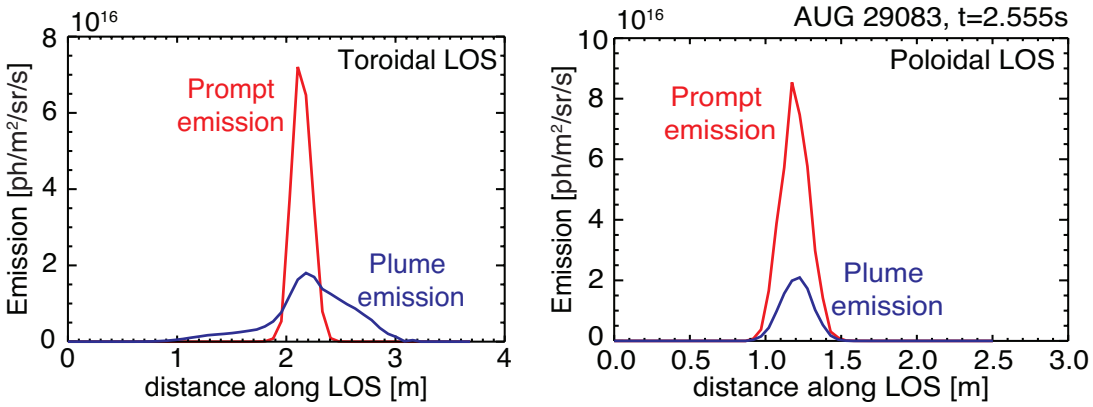

Figure 5.21: Plume and prompt emission along a toroidal and a poloidal line-of-sight.

As an additional check, NBI source Q3 was replaced by NBI source Q1, for several phases of the plasma discharge. NBI Q1 (also shown in Fig. 5.20) is more radial than NBI Q3 and is situated below the toroidal lines-of-sight. Short helium gas puffs were injected from a midplane valve, to increase the helium content and vary, albeit slightly, the shape of the helium density profile.

In Fig. 5.23, the He^{2+} density profiles derived without taking into account the plume effect are shown on the left for both sets of lines-of-sight. It is observed that the experimental density profiles measured by the poloidal and the toroidal lines-of-sight do not agree. This is expected as the lines-of-sight have different geometries in relation to the magnetic field lines and the neutral beam and are therefore affected by the plume differently. The plume-to-prompt ratio for the toroidal lines-of-sight when NBIQ3 is on is higher than the corresponding ratio for the poloidal lines-of-sight, as the path of the poloidal lines-of-sight through the plume cloud is smaller than for the toroidal ones (see also Fig. 5.24). In Fig. 5.21, the predicted prompt and plume emissions collected along a line-of-sight are compared. The plume emission collected from a poloidal line-of-sight is more localised and originates from the same volume as the prompt emission. The toroidal line-of-sight, however, tranverses a longer path through the plume and, therefore, plume emission is collected from an extended region.

Furthermore, the density profiles measured on NBI Q3 and NBI Q1 are also different, despite the fact that the plasma parameters are very similar. When NBI Q1 is on instead of NBI Q3, the situation changes. The toroidal lines-of-sight are above

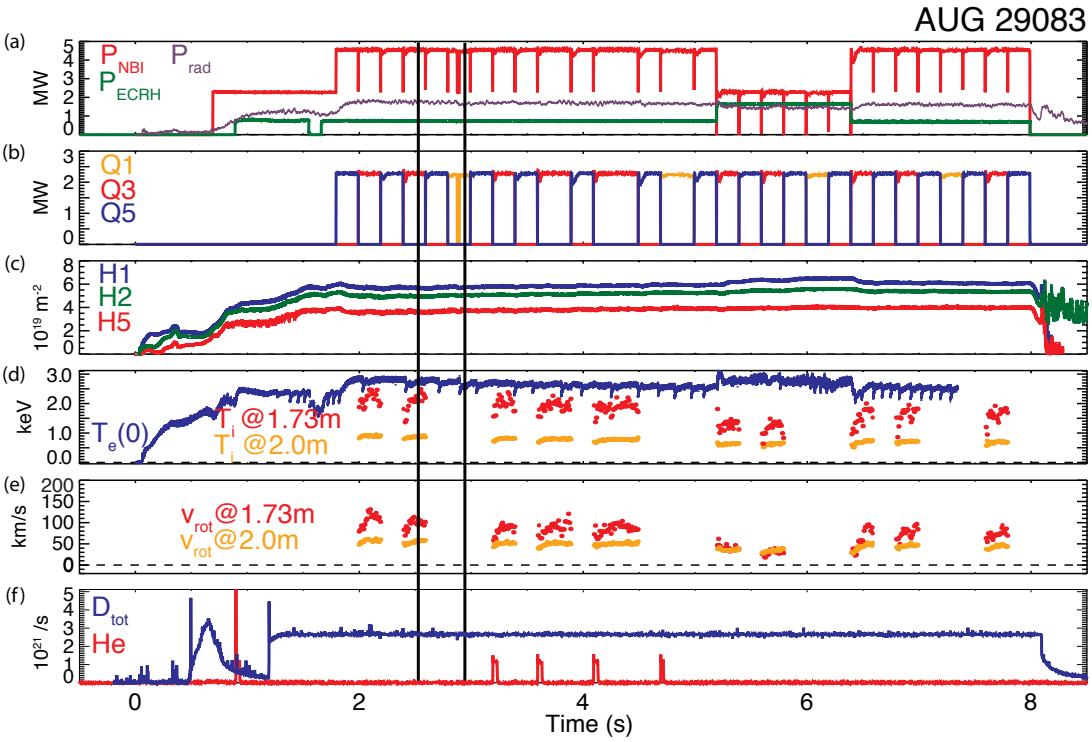

Figure 5.22: Time traces of the relevant parameters for discharge 29083: a) injected and radiated power, b) details of the NBI replacement scheme, c) line integrated electron density, d) electron and ion temperatures, e) plasma rotation, f) total deuterium and helium gas puffs.

the center of NBI Q1 and only view the edge of this source. As such, the prompt CX signal is lower for the toroidal lines-of-sight (by approximately a factor of 3 in the core). However, the toroidal lines-of-sight still measure plume ions produced by NBI Q1 which have followed the magnetic field lines into the lines-of-sight. In this case, the plume-to-prompt ratio in the core is almost a factor of 2 higher than for NBI Q3. The poloidal lines-of-sight barely intersect NBI Q1 and measure almost exclusively the plume originating from NBI Q1. The calculated plume-to-prompt ratio is indeed approximately 10 times higher in comparison to the ratio for the NBI Q3 time point (shown divided by 10 in Fig. 5.24).

In the right plot of Fig. 5.23, however, the He^{2+} density profiles corrected with the plume emission model presented here are shown. The corrected densities are obtained by multiplying the densities in the left plot with a factor of $1/(1 + R)$, where R is the

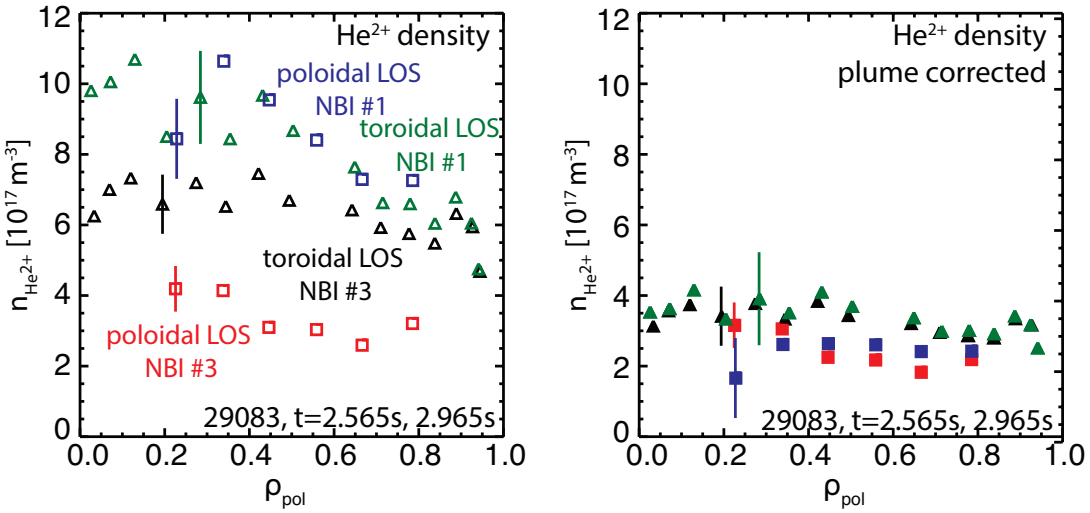

Figure 5.23: He^{2+} density profiles obtained from CX measurements for the ASDEX Upgrade discharge 29083 at 2.565s (NBI Q3 on) and at 2.975s (NBI Q1 on) without the plume effect taken into account and the corrected profiles after the plume effect has been modelled, for the toroidal and poloidal viewing geometry.

ratio of plume emission signal integrated along each line-of-sight to the active CX signal, shown in Fig. 5.24. The corrected density profiles from the toroidal and the poloidal lines-of-sight are now in much better agreement. In addition, as the plasma parameters are similar between the NBI Q1 and NBI Q3 phases, the He^{2+} density profile from the NBI Q1 phase can be compared to the profile measured on NBI Q3. Good agreement is found in this case as well. Part of the remaining discrepancies can be attributed to intensity calibration uncertainties between the two optical heads. As the uncertainties (see error bars in the right plot in Fig. 5.23) may play an important role, the ultimate test of the plume model is whether the line shape of the spectral plume emission can be predicted.

5.5 Reconstruction of the helium spectrum

The model for the helium plume emission provides not only a spatial distribution of the plume ions, but also information on their velocity. It is, therefore, possible to reconstruct the plume emission spectral line. In this section, the reconstruction of the plume emission line is described which, together with the modelled active emission

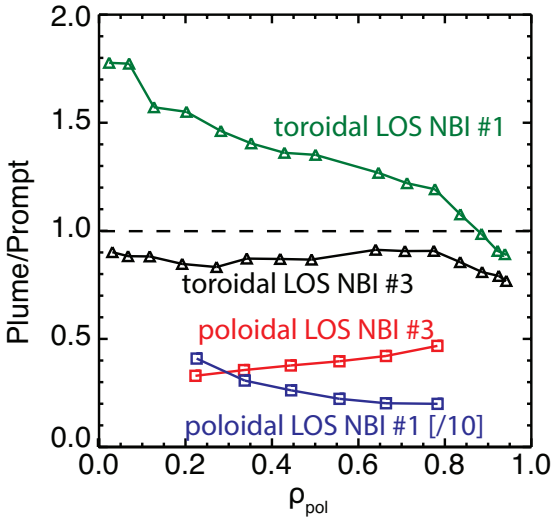

Figure 5.24: The plume-to-prompt intensity ratios calculated for the helium density measurements shown in Fig. 5.23.

line, can be compared to the experimental measurements. Apart from offering a further benchmarking of the helium plume model, modelling the helium plume emission line itself can ultimately allow for the derivation of accurate ion temperature and rotation profiles from the helium charge exchange spectra.

As already discussed in the previous section, it has been observed at ASDEX Upgrade, where charge exchange measurements on more than one impurity are routinely performed, that the ion temperature and rotation profiles derived from the HeII line differ from those measured on the BV or CVI lines if the plume emission line is not corrected for. Assuming that both the passive emission line and the plume emission line are correctly subtracted from the measured spectra, the remaining spectral shape, which is the isolated active charge exchange emission line, should yield ion temperature and rotation profiles that compare well with the boron or carbon measurements. The passive emission line is removed by means of subtracting passive frames during which the neutral beam is switched off, while the plume emission line shape is modelled.

The helium plume model provides the modelled active (prompt) line and the modelled plume emission lines, the sum of which can be compared with the measurements. The prompt emission line for each measurement location is represented by a single

Gaussian shape, with a line shift $\Delta\lambda$ and a line width σ:

$$\begin{aligned} \Delta\lambda &= \frac{v_{rot}^{B}\lambda_0 cos(\gamma)}{c} \\ \sigma &= \sqrt{\frac{T_i^B k}{mc^2}}\lambda_0, \end{aligned} \tag{5.18}$$

where λ_0 is the natural wavelength (468.571nm) and γ is the angle between the line-of-sight and the toroidal direction. The superscript B denotes that boron measurements are used for the T_i and v_ϕ values at this location.

The plume emission line, on the other hand, can not be described by a single Gaussian, due to the non-Maxwellian effects described in Section 5.2. Additionally, the emission comes from many locations along the line-of-sight, which are characterised by different T_i and v_ϕ values. Similar to the description of the active charge exchange emission line given in Chapter 3, the observed spectral plume intensity in terms of velocities along the line-of-sight and for each location along the line-of-sight (l) is given by an equation of the following form:

$$I_{plume}(\upsilon_\lambda, l) = \frac{1}{4\pi} n_e(l) Q_{exc}^{e}(l) dl \int_{\upsilon_x}\int_{\upsilon_y}\int_{\upsilon_z} f_{He^+}(l, \upsilon_x, \upsilon_y, \upsilon_z)\delta(\upsilon_\lambda - \overrightarrow{v}\cdot\cos\theta) d\upsilon_x d\upsilon_y d\upsilon_z, \tag{5.19}$$

where $\overrightarrow{v}$ is the ion velocity, θ the angle between the ion velocity and the line-of-sight (z-axis) and l gives the coordinate along the line-of-sight. The helium plume ions are described by the velocity distribution $f_{He^+}(l, \upsilon_x, \upsilon_y, \upsilon_z)$ obtained by the Monte Carlo simulation.

The Monte Carlo modelling provides directly the distribution of the helium plume ions also in velocity space. The plume ion density is given in terms of velocities along each magnetic field line. Assuming that γ is the angle between line-of-sight and the magnetic field line, the velocity is projected along and perpendicular to the line-of-sight as $\upsilon_{\parallel,los} = \upsilon_{\parallel,\overrightarrow{B}} cos(\gamma)$ and $\upsilon_{\perp,los} = \upsilon_{\parallel,\overrightarrow{B}} sin(\gamma)$, respectively. The plume spectrum is then reconstructed using Eq. (5.19), with $f_{He^+}(l, \upsilon_{\parallel,los}, \upsilon_{\perp,los})$, obtained from the Monte Carlo simulation.

To extract accurate He^{2+} density profiles, the modelling of the helium plume line and the comparison of the modelled emission lines with the spectra has to be iterated. As already described in Section 5.3, the plume emission depends on the shape of the

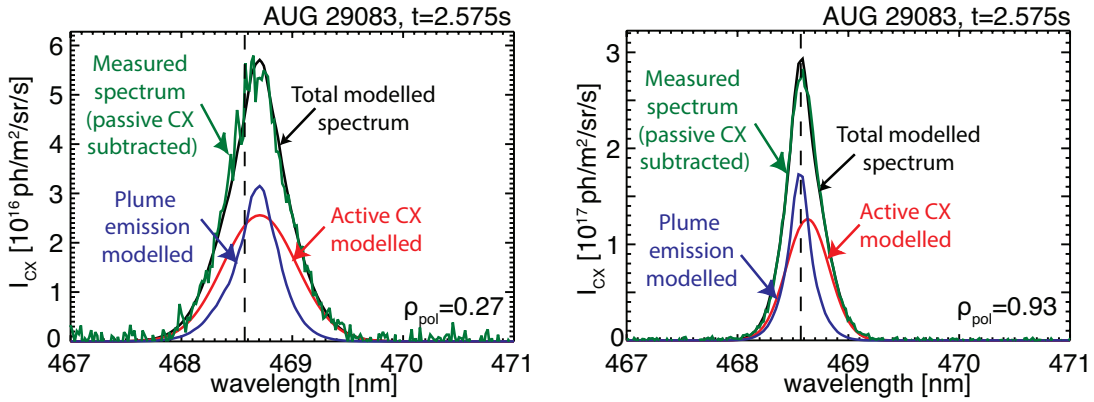

Figure 5.25: Reconstruction of helium charge exchange spectra for the toroidal viewing geometry, for discharge 29083, t=2.575s using the Monte Carlo method, for a core (left) and an edge line-of-sight (right). Very good agreement is found between the sum of the reconstructed prompt and plume emission lines and the measured spectra, from which the passive emission has been subtracted.

He^{2+} density profile. Since this is an input to the modelling, comparison of the output modelled emission lines with the spectra is required and more iterations might be necessary. In simple words, an assumed He^{2+} density profile is used as input to the model: either the He^{2+} densities calculated ignoring the contribution of the plume or He^{2+} density profiles that follow the shape of the electron density profile can be used. The plume and prompt emission lines are reconstructed and compared to the measured spectra. A scaling factor is applied to the modelled emission lines to match the measurement, same for both emission lines, but possibly different between the different lines-of-sight. If the normalised residuals between the modelled and the measured spectrum are not satisfactory, the model is iterated once more, taking into account the scaling factors. The process can be repeated as many times as required to minimise the difference between the modelled and the measured spectrum, but good agreement is typically found within 2-3 iterations, within the error bars of the measured spectrum and the He^{2+} density profiles.

In Fig. 5.26, measured ion temperature and rotation profiles of boron and helium are shown. The helium spectra fitted with a single Gaussian (passive subtracted using beam modulation) are shown in red. In addition, the modelled profile of the plume component is plotted in green, also fitted with one Gaussian. In blue, the profiles obtained from boron measurements and used as input to the modelling, are plotted.

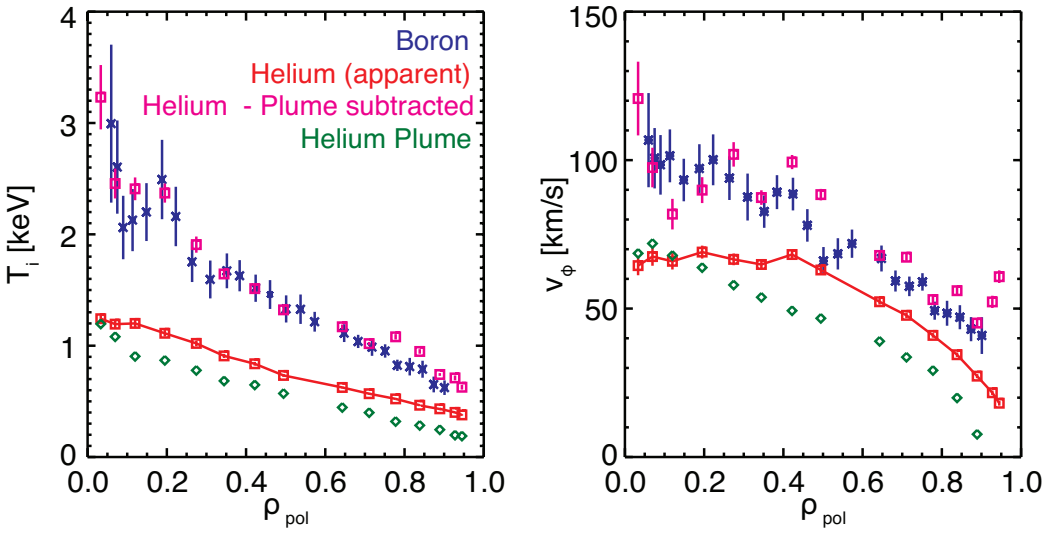

Figure 5.26: Reconstructed ion temperature and rotation profiles for the toroidal viewing geometry, for discharge 29083, t=2.565s. The profiles derived from boron measurements are shown in blue and the ones derived from helium measurements, without correcting for the plume are shown in red. The plume profiles derived from fitting the plume with one Gaussian are shown in green. The profiles derived from helium measurements after correcting for the plume are shown in magenta.

The modelled plume emission line is subtracted from the helium spectra, which are subsequently fitted with a Gaussian, resulting in the profiles shown in magenta. Very good agreement is found with the boron measurements. Ultimately this means that the plume model describes the involved physics to a high degree of accuracy, because not only the relative size of plume to prompt emission is described, but also the distribution of the plume in velocity space is matched. Thus, the observed differences in the He^{2+} density encountered in Fig. 5.23 are probably given by instrumental uncertainties rather than by the plume model.

5.6 Considerations on the plume effect

In the past, a number of studies have been conducted in order to understand the helium plume effect and to model the helium plume emission. The helium plume effect was first described and named by Fonck et al in [9]. In this paper the helium plume effect is identified as a significant disturbance to the helium charge exchange spectra. A simplified model for the evaluation of the plume emission is proposed assuming

one dimensional transport along a magnetic field line. The dependence of the plume emission on parameters such as the diagnostic observation geometry and the beam energy is described. It is also noted that no accurate toroidal rotation profiles can be obtained from the helium charge exchange spectra, if the plume effect is not taken into account. Gerstel et al attempted in [121], to calculate both the plume from the thermal helium content in the plasma, but also the helium beam "plume", as part of the analysis of helium beams. Here a Monte Carlo approach was employed for solving the transport equation of the hydrogenic plume ions. Nevertheless, the helium plume emission is not shown to be taken into account in the fitted helium spectra. In [56], it is mentioned that the plume emission calculated from the model in [121] is overestimated by a factor of 3 in intensity. The helium plume emission was also studied at DIII-D [122], following a method similar to the one described in [9] as well as considering a Maxwellian distribution to describe the plume ions. Here, the plume emission corrections are found to be important only in terms of magnitude, but not significant in terms of profile shapes. A further effort to model the helium plume can be found in [105], where the method found in [9] is also followed.

In this work, the plume effect has been confirmed to be a significant contribution in the helium charge exchange spectra. The plume emission contribution in the spectrum is complicated and depends on a number of plasma parameters, as well as on the diagnostic geometry, and needs to be treated appropriately. Accurate He^{2+} density profiles can be derived only if the plume emission is modelled and subtracted from the measured spectra.

Furthermore, it should be noted that the helium plume effect is important across the whole plasma radius, including the plasma edge. However, as the plume emission line has an apparent lower temperature and velocity than the active charge exchange line, it can easily be mixed with the passive emission line depending, of course, on the viewing geometry and edge plasma parameters. Furthermore, the helium plume effect can be minimised with the use of poloidal views, but still not avoided completely.

For the first time the non-Maxwellian features of the plume emissions from the same plasma radius have been implemented, which resulted in the breakthrough for the modelling not only the helium plume-to-prompt ratio but also for the modelling of the detailed charge exchange including plume and prompt components.

Pushing the helium plume model further and starting from the measured helium charge exchange spectra and the derived T_i and v_ϕ values, which as described are affected by the helium plume emission, an iterative modelling process could be implemented so as to converge to accurate T_i and v_ϕ profiles. This would allow for standalone charge exchange measurements based on the HeII line, without the need for input from other impurity measurements for the modelling of the plume emission.

Looking ahead at future fusion machines, for example ITER, the helium plume effect must be taken into account as charge exchange spectroscopy is expected to provide measurements of the helium "ash". Both the electron impact excitation rates and the electron impact ionisation rates will be lower at the higher electron temperatures of ITER, meaning in general lower plume emission intensities with the increasing electron temperature. The higher electron densities mean shorter ionisation lengths for the He^+ ions, while the electron impact excitation rates drop with increasing density, resulting again into smaller contributions from the plume. In ITER conditions however, ion impact ionisation will also become important. The lines-of-sight of the charge exchange diagnostic on ITER are designed to view the neutral beam with angles almost perpendicular to the magnetic field lines, in order to minimise the helium plume contribution [82]. Nevertheless, it is certain that the helium plume effect will be important for the thermal helium charge exchange measurements on ITER, but the magnitude of this effect has yet to be estimated.

6

Investigation of the thermal helium transport in ASDEX Upgrade plasmas

The shape of the helium density profile in future fusion reactors will have a serious effect on their performance, due to helium "ash" accumulation issues. To predict how

the helium density profile will behave, understanding of the helium transport in fusion plasmas and experimental validation of the current theoretical understanding are required. This is the objective of this chapter. Here, the helium density profiles measured in ASDEX Upgrade will be systematically compared to the available theoretical predictions to validate the theory and shed light on the behaviour of helium in future devices.

Previous investigations of helium transport at DIII-D have shown that the helium density profile has a similar shape to the electron density [122]. At ASDEX Upgrade helium transport studies have not previously been done, but boron studies showed that the normalised logarithmic boron density gradients can be qualitatively reproduced by gyrokinetic modelling if the "roto-diffusive" term, proportional to the normalized gradient of the toroidal rotation, is included [11, 27] as discussed in Section 4.3. Moreover, previous gyrokinetic simulations of helium indicate that the thermodiffusive contribution to the particle flux should be more important for helium than for higher-Z impurities such as boron, leading to different peaking of the two profiles [114].

Taking these works into account, dedicated experiments optimised for both helium and boron charge exchange measurements were performed at ASDEX Upgrade to determine the experimental correlation of these impurity density gradients with theoretically relevant plasma parameters, namely: the normalized gradients of the electron density, the ion temperature and the toroidal rotation. Systematic studies dedicated to multiple impurities simultaneously, such as the one presented here, are necessary in order to have a deeper investigation of the transport physics of these species. Assessing the applicability of the present theoretical models for impurity transport to the experimental observations is very important as such studies allow a more stringent validation of the theoretical predictions.

This study focusses on the confinement region (mid-radius), where neoclassical transport is expected to be negligible and turbulent transport is expected dominate. The database collected for this study and the experimental observations are described in Sections 6.1 and 6.2. Then the experimental data are compared to the theoretical predictions in Section 6.3. The neoclassical contributions to the helium and boron transport are discussed and compared with the transport due to the electrostatic plasma turbulence. Detailed comparisons of the measured impurity density gradients with gy-

rokinetic simulations of the turbulent transport are presented. Conclusions are drawn in Section 6.4.

6.1 Database for the investigation of helium transport

A database of helium and boron density profiles was assembled from a set of experiments performed at ASDEX Upgrade designed specifically for the investigation of helium transport. The plasma discharges were optimised for helium and boron charge exchange measurements. The experiments were performed soon after a boronisation (coating of wall components produced by a glow discharge with 10% B_2D_6 and 90% He [123]), to ensure very good charge exchange signal from both impurities. Fresh boronisation also enables the performance of low density, low collisionality plasmas. The charge exchange measurements are performed on NBI Q3 of ASDEX Upgrade, with two different spectroscopic instruments, boron measurements performed with the spectrometer described in [63] and helium measurements performed with the system described in Section 3.3. Both measurements extend from the plasma center to approximately $\rho_{tor} = 0.85$. The NBI source was modulated and replaced by another injection source at the other side of the torus, so as to enable the subtraction of the passive emissions and reduce the uncertainties in the interpretation of the helium charge exchange spectra while keeping the total injected power constant.

All six discharges included in this database were performed at a plasma current of 600kA and a magnetic field of 2.5T. The goal of these discharges was to provide optimised boron and helium density profiles together with scans of the experimental parameters expected to be relevant to the impurity transport in different turbulence regimes, namely the collisionality and the normalised gradients of the electron density, the ion temperature and the toroidal rotation. Different levels of electron cyclotron and neutral beam heating were applied in order to perform a scan of R/L_{n_e}, R/L_{T_i}, the radial gradient of the toroidal plasma velocity u' and ν_{eff}, where ν_{eff} is the effective collisionality, defined as the ratio of the electron-ion collision frequency to the curvature drift frequency.

The application of central electron cyclotron heating has clear effects on the electron density profile, causing strong peaking as the plasma turbulence regime transitions from ITG to TEM [27]. Furthermore, central deposition of ECRH leads to flat and even

Table 6.1: Parameter space covered in the helium transport database presented in this work at $\rho_{tor} = 0.5$.

Parameter	Value range	Parameter	Value range
R/L_{n_e}	0.03-3.6	$n_e(\rho_{tor} = 0)$	$5 - 8 \cdot 10^{19} m^{-3}$
R/L_{T_e}	3.5-7	$T_e(\rho_{tor} = 0)$	$2 - 6keV$
R/L_{T_i}	3.0-7	$T_i(\rho_{tor} = 0)$	$0.8 - 2.3keV$
u'	-0.15-1.1	$v_\phi(\rho_{tor} = 0)$	$20 - 140km/s$
ν_{eff}	0.3-1.9	q_{95}	6.9-7.4

hollow rotation profiles, an effect connected again to the plasma turbulence [124, 125]. A scan in NBI power was also performed to vary the Mach number, also using a combination of on- and off-axis beams in an attempt to vary the admittedly very stiff ion temperature profile. Different levels of deuterium fuelling were also used during one discharge to change the collisionality. The heating schemes of discharges 30367 and 30379 are shown in Fig. 6.1 as examples. They feature a scan of ECRH power in the first case and a scan of NBI power in the second discharge. Averaged profiles are shown for four example phases.

A total of 131 steady state phases 55-110ms long were selected out of these discharges to form the database analysed here. The data points selected have been ELM-synchronised when ELMs were present, to avoid the strong effect of ELMs on the profiles. With the exception of discharge 29083, no strong sawteeth were documented in this database. When present, the sawteeth existed in the core, with an inversion radius $\rho_{tor} < 0.2$. Furthermore, no modes were present.

An overview of the parameter space explored is shown in Fig. 6.2, with further details given in Table 6.1 for $\rho_{tor} = 0.5$. We succeeded in varying the collisionality ν_{eff} at $\rho_{tor} = 0.5$ by a factor of 6, with a variation of the core electron density from 5 to $8 \cdot 10^{19} m^{-3}$ and core electron temperature from $2 - 6keV$. A factor of 3 in the variation of deuterium Mach number at $\rho_{tor} = 0.5$ was achieved $(0.08 - 0.26)$. The applied electron heating power ranges from 0 to $4MW$ and the NBI power $0 - 7.5MW$. In comparison to previous work investigating light impurity transport (boron) [11], similar ranges in R/L_{n_e} and R/LT_i were achieved, but narrower ranges of R/L_{T_e} and u' (approximately $4 - 10$ and -0.5 to 3, respectively, in [11]). The q_{95} values are on the higher end of the q_{95} values in [11] ($q_{95} = 4 - 7$).

The impurity density profiles were evaluated from the measured charge exchange

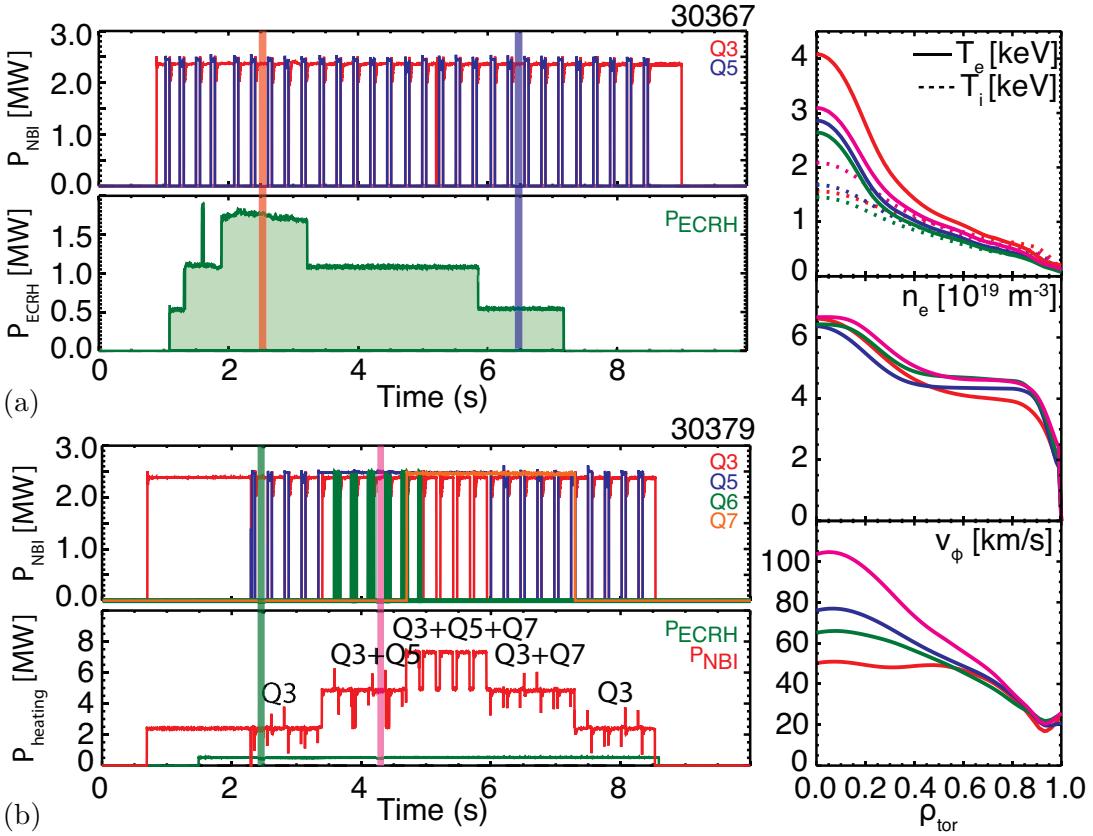

Figure 6.1: Heating schemes of two discharges from the helium transport database. a) In discharge 30367, a scan of ECRH power at constant NBI power was performed, in order to vary the peaking of the electron density profile. b) In discharge 30379, a scan of NBI power at constant ECRH power was performed, in order to see the effect of on- and off-axis beams and NBI power levels on the impurity density profiles.

intensities, using the charge exchange impurity concentration analysis code CHICA, which uses the Monte Carlo neutral beam simulation code FIDASIM [69, 74] for the neutral beam attenuation calculations, including the beam halo. The evaluation of the helium density profiles takes into account the plume emission, using the plume emission forward model described in Chapter 5. Electron density and temperature profiles derived from IDA (see Section 2.3.5) and ion temperature and rotation profiles measured on boron have been used as input to the impurity concentration analysis code and to the plume modelling code.

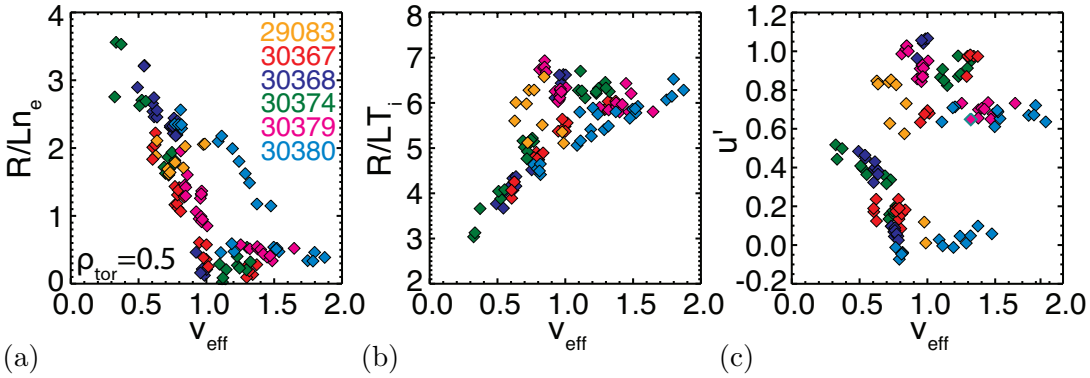

Figure 6.2: Overview of the parameter space in the helium transport database analysed in this work, namely the normalised logarithmic gradients of a) electron density and b) ion temperature and c) the radial gradient of the toroidal plasma velocity as a function of the effective collisionality.

6.2 Experimental observations

In the investigated discharges we obtained a wide variety of experimental helium and boron density profiles. Examples of the profiles are shown in Fig. 6.3. These time points are also indicated in the database in Fig. 6.2. In the database, the helium profiles are observed to vary from extremely flat to very peaked profiles, but it does not become hollow. The boron profiles on the other hand are observed to vary from slightly hollow to very peaked.

The normalised gradients of the impurity and electron density profiles at two plasma locations, namely at $\rho_{tor} = 0.3$ and $\rho_{tor} = 0.5$ are shown in Fig. 6.4. At $\rho_{tor} = 0.5$, the helium and boron impurity gradients are comparable to the electron density gradient, similar to what was observed at DIII-D [122]. At $\rho_{tor} = 0.3$, the impurity profiles are generally less peaked than the electron density, with the exception of helium at high R/L_{n_e} values. While one might naively assume that the helium profiles should lie between the electron density and boron profiles, it is observed that this is not the case, indicating complex mechanisms at play. The error bars plotted in Fig. 6.4 take into account the density profile measurement uncertainty, but not the error from the fitting procedure.

Previous work [11] illustrated the importance of u' on the boron profile. In Fig. 6.5, R/L_{n_Z} is plotted versus u', showing that it decreases with increasing u'. However, the interpretation is not so simple as other plasma parameters are changing at the

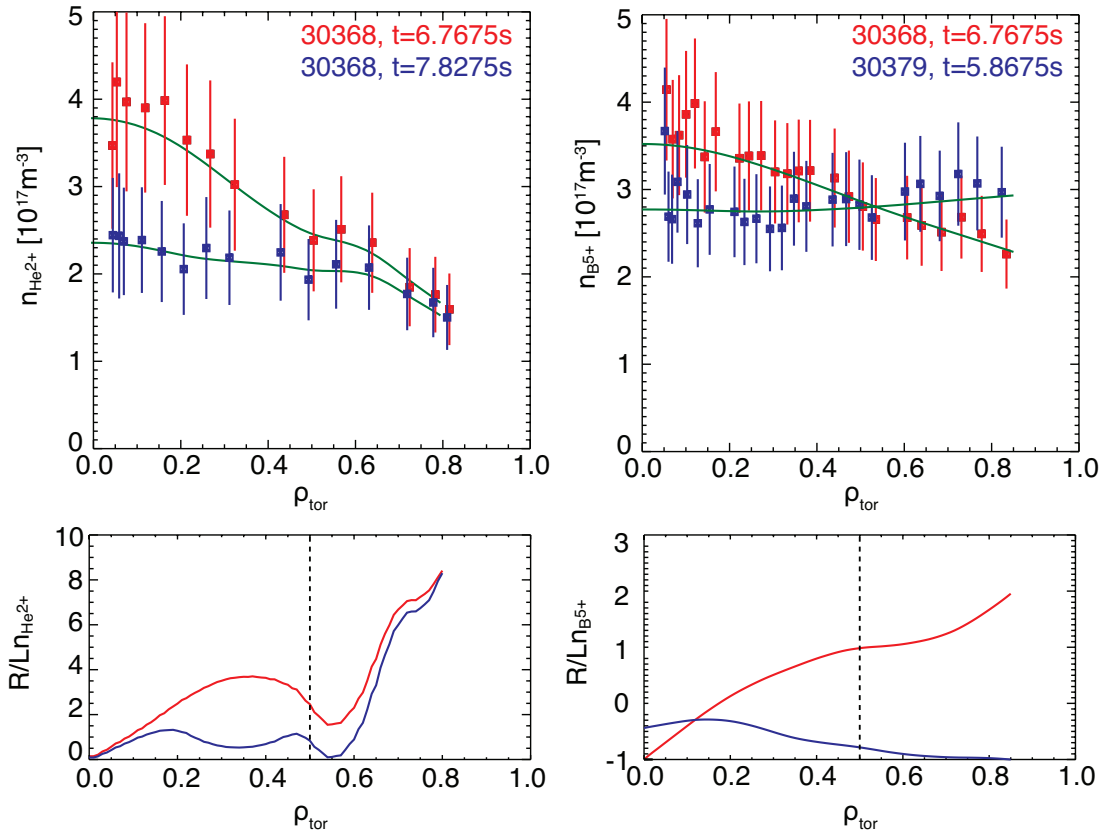

Figure 6.3: Example profiles of helium (left) and boron (right) shown together with the normalised logarithmic impurity density gradients (bottom plots).

same time. As the impurity density profiles at a certain location in the plasma are determined by the interplay of many parameters, it is not straightforward to disentangle the dependencies.

To try and better identify the underlying physics mechanisms at work, theoretical simulations of the neoclassical and turbulent transport expected in these plasmas have been performed and compared to the experiment. This is presented in the next section.

6.3 Comparison to impurity transport theory

6.3.1 Neoclassical transport contributions

All of the points in the database have been modelled with the neoclassical transport code NEOART [89, 90]. Neoclassical transport is expected to be negligible around

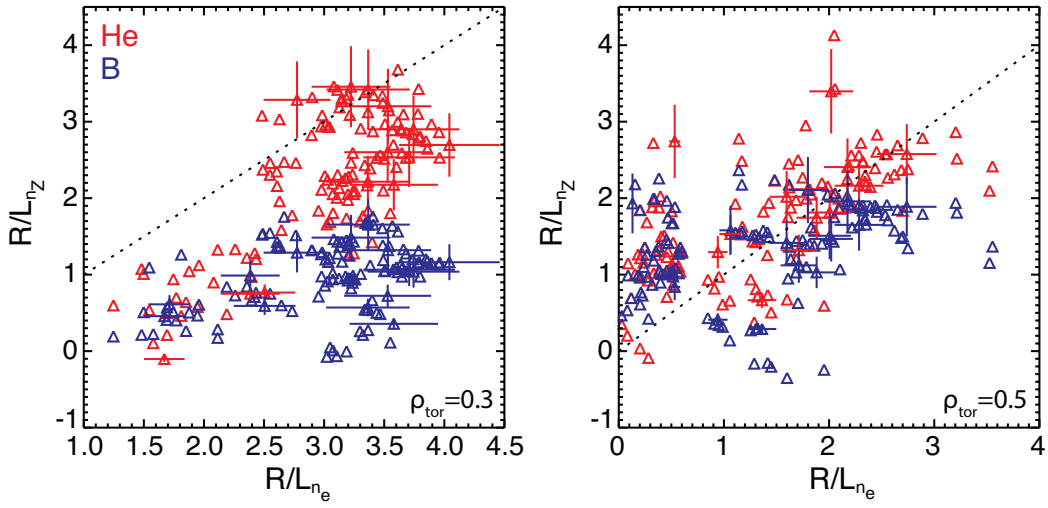

Figure 6.4: Experimentally deduced R/L_{n_B} and $R/L_{n_{He}}$ at $\rho_{tor} = 0.3$ and $\rho_{tor} = 0.5$.

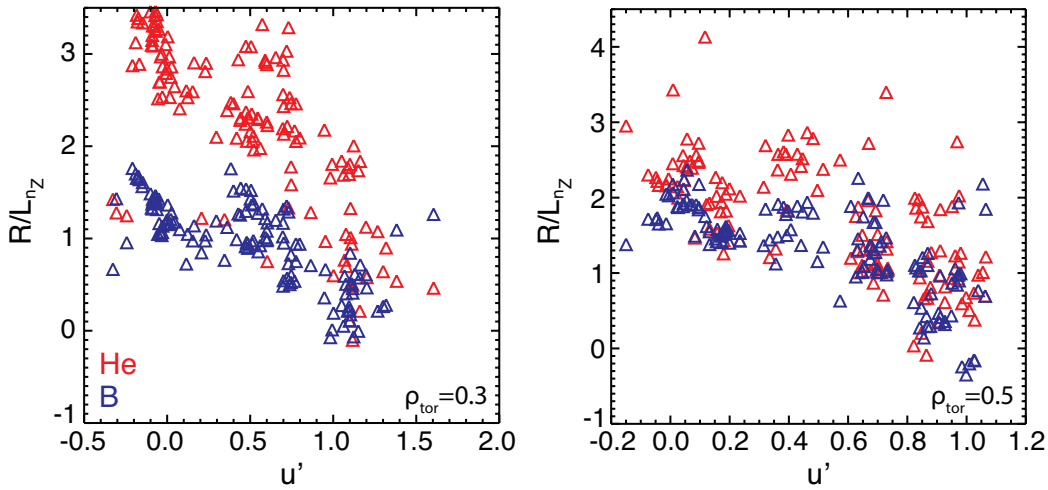

Figure 6.5: Experimentally deduced R/L_{n_B} and $R/L_{n_{He}}$ as a function of u' at $\rho_{tor} = 0.3$ and $\rho_{tor} = 0.5$.

mid-radius [25, 27] in comparison to the turbulent contributions, nevertheless, this has to be confirmed also for the current database.

The diffusion coefficients and drift velocities for helium and boron at $\rho_{tor} = 0.3$ and $\rho_{tor} = 0.5$ derived from NEOART are shown for all time points as a function of the ratio of electron to ion temperature T_e/T_i in Fig. 6.6. The neoclassical drift velocities, shown on the right of Fig. 6.6, are generally directed inward at both locations and for both

impurities, providing a balance against the diffusion. The only exception is for boron at low T_e/T_i. Here, the drift is also outward at mid-radius, meaning that if neoclassical transport is important then these points (highlighted in green) should feature hollow profiles. The actual R/L_{n_B} profiles corresponding to these points however, have values of 0.4-2.4, indicating that neoclassical transport is not the only mechanism here.

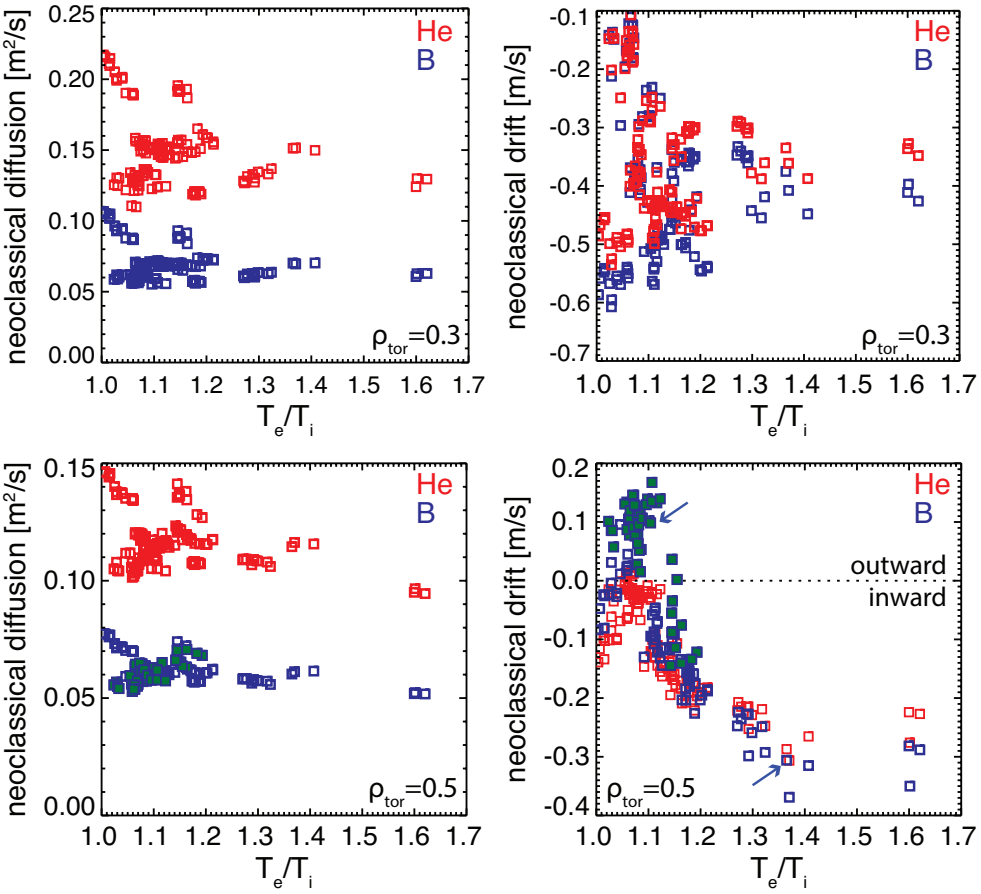

Figure 6.6: Neoclassical diffusion and convection for boron (blue) and helium (red) in the transport database for $\rho_{tor} = 0.3$ (top) and $\rho_{tor} = 0.5$ (bottom). For $\rho_{tor} = 0.5$, the cases where the Pfirsch-Schlüter contribution to the boron diffusion is larger than the banana-plateau contributions are identified with green ($D^{PS} > 1.3D^{BP}$). The arrows indicate the cases of interest that are examined in Fig. 6.7.

Generally we see that diffusion of helium and boron in the plasma core is dominated by the banana-plateau contribution, while the edge by the Pfirsch-Schlüter contribution, as can be seen in Fig. 6.6, where the radial profiles of the neoclassical coefficients are

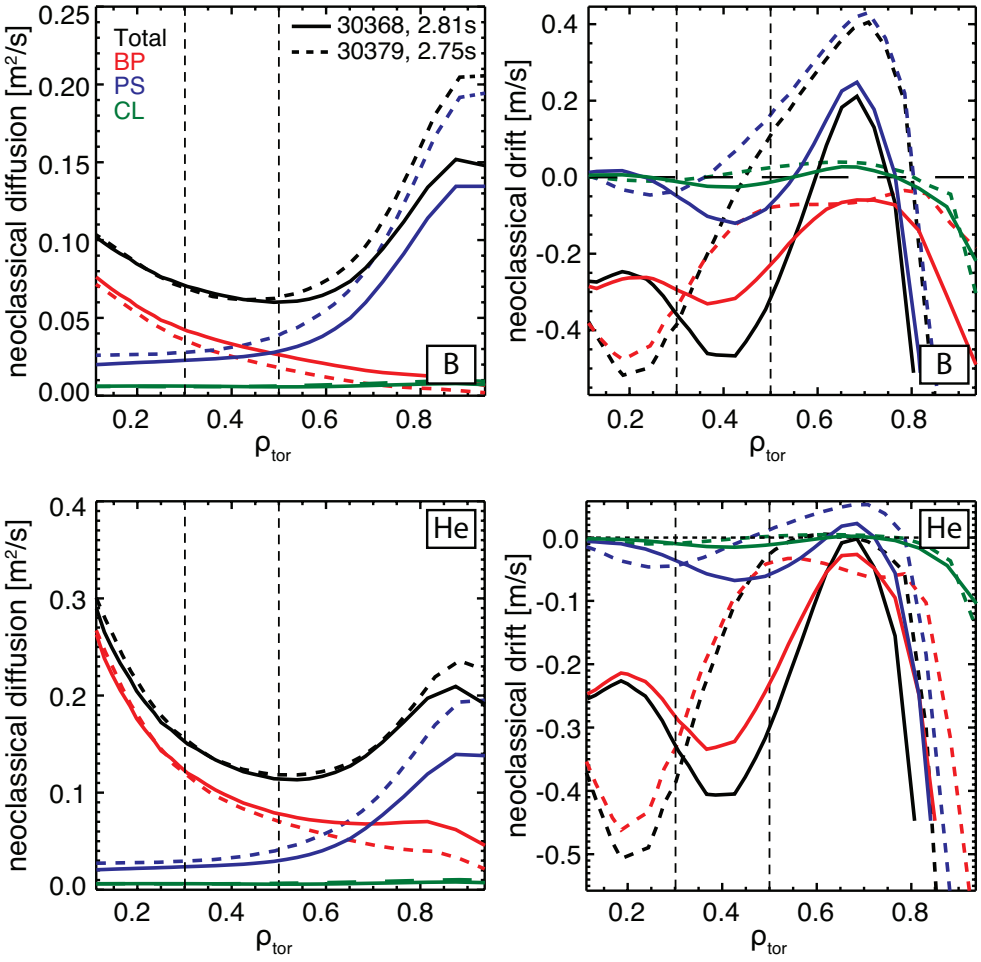

Figure 6.7: Neoclassical diffusion and convection coefficients for boron (top row) and helium (bottom row) in 30368 at 2.81s (solid lines) and 30379 at 2.75s (dashed lines). BP, PS and CL correspond to the banana-plateau, Pfirsch-Schlüter and classical contributions, respectively.

shown. The cases with outward boron drift correspond to cases where the Pfirsch-Schlüter contribution is larger than the banana-plateau one (dashed lines). The outward drift velocities of boron at $\rho_{tor} = 0.5$ can be explained by considering the temperature screening effect. Not only is the temperature screening effect weaker for helium [93], but the temperature screening is also stronger in the Pfirsch-Schlüter regime that is more relevant for boron. To test this explanation, a temperature screening factor f_{TS} can be derived from Eq. (4.9), defined as the multiplication factor of the temperature

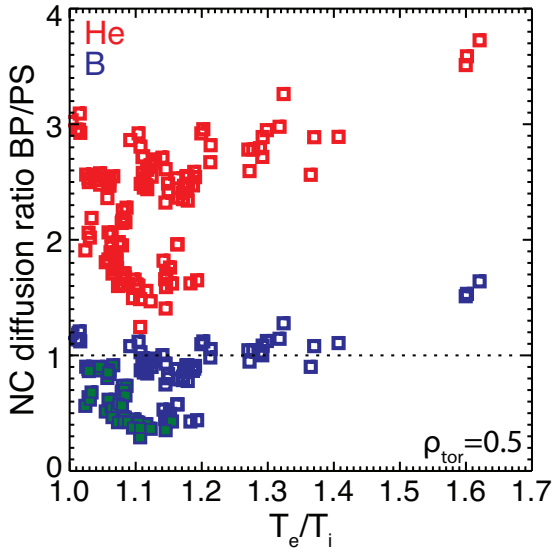

Figure 6.8: Ratio of the banana-plateau to Pfirsch-Schlüter diffusion coefficients for boron and helium at $\rho_{tor} = 0.5$. The cases where the boron drift velocity is directed outwards are indicated with green.

gradient:

$$\begin{aligned} v &= v^{CL} + v^{PS} + v^{BP} = \\ &= Z\left[D^{CL}(n' + f^{CL}T') + D^{PS}(n' + f^{PS}T') + D^{BP}(n' + f^{BP}T')\right] \\ &= Z\left[(D^{CL} + D^{PS} + D^{BP})n' + (D^{CL}f^{CL} + D^{PS}f^{PS} + D^{BP}f^{PS})T'\right], \end{aligned} \tag{6.1}$$

where n' and T' stand for the gradients of the density and temperature, respectively. The temperature screening factors f^{CL},f^{PS},f^{BP}, defined for each neoclassical contribution, give the total temperature screening factor $f_{TS} = D^{CL}f^{CL} + D^{PS}f^{PS} + D^{BP}f^{PS}$.

To illustrate the different effect of the temperature screening on helium and boron, the v/D ratios, normalised with Z, are plotted in Fig. 6.9, for a small subset of the database. The contribution of the density gradient (triangles) and the contribution of the temperature gradient (diamonds) are shown. The density contribution is the same for both impurities. As expected, the temperature gradient contribution in the case of helium is smaller than that of boron but not by much. The total drift parameter v/D, normalised over Z, does become positive for boron (for $T_e/T_i \sim 1.1$), which would mean hollow boron profiles, if neoclassical transport was the only contribution.

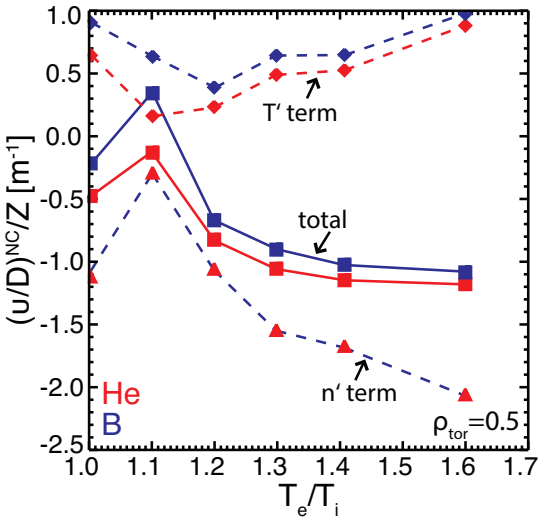

Figure 6.9: Drift parameters v/D for helium and boron for a subset of the database, normalised over Z. The contributions of the density gradient ($\triangle$) and temperature gradient ($\Diamond$) are indicated separately (see Eq. (6.1)).

Impurity density profile gradients calculated taking only the neoclassical transport into account are compared with those obtained from the experiment at $\rho_{tor} = 0.5$ in Fig. 6.10. As expected for this location, neoclassical transport does not seem able to explain the measurement. It predicts R/L_{n_B} in the range of -5 to 10, which are not observed in the experiment. The neoclassical prediction for helium seems better in comparison to the boron, as the boron drift velocities cover a much wider range. However, even if the neoclassical prediction for v/D appears good, the absolute values of v and D are also important as they include also a turbulent part.

In the next section, the neoclassical coefficients calculated here are compared with the contribution of turbulent diffusion and convection, which are expected to be the dominant terms defining the transport of helium and boron at mid-radius, to assure that the neoclassical contribution is negligible and can be ignored in the analysis.

6.3.2 Turbulent contributions

Turbulent transport modelling

The modelling of the turbulent transport in the database has been performed with the gyrokinetic simulation code GKW [126, 127]. GKW is a nonlinear gyrokinetic flux

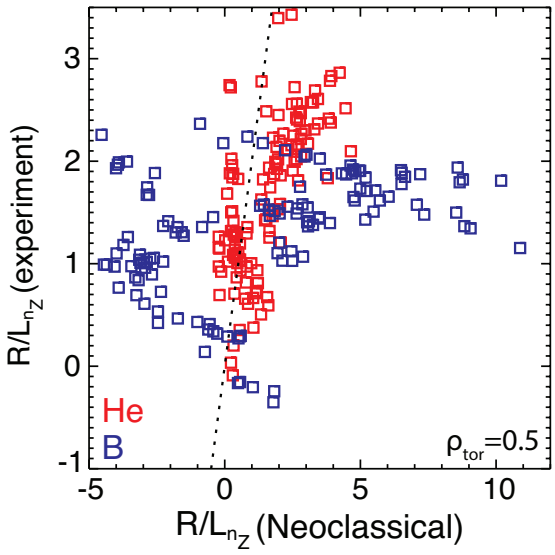

Figure 6.10: R/L_{n_B} and $R/L_{n_{He}}$ from the experiment are compared with the prediction based on neoclassical transport alone, at $\rho_{tor} = 0.5$.

tube code and simulates the tokamak plasma microinstabilities and turbulence. The gyrokinetic equation [114] is solved and the normalised logarithmic impurity density gradients are derived by setting the impurity particle flux to zero. The rotodiffusive contribution to the turbulent transport, as well as the coriolis force are included [115, 127–129]. Centrifugal effects are not included in these simulations, as they are negligible for impurity species such as helium and boron. Linear simulations show good agreement with the nonlinear ones, as shown in [114], and therefore are deemed sufficient for the purpose of this work. Helium and boron are considered trace impurities, an assumption that holds for the database in question, as the concentrations of boron and helium are $c_B \sim 0.3 - 0.8\%$ and $c_{He} \sim 0.5 - 1.5\%$, respectively, and together are the dominant low-Z impurity species after a boronisation.

The gyrokinetic calculations have been performed over a spectrum from $k_y\rho = 0.15$ to 0.65. Spectral averages have been performed considering spectra of the saturated electrostatic potential which are close to those obtained in nonlinear simulations in [11]. The simulations return the turbulent diagonal and off-diagonal contributions of impurity transport, namely the diffusion, thermodiffusion, rotodiffusion and convection, and the frequency of the most unstable mode at wave number $k_y\rho_i = 0.3$. The sum of the

different turbulent contributions provides the simulated normalised logarithmic impurity density gradients which can be compared to the experimentally obtained values.

Turbulent transport terms

The terms contributing to the particle impurity transport encountered in Eq. (4.27), derived from the gyrokinetic modelling, show clear characteristics depending on the frequency of the most unstable mode and the turbulent regimes, but also clear differences for the two impurities analysed in the database. The predicted R/L_{n_B} and $R/L_{n_{He}}$ and the off-diagonal contributions to the turbulent transport of the impurities are plotted as a function of the frequency of the most unstable mode ω_r in Fig. 6.11. Positive values of ω_r correspond to an ITG dominated regime and negative values correspond to a TEM dominated regime. At mid-radius, the database is primarily ITG dominated, but covers the range $-0.4 < \omega_r < 0.9$.

The impurity density logarithmic gradient can be derived by the sum of thermodiffusive, rotodiffusive and pure convective terms:

$$\left.\frac{R}{L_{n_Z}}\right|^{turb} \simeq -\left(C_T \frac{R}{L_{T_I}} + C_U u_I' + C_P\right) \tag{6.2}$$

We now examine each term individually (see Fig. 6.11). The pure convective term is negative at all frequencies, meaning that it always leads to peaking of the profiles. Larger absolute values are predicted deeper in the ITG regime. Similar behavior of the convective term is predicted for both helium and boron. The rotodiffusive term is positive (outward) in the ITG regime and negative (inward) in the TEM dominated regime. Again, similar behavior is predicted for the two impurities, but the rotodiffusive term is stronger for boron than for helium.

The thermodiffusive term is also directed outwards in ITG dominated regimes, leading to flattening of the profiles, and reverses sign as the regime transitions from ITG to TEM leading to inward transport and peaking of the profiles. Here, however, a clear difference between the two impurities is predicted. Due to its inverse charge dependence, the thermodiffusive contribution to the fluxes is expected to be more important for lower-Z impurities. As a result, thermodiffusion is expected to be smaller in absolute values than the pure convection in the case of boron, but becomes much more significant in the case of helium.

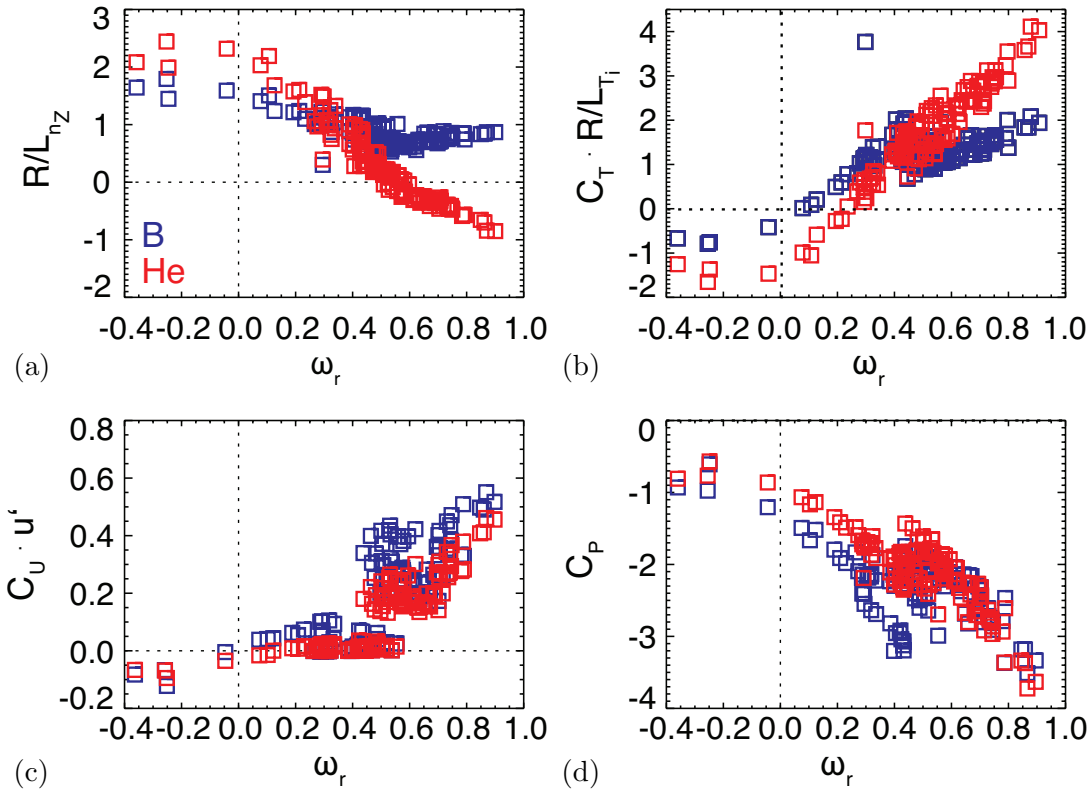

Figure 6.11: Predicted R/L_{n_B} and $R/L_{n_{He}}$ (a) and turbulent contributions to the impurity transport, namely (b) the thermodiffusive term, (c) rotodiffusive term and (d) the pure convection term for each impurity at $\rho_{tor} = 0.5$.

As a result of the thermodiffusive term, the gyrokinetic modelling predicts helium profiles significantly flatter than the boron profiles (or even hollow) in the ITG dominated regime and slightly more peaked than the boron profiles as the transition to the TEM regime occurs. This can be seen in the GKW predictions of $R/L_{n_{He}}$ and R/L_{n_B} shown in the top left plot of Fig. 6.11. Similar observations are made for $\rho_{tor} = 0.3$.

6.3.3 Turbulent versus neoclassical contributions

In this section, the turbulent contributions to the impurity transport derived from the modelling with GKW are compared to the neoclassical contributions obtained from NEOART simulations, described in the previous section. To this end, the neoclassical and the turbulent diagonal diffusion coefficients are plotted as a function of the electron to ion temperature ratio in Fig. 6.12 at two plasma locations, namely $\rho_{tor} = 0.3$ and

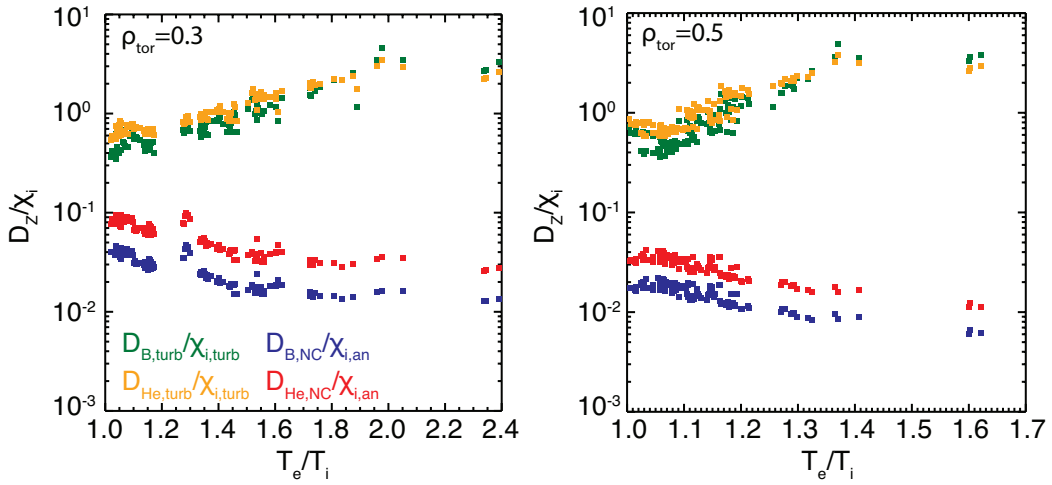

Figure 6.12: Turbulent and neoclassical diffusion coefficients for helium and boron, normalised to the effective ion heat conductivity obtained from the GKW calculations and the anomalous part of the power balance ion heat conductivity, respectively, shown at two locations in the plasma, namely $\rho_{tor} = 0.3$ (left) and $\rho_{tor} = 0.5$ (right).

0.5. Since the simulated turbulent fluxes are very sensitive to the input profiles and their uncertainties, leading potentially to up to an order of magnitude discrepancies in comparison to the actual fluxes [27], the simulated values have to be brought together with the experimental ones. Following the approach in [27] and assuming that the ratio of the transport coefficients to the heat conductivity is weakly dependent on the turbulent transport levels [114], the turbulent diffusion coefficients are normalised with the effective ion heat conductivity $\chi_{i,turb}$ which is calculated by the GKW simulation, while the neoclassical diffusion coefficient is normalised with the anomalous part of the power balance ion heat conductivity, defined as $\chi_{i,an} = \chi_i^{PB} - \chi_i^{NC}$, obtained from TRANSP simulations [78]. It is observed that the turbulent diffusion is larger than the neoclassical by two orders of magnitude at $\rho_{tor} = 0.5$ and one order of magnitude at $\rho_{tor} = 0.3$. It can, therefore, be concluded that the neoclassical contribution to the particle transport is negligible for both impurities at mid-radius in this database, but can become important further into the plasma.

In Fig. 6.13, the predicted normalised logarithmic boron and helium density gradients are shown as a function of the electron density gradient at the two plasma locations, with and without the neoclassical contributions taken into account. The impurity gradi-

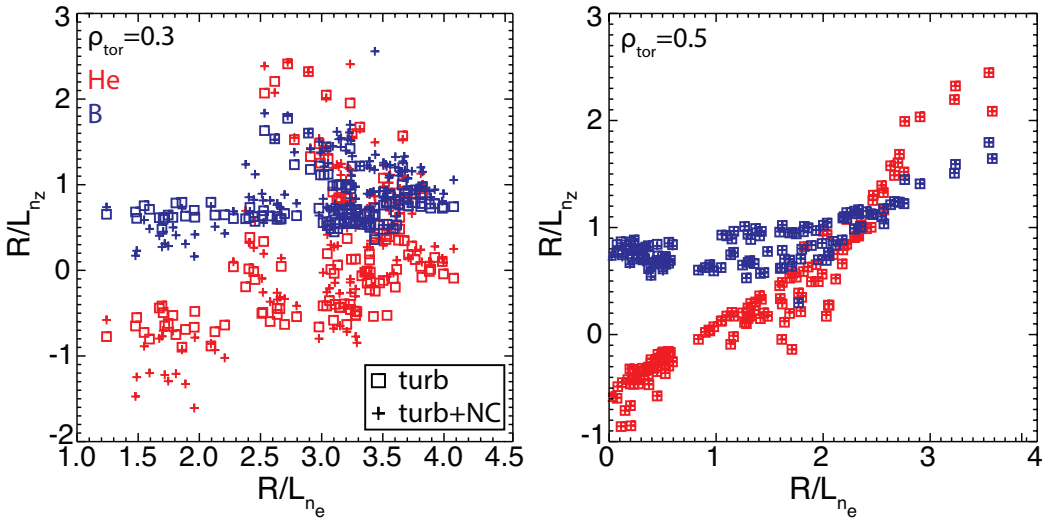

Figure 6.13: Predicted R/L_{n_B} and $R/L_{n_{He}}$ assuming turbulent and neoclassical contributions (+) and only turbulent contributions (□) for $\rho_{tor} = 0.3$ (left) and $\rho_{tor} = 0.5$ (right).

ents with both neoclassical and turbulent contributions are calculated using Eq. (4.26). It is noted that the contribution of the neoclassical transport at $\rho_{tor} = 0.3$ is not negligible, and for this reason all of the predicted R/L_{n_B} and $R/L_{n_{He}}$ values will be calculated including both the turbulent and neoclassical contributions.

6.3.4 Theoretical and experimental R/L_{n_B} and $R/L_{n_{He}}$

The experimentally obtained values of R/L_{n_B} and $R/L_{n_{He}}$ are now compared to the total theoretical predictions. In Fig. 6.14, the experimental values are compared to those derived from the modelling of the turbulent transport. In addition, the theoretical predictions based on both turbulent and neoclassical transport are also plotted in comparison to the experiment. It is noted, that the comparison between the experiment and the theoretical predictions does not change significantly with the inclusion of neoclassical components. The theoretical predictions for R/L_{n_B} are almost constant with respect to variations in R/L_{n_e}, which is not the case for helium, due to the thermodiffusive term.

Since the scatter in the experimental data does not allow to identify relations and trends by eye, a subset of the discharges in the database are analysed individually, to

illustrate how the experiment compares with the theoretical predictions derived from the gyrokinetic modelling with GKW. The discussion is based on $\rho_{tor} = 0.5$, where turbulent transport was shown to be dominant.

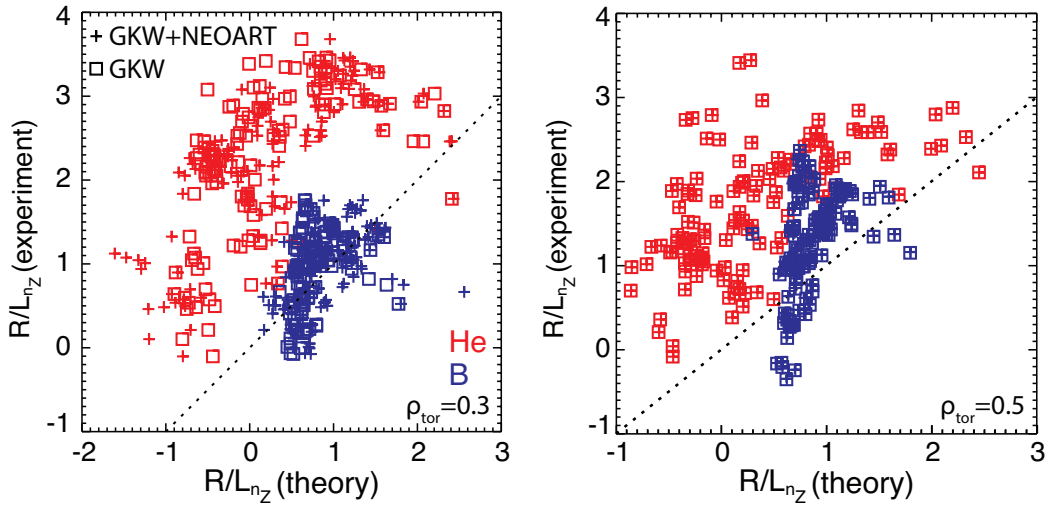

Figure 6.14: $R/L_{n_{He}}$ and R/L_{n_B} deduced from the experiment in comparison to the theoretical predictions at $\rho_{tor} = 0.3$ and $\rho_{tor} = 0.5$, from GKW (only turbulent transport, squares) and from GKW and NEOART (both neoclassical and turbulent transport, crosses).

Discharges with P_{ECRH} scan

In discharges 30367 and 30368, the centrally applied electron cyclotron heating power was scanned up to a maximum of 4MW on a background of 2.5MW of NBI heating (one neutral beam source, on which the charge exchange measurements were performed). The experimentally deduced $R/L_{n_{He}}$ and R/L_{n_B} values are compared with the gyrokinetic modelling predictions in Fig. 6.15 as a function of R/L_{n_e}, R/L_{T_i} and u', which are expected to be important.

The gyrokinetic modelling predicts hollow profiles for helium. For both impurities, the predicted profiles are less peaked than those observed experimentally. Nevertheless, ignoring the fact that the predicted gradients are consistently smaller, qualitative agreement is observed. Helium is measured to peak more strongly than boron with increasing R/L_{n_e}, as predicted by the modelling. Furthermore, the stronger dependence of $R/L_{n_{He}}$ with respect to R/L_{n_B} on the peaking of the ion temperature profile

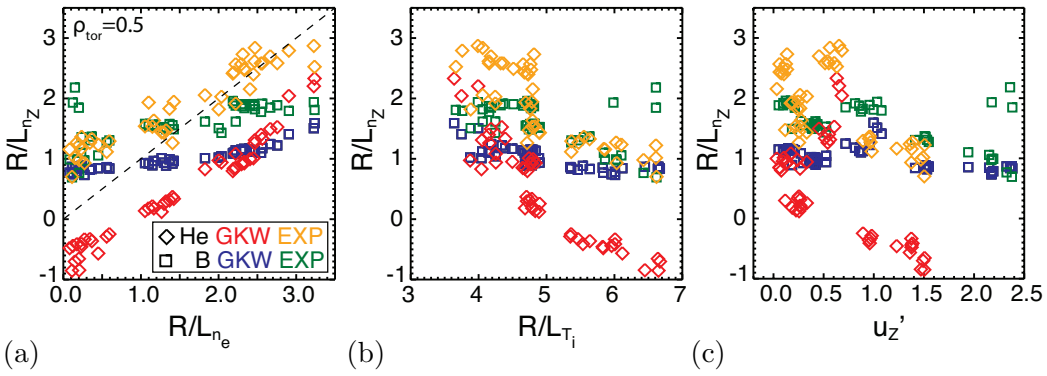

Figure 6.15: $R/L_{n_{He}}$ and R/L_{n_B}, both from gyrokinetic modelling predictions and experimental measurements at $\rho_{tor} = 0.5$, plotted against a) R/L_{n_e}, b) R/L_{T_i} and c) u'_Z, for discharges 30367 and 30368.

is reproduced by the experiment. Lastly, both theory and experiment find increasingly flatter profiles with higher values of u'.

Note, however, that a one to one relation between R/L_{n_Z} with the parameters plotted in the abscissae cannot be derived. The peaking of the impurity density profiles is determined by the magnitude of all three terms contributing to the turbulent transport, namely the thermodiffusion, rotodiffusion and pure convection. The coefficients encountered in each term depend on the mass, charge, impurity temperature and the parameters of the background plasma [114]. The datasets plotted here are not independent. As high R/L_{n_e}, low R/L_{T_i} and low u' all occur together, it is not possible to disentangle the different effects from these plots. This will be attempted in Section 6.3.5, via a regression analysis.

Nevertheless, good qualitative agreement is found between the theoretical predictions and the experimental data from these discharges.

Discharge with P_{NBI} scan

In discharge 30379, a scan of NBI power was performed on a background of 0.5MW of electron cyclotron heating. Comparison of the experimental data with the gyrokinetic modelling predictions of $R/L_{n_{He}}$ and R/L_{n_B} for this case (shown in Fig. 6.16), leads to very different results than those described in the previous section. Here, again there is an overall offset between measurement and theory, but now the qualitative trends are also different. Theory predicts increasing peaking of the helium profile with increasing

R/L_{n_e} and constant R/L_{n_B}, independent of the R/L_{n_e} variation. In the experiment, however, the opposite behavior is observed. Both $R/L_{n_{He}}$ and R/L_{n_B} are observed to decrease as R/L_{n_e} increases. Similar observations can be made looking at the variation with R/L_{T_i} and u'.

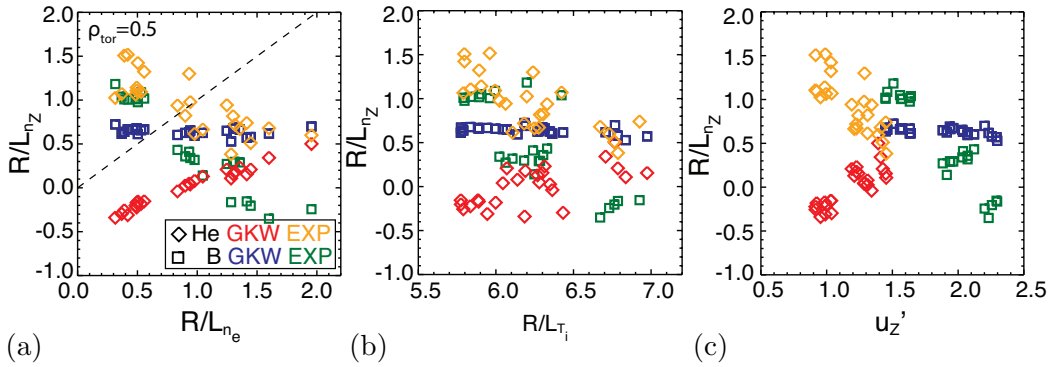

Figure 6.16: $R/L_{n_{He}}$ and R/L_{n_B}, both from gyrokinetic modelling predictions and experimental measurements $\rho_{tor} = 0.5$, plotted against a) R/L_{n_e}, b) R/L_{T_i} and c) u'_Z, for discharge 30379.

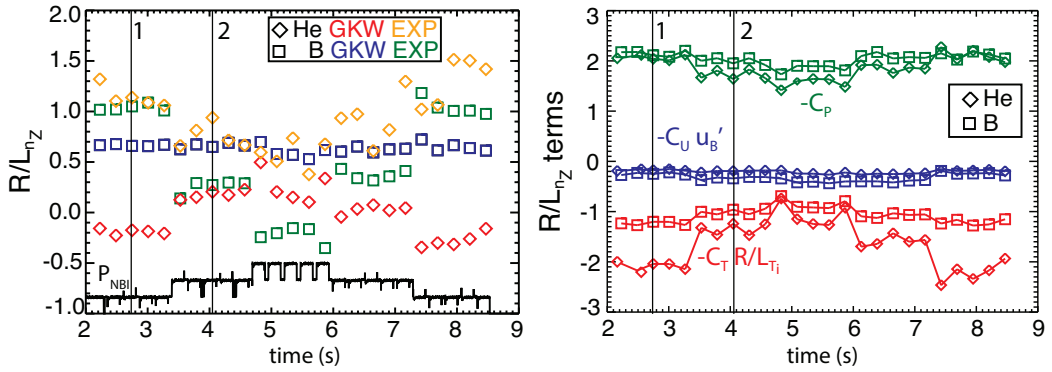

Figure 6.17: $R/L_{n_{He}}$ and R/L_{n_B}, both from gyrokinetic modelling predictions and experimental measurements $\rho_{tor} = 0.5$, plotted in time, for discharge 30379. The NBI power is also shown in arbitrary units.

Looking at the evolution of the impurity gradients in time during this discharge in Fig. 6.17, some light can be shed on this discrepancy. As the injected NBI power is increased, the plasma rotation and, subsequently, u' increases. According to the theoretical understanding of the rotodiffusion mechanism, at higher plasma rotation and higher u' values, less peaked impurity density profiles are expected. A strong rotation

gradient causes a flattening or even hollowing of the impurity density profiles. This is indeed confirmed experimentally for both impurities. However, looking at the theoretical prediction, it is found that almost no variation of R/L_{n_B} is expected through the discharge, while an opposite behavior to the one experimentally observed is predicted for helium.

We examine now each term contributing to the turbulent transport, as predicted by the gyrokinetic modelling, namely the thermodiffusive term $-C_T R/L_{T_i}$, directed outwards in this ITG dominated discharge, the rotodiffusive term $-C_U u'$, also directed outwards, and the pure convective term, directed inwards in all regimes. The contributing terms are plotted on the right hand side of Fig. 6.17. The sum of these terms returns the impurity gradients $R/L_{n_{He}}$ and R/L_{n_B} (see Eq. (4.27)).

The two time points identified with vertical lines in Fig. 6.17 are now compared (cases 1 and 2). These two points correspond to a high and low u' value point. In case 2 (higher u'), the helium thermodiffusive term is directed outwards, but is less strong than in case 1. The outward helium rotodiffusive contribution increases only slightly in case 2. The helium pure convection, which is always directed inwards, becomes less strong. However, the reduction of the outward thermodiffusive flux is larger than the reduction of the inward convective flux, leading to a more peaked predicted helium profile.

The situation is different for boron. The modelling predicts similar convective terms for the two time points. The boron rotodiffusive term leads to slightly stronger outward diffusion in case 2, while the thermodiffusive term is weakened by a similar amount, meaning that the two changes compete with each other, leading to almost no variation in time of R/L_{n_B}. The comparison here between theory and experiment suggests that the theory does not properly capture the u' dependence observed in the experiment, because the rotodiffusive term (blue lines) does not change as u' increases, while the thermodiffusive and pure convective contributions change in the wrong direction. However, as R/L_{T_i} is not constant over the change in u' it is impossible to disentangle these two contributions.

If the helium rotodiffusive term is underpredicted in the gyrokinetic modelling, a mechanism driving the helium ions outwards would be missing. A similar argument can be made for the thermodiffusive term. Additionally, a weaker inward convection would also help to achieve the flatter helium profiles observed around the second time

point. As a result, it is not easy to identify which is the missing mechanism in the theoretical description.

Discharge with deuterium fuelling scan

In discharge 30380, two steps of electron cyclotron power (0.5 and 1.7MW) have been applied on a background NBI heating of 2.5MW, at three different levels of increasing deuterium gas puff, increasing slightly the plasma collisionality with each step. The experiment versus theory comparison for this shot is shown in Fig. 6.18. Referring to this figure, it can be argued that several points at low and high R/L_{n_e} values follow the modelling trends shown here and in the previous sections. However, at $R/L_{n_e} = 1-2$, a subset of data points are found to have much higher values of $R/L_{n_{He}}$ and R/L_{n_B} than those predicted by modelling. Both impurities show comparable peaking in this subset.

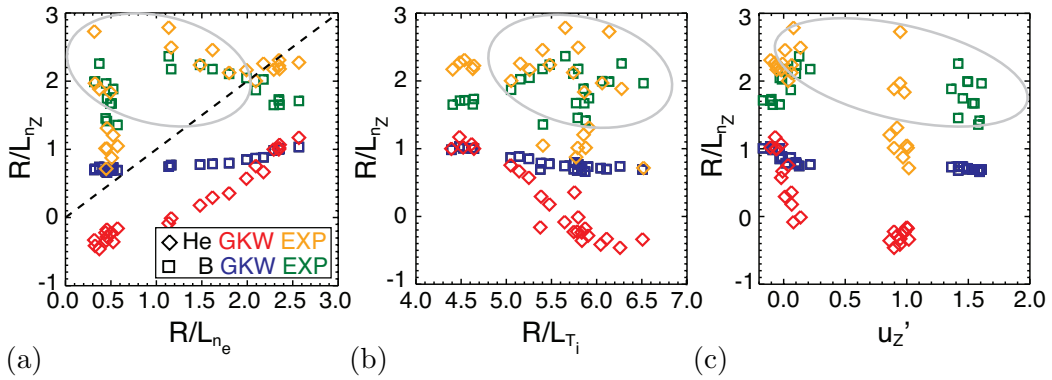

Figure 6.18: $R/L_{n_{He}}$ and R/L_{n_B}, both from gyrokinetic modelling predictions and experimental measurements $\rho_{tor} = 0.5$, plotted against a) R/L_{n_e}, b) R/L_{T_i} and c) u', for discharge 30380. The circles highlight the odd points.

Looking at the time evolution of $R/L_{n_{He}}$ and R/L_{n_B} during the discharge, Fig. 6.19, the discrepancy with the trends in the theoretical predictions appears after 5.5s. The deuterium gas puff is increased at 4.1 and 6.5s. Comparing the time points at the end of 30380 (after 5.5s), with parameters from the rest of the dataset, points with similar R/L_{n_e}, R/L_{T_i}, T_e/T_i, can be identified. This comparison reveals that these points have higher collisionality, as expected due to the increased deuterium puff, and also lower u'. Values of u' close to zero mean that rotodiffusion becomes less important, leaving thermodiffusion and pure convection to determine the transport.

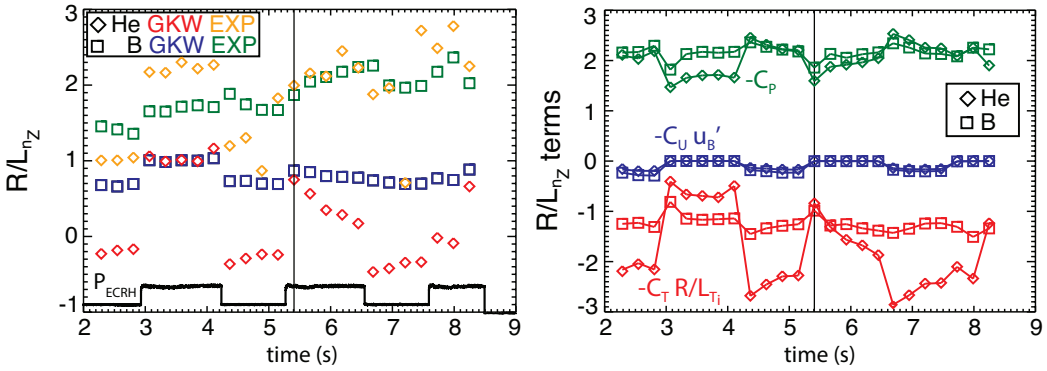

Figure 6.19: $R/L_{n_{He}}$ and R/L_{n_B}, both from gyrokinetic modelling predictions and experimental measurements $\rho_{tor} = 0.5$, plotted in time, for discharge 30380.

Examining each term contributing to the boron turbulent transport, obtained from the gyrokinetic modelling, it is found that the thermodiffusive term (i.e.$-C_T R/L_{T_i}$ on the right hand side of Fig. 6.19 - outward) is always smaller in absolute magnitude than the pure convection term (inward) by about 1 in this plasma discharge. The thermodiffusive term provides a slightly stronger outward diffusion towards the end of the discharge. Rotodiffusion provides a small contribution when $P_{ECRH} = 0$. For helium, the outward diffusion due to thermodiffusion increases rapidly from 5.5-6.5s, becoming almost equal to the inward convection after 6.5s. To explain the very peaked boron and helium profiles observed in the experiment, either pure convection should be much larger than thermodiffusion in absolute values, or thermodiffusion should be a much weaker effect than theoretically predicted.

Alternatively, there could be another, as yet unidentified mechanism at play that is not accounted for in the modelling. Sawteeth, ELMs and MHD activity have all been ruled out as possible culprits.

Complete dataset

For the sake of completion all the discharges in the helium transport database are plotted together in Fig. 6.20. Despite the overall offset and specific cases where the experimental observations do not agree with the modelling results, a general qualitative agreement is observed in the complete dataset. The ranges that the prediction and the measurement cover are similar, though with an offset exists, for both helium and boron.

Similar observation as those described above can be made also for $\rho_{tor} = 0.3$.

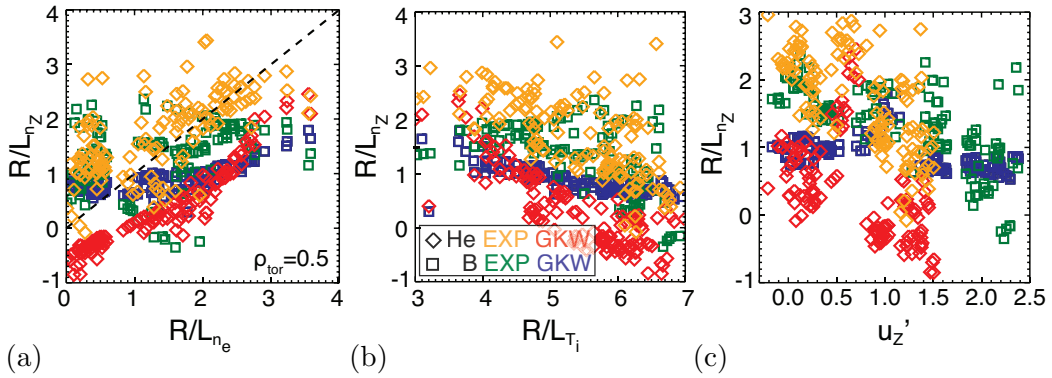

Figure 6.20: $R/L_{n_{He}}$ and R/L_{n_B}, both from gyrokinetic modelling predictions and experimental measurements $\rho_{tor} = 0.5$, plotted against a) R/L_{n_e}, b) R/L_{T_i} and c) u', for all discharges in the helium transport database. Here, neoclassical contributions are not included, as they are negligible at this location.

All of the observations made at $\rho_{tor} = 0.5$ hold for $\rho_{tor} = 0.3$ as well. The offset between theory and experiment remains, while in the case of boron the comparison in absolute values is shown to improve at $\rho_{tor} = 0.3$.

In summary, the trends for both boron and helium appear to agree with the gyrokinetic modelling. The predictions are overall too low, perhaps suggesting that an inward contribution is missing or that an outward contribution is too high. The errors on the data are significant (see Fig. 6.4), but cannot account for the discrepancies observed.

Sensitivity of gyrokinetic modelling to the input magnetic equilibrium

One of the most important sensitivities of the gyrokinetic modelling in terms of uncertainties in the input parameters is the uncertainty of the input magnetic equilibrium, as discussed extensively by Casson et al [11] (another very important uncertainty being the gradient of the input electron density profile). Uncertainties in the q profile influence the mode frequency and the coefficients of the turbulent transport terms, resulting in significant variations in the predicted R/L_{n_Z}.

Since no direct measurement of q is available for the shots in the database, the magnetic equilibrium is reconstructed from magnetic measurements. To check the sensitivity of the results presented here on the magnetic equilibrium, a pressure constrained magnetic equilibrium [13, 14], using the sawteeth inversion radius as a constrain for

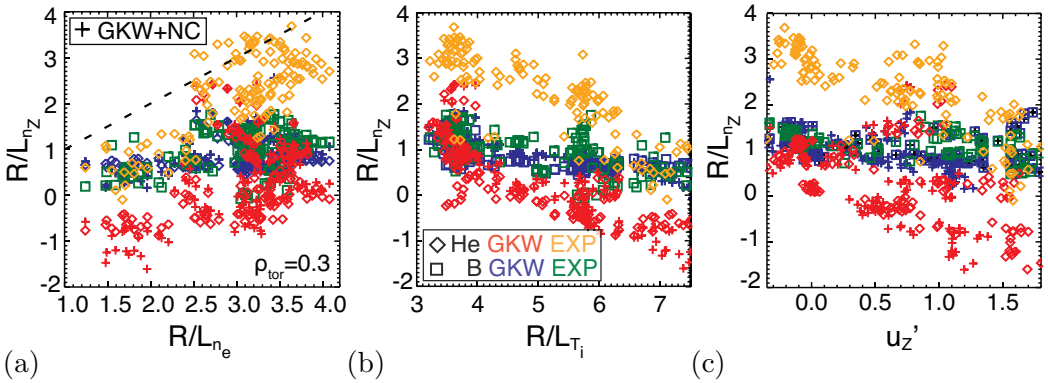

Figure 6.21: $R/L_{n_{He}}$ and R/L_{n_B}, both from gyrokinetic modelling predictions and experimental measurements $\rho_{tor} = 0.3$, plotted against a) R/L_{n_e}, b) R/L_{T_i} and c) u', for all discharges in the helium transport database. Squares and diamonds correspond to the theoretical predictions from GKW, while crosses correspond to the prediction taking into account both turbulent and neoclassical transport.

Table 6.2: Comparison of the gyrokinetic modelling predictions for the two equilibria.

	EQI, standard	EQI, improved
$R/L_{n_B}(\rho_{tor} = 0.3)$	0.7450	0.9086
$R/L_{n_{He}}(\rho_{tor} = 0.3)$	0.0460	-0.3472
$R/L_{n_B}(\rho_{tor} = 0.5)$	0.9365	1.5240
$R/L_{n_{He}}(\rho_{tor} = 0.5)$	0.2487	-0.1517

the $q = 1$ surface, is used as input to GKW. In Fig. 6.22, the standard and pressure constrained q-profiles and the magnetic shear profiles are shown.

The results of this exercise provide quite striking results. As expected, a significant variation in the predicted R/L_{n_B} and $R/L_{n_{He}}$ is found, but the effect is opposite for the two impurities. The exact values can be seen in Table 6.2. For boron the improved equilibrium with lower q and higher magnetic shear enhanced the peaking at both locations. For helium, however, the predicted profiles become hollow, increasing the discrepancy even further.

The effect of the magnetic equilibrium is large and, therefore, further analysis is required to pinpoint the reason that the effect is different for the two impurities. A scan of q and magnetic shear should be performed within the gyrokinetic modelling to clarify this observation.

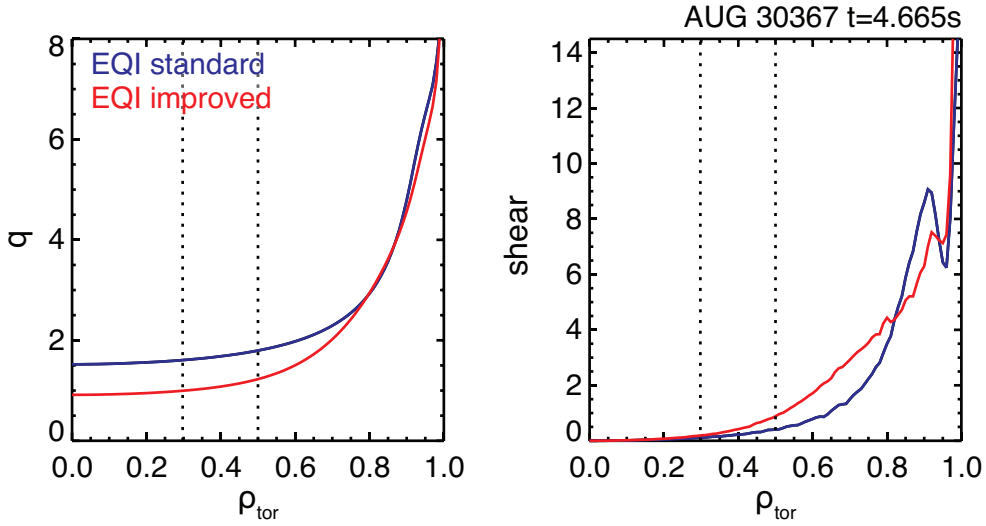

Figure 6.22: q and magnetic shear ($(1/r)(\mathrm{d}q/\mathrm{d}r)$) profiles taken from the standard and improved equilibrium.

6.3.5 Regression analysis

As the impurity density profiles at a certain location in the plasma are defined by the interplay of many plasma parameters, it is not straightforward to disentangle the dependencies with the different parameters in the experiment. For this reason, we perform a multi-variable regression analysis in order to identify strong correlations of $R/L_{n_{He}}$ and R/L_{n_B} with the plasma parameters expected to be important for turbulent transport. Examining the correlations, the best regressions of $R/L_{n_{He}}$ and R/L_{n_B} predicted by the gyrokinetic modelling are as follows:

$$\begin{aligned}\frac{R}{L_{n_{He}}}\Big|^{GKW} = 0.838 &- (0.298 \pm 0.028)\frac{R}{L_{T_i}} \\ &+ (0.306 \pm 0.042)u' \\ &+ (0.094 \pm 0.020)\frac{R}{L_{n_e}}\end{aligned} \tag{6.3}$$

$$\frac{R}{L_{n_B}}\Big|^{GKW} = 1.673 - (0.190 \pm 0.024)\frac{R}{L_{T_i}} + (0.080 \pm 0.022)u' + (0.094 \pm 0.020)\frac{R}{L_{n_e}} \tag{6.4}$$

The root mean square errors for the regressions are ~ 0.16 and ~ 0.13 for helium and boron, respectively. All three variables were found to be statistical significant, where significance is defined as the regression coefficient of the variable divided by its standard deviation. The criterion was $R/\sigma_R > 2$, where R is the regression coefficient and σ_R its standard deviation. Variables that have been found to be statistically insignificant have been removed. The success of the regression is shown on the left hand side of Fig. 6.23.

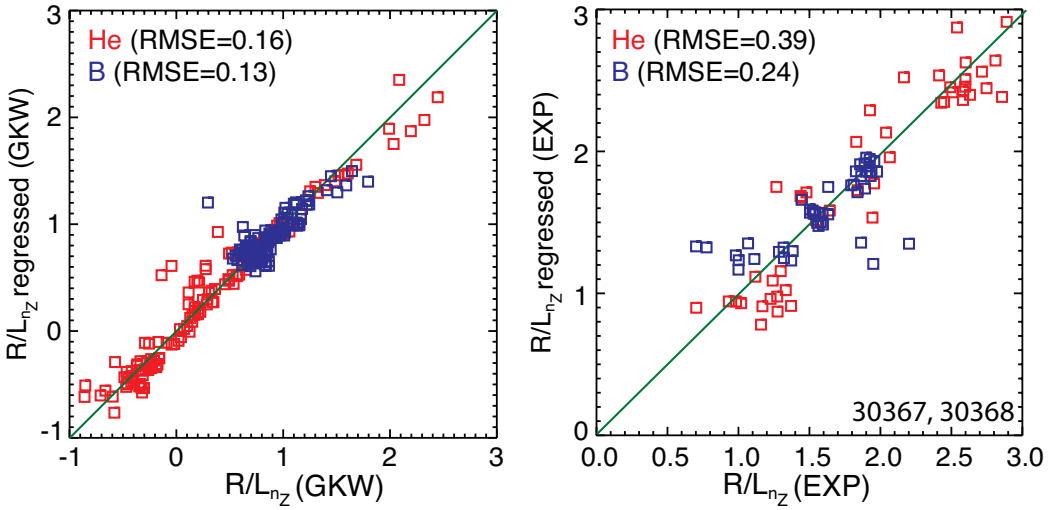

Figure 6.23: The regression of the predicted $R/L_{n_{He}}$ and R/L_{n_B} (left) and the experimentally measured values for discharges 30367 and 30368 (right).

In addition, the experimental values of $R/L_{n_{He}}$ and R/L_{n_B} have also been regressed against the same variables. However, these regressions are not as successful. This indicates that the scatter in the experimental data is too large or that an important (or several important) variables on which the true gradients depend have not been included in the analysis. All other attempts to regress the experimental $R/L_{n_{He}}$ and

R/L_{n_B} values using other parameters also failed. As was shown in Section 6.3.4, the gyrokinetic modelling qualitatively reproduces a subset of the data points very well, we attempt to regress only those. The regression gives:

$$\begin{aligned}\frac{R}{L_{n_{He}}}|^{exp} = 0.092 &+ (0.142 \pm 0.181)\frac{R}{L_{T_i}} \\ &- (0.149 \pm 0.192)u' \\ &+ (0.730 \pm 0.130)\frac{R}{L_{n_e}}\end{aligned} \tag{6.5}$$

$$\begin{aligned}\frac{R}{L_{n_B}}|^{exp} = 0.117 &+ (0.220 \pm 0.111)\frac{R}{L_{T_i}} \\ &- (0.121 \pm 0.074)u' \\ &+ (0.328 \pm 0.079)\frac{R}{L_{n_e}}\end{aligned} \tag{6.6}$$

with root mean square errors of ~ 0.39 and ~ 0.24 for helium and boron, respectively, meaning the experimental measurements are still not well reproduced by this regression. Note that for both of the experimental regressions all of the variables apart from R/L_{n_e} can be dropped due to very low statistical significance. The correlation of $R/L_{n_{He}}$ with R/L_{n_e} is stronger than that of R/L_{n_B}. In contrast to the theoretical predictions, the experimental data do not show any correlation with either R/L_{T_i} or u', the two parameters indicated in the theory equations. The only thing they have in common is R/L_{n_e}, which is perhaps the dominant parameter in creating the qualitative trends observed in Fig. 6.15 .

6.4 Conclusions

As helium will be a critical parameter in the successful operation of fusion reactors, understanding the processes that determine the helium density profile is necessary. Transport theory provides predictions of the behavior of helium in ITER. Nevertheless, the current theoretical understanding has to be tested and validated against experimental measurements in present devices. This has been the focus of the work described in this chapter.

Parameters theoretically relevant to the turbulent impurity transport were varied

in a set of experiments performed on ASDEX Upgrade, in order to study the transport properties of helium and boron. The boron density profile is always found to be less peaked than the electron density profile, while the helium density profile is found to be similar to the electron density. This is consistent with previous observations of helium transport performed in DIII-D [122].

As neoclassical contribution are small or negligible, gyrokinetic modelling of these discharges gives the theoretical predictions for the behaviour of the impurities, in terms of the normalised logarithmic impurity density gradients R/L_{n_B} and $R/L_{n_{He}}$. Comparison of the experimentally deduced R/L_{n_B} and $R/L_{n_{He}}$ with the results of gyrokinetic modelling shows, under some conditions, qualitative agreement and for boron almost quantitative agreement, as has been shown in previous boron studies performed [11, 27]. However, several cases have also been identified where the turbulent modelling cannot describe the experimental observations. Moreover, a regression of predicted versus measured data shows little in the way of commonality except for their mutual correlation with R/L_{n_e}. This might play a role in explaining the qualitative agreement observed in the comparison. If the helium profile follows closely the electron density profile in ITER, as suggested by the DIII-D and ASDEX Upgrade experimental data, this would result in detrimental effects on plasma operation due to the increased content of thermal helium in the plasma core. The interactions with respect to the modelling between the different plasma parameters, as well as the dependencies of the coefficients are complicated. No direct conclusion can be drawn on which term is responsible for the discrepancy with the experimental observations. Additional experiments are required in order to disentangle these dependencies, preferably in plasma discharges where only one parameter is varied at a time, within the limits of what is experimentally possible. Furthermore, a completely different mechanism or parameter dependence might be responsible for the observed profile peaking that is not included in the turbulent transport theoretical framework. Further work on the theoretical side is motivated by these results.

As the gyrokinetic modelling is sensitive to input parameters such as the plasma equilibrium, further investigations are required to characterise the uncertainties of the modelled R/L_{n_B} and $R/L_{n_{He}}$ values in this database. Although linear gyrokinetic simulations are generally found to be in good agreement with non-linear gyrokinetic

simulations [114], non-linear calculations can potentially produce additional information on the sources of the discrepancy.

7

Feasibility of charge exchange measurements of slowing down alpha particles on ITER

Charge exchange recombination spectroscopy is a successful diagnostic in providing the ion temperature and rotation profiles as well as impurity densities and, as such, it is foreseen for ITER to diagnose the helium ash. In addition to thermal helium measurements, CXRS can potentially play a role in diagnosing the non-thermal fusion products. Fast α densities and information on the properties of the distribution function of fast particles can be obtained by looking at the wings of the CX spectrum.

ITER will be the first burning plasma physics experiment with dominant α particle heating. The D-T plasma will be heated by the slowing down of the fusion produced

α particles, born at 3.5MeV. One step further, in a fusion reactor, the α power must balance the bremsstrahlung and thermal conduction losses, in order to achieve ignition. As such, the study of issues relevant to the energetic α's, such as fast ion transport and interaction with plasma instabilities will be a priority for ITER operation.

Magnetohydrodynamic instabilities such as sawteeth or toroidal Alfvén eigenmodes may enhance the transport or cause the redistribution or loss of these energetic particles. Moreover, these instabilities might be driven by the energetic particles themselves.

The importance of understanding the α particle confinement and slowing down process is threefold: Firstly, poor energetic α particle confinement reduces the chance of achieving a self-heated plasma. Secondly, it also means that expelled high energy ions might cause damage to the plasma facing components. Finally, the helium "ash", the α's that have slowed down and transferred almost all their energy to the plasma, have to be removed to avoid dilution of the fusion fuel and prevent choking the fusion reactions.

Measurements of the confined α particle properties are needed to study their confinement and transport mechanisms. Diagnostics that can provide information on the profiles and velocity distribution are needed. Specifically, according to ITER requirements, the energy spectrum and density profiles of confined α's of 0.1 to 3.5 MeV should be measured with an accuracy of 20%, with a time resolution of 100ms and a spatial resolution of $a/10$, where a is the tokamak minor radius [81]. CXRS is one of the two diagnostics that can potentially provide information on fast α's, the other being collective thomson scattering [130]. Both, however, are limited by the fact that an inversion of the measurements to infer the distribution function unambiguously is not possible with a limited number of lines-of-sight.

The use of CXRS for fast α particles diagnosis on ITER will be hindered by the small fast ion signal in comparison to the background emission. Nevertheless, CXRS will be part of the ITER diagnostic suite with the main goal of contributing to the helium ash and impurity studies. The main goal of this chapter is to examine whether the core ITER CXRS diagnostic can serve as a diagnostic for non-thermal helium and what its capabilities are for this type of measurement.

In Section 7.1 the CXRS diagnostic technique for fast α's is explained. Thereafter, the simulation package used for the modelling of the fast helium CX spectrum is

described in Section 7.2 and the results obtained are presented in Section 7.3. Afterwards, in Section 7.4, the outcome of this feasibility study is discussed and compared with previous studies of this type [131] as well as alternative measurements of fast helium on ITER. Finally, though this chapter concentrates on reviewing the feasibility of non-thermal helium charge exchange measurements on ITER, a brief consideration of what charge exchange can achieve by measuring the helium "ash" on ITER is given in Section 7.5. The contents of this chapter have been published in [132].

7.1 Fast ion charge exchange diagnostic technique

The technique of fast ion CXRS has been applied successfully on a number of devices, for instance to measure beam injected fast helium at JET [60], beam injected fast deuterium at ASDEX-Upgrade [74], TEXTOR [133] and DIII-D [75] and for fusion produced α's at TFTR [134]. The diagnostic technique for measuring fusion produced α's is the same for thermal helium or beam ions, with the difference that the information on the fusion produced α's, which have a much higher energy, is found in the wings of the helium charge exchange line. Nevertheless, the distribution function of fast α's differs from both the thermal and beam ions and as a result the interpretation of the measurements is different. The distribution function of fusion-produced α's is considered to be isotropic [135] (though finite orbit width effects can cause the distribution function to be anisotropic), in contrast to beam originating fast ions which have a strongly anisotropic distribution function [75, 136].

Assuming only Coulomb collisions, without any transport due to instabilities, the distribution function that describes the slowing down fusion produced alpha particles is approximately [135]:

$$f_{sd}(v_\alpha) = \frac{S_\alpha \tau_{se}}{v_\alpha^3 + v_c^3}. \tag{7.1}$$

S_α is the α particle source rate, $S_\alpha = n_D n_T \langle \sigma v \rangle (T_i)$, where n_D and n_T are the deuterium and tritium densities diluted due to impurities and $\langle \sigma v \rangle$ are the velocity averaged fusion cross sections, which depend on the ion temperature T_i. The α particle source rate is rather peaked, following the shape of the ion temperature profile. The slowing down distribution function is zero for velocities higher than the birth velocity of the α's, so Eq. (7.1) should in principle be multiplied by a step function. It should be noted, however, that Doppler shifts give a spread of birth energies of order $\sqrt{QT_i}$, where Q is

the energy released in the reaction, in other words, no single υ_α can be defined. Furthermore, due to Coulomb collisions, there is an exponential tail with slope of order T_e and T_i above the birth energy. υ_c is the critical velocity where fast-ion drag on thermal electrons equals fast-ion drag on thermal ions, and can be defined as [137]:

$$\upsilon_c^3 = \frac{3\sqrt{\pi}m_e}{4n_e}\left(\frac{2T_e}{m_e}\right)^{3/2}\sum_j \frac{n_j}{m_j}Z_j^2, \tag{7.2}$$

where the summation is performed for all plasma ions. In Eq. (7.1), τ_{se} stands for the Spitzer slowing down time, which takes into account only the slowing down due to the electrons. The actual (effective) slowing down time (the time that the fast α particle needs to thermalise) is smaller than τ_{se}, as it takes ion collisions into account as well and is a function of υ_α:

$$\tau_{sd} = \frac{\tau_{se}}{3}\ln\left(1+\left(\frac{\upsilon_\alpha}{\upsilon_c}\right)^3\right). \tag{7.3}$$

The main difficulty in using CXRS for fast ions measurements is the small fast ion signal in comparison to the background emission. The measured fast ion CX spectrum is a convolution of the fast ion velocity distribution function and the collision energy dependent CX cross-sections multiplied by the neutral beam density projected on the line-of-sight. The fast ion charge exchange signal is, therefore, proportional to the α particle density in the plasma and the local density of the neutral beam. More precisely, the α particle density is given by:

$$n_\alpha = \int f_{sd}(\upsilon)\upsilon^2 d\upsilon = \tau_{sd}S_\alpha = \frac{S_\alpha\tau_{se}}{3}\ln\left(1+\left(\frac{\upsilon_{birth}}{\upsilon_c}\right)^3\right). \tag{7.4}$$

The local neutral beam density depends on the beam attenuation along the beam path, given simply by $n_b = n_b(0)exp(-\int dl\sigma_{stop}n_e)$. Here $n_b(0)$ is the neutral beam density when the beam enters the plasma, n_e is the electron density and σ_{stop} are the beam stopping cross sections. Even if the neutral beam attenuation is strong, it is not expected to induce a large systematic error as the local beam density can be derived from beam emission spectroscopy [133]. Rather, the uncertainty on the measurement is expected to come from the photon noise, which is approximately the square root of the signal. However, the signal is dominated by the bremsstrahlung background emission. The bremsstrahlung level is orders of magnitude larger than the CX signal for fast ions

and proportional to $n_e^2 Z_{\text{eff}} T_e^{-1/2}$, where T_e is the electron temperature and Z_{eff} is the effective charge of the ions in the plasma.

The energy dependent charge exchange cross sections Q_{CX} for the charge exchange reaction $\text{H}(\text{n} = 1, 2) + \text{He}^{2+} \rightarrow \text{H}^{+} + \text{He}^{+}(\text{n} = 4)$ are shown in Fig. 3.6. The fraction of hydrogen in the first excited state is small (approximately 1.5%), but due to much higher cross-sections, it is also important. For the contribution of hydrogen in the ground state the charge exchange cross-sections have a maximum around a helium - beam neutral collision energy of 35keV/amu, dropping fast for higher energies. The collision energies of a 100keV/amu beam with 1MeV ions, for example, will range from 0.9 to 1.1 MeV and thus far away from the maximum of the cross-sections. The collision energies of a higher energy beam, for example 1MeV/amu neutral beam, with 1MeV ions, will range from 0 to 2 MeV, including the 35keV/amu where the cross-sections are maximum, providing a chance to detect these high energy ions. Apart from the collision energy dependence, the charge exchange cross-sections Q_{CX} and the beam stopping cross-sections σ_{stop} also depend on the local values of n_e, T_e, T_i and the impurity concentration.

The charge exchange measurements of fast helium on ITER will be more difficult than in any present day device. For example, in the D-T operation of TFTR the fast helium signal over the bremsstrahlung level was already very low, less than 1% [134]. In comparison, the ITER case differs in the following aspects: Firstly, due to the higher density, the bremsstrahlung level will be higher (factor 5-10). Secondly, for the same reason, the diagnostic beam penetration will be lower (factor 10-100). The heating beam will have a lower beam particle flux (factor 10) and directionally very selective cross-sections. All these issues considered, the signal-to-noise ratio will be 100 times worse than in TFTR, despite the fact that the α particle density will be 30 times higher on ITER.

7.2 Simulation package for charge exchange spectroscopy

A simulation package has been used to assess the feasibility of fast helium CX measurements on ITER by modelling the expected CX spectra [138, 139]. The code simulates the geometry of the tokamak and the neutral beam injection system. The plasma profiles and beam parameters are inputs, with the option to use real profiles from current

tokamaks. The dilution of the plasma due to impurities is also taken into account and the impurity composition can be specified in order to calculate Z_{eff} and the beam attenuation. Only the helium line is simulated. Other impurity lines that may be present in the same wavelength range are not included in the simulation.

The charge exchange emission rates and the beam stopping cross-sections are taken from ADAS [71]. In addition, the instrumentation specifications of a virtual spectrometer, parametrised by the effective transmission, are defined in order to allow for the reconstruction of the observed spectrum. The geometry and specifications of several existing fusion devices can be simulated in addition to ITER.

The spectra of both fusion produced α's and beam injected fast ions can be simulated. Specifically, the source rate of the fast ions is calculated and multiplied with the slowing down distribution function (Eq. (7.1)), so as to obtain the fast ion velocity distribution [140]. The distribution function is convoluted with the collision energy dependent charge exchange emission rates and subsequently projected on a line-of-sight. The result is multiplied with the local density of the neutral beam acquired from a beam attenuation calculation and then summed up, giving the observed fast ion spectral shape [60]. Finally, bremsstrahlung is added to the simulated spectrum, taking into account the optical throughput and quantum efficiency of the virtual diagnostic. Poisson noise is assumed to be the dominant source of noise limiting the signal-to-noise ratio (S/N) on ITER. It is this S/N ratio that will be used as a figure of merit to determine the feasibility of CX measurements of fast helium in this work.

Before proceeding with the study of ITER, an attempt was made to benchmark the simulation results of the fast α CX spectra against the $\alpha-$CHERS TFTR measurements [134]. The instrument specifications and experiment details given in [66, 134], in combination with the TFTR beam geometry were used in order to simulate the spectra from the 6MW fusion power shots. For fast α densities of approximately 10^{17}m^{-3}, the simulation code gives a S/N of about 10, comparable to the values of 5-10 mentioned in the $\alpha-$CHERS publications. The intensity of the fast helium signal is about 1% of the bremsstrahlung level in our calculations, while it is stated to be less than 1% in the publications. It should be mentioned that assumptions have been made regarding the plasma profile shapes and spectrometer parameters used as input in the code. However, a sensitivity study has been carried out to estimate the effect of input changes on the final results, coming to the conclusion that the S/N and the signal to bremsstrahlung

emission ratio remain of the same order of magnitude as was measured. Consequently, the code can be used with confidence to evaluate the ITER fast α spectrum and noise levels, with the aim to assess the feasibility of non-thermal helium measurements.

7.3 Simulation of the non-thermal helium charge exchange spectrum

In order to assess the feasibility of CXRS measurements of fast helium on ITER, the active CX fast helium spectrum is modelled. The collision energy dependent cross sections and the effective throughput of the detection system are taken into account to enable a quantitative study. The simulation for ITER focuses on the n=4-3 transition in He^+ at 4686Å, for charge exchange between He^{2+} and H(n=1,2). The design parameters of the spectrometer and the plasma conditions used as input to this simulation can be seen in Table 7.1. A 600MW fusion power shot with a fuel mixture of 50% D and 50% T and a fast α density of $1.5 \cdot 10^{18} \mathrm{m}^{-3}$ are assumed as input parameters.

On ITER two neutral beams will be available for CX measurements, the diagnostic neutral beam (DNB, hydrogen) with an energy of 100keV/amu [141] is specifically intended for CX measurements, and the heating neutral beam 2 (HNB, deuterium) with an energy of 500keV/amu [142]. The lines-of-sight of the CX system foreseen for ITER and the path of the neutral beams are shown in Fig. 7.1.

To illustrate the main problem, simulated ITER spectra for CX on the DNB and the HNB are shown in Fig. 7.2. The expected CX spectra from the two neutral beams are very different and the feasibility of CXRS measurements on each of the beams has to be examined separately. As discussed before, only with the higher energy beam it will be possible to detect higher energy ions. One sees that the fast ion signal is two orders of magnitude lower than the thermal signal for the DNB case, while the fast ion signal on the HNB has an even lower intensity.

The CXRS measurements on the DNB and the HNB are simulated, with a dispersion of 0.2Å/px (according to ITER requirements) at normalised radius $\rho \approx r/\alpha = 0.5$. The choice for the location of the simulated spectra shown here ($\rho = 0.5$) can be explained by examining Fig. 7.3. Here, the attenuation of the two neutral beams and the α particle density are shown in the left plot. Despite the fact that the HNB is not as strongly attenuated as the DNB, the HNB enters the plasma with a much lower neutral density,

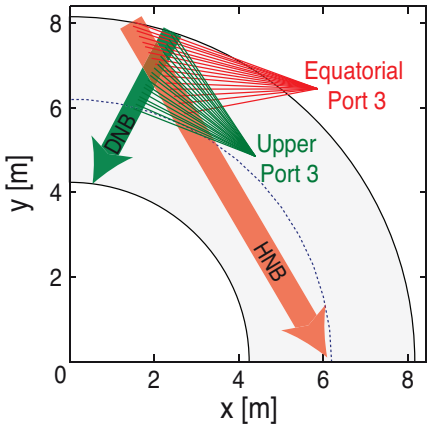

Figure 7.1: Illustration of the top down view of the diagnostic neutral beam (DNB, injected from Equatorial Port 4) and heating neutral beam (HNB, injected between Equatorial Ports 4 and 5) geometry on ITER, together with the lines-of-sight of the charge exchange diagnostic, looking from Upper Port 3 and from Equatorial MSE Port 3 respectively.

which means lower CX signal for the same cross-sections. An impression of where the fast α CX intensity will be highest can be obtained by looking at the product of the neutral beam density and the fast α density plotted in the bottom panel. If there is a possibility to measure the fast α's, it will be in the region $\rho = 0.4 - 0.8$. It should be stressed that this is not the complete picture: The actual CX intensity in the simulation code is calculated taking into account the slowing down distribution function of the α's, the charge exchange cross-sections and the geometry of the line-of-sight and the neutral beam. The location $\rho = 0.5$ was chosen based on the desire to measure fast alphas as close to the center of the plasma as possible, where they are born, while still maintaining a good signal. Furthermore, $\rho = 0.5$ is associated with the q=1 surface on ITER, which is of interest for example for sawteeth studies. The signal-to-noise ratio of the measurements drops rapidly for $\rho < 0.4$, due to the beam attenuation.

The simulated CX spectrum for the DNB, looking from Upper Port 3, and the HNB, looking from Equatorial MSE Port 3, are shown in Fig. 7.4. They are plotted as a function of the α particle energy along the line-of-sight (Doppler shift). Since otherwise it would be very difficult to distinguish the fast ion signal, the CX intensity is plotted without the noise added to the signal. In this figure the noise level per pixel (0.2Å) is indicated separately and is calculated with an effective optical throughput

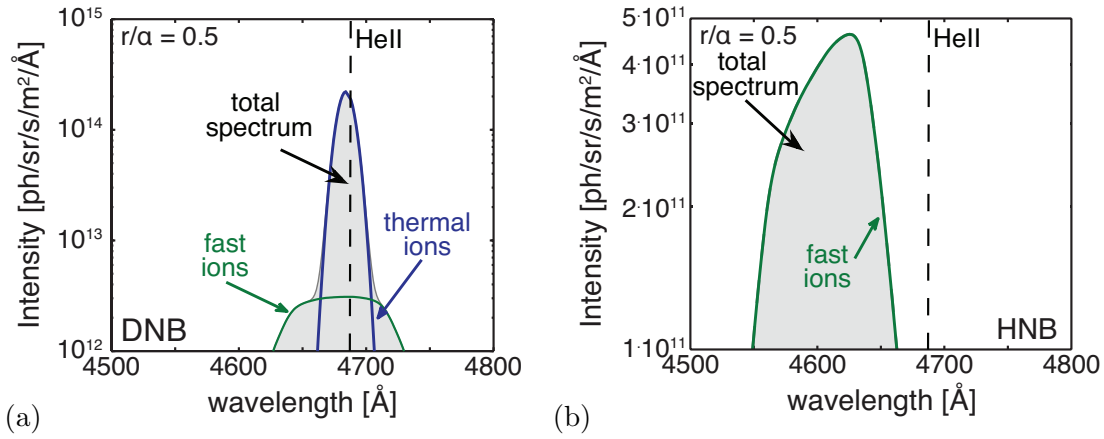

(a) (b)

Figure 7.2: Simulation of the CX spectra in ITER for (a) the diagnostic neutral beam and (b) the heating neutral beam at $\rho \approx r/\alpha = 0.5$. The wavelength of the HeII line (n=4-3 transition) at 4686Å is indicated. The fast ion spectra are shown in addition to the thermal ion spectra. The fast ion signal is very low in comparison to the thermal ion signal for the spectrum on the DNB. On the contrary, it is the main contribution to the CX spectrum for the measurements on the HNB, though at least an order of magnitude smaller. Here the thermal ion contribution is on the order of 10^6 and, therefore, not visible in this scale. Note, however, the change in the range of values of the CX intensity axis. The bremsstrahlung background value in this case is $5.82 \cdot 10^{15}$ph/sr/s/Å/m^2.

$\eta = \varepsilon\ t_{exp}\ QE\ T = 4.5 \cdot 10^{-8}$mm^{2}srs, assuming Poisson noise on the bremsstrahlung radiation, where ε is the étendue, t_{exp} the exposure time, QE the quantum efficiency and T the optical transmission.

It is observed that the DNB based diagnostic will be sensitive only to lower energy

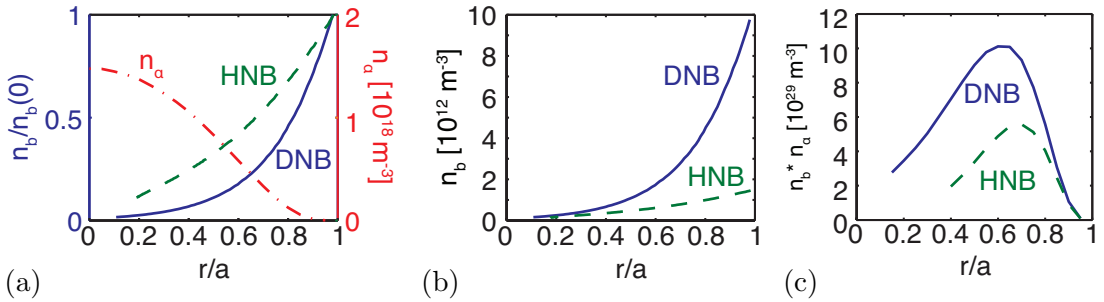

(a) (b) (c)

Figure 7.3: a) The attenuation factor of the diagnostic (DNB, ——) and the heating (HNB, - - - -) neutral beam along the beam path, for the plasma parameters in Table 7.1. The α density is also shown (— · —). b) The density of the diagnostic and the heating beams, for the normalised radius ρ. c) The product of the beam density (DNB, ——, HNB, - - - -) and the fast α particle density is plotted, for the plasma parameters in Table 7.1.

Table 7.1: The specifications of the ITER core CXRS spectrometer and the plasma and heating (HNB) and diagnostic (DNB) neutral beam parameters that are used as input in the simulation code.

ITER core CXRS		Plasma parameters
Etendue	$\varepsilon = 1\text{mm}^2\text{sr}$	$n_e = 10^{20}(1-\rho^2)^{0.1}\text{m}^{-3}$
Quantum efficiency	$QE = 90\%$	$T_e = 25(1-\rho^2)^{0.5}\text{keV}$
Optical transmission	$T = 5\%$	$T_i = 21(1-\rho^2)^{0.8}\text{keV}$
Dispersion	0.2Å/px	$v_{tor} = 200(1-\rho^2)^{0.5}\text{km/s}$
Slit width	1mm	$Z_{\text{eff}} = 1.62$
Neutral beams	HNB	DNB
Species	Deuterium	Hydrogen
Energy	500keV/amu	100keV/amu
Power	17MW	3.6MW
Divergence	7mrad	10mrad
$w_\perp$ (at duct)	0.18m	0.20m

ions (thermal α's). The blue shifted wing is the preferred wing for α particle detection, because both the Equatorial and Upper Port 3 look towards the beams and the CX cross sections are higher for fast ions moving along the beam. Using the DNB, CXRS can provide useful information for α's of a few hundreds keV, while in the case of the HNB the signal-to-noise ratio is less than one for all energies. Higher energy neutral beams would be necessary in order to extend the range of α particle energy (along the line-of-sight) that can be diagnosed with CXRS to 3.5MeV. With the current beam configuration planned for ITER, only fusion produced α's that have slowed down considerably (much less than 1MeV ions) can be detected.

Note, these calculations were performed assuming the reference design of the CXRS diagnostic. If the optical throughput of the diagnostic changes, and energy binning of the signal is applied, these measurements can be improved. This is explained in the next section.

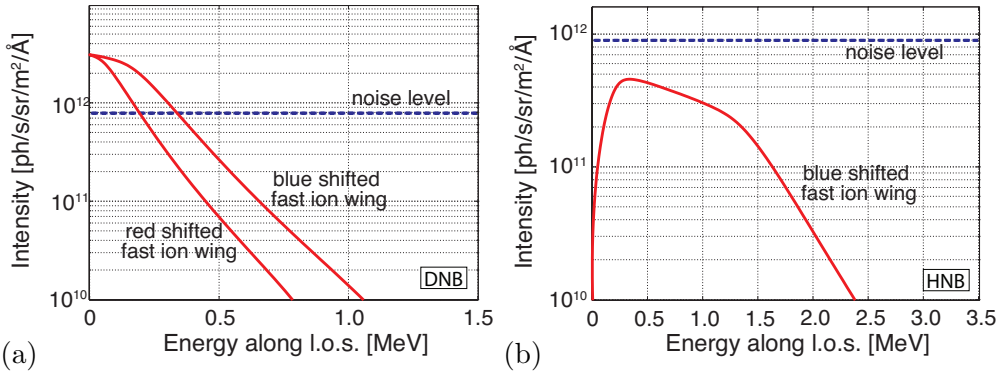

Figure 7.4: Modelled fast helium slowing down spectra for ITER, at full spectral resolution of 0.2Å/px, with an exposure time $t_{exp} = 1$s. The modelled spectra are shown this time without the noise added to the signal. The noise level per pixel is also indicated.

7.3.1 Signal-to-noise ratio

The signal-to-noise ratio is used as a figure of merit to determine whether non-thermal helium measurements will be feasible on ITER. The accuracy of the fast particle density measurement is related to the S/N, assuming that the error in the local neutral beam density is negligible. Keeping in mind that in the measured signal the bremsstrahlung contribution is much larger than the fast ion signal, it can be concluded that:

$$\frac{\delta n_{fast}}{n_{fast}} \propto \frac{\delta S}{S} \approx \frac{N}{S} = \frac{1}{S/N}, \tag{7.5}$$

where n_{fast} is the fast particle density, while S and N are the CX signal and noise, respectively. In other words, the accuracy of the fast ion measurements is inversely proportional to the signal-to-noise ratio.

The signal-to-noise ratio is partly determined by the diagnostic instrumentation, i.e. the optical throughput, étendue, optical transmission and exposure time of the CX spectrometer [60, 143]. By increasing the effective throughput of the system, one can try to compensate for the low signal-to-noise ratio. In an attempt to improve the signal-to-noise ratio, a lower energy resolution is chosen and the signal is binned in energy bins. For the CXRS diagnostic on the DNB, bins of 100keV are used (corresponding to $\Delta\lambda \sim 8 - 14$Å), while larger bins up to 400keV are selected for the HNB case (corresponding to $\Delta\lambda \sim 24$Å).

To characterize the diagnostic instrumentation, the 'effective' optical throughput

of the spectrometer is defined as $\eta = \varepsilon\ t_{exp}\ QE\ T$, incorporating all the diagnostic design parameters that have an effect on the S/N. The parameter η corresponds to the efficiency with which photons are collected: The signal S is proportional to η and the noise N is proportional to $\sqrt{\eta}$, leading to the following equation for the S/N:

$$\frac{S}{N} = \frac{\int S\,\mathrm{d}\lambda}{\frac{1}{\eta}\sqrt{(\int S\,\mathrm{d}\lambda + \int C\,\mathrm{d}\lambda)\eta}} \approx \sqrt{\frac{\eta\Delta\lambda}{C}} \int S\,\mathrm{d}\lambda, \tag{7.6}$$

where $\int S\,\mathrm{d}\lambda$ and $\int C\,\mathrm{d}\lambda$ are the fast helium signal and the continuum level integrated over a wavelength range $\Delta\lambda$, equivalent to a ΔE energy range. A higher η, and thus a higher S/N, can be achieved with a higher transmission and/or étendue, or by increasing the exposure time (lower time resolution). The fitting of the bremsstrahlung is assumed to induce no errors. The determination of the background emission, such as impurity lines, can be done using beam modulation in the case of the DNB. This information can subsequently be used for the interpretation of the background emission for the lines-of-sight through the HNB. The beam modulation subtraction increases the noise and the S/N should be approximately divided by $\sqrt{2}$ if beam modulation were used to subtract the passive emission, as the background intensity is much higher than the active signal and Poisson noise scales as the square root of the total signal. The S/N as a function of η is plotted in Fig. 7.5 for the DNB and the HNB for the different energy bins. The dashed vertical line on the left corresponds to the reference values of the CXRS diagnostic design and an exposure time of 1s. The spectra shown in 7.4 correspond to this vertical line.

A better time resolution could be obtained for a higher étendue of the spectrometer. Nonetheless, there is an upper limit for the étendue that can be achieved: The distance from the mirror to the point of intersection between the neutral beam and the line-of-sight is 5.1m for the DNB and 3.5m for the HNB. Assuming a mirror diameter of 10cm and a 10cm beam spot size, the étendue on the plasma side is 2.37mm^{2}sr for the port looking to the DNB and 5.03mm^{2}sr for the port looking to the HNB. Following the principle of conservation of étendue and assuming that this étendue can be conserved along the optical path, the maximum étendue on the spectrometer side is also 2.37mm^{2}sr and 5.03mm^{2}sr, limited by the tokamak optics.

A higher optical transmission can be assumed as well. However, the maximum

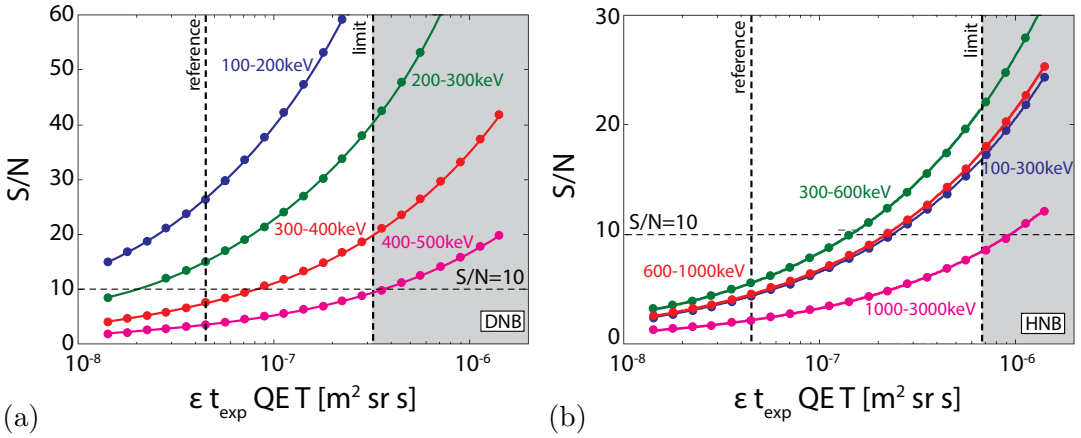

Figure 7.5: The signal-to-noise ratio for CXRS on fast helium is plotted as a function of the effective optical throughput of the diagnostic. The signal is binned over energy bins of 100keV for the DNB case (a), while larger energy bins are used for the HNB case (b). The reference values of the core CXRS diagnostic design, but with an exposure time of 1s are indicated by the vertical dashed line on the left ($\epsilon = 1\text{mm}^2\text{sr}$, $t_{exp} = 1\text{s}$, $T = 5\%$, $QE = 90\%$). A higher throughput but also limiting set of diagnostic design parameters are indicated by the vertical dashed line on the right ($\epsilon = 5.03\text{mm}^2\text{sr}$, $t_{exp} = 1\text{s}$, $T = 15\%$, $QE = 90\%$). The grey area is inaccessible due to the limitations on the 'effective' optical throughput. The S/N of 10 corresponds to a 1-σ accuracy of 10%. The fast ion signal and continuum level can be seen in Figure 7.4.

transmission is also limited by the first mirror reflectivity, the optical transmission of the periscopes and the losses along the optical path, including the spectrometer. As a result, only an improved transmission of 15% can be assumed. Stretching the design to the optimum, in other words using the maximum étendue and the improved transmission, for an exposure time of 1s, the values indicated by the second vertical dashed line on the right of Fig. 7.5 are obtained. It should be emphasized that the higher throughput diagnostic described here, is not just a more optimistic design, but a limitation in what can be achieved. It is not the optics and performance of the spectrometer that is the limiting factor here, but the optics on the tokamak side.

The S/N that is needed for reliable measurements can be related to the accuracy that can be obtained in the CX intensity. A S/N=10, which is also denoted by a horizontal dashed line in Fig. 7.5 corresponds to a 1-σ accuracy of 10% on the fast α CX intensity. If a lower measurement accuracy can be tolerated, a lower S/N can be chosen. Consequently, a CX spectrometer diagnostic with the reference design parameters mentioned earlier and indicated by the left vertical dashed line in Fig. 7.5, can provide

information on the fast ions of energy 0.1-1MeV, when looking at both the DNB and the HNB, at a time resolution of 2s and an accuracy of 10%. If the higher throughput instrumentation described is used to look and the DNB and HNB, with design parameters indicated by the second vertical dashed line, a better exposure time of 200ms can be achieved for α's up to 1MeV.

7.3.2 ITER operating scenarios

For this study, certain plasma parameters and profile shapes have been assumed as input to the simulation code (Table 7.1). The exact plasma parameters of ITER operation are not known, so assumptions have to be made. To assess how much these assumptions affect the resulting S/N ratios that have been shown, an attempt is made to evaluate the sensitivity of S/N on changes in the plasma parameters, namely n_e, T_e, T_i and Z_{eff}. To characterize the complex dependence of S/N on local plasma conditions, the simulation code is used to simulate shots that have a fusion power output $\approx 600MW$, varying the plasma parameters. The S/N decreases with increasing n_e and Z_{eff}, while no strong effect of T_e is apparent. There is no effect of T_i, except for the fact that the changes in n_e need to be compensated with a change in T_i to have the same fusion power output.

The effect of n_e on the S/N is the strongest one and so the electron density is considered to be the decisive plasma parameter for the S/N. An increase in electron density implies a quadratic increase of the continuum level and a much stronger attenuation of the beam used for CX, resulting in a worse situation for CXRS measurements. A decreased electron density improves the conditions, but the fusion power (and thus the number of α's and fast ion signal) also decreases quadratically. It should be noted, however, that since the presence of impurities means dilution of the fuel, the higher the impurity concentrations (higher Z_{eff}) the lower the α particle source rate.

As a further test of our arguments, the plasma profiles calculated with the CRONOS suite of codes for integrated tokamak modelling [144] for the ITER operating scenarios have been used as input to the simulation code. The feasibility of fast helium measurements at $\rho = 0.5$ and $t_{exp} = 1$s is examined for each of those scenarios, following the same idea of binning the signal into energy bins and using the effective optical throughput to describe the part of the S/N determined by the diagnostic design. The results of this study can be found in Table 7.2.

Table 7.2: Simulation results for each of the ITER operating scenarios calculated with the CRONOS suite of codes for integrated tokamak modelling [144]. In the second column the plasma parameters used as input to the simulation code are shown, but more details can be found in [144–146]. In the third column, the signal-to-noise ratios for the different ranges of alpha particle energy are presented combining the simulated measurements on both neutral beams. The exposure time assumed is 1s. The signal is binned in 100keV bins for the measurements on the DNB and in larger bins for the measurements on the HNB. The simulations are for normalised radius $\rho = 0.5$ and the plasma parameters at this location are given.

		Results (S/N)	
ITER scenario	Plasma parameters	Reference parameters	Optimistic parameters
scenario 2 (Baseline or reference scenario)	$T_e(\rho=0) = 23$keV, $T_e(\rho=0.5) = 14$keV $T_i(\rho=0) = 22$keV, $T_i(\rho=0.5) = 13$keV $n_e(\rho=0.5) = 1.19e10^{20}\mathrm{m}^{-3}$ $Z_{\mathrm{eff}} = 1.62$, $P_f = 622$MW	$E_\alpha > 100$keV: $S/N \leq 5$	$E_\alpha < 200$keV: $S/N \approx 13$ $E_\alpha > 200$keV: $S/N < 10$
scenario 3 (Hybrid scenario)	$T_e(\rho=0) = 21$keV, $T_e(\rho=0.5) = 14$keV $T_i(\rho=0) = 19$keV, $T_i(\rho=0.5) = 13$keV $n_e(\rho=0.5) = 0.9e10^{20}\mathrm{m}^{-3}$ $Z_{\mathrm{eff}} = 1.62$, $P_f = 333$MW	$E_\alpha < 200$keV: $S/N \approx 11$ $E_\alpha > 200$keV: $S/N > 10$	$E_\alpha < 300$keV: $S/N > 15$ $E_\alpha > 300$keV: $S/N < 10$
scenario 4 (Steady state scenario)	$T_e(\rho=0) = 31$keV, $T_e(\rho=0.5) = 17$keV $T_i(\rho=0) = 30$keV, $T_i(\rho=0.5) = 16$keV $n_e(\rho=0.5) = 0.8e10^{20}\mathrm{m}^{-3}$ $Z_{\mathrm{eff}} = 1.62$, $P_f = 388$MW	$E_\alpha < 400$keV: $S/N \geq 10$ $E_\alpha > 400$keV: $S/N < 10$	$E_\alpha < 1000$keV: $S/N > 10$ $E_\alpha > 1000$keV: $S/N < 10$

The results for the different ITER scenarios cannot be directly compared to the simulations presented in Fig. 7.5, due to significant differences in the profile shapes. For the steady state ITER scenario 4, the lower electron density means higher S/N. For ITER scenarios 2 and 3, the CXRS measurements will be limited to the use of DNB due to the low S/N of the measurements on the HNB. Nevertheless, when ITER operates under scenario 4, CXRS will be able to contribute to measurements of higher energy α's.

7.4 Discussion

The feasibility of CXRS measurements of fast helium on ITER has been considered in previous publications. In [147], fast helium CX measurements on ITER are discussed, but the S/N mentioned are from calculations regarding thermal helium. Simulated fast α spectra and noise levels are also published in [131], mentioning a S/N=5 at 5ms time resolution. However, the étendue of 25mm^{2}sr that is used for the calculations is too

large, as discussed in the previous section. No spectral resolution is mentioned and due to a coding error the continuum level was incorrectly calculated, resulting in a S/N 5.6 times higher. With respect to the results presented here, fast helium CX on ITER is certainly much less optimistic than previous studies have assumed.

The fusion produced slowing down particles in the plasma conditions assumed in this study need less than a second to thermalise. This time should be compared with the time resolution of the reference design and the higher optical throughput instrumentation assumed here, 1s and 200ms, respectively. The time resolution is also smaller than the sawtooth periods expected on ITER ('monster' sawteeth with periods of tens of seconds).

The study presented here has also shown that the measurements are limited to energies of up to 1 MeV. In other words, α's with velocities up to $7 \cdot 10^6$m/s can be measured. This velocity is very close to the Alfvén velocity which is $> 7.4 \cdot 10^6$m/s for an ITER plasma with $n_e = 1 \cdot 10^{20}\mathrm{m}^{-3}$ and $B = 5.3$T. As a result, instabilities like the toroidal Alfvén eigenmodes which are associated with α's of velocities close to or higher than the Alfvén velocity can be studied under appropriate experimental conditions.

The combination of lines-of-sight on the DNB and HNB will, therefore, provide information on the fast α's in an interesting region where the instabilities occur, with a low time resolution but sufficiently fast to analyse transport events.

In the event of a new D-T experimental campaign at JET, measurements of slowing down α's could contribute to the energetic α particle transport and confinement studies. With this motivation, a qualitative study for JET in the case of a future D-T campaign was also conducted. The optical throughput needed for charge exchange measurements of fast α's and the energy range that can be probed is estimated. For the equatorial viewing lines, taking into account the neutral beam enhancement that was performed at JET [148], for an energy resolution of 100keV, an effective optical throughput of $\eta = \varepsilon\ t_{exp}\ QE\ T \approx 2 \cdot 10^{-10}\mathrm{m}^2\mathrm{sr\,s}$ is needed to detect α's of up to 500 keV. This value of η is an order of magnitude higher than the optical throughput values found in the current spectrometers, which are estimated to be in the order of $10^{-11}\mathrm{m}^2\mathrm{sr\,s}$ for an exposure time of 100ms. As a result, a higher throughput instrument is needed for measurements of fast helium, or sacrifices must be made in the time or energy resolution that can be obtained.

It should be made clear that there are more issues not taken into account in the simulation. A number of impurity lines contaminate the spectrum in the wavelength of interest, especially on the blue shifted wing of the HeII CX line. Several high intensity carbon lines appear in the spectrum, namely CIV at 465.8nm and the CIII triplet edge emission at 465nm, as well as two BeIV lines, the n=6-5 transition at 465.8nm and the n=8-6 transition at 468.5nm which coincides with the HeII line, the BeII line at 467.3nm and the HeI line at 471.3nm. CX emission lines from seeding impurities such as nitrogen and krypton as well as tungsten lines, especially for the lines-of-sight viewing the divertor can be added to this list. These lines adding to the background emission have not been taken into account, but would lead to a further reduction of S/N and a much harder choice of impurity free wavelength bins. Nevertheless, the modulation of the DNB can be used to subtract the background emission. The heating beam cannot be modulated, but a careful assessment of the background contribution will enable the removal of these impurity lines. What is more, internal reflections on the metallic vessel wall might result in further contamination of the spectrum [149]. The helium plume is not taken into account, but the contribution of the helium plume is expected to be small for fast ions [9, 134]. In general, the plume effect is more important for thermal energies. In addition, the CX diagnostic viewing geometry (lines-of-sight from Upper Port 3 to the DNB) is designed to minimise, although not completely avoid, the plume emission collected, as the lines-of-sight are almost perpendicular to the magnetic field lines. Lastly, the much larger velocity of the plume ions born from charge exchange reactions of fusion-produced, not yet thermalised α particles with the neutral beams means they travel further away from the lines-of-sight than the thermal helium plume ions. Furthermore, no transport effects have been considered for this study.

7.4.1 Suggestions and alternatives to measure the slowing down α particles on ITER

A number of suggestions and alternative approaches for fast helium CX on ITER can be proposed. The S/N could be improved with the use of better focused neutral beams. The signal and, therefore, the signal-to-noise ratio is inversely proportional to the width of the beam perpendicular to the line-of-sight. For example, if the divergence of the diagnostic neutral beam is 5mrad, instead of the 10mrad that has been assumed here,

the S/N will be increased by a factor of 2. A neutral beam with higher neutral particle density would also improve the S/N.

So far the discussion has been for a hydrogen diagnostic beam and a deuterium heating beam, for the HeII n=4-3 transition. Other approaches include looking at different transitions or different beam species. However, none of these offers a viable solution. The n=3-2 or n=2-1 transitions in helium have a higher intensity, but they have the disadvantage of being in the UV (wavelengths 164nm and 30.4nm, respectively) and having a higher bremsstrahlung background, plus strong impurity emission lines in the vicinity of the 30.4nm line [150].

The option to use helium or lithium beams for CX is considered since the CX cross sections for helium and lithium beams are higher at high energies than for hydrogen beams. A lithium beam could be used to look at the n=3-2 transition [150], but it will not penetrate to the center. Beam stopping cross sections are lower for helium beams (comparing beams with the same energy per atomic mass unit). If helium is used instead of hydrogen in the DNB production system though, with the same accelerator, the neutral beam will have an energy of only 25keV/amu. A different neutral beam system should be designed to provide higher energy beam neutrals. Yet, difficulties in the production of highly energetic helium or lithium beams, especially using the negative ion beam technology, should be taken into consideration.

Another suggestion is to look at emission lines of helium following double charge exchange, which has the advantage of no strong impurity lines in the measured wavelength range. However, the cross sections are not favorable at high energies [55].

A number of other diagnostics, besides CXRS, can provide information on the confined α particles. Collective Thomson Scattering will also measure a projection of the α velocity distribution. The system based on a probe frequency of 60GHz is expected to have a spatial resolution of $\alpha/10$ for almost the whole radial range, with a time resolution of 40ms, while probing α's of energies up to 3.5MeV. These characteristics satisfy the ITER requirements, but the main challenge is the development of an 1MW long pulse gyrotron at 60GHz [130, 151] and the diagnostic is not yet enabled on ITER. Passive spectroscopy (γ-ray spectroscopy) can also measure the confined α particles for energies 1.7MeV and coarse energy resolution [152]. However, a radial distribution of the reacting element (Be or B) should be provided from another diagnostic and it can be applied only in limited operating regimes [81]. Neutral Particle Analysers can

provide information on fusion α's of 0.1-4MeV with an energy resolution of 10% [153]. In addition, measurements of lost α's can provide the pitch angle and the energy distribution of the escaping particles, but new techniques suitable to the high radiation environment have to be developed [154]. Consequently, there is currently no diagnostic planned for ITER that will be able to provide all the necessary information. Nevertheless, complementary use of these diagnostics can contribute towards obtaining a fuller description of the behaviour of confined α particles.

7.4.2 Conclusions on the feasibility of non-thermal helium measurements on ITER with CXRS

The expected signal-to-noise ratios have been presented for the fast HeII CX spectra on ITER. A S/N of 10 can be obtained on fast helium measurements for an optical throughput of $\varepsilon\ t_{exp}\ QE\ T \approx 10^{-7} m^2 sr\, s$, applying energy binning. Both the DNB and the HNB will be needed for fast helium measurements on ITER, as the DNB provides better S/N for lower energy ions and HNB provides information, albeit limited, on the faster ions. No information will be provided on fast ions of energies larger than 1MeV. Nevertheless, the fast α CX measurements do not come for free: the effective optical throughput η has to be improved with respect to the CXRS diagnostic designed for thermal ion measurements, making the need for a dedicated system much stronger. Even in the best case though, the optics on the torus side pose a limit on the S/N that can be achieved. Therefore, in addition to a higher throughput diagnostic, improvements in the neutral beam focus and luminosity are needed.

The time and energy resolutions do not meet the ITER requirements for confined α properties, but the time resolution and energy range probed are still of great use for physics studies. Using both the diagnostic and the heating neutral beams, steady state density profiles of the non-thermal helium can be examined with CXRS.

7.5 Feasibility of charge exchange measurements of the helium "ash" on ITER

Charge exchange recombination spectroscopy has been identified as the only diagnostic method that can measure the thermalised helium (helium "ash") in the plasma core and is foreseen as such to be part of the diagnostic suite for ITER. No alternative

solution exists. The minimum requirements for core helium density diagnostics on ITER prescribe the availability of measurements inside $r/a < 0.9$, with a radial resolution of $a/10$ and a time resolution of 100ms. The minimum required accuracy for helium density measurements is set to 10% (20% for other impurities) [81]. In this section, a review is given on what CXRS can offer in terms of helium "ash" (thermal helium) measurements on ITER.

As already described, observation views from two different ports (Upper Port 3 and Equatorial Port 3) are planned for the core charge exchange system on ITER. The main reason is that in this way the required and optimum spatial resolution is achieved. Measurements with the upper port system can achieve a higher spatial resolution in the plasma center, while the equatorial port system has a better resolution at the outer part of the plasma [155]. In addition, complementary measurements of the toroidal and poloidal velocity will be obtained with the two systems [156].

A large part of the design procedures for the ITER CXRS systems is made on modelling of the spectra and the system performance. For example, the simulation package described in Section 7.2 can be used. Considering again the signal-to-noise ratio as a figure of merit and a minimum signal-to-noise ratio of 10 required for the desired accuracy, it is reported in [155] that the spectral signal-to-noise ratio for HeII is estimated to be around 5 in the core region ($r/\alpha < 0.3$). It is also estimated that the errors in the HeII intensity measurements are expected to be acceptable even if beam modulation is not satisfactory enough to subtract all passive emissions, due to significant changes in the neutral density background between the on- and off- beam phases, giving positive views on the measurements of He^{2+} density profiles on ITER.

Nevertheless, high étendue, high resolution spectrometers are required [157]. A minimum spectral resolution of 0.25nm is proposed and an étendue of $1mm^2sr$ is needed to comply with the requirements of helium "ash" measurements and to achieve the signal-to-noise ratios mentioned above. One high throughput system per radial channel is foreseen for the core and one per two radial channels for the edge. Such a system has been tested and validated on TEXTOR by Jaspers et al [158], while a high étendue spectrometer suitable for charge exchange spectroscopy on ITER [79] has been installed on ASDEX Upgrade and used in the course of this thesis (see Chapter 3).

Other complications in achieving the measurement requirements include the error propagation in the determination of the neutral beam attenuation and the rapid de-

terioration of the optics, which would mean inaccurate intensity calibrations of the diagnostic. Both of these problems can be counteracted by combining charge exchange and beam emission spectroscopy, as described in Section 2.3.11 and Appendix A, removing the need for beam stopping calculations and providing a means of in situ calibration of the diagnostics.

Interpretation of the helium charge exchange spectra on ITER will also involve treating the helium plume effect. The upper port system is designed to view the neutral beam with lines-of-sight approximately perpendicular to the magnetic field lines, in order to minimise the collected plume emission [82], but still the plume emission should be taken into account, as discussed in Chapter 5. Modelling of the plume emission contribution will be significantly easier if measurements of other impurities, such as carbon, are available.

Details on the challenges faced in the port plug and periscope design, as well as in the realisation of the negative ion source diagnostic neutral beam as needed for the CXRS measurements, which are beyond the scope of this work, can be found among others in [155, 156]. Apart from the challenges, however, studies show that charge exchange spectroscopy will be able to fulfill the requirements for helium "ash" measurements on ITER.

7. FEASIBILITY OF CHARGE EXCHANGE MEASUREMENTS OF SLOWING DOWN ALPHA PARTICLES ON ITER

8

Conclusions and outlook

The successful operation of future fusion reactors relies strongly on the understanding of helium transport in the plasma, as accumulation of helium "ash" in the plasma core would dilute the fusion fuel. Furthermore, the fusion produced α particles should transfer as much of their energy as possible to the plasma bulk to maintain a self-sustained burning plasma state. In this thesis, the behavior of helium in ASDEX Upgrade plasmas has been studied with charge exchange recombination spectroscopy.

In the course of this work, a high etendue charge exchange spectrometer, which measures simultaneously three impurities, namely carbon, helium and deuterium (the beam emission spectrum), has been installed and operated on ASDEX Upgrade [79]. Special interest was placed on the helium measurements, as they are the main focus of this thesis. Helium based CXRS profiles have been routinely provided in all ASDEX Upgrade plasma discharges for the last three experimental campaigns (2012-present). Experiments especially designed for the investigation of helium transport were conducted and are presented in this thesis.

8.1 Helium transport investigations at ASDEX Upgrade

In the next section, the answers to the questions posed in the introduction of this work (Section 1.3) are presented and discussed.

A model for the helium plume effect

A detailed model for the helium plume emission [9], which takes into account the diagnostic observation geometry, the reconstructed magnetic equilibrium and the appropriate atomic data has been developed for ASDEX Upgrade and was described in Chapter 5. The intensity of the helium plume emission for the geometry of the diagnostic used in this work was found to be comparable to the intensity of the active (prompt) charge exchange signal and is, therefore, a significant contribution that cannot be ignored. Moreover, it is still an important contribution regardless of the geometry. The helium plume model was benchmarked against experimental measurements by comparing the He^{2+} density profiles measured from two optical heads with different geometries (predominantly toroidal and predominantly poloidal lines-of-sight), after applying corrections for the helium plume emission.

The cold plume emission line seen in the experiment, identified through the low apparent ion temperature and rotation profiles obtained from the helium spectra, provide an indication of non-Maxwellian features of the plume. It was found that to reproduce these features and capture the underlying physics a Monte Carlo approach to the plume distribution along the magnetic field lines in both real and velocity space was needed. This approach enables the spectral reconstruction of the plume emission that would be seen by the diagnostic and hence, for the first time, enables true ion temperature and

rotation profiles to be extracted from the experimental spectra. A simpler approach, using just a Maxwellian distribution for the plume ions can not reproduce correct ion temperature and rotation profiles, demonstrating the superiority of the Monte Carlo method.

Investigation of helium transport and comparison to theoretical predictions

To study the behavior of the helium density profile, a database of experimental measurements of helium and boron density profiles was assembled via specially designed experiments performed in ASDEX Upgrade. The experimental correlation of the impurity density normalised logarithmic gradients with theoretically relevant plasma parameters, namely the normalised gradients of the electron density, the ion temperature and the toroidal rotation were investigated. The analysis of the experimental observations in Chapter 6 showed that the helium density profile generally has a very similar shape to the electron density profile, as previously observed at DIII-D [122]. The helium density profiles are found to vary from flat to very peaked. In comparison, the boron profiles were always found to be less peaked and occasionally even hollow. An effect of rotation on the peaking of the impurity density profiles was also observed, with the peaking of the profiles decreasing with increasing rotation gradient.

The experimental measurements were compared to both neoclassical and turbulent transport predictions. It was found that the neoclassical fluxes are much too small to explain the observations and that turbulent transport is required. Comparison of the experimentally deduced impurity density gradients with the theoretical predictions based on gyrokinetic modelling of the turbulent impurity transport with the GKW gyrokinetic code [127], revealed contradictory results. In certain cases, good qualitative agreement was found between the experiment and the simulation, as in previous investigations [27], while in other cases the turbulent transport simulations cannot describe the experimental observations and considerably different trends are observed. However, since the shape of the impurity profiles are an interplay of many plasma parameters, some of which are changing simultaneously, it is not straightforward to identify the dependencies and the strengths or weaknesses of the theoretical predictions. Sensitivities of the gyrokinetic modelling, such as the strong effect of the input magnetic equilibrium on the final result [11], make this an even more challenging task. Furthermore,

different mechanisms or parameters which are not taken into account in the theoretical description might be responsible.

Feasibility of slowing-down α particle measurements with charge exchange spectroscopy on ITER

As charge exchange spectroscopy will be part of the ITER diagnostic suite, expected to provide ion temperature, rotation and impurity density profiles, it is worthwhile to examine whether it will also be able to provide information on the slowing-down confined α particles. The use of CXRS for fast α particles diagnosis on ITER will be hindered by the small fast ion signal in comparison to the background emission. For this reason the fast HeII charge exchange spectra expected on ITER were modelled and the expected signal-to-noise ratios were presented in Chapter 7 [132].

The signal-to-noise ratio was examined in terms of the effective optical throughput of the diagnostic, defined as $\eta = \varepsilon\ t_{exp}\ QE\ T$. With the reference design parameters planned for the core CXRS diagnostic on ITER, information can be provided on fast α's of energy 0.1-1MeV, combining measurements both on the diagnostic and heating neutral beams, at a time resolution of 2s and an accuracy of 10%. If a higher throughput instrumentation is used, a better exposure time of 200ms can be achieved for α's up to 1MeV. However, it must be emphasized that the optics on the torus side pose a limit on the S/N that can be achieved. Therefore, in addition to a higher throughput diagnostic, improvements in the neutral beam focus and particle flux would be required for CXRS measurements of slowing down α particles in ITER.

In conclusion, at ASDEX Upgrade a helium plume model has been implemented that for the first time is shown to be able to accurately reproduce the experimental spectra. This demonstrates an advanced understanding of the helium CXRS spectra, which will be useful on other devices including ITER, and enables helium transport studies to be performed via CXRS measurements. The ASDEX Upgrade results show that experimental helium profiles tend to be very similar to the electron density profile and that further work is needed to gain a theoretical understanding of the processes involved in low-Z impurity transport.

8.2 Outlook

The investigations presented in this work lead to a number of further questions and issues to be explored. Low-Z impurity transport in tokamak plasmas is by no means understood despite being a subject of research at many tokamaks. Experimentally helium presents a particularly challenging case, due to the complications in interpreting the charge exchange measurements. However, in this work the measured spectra were successfully reproduced, giving confidence that the derived helium profiles are correct within the given uncertainties. Even so, the comparison to theory yielded puzzling results, bringing our theoretical understanding of low-Z impurity transport into question.

To clarify the discrepancies between the exerimental and theoretical results, a number of steps should be undertaken: first, non-linear gyrokinetic simulations may provide additional information on the sources of the disagreement. Second, a more detailed investigation dependence of the gyrokinetic prediction on the input equilibrium in this database should be performed. Third, more experimental efforts are required to disentangle the complicated dependencies of helium transport. Though the possibility to vary one plasma parameter at a time in the experiment is somewhat limited, extending the current database can help in this regard.

An additional subject of utmost importance is the effect of helium on confinement. The influence of helium concentration on the H-mode confinement has been studied on ASDEX Upgrade by means of passive divertor spectroscopy [159], it was identified that helium concentrations of $\sim 20\%$, leads to a drop of the H-factor from above 1 to 0.8. Recent findings at ASDEX Upgrade, where accurate measurements of the helium concentration in the plasma core were available (as shown in this work), have shown that much lower concentrations of helium (on the order of 10%), obtained after a strong helium gas puff, are sufficient to cause a significant reduction in confinement. Analysis on this front is ongoing.

Efforts to study the effect of sawtooth crashes on the helium density profiles at ASDEX Upgrade have been undertaken in the course of this work. However, these efforts were not yet fruitful, as in all experimental attempts either the sawteeth were insufficiently strong or the helium density profiles were not sufficiently peaked for a clear effect to be observed. An example of the minimal, if any, effect on the helium density profile in discharges with strong sawtooth crashes is given in Appendix B. Despite the

lack of success so far, further efforts are planned to study the effect of sawteeth on the thermal helium density profiles.

Furthermore, the possibility to study the transport of energetic beam-injected helium at ASDEX Upgrade is of great interest. Deuterium beams with a small percentage of helium ($\sim 5\%$) were injected in low density experiments at ASDEX Upgrade to investigate if sufficient fast helium signal is present in the charge exchange spectra to allow fast helium studies to be performed. It was established that this is the case, as shown in Appendix C. The successful measurement of fast helium charge exchange signal at ASDEX Upgrade motivates further helium beam experiments to study the behavior of the fast helium ions and their interactions with sawteeth.

Appendices

Appendix A

Method to obtain absolute impurity density profiles combining charge exchange and beam emission spectroscopy

Investigation of impurity transport properties in tokamak plasmas is essential and a diagnostic that can provide information on the impurity content is required. Combining charge exchange recombination spectroscopy (CXRS) and beam emission spectroscopy (BES), absolute radial profiles of impurity densities can be obtained from the CXRS and BES intensities, electron density and CXRS and BES emission rates, without requiring any absolute calibration of the spectra. The technique is demonstrated here with absolute impurity density profiles obtained in TEXTOR plasmas, using a high efficiency charge exchange spectrometer with high étendue, that measures the CXRS and BES spectra along the same lines-of-sight, offering an additional advantage for the determination of absolute impurity densities. The contents of this section have been published in [49] and presented in the High Temperature Plasma Diagnostics conference, in Monterey, CA in 2012.

Introduction

Impurities in fusion plasmas have both beneficial and detrimental effects: on the one hand they contribute to the improvement of confinement and divertor protection by means of radiative edge cooling, on the other hand, impurities in the plasma imply fuel dilution and core radiation losses. In addition, monitoring and removal of the helium "ash", the thermalised fusion product, is a significant issue. The investigation of impurity transport properties is obviously essential and therefore a diagnostic that can provide information on the impurity content is required. Charge exchange recombination spectroscopy (CXRS) is a diagnostic capable of observing plasma impurities and is the only diagnostic that will be able to provide helium"ash" measurements on ITER [81].

CXRS measures the light emitted by impurity ions in the plasma after they have undergone a charge exchange process with the neutral atoms from a neutral beam injected in the plasma. The measurement is local, as the active charge exchange signal comes from the location where the neutral beam intersects the lines of sight of the spectrometer. The intensity of the light measured is this local emission integrated along the line-of-sight. The emitted light depends on the impurity density n_i and the neutral beam density n_b, as well as the charge exchange emission rates Q_{CX}, which in turn depends on the local plasma and beam parameters (electron temperature T_e, electron density n_e, impurity density n_i and beam energy E). Consequently, CXRS can provide a measurement of the impurity densities in the plasma[53], assuming that the neutral beam density is known.

The neutral beam density in the plasma can be derived either from calculations of the neutral beam attenuation in the plasma as: $n_b = n_b(0)exp(-\int \sigma_{stop} n_e)$, or from beam emission spectroscopy (BES). BES measures the light emitted from neutral beam particles after excitation by ion and electron impact. The measured intensity is now dependent on the integral of the neutral beam density along the line-of-sight, the electron density and the beam emission rates Q_{BES}. The beam emission rates are also dependent on T_e,n_e, n_i and E. As such, the neutral beam density can be obtained from the BES spectrum.

Combining CXRS and BES, absolute radial profiles of impurity densities can readily be obtained [47, 48]. This method is described in detail in section A. A spectrometer

designed according to ITER requirements that measures both CXRS and BES is then used to showcase the method. The application of the technique is described in section A and an example of absolute carbon impurity density profiles from a TEXTOR plasma is given. Nevertheless, as discussed in the last section, validation of the technique is required.

Impurity density profiles combining CXRS and BES

For positive ion neutral beams, such as the neutral beams at the TEXTOR tokamak, the three beam energy components E, E/2, E/3 have to be taken into account and the CXRS and BES measured light intensities are:

$$I_{CX} \propto \int_{los} n_i \sum_{E=E,E/2,E/3,Halo} Q_{CX}^{E} n_b^{E} dl \tag{A.1}$$

$$I_{BES} \propto n_e Q_{BES} \int_{los} n_b^{E} dl \tag{A.2}$$

If the same lines-of-sight are used, determination of the intersection integral between the neutral beam and the line-of-sight is not needed and for neutral beam density equal to $n_b^E = f^E \frac{I_{BES}}{Q_{BES} n_e}$, the impurity concentration is given by [47]:

$$c_i = \frac{n_i}{n_e} = I_{CX} \sum_{E=E,E/2,E/3} \frac{Q_{BES}}{Q_{CX} I_{BES}} \tag{A.3}$$

However, it should be taken into account that the sensitivity of the two detectors measuring the CXRS and BES spectra are not equal. In other words, there are calibration factors (A_{CX} and A_{BES}) that should be included in the CXRS and BES intensities. The ratio of these calibration factors can be derived from the spectra, by looking at the bremsstrahlung level at the specific wavelength, performing a cross-calibration of the two detectors[70]:

$$\frac{A_{CX}}{A_{BES}} = \frac{C_{CX}}{C_{BES}} \frac{\lambda_{CX}}{\lambda_{BES}}, \tag{A.4}$$

where C_{CX} and C_{BES} are the continuum level for each of the spectra at the specific wavelength λ_{CX} and λ_{BES} respectively.

Using this method, no absolute calibration of the detectors is required. All the required information to obtain absolute impurity density profiles can be found in the

spectrum itself. It can be argued that even the radial locations of the measurement can be extracted from the BES spectra, by calculating the doppler shift of the first beam energy component in relation to the D_α or a reference line.

A technique like this, apart from reducing any errors due to beam attenuation calculations, provides an additional advantage in reactor or ITER like situations, where access to the instrument and torus hall will not be always possible. In the next section, an attempt is made to apply this method in practice.

Application of the method on TEXTOR

High etendue spectrometer for ITER core CXRS measurements

An attempt to apply this technique to extract impurity density profiles has been made using a spectrometer designed for core CXRS on ITER [79], which was installed on the TEXTOR tokamak during the last experimental campaigns.

The spectrometer is a highly efficient optical system with high etendue and high resolution, following the ITER requirements for charge exchange measurements [155]. The light from the tokamak arrives to the spectrometer with a single fiber bundle and is split into three wavelength ranges, allowing simultaneous measurement of carbon, helium and hydrogen spectra on three different detectors. Consequently, the impurity spectrum, namely carbon or helium, and the beam emission spectrum are measured on exactly the same lines of sight. The spectrometer is looking at neutral beam 2 on TEXTOR and an illustration of the observation geometry and the lines-of-sight can be seen in Fig.A.1. The high etendue of the system would also allow for fast measurements (down to a few milliseconds, depending on the readout time of the detectors), making the spectrometer suitable for impurity transport studies.

Carbon density profiles from a TEXTOR discharge

The CVI charge exchange spectrum and the BES spectrum from a TEXTOR discharge ($\mathrm{I_p} = 400\mathrm{kA}, \mathrm{B_t} = 2.6\mathrm{T}$) are fitted to obtain the measured light intensity, in order to obtain absolute density profiles of C^{6+}. The relatively calibrated intensities for discharge 115155 at 2.06s are shown in Fig. A.2. At this time point only NBI 2 (hydrogen), the neutral beam which the CX spectrometer uses, is switched on at 50kV voltage.

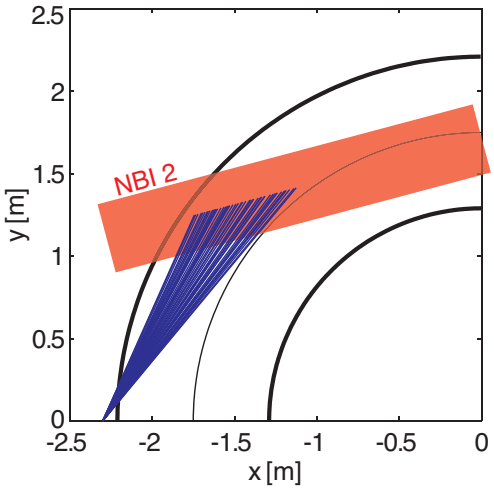

Figure A.1: A top view illustration of the lines-of-sight of the spectrometer on neutral beam 2 on TEXTOR (major radius 1.75m, minor radius 0.46m).

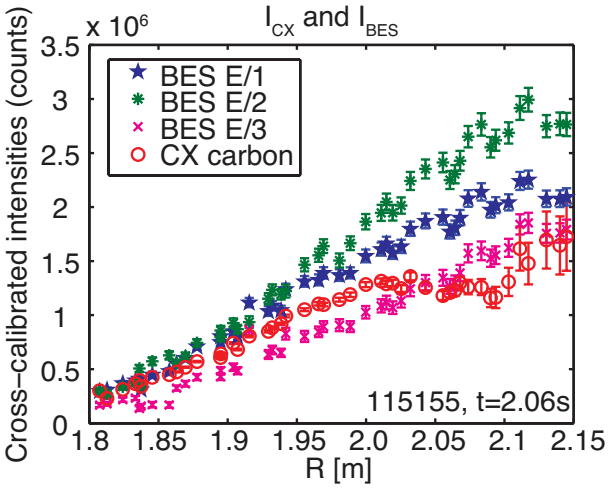

Figure A.2: The CX intensity from the carbon spectrum for TEXTOR discharge 115155 and the intensities of the three beam energy components from the BES spectrum. The data are already cross-calibrated at this point (the carbon CX intensity is multiplied with A_{BES}/A_{CX}). The error bars correspond to the errors in the fit.

Subsequently, the charge exchange and beam emission rates are calculated for the local plasma parameters and the neutral beam energy. A value of 1.9 is assumed for Z_{eff}. As the accuracy of the atomic data is crucial for this technique, the updated ADAS [71] atomic data for the neutral beam emission rates are used [68]. The excited

beam neutrals are also taken into account. However, the neutral beam halo was not included in the analysis. The plume effect is negligible for carbon.

The bremsstrahlung levels from the fitted spectra are extracted in order to perform a cross-calibration of the BES and CXRS spectra, as described in the previous section. The resulting C^{6+} concentration profiles are shown in Fig. A.3. The carbon concentration is about 1% for this example. In Fig. A.3 the carbon density is compared to the electron density, plotted here in scale. Very good agreement in profile shape is observed.

The vertical error bars in Fig. A.3 are from the fit, while the horizontal error bars indicate the error in the determination of the radial location in the plasma where the lines-of-sight intersect the neutral beam. The uncertainty in the intersection point is about 3-6cm, which is reasonable taking into account that the neutral beam has a FWHM of about 18cm.

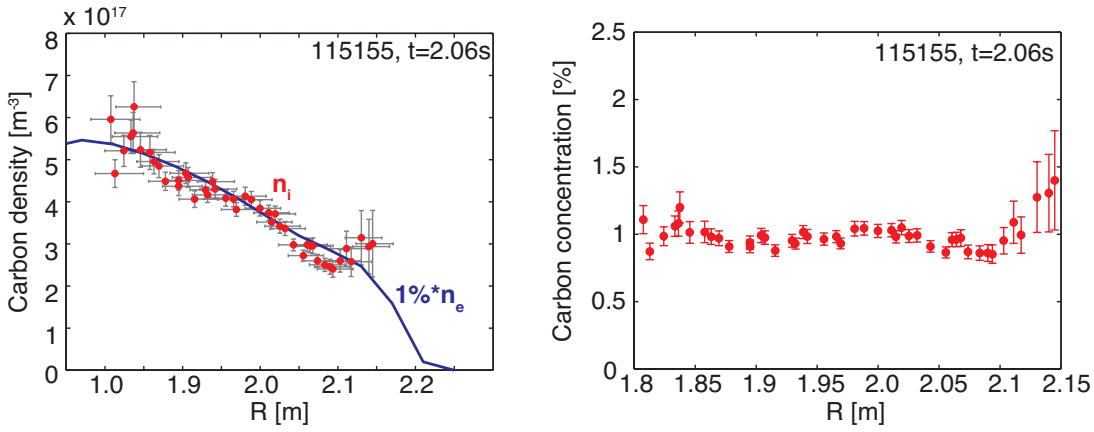

Figure A.3: On the left, the carbon (C^{6+}) absolute density profile is plotted together with the electron density profile (multiplied by 1%) for comparison. The uncertainty in the radial location in the plasma is also indicated. On the right, the C^{6+} concentration for TEXTOR discharge 115155 at t=2.06s derived from the cross-calibrated CXRS and BES spectra. The vertical errorbars come from the fitting of the spectra.

Discussion

In section A an absolute density profile of carbon (C^{6+}) has been shown and compared with the electron density for a TEXTOR discharge. The values obtained are still to be

checked, for example against measurements of Z_{eff}, which have not been available.

Regarding the method itself, it should be noted that the cross-calibration of the BES and CXRS spectra in order to achieve accurate results, implies that there should be a line free wavelength range in the measured spectra. The situation becomes even more difficult when the continuum level is very close to the noise level.

The method is shown to be useful and applicable to extract absolute density profiles of impurities in tokamak plasmas, with minimum calibration requirements. However, validation of the method is required where the impurity density profiles should be checked against other diagnostic measurements.

A. IMPURITY DENSITY PROFILES COMBINING CXRS AND BES

Appendix B

Effect of sawtooth crashes on the thermal helium profile

Experimental attempts to document the effect of sawtooth crashes on the helium density profiles at ASDEX Upgrade have not yet been fruitful, as either the sawteeth were insufficiently strong or the helium density profiles were not sufficiently peaked for a clear effect to be observed. Increased peaking of the helium density profile can be achieved with the application of electron cyclotron heating in the plasma center. Yet, this has a stabilising effect on the sawteeth, hindering this studies.

In Fig. C.1, the plasma profiles in a discharge with strong sawtooth crashes are shown. The effect of the sawtooth crash is very clear in the toroidal rotation, ion and electron temperature and electron density profile, while it is barely observable in the helium density profiles.

Further attempts to investigate this subject will be made in low collisionality, low density plasmas, avoiding the additional electron cyclotron heating.

B. EFFECT OF SAWTOOTH CRASHES ON THE THERMAL HELIUM PROFILE

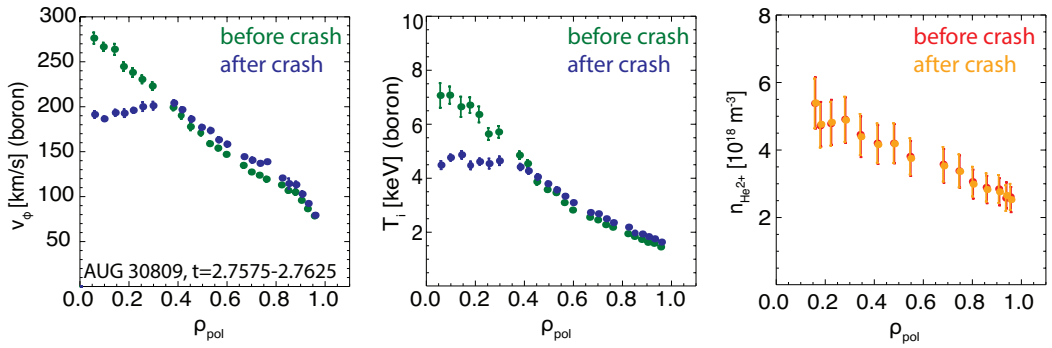

Figure B.1: Strong sawteeth affect the ion temperature and rotation profiles, but no effect is observed on the He^{2+} density profiles.

Appendix C

Feasibility of energetic helium studies at ASDEX Upgrade

The possibility to study the transport of energetic beam-injected helium at ASDEX Upgrade was investigated in the course of this work. Deuterium beams with a small percentage of helium ($\sim$ 5%) [160, 161] were injected in low density experiments at ASDEX Upgrade. It was confirmed that sufficient fast helium signal is present in the charge exchange spectra to allow fast helium studies to be performed, as shown in Fig. C.1.

Nevertheless, the interpretation of the fast helium measurement is complex. All the atomic processes involved in the attenuation of the helium beams should be considered, which is even more complicated by the presence of helium metastables [162]. Furthermore, the additional beam plume (plume emission due to the higher velocity helium ions from the beam) [121] should be considered. The analysis on this from and the implementation of helium beams in the forward modelling Monte Carlo code FIDASIM [65, 69] is ongoing.

C. FEASIBILITY OF ENERGETIC HELIUM STUDIES AT ASDEX UPGRADE

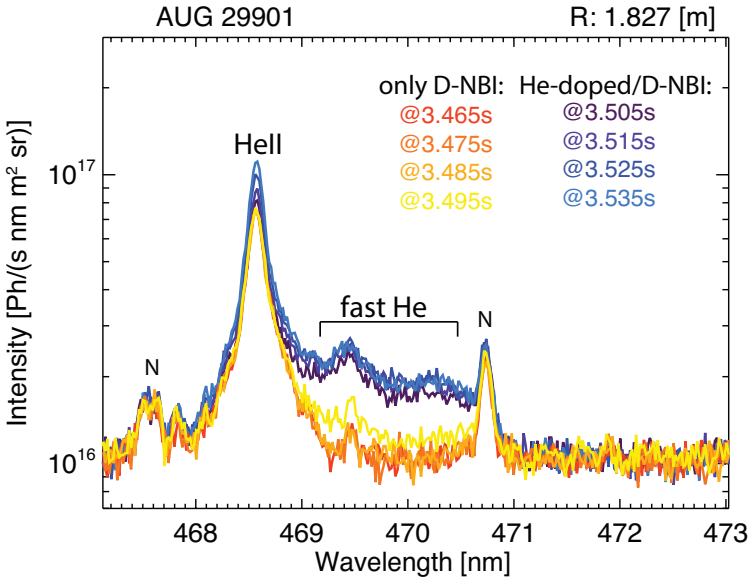

Figure C.1: Helium charge exchange spectra before and after the addition of a helium component in the deuterium beam.

Acknowledgements

A PhD thesis is never the result of the efforts of a single person. I would like to thank all those people that contributed, directly or indirectly, to the completion of this work.

First of all, I would like to thank my promotor Tony Donné for his support and encouragement and for his eagerness to follow my progress. I would like to thank my supervisor Roger Jaspers for his guidance and continuous support and for being always one phone call away. Roger, thank you for reminding me to always keep in mind what the goal of what we are trying to achieve is. A big thank you goes also to my ex-group leader Peter de Vries, who always managed to motivate me despite being in a different country.

I would like to express my deepest gratitude to Rachael McDermott, who has been my supervisor at ASDEX Upgrade. Rachael, no matter what I write here, it is not enough to express how thankful I am. I have learned so much from you; from how to efficiently run a diagnostic to how to write grammatically correct sentences. I have enjoyed working with you during the last two and a half years. Thank you for your guidance and patience and for always finding time for me.

I am deeply indebted to Manfred Von Hellermann for his support and encouragement in the beginning of my PhD and for infecting me with his passion for charge exchange spectroscopy. I am grateful to Thomas Pütterich for his contribution to the development of the plume emission model and all the discussions that led to this successful result. I would also like to thank Ralph Dux for his help, explanations and support since the first day I came to ASDEX Upgrade. Many thanks go also to Clemente Angioni, who contributed the gyrokinetic modelling for this work and helped me understand a little more about turbulent transport. I thank also Christian Hopf for his efforts with the helium-doped neutral beams, as well as Ben Geiger for helping me with FIDASIM.

I spent the first one and a half years of my PhD at the Technical University of Eindhoven. Everybody in the Fusion Science and Technology group made me feel immediately at home. I would particularly like to thank my ex-officemate Merlijn Jakobs for the nice discussions we had and Mark Scheffer for his help and support in all ICT things.

Then I came to ASDEX Upgrade, where I spent the remaining two and a half years of my PhD. Once more, I felt immediately like part of the team. I would like to thank the spectroscopy group and all the colleagues at ASDEX Upgrade for their help. Thanks must go to the experiment leaders and everybody in the control room that made my experiments possible. I thank all the people that were always eager to help, whenever I asked a question. For their help in setting up my diagnostics, I am greatful to Helmut Blank, Andreas Lohs, Roland Merkel and Karl Behler. I would also like to thank Ivo Classen and all the members of the DIFFER Plasma Diagnostics Group, which is split between ASDEX Upgrade and JET.

I would like to thank Eli Viezzer, Mike Dunne, Christian Vorpahl, Andreas Burckhart, Sina Fietz, Steffen Potzel, Ben Geiger, Marco Cavedon, Philip Schneider, Felix Reimold, Fabian Sommer, Livia Casali, Matthias Willensdorfer, Gregor Birkenmeier, Tim Happel, Hauke Doerk, Leena Aho-Mantila, Laura Barrera, Daniel Carralero, Patrick Simon, Alex Lebschy, Tomas Odstrcil, Markus Weiland and everybody else that made my time at IPP both inspiring and fun. A special thank you goes to Matthias Bernert for his help and for surviving in the same office with me all this time. Thank you all for the motivation and the encouragement, I feel very fortunate to work with people like you.

I would also like to thank a number of people who reminded me that there is life outside of work. I thank Louisa Papachristodoulou, Döndü Sahin, Seray Candar and Chiara Tamiello for the wonderful times in Eindhoven. I am greatful to my friends in Greece, Ioanna Tatsika and Eleni Koutoupi for always being there for me despite the fact that we meet twice a year. I thank Christos Ntailianas for his care and support throughout the years.

Finally, I am very grateful to my parents, Pavlos Kappatos and Kyriaki Tsanaktsidou, who always support every decision I make, for their unconditional love. I thank them for teaching me how to be confident and persistent in following my dreams.

Curriculum Vitae

I was born on the 26th of September 1986 in Thessaloniki and I grew up in Naousa, Greece. In 2003, I graduated from the 1st Lyceum of Naousa and participated in the panhellenic national entrance examinations. I was admitted to the School of Applied Mathematics and Physics at the National Technical University of Athens, Greece, with the highest grade among the high-school graduates admitted in the School.

During my undergraduate studies, I performed a three-month internship at the Joint European Torus (JET) in the United Kingdom, where I worked with the correlation reflectometry diagnostic. I returned to JET once again for my Diploma thesis, which focused on the study of the discrepancy between electron temperature measurements obtained from the electron cyclotron emission and Thomson Scattering diagnostics. I graduated in 2010 with a Diploma in Applied Physics, with specialisations in Nuclear Physics and Optoelectronics.

After my graduation, I started a PhD project in the Plasma Diagnostics Group of the Dutch Institute for Fundamental Energy Research in the Netherlands (FOM-DIFFER, then FOM Institute for Plasma Physics Rijnhuizen). I spent the first one and a half years at the Technical University of Eindhoven (TU/e). From the beginning of 2012, I was seconded to the Max-Planck-Institut für Plasmaphysik in Garching bei München, to continue my research project at the ASDEX Upgrade tokamak. This project focuses on the investigation of helium transport in ASDEX Upgrade plasmas with charge exchange recombination spectroscopy and the results are presented in this dissertation.

List of symbols

τ_E energy confinement time. 72

τ_{He} helium confinement time. 72

τ^*_{He} effective helium confinement time. 72

D diffusion coefficient. 55

υ_d drift velocity. 55

Z_{eff} effective charge. 20

n_e electron density. 16

T_e electron temperature. 16

n_{imp} impurity density. 37

T_i ion temperature. 36

υ_{th} ion thermal velocity. 83

λ_{ion} ionisation length. 83

τ_{ion} ionisation time. 83

R/L_X local normalised logarithmic gradient. 67

ν_{eff} effective plasma collisionality. 119

ν^* plasma collisionality. 55

υ_{rot} rotation velocity. 37

q safety factor. 9

u' radial gradient of the toroidal plasma velocity. 67

List of acronyms

ASDEX Upgrade Axially Symmetric Divertor EXperiment Upgrade. 8

BES Beam Emission Spectroscopy. 22

CXRS Charge Exchange Recombination Spectroscopy. 26

ECE Electron Cyclotron Emission. 17

ECRH Electron Cyclotron Resonance Heating. 12

ELM Edge Localised Mode. 11

ICRH Ion Cyclotron Resonance Heating. 12

IDA Integrated Data Analysis. 19

ITER International Thermonuclear Experimental Reactor. 2

ITG Ion Temperature Gradient. 63

JET Joint European Torus. 3

MHD Magnetohydrodynamics. 8

NBI Neutral Beam Injection. 12

TEM Trapped Electron Mode. 63

List of Figures

References

[1] S. Chu and A. Majumdar. *Nature*, 488(7411):294–303, 2012. 1

[2] J. Ongena and G. Van Oost. *Transactions of fusion science and technology*, 45:3–14, 2004. 1

[3] J. Jacquinot and the JET Team. *Plasma Physics and Controlled Fusion*, 41:A13–A46, 1999. 2

[4] W. D. D'Haeseleer. *Plasma Physics and Controlled Fusion*, 41:B25–37, 1999. 2

[5] D. Reiter and G. H. Wolf. *Nuclear Fusion*, 2141, 1990. 3, 72

[6] E. Rebhan, U. Vieth, D. Reiter, and G. H. Wolf. *Nuclear Fusion*, 36(2):264–269, 1996. 3

[7] W. W. Heidbrink and G. J. Sadler. *Nuclear Fusion*, 34:535, 1994. 4

[8] Y. Gribov, D. A. Humphreys, K. Kajiwara, et al. *Nuclear Fusion*, 47(6):S385–S403, 2007. 4

[9] R. J. Fonck, D. S. Darrow, and K. P. Jaehnig. *Physical Review A*, 29(6), 1984. 5, 25, 26, 76, 77, 96, 102, 113, 114, 163, 170

[10] J. Wesson. *Tokamaks*. Clarendon Press, Oxford, 3rd edition, 2004. 7, 63

[11] F. J. Casson, R. M. McDermott, C. Angioni, et al. *Nuclear Fusion*, 53(6):063026, 2013. 8, 68, 71, 118, 120, 122, 129, 140, 145, 171

[12] P. J. McCarthy. *Physics of Plasmas*, 6(9):3554, 1999. 9

[13] M. G. Dunne, P. J. McCarthy, E. Wolfrum, et al. *Nuclear Fusion*, 52(12):123014, 2012. 9, 140

[14] P. J. McCarthy. *Plasma Physics and Controlled Fusion*, 54(1):015010, 2012. 9, 140

[15] S. Von Goeler, W. Stodiek, and N. Sauthoff. *Physical Review Letters*, 33(20):1201, 1974. 10

[16] F. Porcelli. *Plasma Physics and Controlled Fusion*, 38:2163, 1996. 10

[17] R. Neu, M. Balden, V. Bobkov, et al. *Plasma Physics and Controlled Fusion*, 49(12B):B59–B70, 2007. 10

[18] F. Wagner, G. Becker, K. Behringer, et al. *Physical Review Letters*, 49(19):1408–1412, 1982. 11

[19] A. Kallenbach and ASDEX Upgrade team. *Nuclear Fusion*, 51:094012, 2011. 11

[20] K.-D. Zastrow and W. G. F. Core. *Nuclear Fusion*, 38:257, 1998. 12

[21] B. Streibl, P. T. Lang, F. Leuterer, J. M. Noterdaeme, and A. Stäbler. 2003. 13

[22] C. Hopf et al. Neutral beam injection on ASDEX Upgrade. Technical report, Max-Planck Institut für Plasma Physik, 2014. https://www.aug.ipp.mpg.de/augtwiki/bin/view/ITED/NiAU. 13

[23] M. Bornatici, R. Cano, O. De Barbieri, and F. Engelmann. *Nuclear Fusion*, 1153, 1983. 14, 16

[24] J. Stober, A. Bock, H. Höhnle, et al. *EPJ Web of Conferences*, 32:02011, 2012. 14

[25] R. Dux, C. Giroud, R. Neu, et al. *Journal of Nuclear Materials*, 313:1150–1155, 2003. 14, 60, 61, 124

[26] C. Angioni, A. G. Peeters, X. Garbet, et al. *Nuclear Fusion*, 44(8):827–845, 2004. 14, 69

[27] C. Angioni, R. M. McDermott, E. Fable, et al. *Nuclear Fusion*, 51(2):023006, 2011. 14, 61, 68, 69, 70, 71, 118, 119, 124, 132, 145, 171

[28] D. G. Swanson. *Physics of Fluids*, 28(9):2645–2677, 1985. 15

[29] H. Faugel, P. Angene, W. Becker, et al. *Fusion Engineering and Design*, 74(1-4):319–324, 2005. 15

[30] I. H. Hutchinson. *Principles of plasma diagnostics*. Cambridge University Press, 2005. 15, 16

[31] I. G. J. Classen, J. E. Boom, W. Suttrop, et al. *Review of Scientific Instruments*, 81(10):10D929, 2010. 16

[32] B. Kurzan and H. D. Murmann. *Review of scientific instruments*, 82(10):103501, 2011. 17

[33] J. Schweinzer and E. Wolfrum. *Plasma Physics and Controlled Fusion*, 1173, 1992. 17

[34] R. Fischer, E. Wolfrum, and J. Schweinzer. *Plasma Physics and Controlled Fusion*, 50(8):085009, 2008. 17

[35] E. Wolfrum, J. Schweinzer, M. Reich, L. D. Horton, and C. F. Maggi. *Review of Scientific Instruments*, 77(3):033507, 2006. 17

[36] M. Willensdorfer, E. Wolfrum, R. Fischer, et al. *Review of scientific instruments*, 83(2):023501, 2012. 17

[37] A. Mlynek, G. Schramm, H. Eixenberger, et al. *Review of Scientific Instruments*, 81(3):033507, 2010. 18

[38] R. Fischer, C. J. Fuchs, B. Kurzan, and W. Suttrop. *Fusion science and technology*, 2010. 18

[39] M. García-Muñoz, H.-U. Fahrbach, and H. Zohm. *Review of Scientific Instruments*, 80(5):053503, 2009. 18

[40] K. Shinohara, D. S. Darrow, A. L. Roquemore, S. S. Medley, and F. E. Cecil. *Review of Scientific Instruments*, 75(10):3640, 2004. 19

[41] R. Bartiromo, G. Bracco, M. Brusati, et al. *Review of Scientific Instruments*, 58(5):788, 1987. 19

[42] H. Bindslev, J. A. Hoekzema, and J. Egedal. *Physical review letters*, 83(16):3206, 1999. 19

[43] S. Michelsen, S. B. Korsholm, H. Bindslev, et al. *Review of Scientific Instruments*, 75(10):3634, 2004. 19

[44] M. Salewski, F. Meo, M. Stejner, et al. *Nuclear Fusion*, 50(3):035012, 2010. 19

[45] S. K. Rathgeber, R. Fischer, S. Fietz, et al. *Plasma Physics and Controlled Fusion*, 52(9):095008, 2010. 20, 33

[46] V. Igochine, A. Gude, M. Maraschek, and ASDEX Upgrade team. Hotlink based soft x-ray diagnostic on ASDEX upgrade. Technical Report 1/338, IPP-report, 2010. 20

[47] W. Mandl, R. C. Wolf, M. G. von Hellermann, and H. P. Summers. *Plasma Physics and Controlled Fusion*, 35:1373, 1993. 22, 39, 178, 179

[48] R. Dux, B. Geiger, R. M. McDermott, et al. Impurity density determination using charge exchange and beam emission spectroscopy at ASDEX Upgrade. In *38th EPS Conference on Plasma Physics*, 2011. 22, 178

[49] A. Kappatou, R. J. E. Jaspers, E. Delabie, et al. *Review of scientific instruments*, 83(10):10D519, 2012. 22, 177

[50] A. Lebschy. private communication - diploma thesis in progress. 22

[51] R. Isler. *Physical Review Letters*, 38(23):1359–1362, 1977. 25

[52] V. V. Afrosimov, Y. S. Gordeev, A. N. Zinov'ev, and A. A. Korotkov. *JETP Letters*, 28(8):500–502, 1978.

[53] A. Boileau, M. G. von Hellermann, L. D. Horton, J. Spence, and H. P. Summers. *Plasma Physics and Controlled Fusion*, 31(5):779–804, 1989. 178

[54] R. C. Isler. *Plasma Physics and Controlled Fusion*, 36:171, 1994. 25

[55] K.-D. Zastrow, M. O'Mullane, M. Brix, et al. *Plasma Physics and Controlled Fusion*, 45(9):1747–1756, 2003. 26, 164

[56] M. G. von Hellermann, G. Bertschinger, W. Biel, et al. *Physica Scripta*, T120:19–29, 2005. 26, 114

[57] F. Guzmán, L. F. Errea, C. Illescas, L. Méndez, and B. Pons. *Journal of Physics B: Atomic, Molecular and Optical Physics*, 43(14):144007, 2010. 27, 29, 40

[58] R. Hoekstra and H. Anderson. *Plasma physics and Controlled Fusion*, 40:1541, 1998. 27, 29

[59] M. Tunklev, P. Breger, K. Guenther, et al. *Plasma Physics and Controlled Fusion*, 41:985–1004, 1999. 29, 30

[60] M. G. von Hellermann, W. G. F Core, J. Frieling, et al. *Plasma Physics and Controlled Fusion*, 35:799, 1993. 29, 30, 35, 149, 152, 157

[61] M. G. von Hellermann, W. Mandl, and H. P. Summers. *Plasma Physics and Controlled Fusion*, 33(14):1805, 1991. 30

[62] E. J. Synakowski, R. E. Bell, R. V. Budny, and C. E. Bush. *Physical review letters*, 1995. 30, 72

[63] E. Viezzer, Pütterich T., R. Dux, R. M. McDermott, and ASDEX Upgrade. *Review of Scientific Instruments*, 2012. 30, 31, 44, 48, 119

[64] E. Viezzer. *Measuring and modelling the radial emissivity profile of passive emission lines in the plasma edge of ASDEX Upgrade.* PhD thesis, LMU, München, 2009. 31, 32

[65] W. W. Heidbrink. *Communications in Computational Physics*, 10(3):716–741, 2011. 33, 39, 187

[66] G. R. McKee, R. J. Fonck, B. C. Stratton, R. Bell, and R. V. Budny. *Physical Review Letters*, 75(4):649, 1995. 35, 152

[67] A. D. Whiteford, M. G. von Hellermann, L. D. Horton, and K.-D. Zastrow. CXSFIT - User Manual. Technical Report ADAS-R(07)01, Atomic Data and Analysis Structure, 2007. 37

[68] E. Delabie, M. Brix, C. Giroud, et al. *Plasma Physics and Controlled Fusion*, 52(12):125008, 2010. 38, 181

[69] B. Geiger. *Fast ion transport studies using FIDA spectroscopy at the ASDEX Upgrade tokamak*. PhD thesis, LMU, München, 2012. 39, 81, 121, 187

[70] M. F. M. De Bock, K. Jakubowska, M. G. von Hellermann, et al. *Review of Scientific Instruments*, 75(10):4155, 2004. 39, 179

[71] H. P. Summers. *The ADAS User Manual, version 2.6 http://www.adas.ac.uk*, 2004. 41, 83, 152, 181

[72] M. G. von Hellermann, P. Breger, and J. Frieling. *Plasma Physics and Controlled Fusion*, 37:71–94, 1995. 40, 41, 42, 43

[73] W. W. Heidbrink. *Review of Scientific Instruments*, 81(10):10D727, 2010. 43, 44

[74] B. Geiger, M. García-Muñoz, W. W. Heidbrink, et al. *Plasma Physics and Controlled Fusion*, 53(6):065010, 2011. 43, 44, 121, 149

[75] W. W. Heidbrink, Y. Luo, K. H. Burrell, et al. *Plasma Physics and Controlled Fusion*, 49(9):1457–1475, 2007. 44, 149

[76] M. Salewski, B. Geiger, S.K. Nielsen, et al. *Nuclear Fusion*, 52(10):103008, October 2012. 44

[77] R. V. Budny. *Nuclear Fusion*, 34(9):1247–1262, 1994. 44

[78] TRANSP references http://w3.pppl.gov/transp/refs, 1998. 44, 132

[79] R. J. E. Jaspers, M. Scheffer, A. Kappatou, et al. *Review of scientific instruments*, 83(10):10D515, 2012. 44, 47, 106, 166, 170, 180

[80] M. Rubel, G. De Temmerman, P. Sundelin, et al. *Journal of Nuclear Materials*, 390-391:1066–1069, 2009. 45

[81] A. J. H. Donné, A. E. Costley, R. Barnsley, et al. *Nuclear Fusion*, 47(6):S337–S384, 2007. 46, 148, 164, 166, 178

[82] M. G. von Hellermann, R. J. E. Jaspers, and P. Lotte. Progress in Charge Exchange Recombination Spectroscopy (CXRS) and Beam Emission Spectroscopy (BES) for ITER. In *Proc. 29th EPS Conf.*, volume 26B, 2002. 45, 115, 167

[83] FARO 3D measurement technology. www.faro.com. 49

[84] P. Helander. *Transactions of Fusion Science and Technology*, 61:133–141, 2012. 54, 56

[85] S. I. Braginskii. *Reviews of Plasma Physics*, volume 1. Consultants Bureau, New York, 1965.

[86] S. Chapman. *Philosophical Transactions of the Royal Society A: Mathematical, Physical and Engineering Sciences*, 216(538-548):279–348, 1916.

[87] D. Enskog. *Kinetische Theorie der Vorgänge in mässig verdünnten Gasen*. Almqvist & Wiksel, Uppsala, 1917. 54

[88] S. P. Hirshman and D. J. Sigmar. *Nuclear Fusion*, 1079, 1981. 54, 56

[89] R. Dux and A. G. Peeters. *Nuclear Fusion*, 40(10):1722, 2000. 56, 58, 123

[90] A. G. Peeters. *Physics of Plasmas*, 7(1):268, 2000. 58, 61, 123

[91] R. Dux, A. G. Peeters, A. Gude, et al. *Nuclear Fusion*, 39(11):1509, 1999. 58, 59, 60

[92] R. Guirlet, C. Giroud, and T. Parisot. *Plasma physics and Controlled Fusion*, (06):3–15, 2006. 58, 59, 61

[93] R. Dux. *Impurity transport in tokamak plasmas*. Habilitation at Universität Augsburg, 2004. 59, 60, 126

[94] M. R. Wade, W. A. Houlberg, and L. R. Baylor. *Physical review letters*, 84(2):282–5, 2000. 59, 62

[95] A. A. Ware. *Physical Review Letters*, (1):1–3, 1970. 60, 69

[96] C. Giroud, R. Barnsley, P. Buratti, et al. *Nuclear Fusion*, 47(4):313–330, 2007. 61

[97] N. T. Howard, M. Greenwald, D. R. Mikkelsen, et al. *Nuclear Fusion*, 52(6):063002, 2012. 61

[98] T. Pütterich, R. Dux, M. A. Janzer, and R. M. McDermott. *Journal of Nuclear Materials*, 415(1):S334–S339, 2011. 61

[99] E. J. Synakowski, B. C. Stratton, P. C. Efthimion, et al. *Physical Review Letters*, 65(18):2255–2258, 1990. 61

[100] E. J. Synakowski, P. C. Efthimion, G. Rewoldt, et al. *Physics of Fluids B: Plasma Physics*, 5(7):2215, 1993. 61, 72

[101] W. A. Houlberg, K. C. Shaing, S. P. Hirshman, and M. C. Zarnstorff. *Physics of Plasmas*, 4(9):3230, 1997. 62

[102] P. C. Efthimion, S. von Goeler, W. A. Houlberg, et al. *Physics of Plasmas*, 5(5):1832, 1998. 62

[103] P. C. Efthimion, S. Von Goeler, W. A. Houlberg, et al. *Nuclear Fusion*, 39(11Y):1905–1909, 1999. 62

[104] G. L. Jackson, J. Winter, T. S. Taylor, et al. *Physical Review Letters*, 67(22):3098–3101, 1991. 62

[105] S. de Peña Hempel. *Untersuchungen zum Transport leichter Verunreinigungen an ASDEX Upgrade*. PhD thesis, Technische Universität Mnchen, 1997. 62, 114

[106] L. D. Pearlstein and H. L. Berk. *Physical Review Letters*, 2(5):220–222, 1969. 65

[107] D. W. Ross and S. M. Mahajan. *Physical Review Letters*, 40(5):324–327, 1978. 65

[108] W. M. Manheimer and J. P. Boris. *Physical Review Letters*, 37(0):3–6, 1976. 65

[109] B. B. Kadomtsev and O. P. Pogutse. *Nuclear Fusion*, 67, 1971. 65

[110] C. W. Horton. *Physics of Fluids*, 15(4):620, 1972. 66

[111] S. C. Guo and F. Romanelli. *Physics of Fluids B: Plasma Physics*, 5(2):520, 1993. 66

[112] M. Frojdh, M. Liljestrom, and H. Nordman. *Nuclear Fusion*, 31(3):419, 1992. 67

[113] C. Angioni and A. G. Peeters. *Physical Review Letters*, 96(9):095003, 2006. 68

[114] C. Angioni, A. G. Peeters, G. V. Pereverzev, et al. *Nuclear Fusion*, 49(5):055013, 2009. 72, 118, 129, 132, 135, 146

[115] Y. Camenen, A. G. Peeters, C. Angioni, et al. *Physics of Plasmas*, 16(1):012503, 2009. 67, 68, 129

[116] C. Angioni, Y. Camenen, F. J. Casson, et al. *Nuclear Fusion*, 52(11):114003, 2012. 68

[117] D. L. Hillis, J. T. Hogan, K. H. Finken, et al. 196-198:35–44, 1992. 72

[118] H.-S. Bosch, W. Ullrich, D. Coster, et al. *Journal of Nuclear Materials*, 290-293:836–839, 2001. 73

[119] D. Reiter and S. Wiesen. *Transactions of fusion science and technology*, 45:261–270, 2004. 73

[120] A.Yu. Dnestrovskij, V.A. Krupin, L.A. Klyuchnikov, et al. Underestimation of ion temperature in CXRS diagnostics of D-alpha spectra. In *Proceedings of the 40th EPS Conference on Plasma Physics*, 2013. 86

[121] U. Gerstel, L. Horton, H. P. Summers, M. G. Von Hellermann, and B. Wolle. *Plasma Physics and Controlled Fusion*, 39(5):737–756, 1997. 114, 187

[122] Finkenthal D.F. *The measurement of absolute helium ion density profiles on the DIII-D tokamak using charge exchange recombination spectroscopy.* PhD thesis, University of California, Berkeley, 1994. 114, 118, 122, 145, 171

[123] V. Rohde, R. Neu, and R. Dux. *26th EPS Conference on Controlled Fusion and Plasma Physics*, 23:1513–1516, 1999. 119

[124] R. M. McDermott, C. Angioni, R. Dux, et al. *Plasma Physics and Controlled Fusion*, 53(12):124013, 2011. 120

[125] R. M. McDermott, C. Angioni, R. Dux, et al. *Plasma Physics and Controlled Fusion*, 53(3):035007, 2011. 120

[126] A. G. Peeters and D. Strintzi. *Physics of Plasmas*, 11(8):3748, 2004. 128

[127] A. G. Peeters, Y. Camenen, F. J. Casson, et al. *Computer Physics Communications*, 180(12):2650–2672, 2009. 128, 129, 171

[128] A. G. Peeters, C. Angioni, and D. Strintzi. *Physical Review Letters*, 98(26):265003, 2007.

[129] F. J. Casson, A. G. Peeters, C. Angioni, et al. *Physics of Plasmas*, 17(10):102305, 2010. 129

[130] H. Bindslev, F. Meo, E. L. Tsakadze, S. B. Korsholm, and P. Woskov. *Review of Scientific Instruments*, 75(10):3598, 2004. 148, 164

[131] R. De Angelis, M. G. von Hellermann, F. P. Orsitto, and S. Tugarinov. *Review of Scientific Instruments*, 79(10):10E517, 2008. 149, 161

[132] A. Kappatou, E. Delabie, R. J. E. Jaspers, and M. G. von Hellermann. *Nuclear Fusion*, 52(4):043007, 2012. 149, 172

[133] E. Delabie, R. J. E. Jaspers, M. G. von Hellermann, S. K. Nielsen, and O. Marchuk. *Review of Scientific Instruments*, 79(10):10E522, 2008. 149, 150

[134] G. R. McKee, R. J. Fonck, B. C. Stratton, et al. *Nuclear Fusion*, 37(4):501, 1997. 149, 151, 152, 163

[135] D. E. Post, D. R. Mikkelsen, R. A. Hulse, L. D. Stewart, and J. C. Weisheit. *Journal of Fusion Energy*, 1(2):129–142, 1981. 149

[136] M. Salewski, S. K. Nielsen, H. Bindslev, et al. *Nuclear Fusion*, 51(8):083014, 2011. 149

[137] W. G. F. Core. *Nuclear Fusion*, 29:1101, 1989. 150

[138] M. G. von Hellermann, E. Delabie, R. Jaspers, P. Lotte, and H. P. Summers. *AIP Conference Proceedings*, 1058(1):187–194, 2008. 151

[139] M. G. von Hellermann, R. Barnsley, W. Biel, et al. *Nuclear Instruments and Methods in Physics Research Section A: Accelerators, Spectrometers, Detectors and Associated Equipment*, 623(2):720–725, 2010. 151

[140] M. G. von Hellermann, W. Mandl, and H. P. Summers. *Plasma Physics and Controlled Fusion*, 33(14):1805, 1991. 152

[141] E. Di Pietro, A. Costley, T. Inoue, et al. *Fusion Engineering and Design*, 56-57:929–934, 2001. 153

[142] R. Hemsworth, H. Decamps, J. Graceffa, et al. *Nuclear Fusion*, 49(4):045006, 2009. 153

[143] M. G. Von Hellermann, W. G. F. Core, and A. Howman. Feasibility of quantitative spectroscopy on ITER. In *Diagnostics for Experimental Thermonuclear Fusion Reactors*, pages 321–330. 1996. 157

[144] J. F. Artaud, V. Basiuk, F. Imbeaux, et al. *Nuclear Fusion*, 50(4):043001, 2010. 160, 161

[145] J. Citrin, J.F. Artaud, J. García, G. M. D. Hogeweij, and F. Imbeaux. *Nuclear Fusion*, 50(11):115007, 2010.

[146] J. García, G. Giruzzi, J. Artaud, et al. *Physical Review Letters*, 100(25):1–4, 2008. 161

[147] F. P. Orsitto, J.-M. Noterdaeme, A. E. Costley, and A. J. H. Donné. *Nuclear Fusion*, 47(9):1311–1317, 2007. 161

[148] D. Ciric, B. C. Crowley, I. E. Day, et al. Performance of Upgraded JET Neutral Beam Injectors. Technical Report EFDAJETCP(10)07/16, 2010. 162

[149] S. Banerjee, P. Vasu, M. G. von Hellermann, and R. J. E. Jaspers. *Plasma Physics and Controlled Fusion*, 52(12):125006, 2010. 163

[150] R. J. Fonck. *Review of Scientific Instruments*, 56(5):885–890, 1985. 164

[151] F. Meo, H. Bindslev, S. B. Korsholm, E. L. Tsakadze, and C. I. Walker. *Review of Scientific Instruments*, 3585(2004), 2012. 164

[152] V. G. Kiptily, F. E. Cecil, and S. S. Medley. *Plasma Physics and Controlled Fusion*, 48:R59–R82, 2006. 164

[153] V. I. Afanasyev, M. I. Mironov, S. V. Konovalov, A. V. Khudoleev, and M. P. Petrov. 177(1), 2011. 165

[154] M. Sasao, M. Isobe, M. Nishiura, et al. Integration of Lost Alpha-Particle Diagnostic Systems on ITER. In *Proc. 9th IAEA Technical Meeting on Energetic Particles in Magnetic Confinement Systems (Takayama, Japan)*, 1995. 165

[155] M. G. von Hellermann, R. J. E. Jaspers, W. Biel, et al. *Review of Scientific Instruments*, 77(10):10F516, 2006. 166, 167, 180

[156] M. G. von Hellermann, R. Barnsley, W. Biel, et al. *Nuclear Instruments and Methods in Physics Research Section A: Accelerators, Spectrometers, Detectors and Associated Equipment*, 623(2):720–725, 2010. 166, 167

[157] S. Tugarinov, A. Krasilnikov, V. Dokouka, et al. *Review of Scientific Instruments*, 74(3):2075, 2003. 166

[158] R. J. E. Jaspers, M. G. von Hellermann, E. Delabie, et al. *Review of Scientific Instruments*, 79(10):10F526, 2008. 166

[159] R. Neu, R. Dux, and A. Kallenbach. Influence of the 4He concentration on H-mode confinement and transport in ASDEX Upgrade. In *35th EPS Conference on Plasma Physics*, volume 32, 2008. 173

[160] S. Menhart. *On the applicability of fast neutral He beams for fusion plasma diagnostics*. PhD thesis, Vienna University of Technology, 2000. 187

[161] H. D. Falter, M. Proschek, S. Menhart, et al. *Review of Scientific Instruments*, 71(10):3723, 2000. 187

[162] H. Anderson. *Collisional-radiative modelling of neutral beam attenuation and emission*. PhD thesis, University of Strathclyde, 1999. 187